INFORMATION TO USERS

This manuscript has been reproduced from the microfilm master. UMI films the text directly from the original or copy submitted. Thus, some thesis and dissertation copies are in typewriter face, while others may be from any type of computer printer.

The quality of this reproduction is dependent upon the quality of the copy submitted. Broken or indistinct print, colored or poor quality illustrations and photographs, print bleedthrough, substandard margins, and improper alignment can adversely affect reproduction.

In the unlikely event that the author did not send UMI a complete manuscript and there are missing pages, these will be noted. Also, if unauthorized copyright material had to be removed, a note will indicate the deletion.

Oversize materials (e.g., maps, drawings, charts) are reproduced by sectioning the original, beginning at the upper left-hand corner and continuing from left to right in equal sections with small overlaps. Each original is also photographed in one exposure and is included in reduced form at the back of the book.

Photographs included in the original manuscript have been reproduced xerographically in this copy. Higher quality 6" x 9" black and white photographic prints are available for any photographs or illustrations appearing in this copy for an additional charge. Contact UMI directly to order.

U·M·I

University Microfilms International
A Bell & Howell Information Company
300 North Zeeb Road, Ann Arbor, MI 48106-1346 USA
313/761-4700 800/521-0600

Order Number 9128954

Electron irradiation damage in transition metal oxides

Buckett, Mary Irene, Ph.D.

Northwestern University, 1991

U·M·I
300 N. Zeeb Rd.
Ann Arbor, MI 48106

NORTHWESTERN UNIVERSITY

ELECTRON IRRADIATION DAMAGE IN TRANSITION METAL OXIDES

A DISSERTATION

SUBMITTED TO THE GRADUATE SCHOOL

IN PARTIAL FULFILLMENT OF THE REQUIREMENTS

for the degree

DOCTOR OF PHILOSOPHY

Field of Materials Science and Engineering

By

Mary I. Buckett

EVANSTON, ILLINOIS

June 1991

ABSTRACT

ELECTRON IRRADIATION DAMAGE IN TRANSITION METAL OXIDES

Mary I. Buckett

It is well known that bombardment of oxides with low energy electrons or ions often leads to marked changes at the surface which can be attributed to effects that are initiated by both ballistic and electronic processes. This study focuses on the electron irradiation behavior of NiO, TiO_2 , and other transition metal oxides, occurring in-situ in the electron microscope. Surface-initiated radiation damage effects were investigated in terms of beam energy and flux, crystal orientation, and surface environment, under both UHV and non-UHV conditions. The sample environment was determined to be a major factor in the type of surface damage observed for NiO. Under UHV conditions, only ballistic surface erosion was observed, which resulted in the slow preferential sputtering of oxygen during 300 keV irradiation. Under non-UHV conditions, electron-stimulated reactions occurred in competition with ballistic processes. The synergistic response to both ionization and ballistic damage mechanisms generally resulted in more complicated surface structural changes and accelerated the erosion process. Reaction of the NiO surface with oxygen resulted in the formation of a Ni_3O_4 spinel phase. In the presence of carbon or CO, the NiO surface reduced to metallic nickel. Encapsulation by a graphitic carbon layer provided protection of the surface from electron irradiation damage.

Maximum valence transition metal oxides such as TiO_2, V_2O_5, MoO_3, WO_3, Nb_2O_5 and Ta_2O_5 were susceptible to electrons even at subthreshold energies.

In all cases, either reduction to the metal monoxide phase or to the base metal was observed. The extent and rate varied with each oxide.

The observed final phases did not fit criteria based on surface binding energy arguments, which have previously been used successfully for ion irradiation studies. Damage processes in the electron microscope did follow a simple symmetry selection rule, exhibited characteristics of radiation-enhanced diffusional processes, and were sensitive to the surface environment. It is concluded that the contribution of electronic damage mechanisms are significant even at the energies used for electron microscopy. The synergistic operation of defect migration processes contributes to an accelerated damage rate over and above that which would be predicted by any singular mechanism.

Approved:

_____

Dr. Laurence D. Marks

Department of Materials Science and Engineering
The Robert R. McCormick School of Engineering and Applied Science
Northwestern University
Evanston, Illinois
June 1991

ACKNOWLEDGEMENTS

Throughout the course of this work, there have been many people whose help and support were invaluable to me. First among these is Laurie Marks, under whose guidance, support, and motivation I have learned a great deal. We didn't always agree, but somehow, somewhere along this adventure I grew in character and confidence to be rewarded in the end with a piece of work we can both be satisfied with.

Secondly, my thanks goes out to the members of the Surface Radiation Damage Studies group and other members of our lab group. The type of research that we do demands total cooperation from everyone involved. These people are not only intelligent and insightful; they are diligent, hard workers. I feel extremely fortunate to have had the opportunity to work with them, and hope they feel the same about me.

Thirdly, I would like to thank the people whose discussions and suggestions over the years were extremely helpful: Prof. D. Seidman, Dr. J. P. Zhang, Dr. T. Wagner, Prof. D. Luzzi, Dr. K. Merkle, as well as the many people on the Argonne National Laboratory staff, and the members of the National Research Institute for Metals in Japan where I spent a very successful and enlightening summer.

Thanks also to the people who really run the show: Donna, our secretary, Joanna Gwinn, and the women in the departmental office.

I'd also like to acknowledge the many friends and acquaintances who've made these graduate school years most enjoyable - especially Rick, Shelly, John, Derren, Mr. Ma, Ajayan, Rena, Kathy, George, Kristen, Bruce, Jay, and the bright undergraduates whom I had the privilege to meet through being a teaching assistant, and who awarded me with one of my most prized possessions.

Last but not least, I would like to thank Norman, my parents and his, for their years of patience, understanding, and constant support. It is to Norman, who shared in all my triumphs and pitfalls, that I would like to dedicate this work. Upon acceptance of this thesis, I may finally graduate into the "real world" and new adventures to come.

This research was supported by the Air Force Office of Scientific Research grant 860344 DEF.

TABLE OF CONTENTS

LIST OF FIGURES

LIST OF TABLES

CHAPTER 1
INTRODUCTION

"The more one looks, the less one sees". - W. Heisenberg

The electron beam is one of the most sensitive probes to the atomic structure and chemistry of solids and among the most spatially specific. It is not, however, entirely benign. Generally electron microscopists try to minimize the effect of the ionizing beam on their experiments, but they are not always successful. It's a classic case of the experimenter unavoidably perturbing his experiment. For example, a number of microscopy studies have noted structural changes at the surface of oxides during observation. From the surface science literature, it is well known that bombardment of oxides with electrons or ions often leads to marked compositional and structural changes at or near the surface which can be attributed to effects that include collisional, electronic and thermal processes. The goal of this study is to exploit the radiation damage effects of the electron microscope beam in order to do in-situ structural characterization of the surface region and to elucidate the nature of the damage mechanism(s).

This study is funded by the Air Force Office of Scientific Research which is interested in the general effect of ionizing radiation in the space environment. The shuttle and other satellites orbit at altitudes between 250 – 300 km above the earth's surface. Base pressure at that altitude, known as low earth orbit (LEO), is approximately 10^{-9} Torr and the chemical composition is much more reactive, being comprised of ~80% atomic oxygen as shown in Figure 1.1. Spacecraft in LEO thus encounter a harsh environment which limits the survivability of their protective coatings (Haffner et al. 1988).

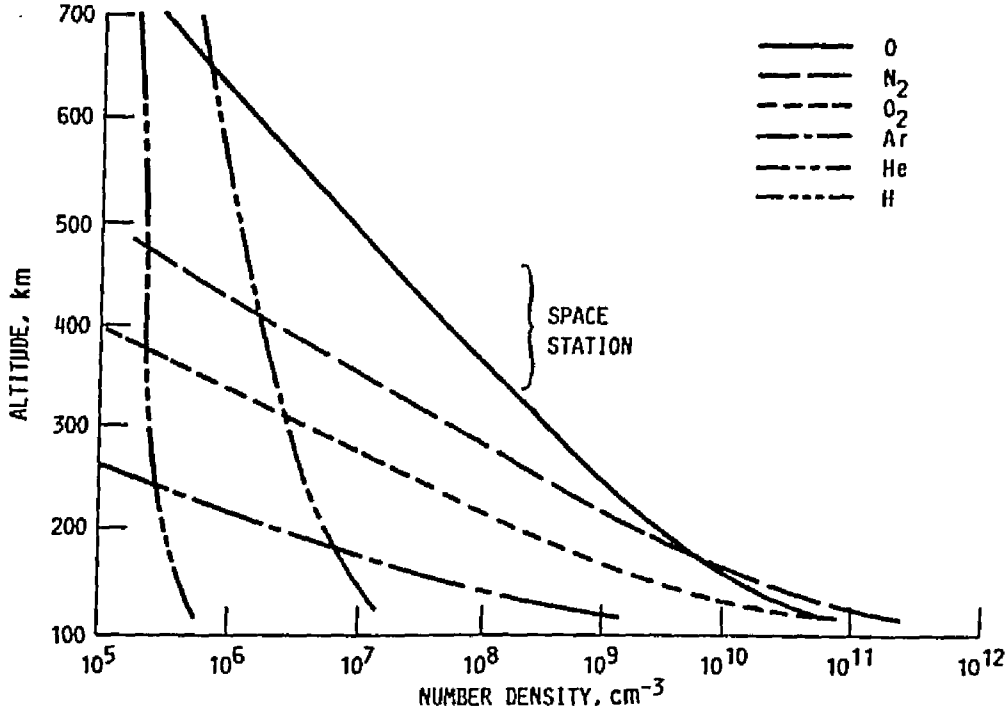

FIGURE 1.1 a) Atmospheric composition of LEO as a function of altitude. (U. S. Standard Atmosphere, 1976)

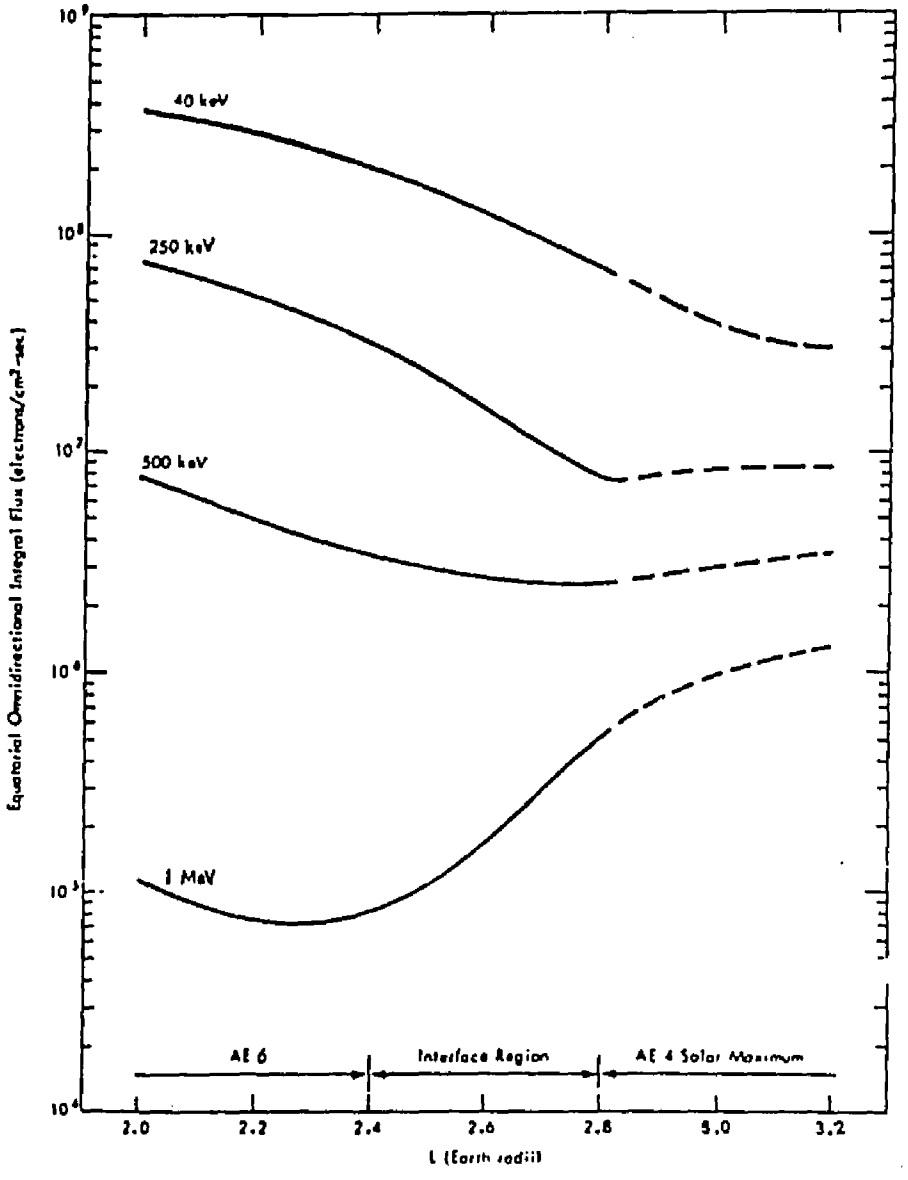

FIGURE 1.1 b) Calculated electron flux profile (e-/cm^{2}s) as a function of distance in earth radii, L. (courtesy of J. Lazar, Argonne National Laboratory).

A number of surface-related problems due to ionizing radiation have been encountered on the shuttle and other spacecraft: erosion; loss of gloss of thermal control paints; discoloring; loss of transparency and charging of protective coatings (Fellas and Richardson 1981); oxidation of thin films; and as shown in Figure 1.2, the shuttle glow phenomenon (Green and Murad 1986). This faint yellow-red glow is presumably due to a surface reaction initiated by atomic oxygen striking certain non-metallic surfaces which face into the orbital wind, leading to the formation of excited complexes. Atomic oxygen, a primary component of the LEO environment, has long been recognized as one of the leading causes of the glow as well as degradation to materials such as polyimides and carbon compounds. Preliminary analyses of spaceflight-exposed samples indicate that thin film metal oxides show potential as protective coatings for polyimide surfaces against atomic oxygen (Banks et al. 1985). How these oxides will fare after long duration exposures as well as a general criteria for stability of oxides towards radiation damage in ionizing environments are not well-established, thus the need for fundamental structural studies on the resulting surfaces.

For the purposes of this study, radiation damage will be defined as the primary microscopic events which precede the gross change and degradation in the macroscopic properties of a solid during irradiation. The study of radiation damage has two broad aspects. One is the qualitative characterization and classification of the types of damage. The other is concerned with the quantitative evaluation of effects under the most fundamental conditions in order to understand the underlying damage mechanisms. Under the appropriate experimental conditions, both of these aspects can be achieved with electron microscopy.

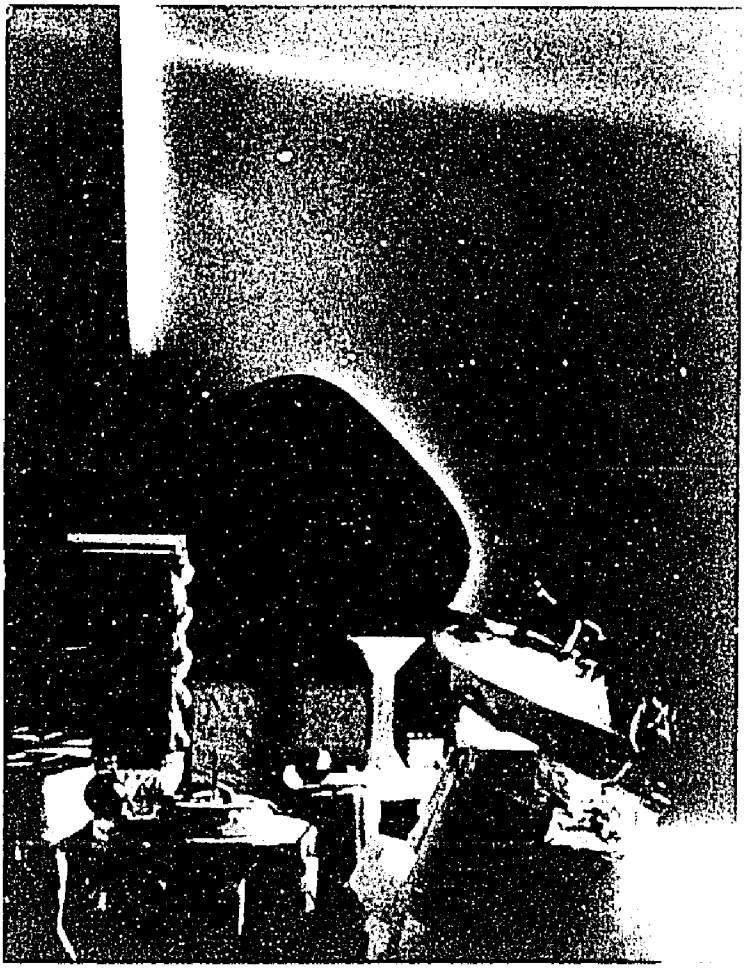

FIGURE 1.2 The yellow-orange shuttle glow phenomenon above nonmetallic surfaces facing into the orbital wind. Photo is of the exterior of the shuttle, looking into the payload bay. (Photo courtesy of E. Murad, Jet Propulsion Lab.)

Radiation damage of non-metallic solids in the electron microscope can be divided into two main categories as shown in Figure 1.3: **ballistic damage** due to direct knock-on momentum transfer and **ionization damage**, due to an initial electronic excitation which is coupled into atom displacement or expulsion from the surface via an indirect mechanism. Although the consequence may be the same for both, atomic displacements

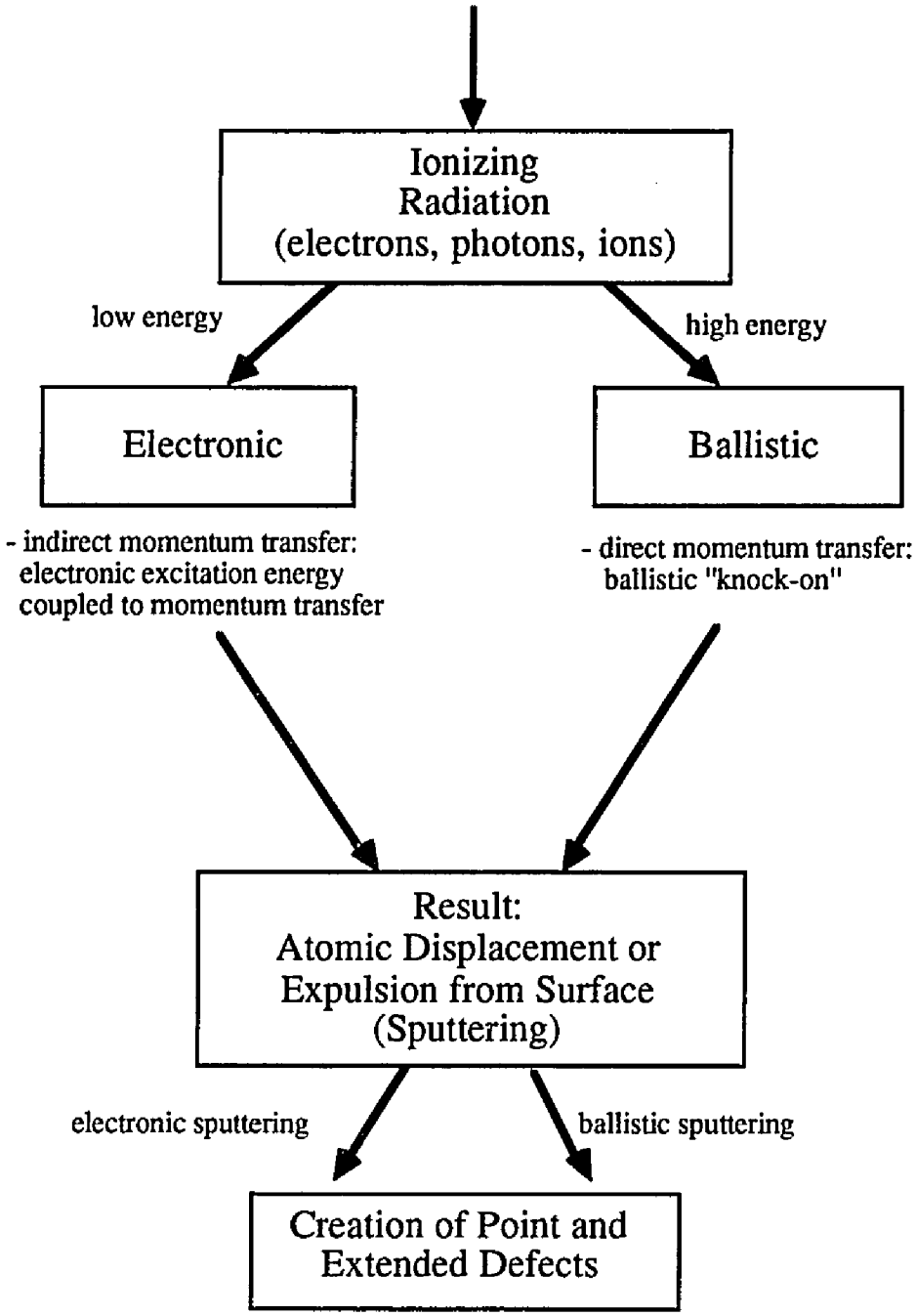

FIGURE 1.3 Schematic diagram of the pathways to radiation damage in the electron microscope.

or expulsion from the surface, the mechanisms by which they occur are certainly not similar and one can't really assume that the resulting structure would be either. For example, whereas both ions and high energy electrons can impart a substantial recoil energy to an atomic nucleus, only electrons are capable of imparting substantial ionization damage in these materials. Conventional microscopes operate with a beam energy large enough such that ballistic as well as electronic sputtering of the surface is possible in oxides. Chapter 2 of this study addresses the theoretical aspects of beam-solid interactions: energy deposition, and the primary mechanisms leading to radiation damage.

Shown in Table 1.1 is a comparison of the electron microscope and other ionizing environments. With the exception of actually sending materials up into space or placing them inside reactors, the electron microscope has long been recognized as an ideal place to study radiation damage under accelerated testing conditions. Electrons in the microscope are slowed as they pass through a crystal, losing kinetic energy at the rate of 10^7 eV/cm in most solids. Energy is being deposited at a density of approximately 10^5 J/mm^3 and at a rate of approximately 1 – 100 kW/mm^3. The survivability of materials in ionizing environments - such as fusion and fission reactors, and ion accelerators - has in fact been simulated and studied for a number of years with conventional electron microscopy (Clinard and Hobbs 1986).

An overwhelming majority of the existing microscopy studies of radiation damage have, however, focused on metals. The emphasis has been on bulk behavior such as amorphization, disordering, void and loop formation - involving high energy electrons (in the MeV range) and ballistic knock-on damage. This is at least in part due to: 1) the interest in fission and fusion reactor environments (fast neutrons, fission fragments); 2) the limitations in vacuum and instrument resolution; and 3) a slow development of the

TABLE 1.1

Typical radiation environments

A. Comparison of Various Ionizing Environments (Clinard and Hobbs 1986)

1. TEM
   type of radiation: 0.1 to 1.2 MeV ß
   typical dose rate (flux): $5x10^{19}$ e-/cm^{2}s = 8.0 C/cm^{2}s

   * need 10^4 to 10^5 e- / Å^2 to expose TEM film:
   10^4 e-/Å^2 = 16C/cm^2 (2 second exposure)

2. Space (maximum anticipated exposures)

   type of radiation: 10 keV to > 4 MeV ß
   typical dose rate (flux): $5x10^8$ e-/cm^{2}s = $8.0x10^{-11}$ C/cm^{2}s
   (flux varies with location and altitude, see below and Figure 1.1)

3. Fission Reactor

   Thermal
   type of radiation: 0.1 - 5 MeV neutrons
   typical dose rate (flux): $5x10^{13}$/cm^{2}s

   Breeder
   type of radiation: 0.1 - 5 MeV neutrons
   typical dose rate (flux): $1x10^{15}$ /cm^{2}s

4. Fusion Reactor

   type of radiation: 0.1 - 14 MeV neutrons
   typical dose rate (flux): $8x10^{14}$ /cm^{2}s

B. Typical Flux Data (e-/cm^{2}s), during a magnetic storm which started on June 11, 1980, measured by the USAF Space Test Program P78-2 spacecraft (Gaines et al. 1981).

e- Energy (MeV)	AE-4 (time ave. model)	June 10,1980	June 13, 1980	June 14,1980
1.0	$1.2x10^6$	$1.1x10^6$	$3.9x10^6$	$4.1x10^6$
1.5	$4.0x10^5$	$2.3x10^5$	$1.2x10^6$	$1.6x10^6$
2.0	$1.2x10^5$	$4.9x10^4$	$4.1x10^5$	$6.4x10^5$
2.5	$3.8x10^4$	$1.1x10^4$	$1.3x10^5$	$2.5x10^5$
3.0	$8.5x10^3$	$2.4x10^3$	$4.2x10^4$	$9.9x10^4$

microscopy theory and practice for imaging surfaces. The study of surfaces using electron microscopy techniques has therefore been limited.

With regard to radiation damage of surfaces, the overwhelming majority of studies look at the solid from the point of view of an ion or electron going in and a particle coming out. Thus there is substantially more information about the nature of the species exiting the surface - as produced by surface science experiments - than on the resulting structure left behind, where High Resolution Electron Microscopy (HREM) could make a contribution. In the past few years, new microscopy techniques - the most prominent of which is surface profile imaging - have been developed and instrumentation has been improved for the explicit study of surfaces. Publications have recently come out in the microscopy literature showing that a number of transition metal oxides surfaces undergo reduction during electron bombardment. These observations have been generally attributed to an electron-stimulated desorption mechanism first described by Knotek and Feibelman (1978a). There exists, however, considerable variation in the reported reduction path as well as the final phase identification. Chapter 3 of this study surveys the mechanisms of surface radiation damage in oxides.

Our group at the Surface Radiation Damage Studies Center, Northwestern University, is working toward the development of an Ultrahigh Vacuum (UHV) microscope with attached side transfer chamber (STC) for surface studies. At the outset it was recognized that HREM contributions to surface studies of electron-stimulated desorption (ESD) or electron-stimulated reaction (ESR) could only be considered valid if performed under surface science conditions or at least in controlled environments. The approach to the problem has been to set up a system where both species coming off the surface and the structure left behind can be studied as shown in Figure 1.4.

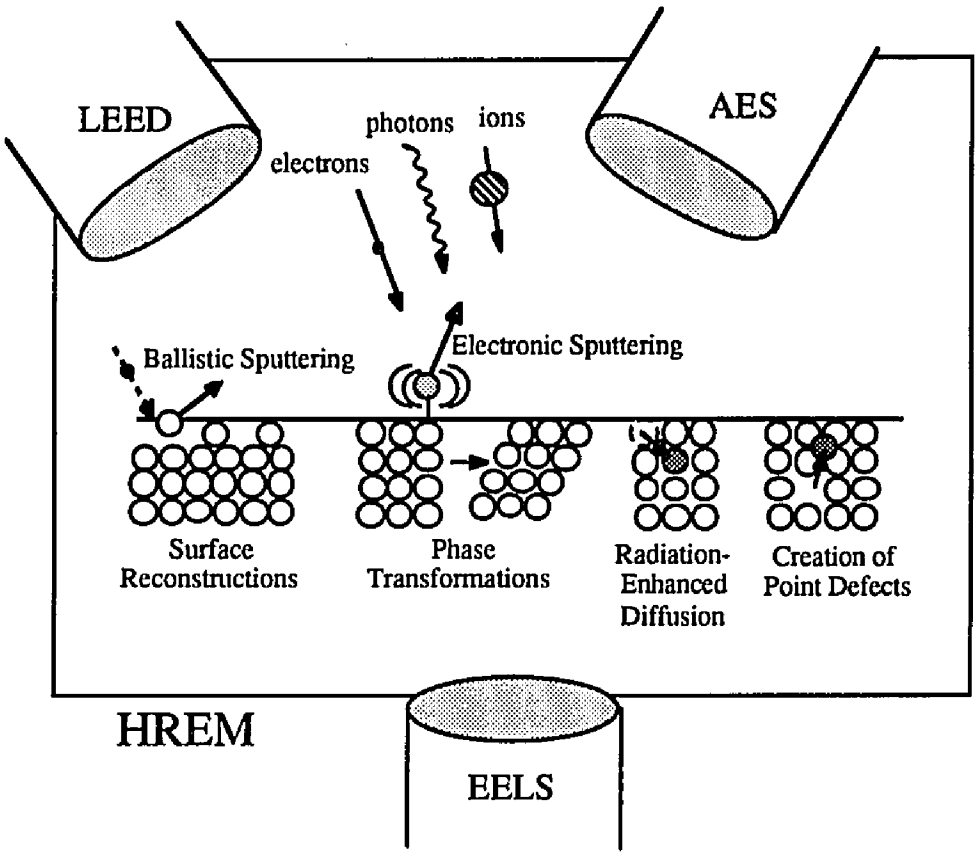

FIGURE 1.4 Schematic diagram of the types of surface processes occurring in the UHV-H9000 microscope and the analytical instrumentation available.

Unlike previous systems where an existing microscope was modified to accommodate UHV, the UHV-H9000 was designed at the outset to be a surface analytical instrument. The goal was to turn the conventional HREM into a UHV minilab to maximize the information that can be extracted form a given experiment. The system is being equipped with various analytical capabilities including Auger Electron Spectroscopy (AES), Electron Energy Loss Spectroscopy (EELS), and Low Energy Electron Diffraction (LEED), as well as instrumentation which includes various ion sputtering sources, an optical annealing source, a laser source, and an evaporation unit. Chapter 4

describes the instrumentation and outlines the experimental techniques which have been used in this study. It is the premise of the present investigation that, thus far, the existing HREM literature fails to consider two critical aspects of radiation damage in the electron microscope: 1) the possibility of a synergistic response of the material to both ballistic and electronic damage mechanisms; and 2) the previous studies were not done in UHV, therefore the ambient effects of the surface environment cannot be ruled out. Experiments were therefore set up such that the structural and chemical changes which occur in specific ionizing environments due to either electrons or ions of varying energy and flux could be studied. The incident electron energy was varied from the eV to the keV range and the incident flux was varied from a few A/cm^2 to over 100 A/cm^2, which is of the order of 10^{12} times the typical electron flux in space. Thus the electronic versus ballistic effects could be determined, which is an important consideration for ionic and semiconducting solids. The experiments were also set up to allow the surface environment to be varied in a controlled manner in order to evaluate the influence of vacuum conditions in the interpretation of results.

The approach of this study was to first survey a number of transition metal oxides to determine their relative stability under electron irradiation. Two oxides were then chosen for further detailed investigation - NiO and TiO_2. The surface science literature reports that NiO is generally stable under electron irradiation. A systematic, detailed investigation of electron irradiation damage in NiO was completed in terms of the dependence of electron energy and flux, crystal orientation, and ambient surface environment. Related oxides in the same series - CoO, MnO, and FeO - were also investigated. TiO_2 was chosen for further investigation primarily because it is considered to be the classic example of a material which undergoes electron-stimulated desorption

(ESD) due to an inter-atomic Auger decay mechanism valid for maximum valence transition metal oxides. Electron irradiation damage in TiO_2 was investigated in terms of electron energy and flux, and the ambient surface environment. A number of other maximum valence transition metal oxides were also investigated under similar irradiation conditions.

The goals of this study are threefold. The first is to characterize the evolving structure of the irradiated surface and the extent to which the damage penetrates into the bulk under conditions where effects of the surface environment are minimized, unlike all previous studies to date. The second is to evaluate the role of ballistic, electronic, and thermal effects contributing to damage production. The third is to investigate the extent to which the ambient surface environment affects the damage process under controlled conditions. These results are presented and discussed in Chapters 5 and 6. Finally, conclusions of the present study, suggestions for further investigation, and future directions of this work are given in Chapter 7.

CHAPTER 2
RADIATION DAMAGE IN SOLIDS
THEORETICAL CONSIDERATIONS

In this chapter the status of our understanding of radiation damage in nonmetallic solids is reviewed. Because of the wide variation in bonding and structure types, radiation damage in nonmetallic systems is more varied and complex than their well-studied metal counterparts. For example, in materials with multiple components, knock-on damage can be selective to one component over the other. Damage initiated on one sublattice often tends to stay on that sublattice, giving rise to specific orientation requirements for the direction of damage propagation. There can be very important differences in defects depending on their charge and/or excited state. Furthermore, impurities can play a critical role in defect processes (Sonder and Sibley 1972). These complexities are readily seen in the computer simulations (which have been applied quite successfully to the study of dynamic radiation damage processes in metals) of nonmetallic systems, where charge state and polarization effects need to be taken into account (Gehlen et al. 1972). But despite these substantial differences, there are also substantial similarities in the basic concepts. These concepts, which involve beam-solid interactions: energy transfer, cross sections, and stopping power, are discussed in Chapter 2.

2.1 - BEAM-SOLID INTERACTIONS: THE PHYSICAL PICTURE

The general fate of an irradiating particle is outlined in this section. Electrons and ions are charged particles and therefore interact via Coulomb fields with both **atomic nuclei** and **atomic electrons**, transferring energy via nuclear and electronic processes. Some of these processes will result in permanent atom displacements, while others will

give rise to only heat or some alternate non-damaging decay process. It is the permanent displacements which result in radiation damage: changes to the atomic structure, chemistry, electronic and optical properties (Figure 2.1); which lead to the formation of bulk defects, and finally to degradation of the structural integrity in the solid and macroscopic failure.

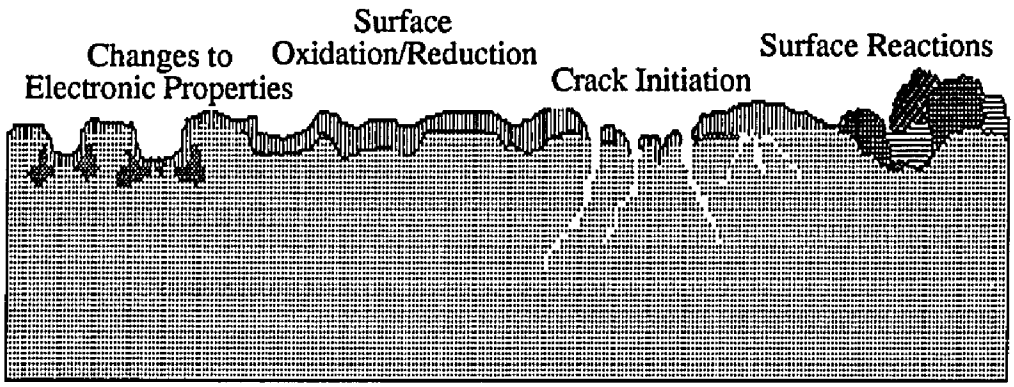

FIGURE 2.1 Macroscopic consequences of surface radiation damage.

Shown in Table 2.1 is a time scale of events along the radiation damage path. The primary beam-solid interaction occurs within a time frame of 10^{-19} to 10^{-23} second, with electron excitation lifetimes as well as atomic displacement occurring within 10^{-13} second, and subsequent processes requiring much larger time frames. Diffusion of radiation-induced point defects to sinks or recombination of electronic defects occurs in the order of 10^{-3} second. Phase transformations, the nucleation and growth of voids, sputtering of the surface, and other such structural changes occur within time periods of minutes to months. Finally, macroscopic, observable, and technologically critical structural effects occur after what may be months to years in real systems. The interplay of these damage processes involve a combination of ballistic, electronic, and thermal effects.

TABLE 2.1

Time scales for the various processes which affect radiation damage.

10^{-17} - 10^{-23} sec	Primary interactions of ionizing radiation.
10^{-16} - 10^{-17} sec	Typical hole or electron hopping times; typical lifetime for one electron excitations on surfaces; electronic relaxation in metals.
10^{-15} sec	Atomic motion may be affected by the presence of an electronic excitation.
10^{-15} sec	Time scale for the decay of deep-valence semiconductor holes.
10^{-14} - 10^{-15} sec	Time scale of valence Auger decay processes.
10^{-14} sec	Typical time scale for the decay of delocalized electronic excitations.
10^{-13}-10^{-14} sec	Displacement of atomic positions.
10^{-13} sec	Modification of the escaping species as it recedes from the surface.
10^{-13} sec	Time scale of a lattice vibration.
10^{-12} sec	Hole or exciton trapping at room temperature.
10^{-11} sec	Time scale of the low-energy excited electron states of the solid - decay of excitons in alkali halides to produce Frenkel pair, defect creation in amorphous semiconductors.
10^{-6} - 10^{-9} sec	Typical lifetime for allowed optic transitions.
10^{-3} sec	Typical lifetime for spin forbidden optic transitions.
$>10^{-3}$ sec	Diffusional processes.
$>10^{5}$ sec	Macroscopic property changes.

References: (Jennison 1983; Shvarts 1983; Hayes and Stoneham 1985)

2.1.1 - NUCLEAR VS. ELECTRONIC INTERACTIONS

Displacement damage resulting from interaction of the incident particle with an atomic nucleus is generally called knock-on, collisional, or ballistic damage. Nuclear collisions are the primary form of radiation damage in metals. They result in displacements from direct momentum and energy transfer from the irradiating particles if the energy imparted is large enough to displace an atom to an interstitial site or cause a Replacement Collision Sequence (RCS), which is an energy transfer process by nearly head-on collisions along a row of atoms with the net result that a vacant site appears at the starting location and an interstitial is lodged somewhere far down the line of atoms. Thus a displacement threshold energy, E_d, must be exceeded in order to create defects through collisions of this type. Energy transfer below E_d, results in low energy ($T_{min} \approx 10^{-2}$ eV) delocalized nuclear excitations or phonons which give rise primarily to heat.

Displacement damage resulting from interaction of the incident particle with the atomic electrons of the solid is called ionization damage or radiolysis. Electronic interactions encompass all processes where an electronic state is changed or charge is moved about by the absorption of energy (electronic excitation), with a number of possible energy transfer mechanisms ranging from heat to atomic displacements. Not all electronic interactions result in permanent displacements. In metals, for example, electronic interactions generally do not displace atoms as alternative energy decay processes are more favorable. In all systems, alternative energy transfer processes occur in competition with displacement or sputtering events. These include plasmon excitation, again producing heat, and radiative decay producing characteristic luminescence spectra.

In order for displacements to occur as a result of electronic interactions, a mechanism for conversion of the potential energy of the excitation into nuclear

momentum must exist. The criteria for damage production due to electronic excitation according to Hobbs (1979), are: (1) The excitation must be localized to only a few atom sites at most. (2) The excitation must have a lifetime comparable with phonon periods in order to couple into a mechanical response of the nuclear mass ($\approx 10^{-13}$ s). (3) The available excitation energy must be comparable to the atom displacement energy in its excited state. (4) The recombination energy must be substantially larger than the energy (heat of formation) required to form lattice defects. (5) An energy-to-momentum conversion must exist and compete favorably with other excitation decay modes.

In consideration of the above criteria, metals will not damage via electronic excitation because the excitations can be delocalized rapidly via the conduction band in times of the order of 10^{-14} second. On the other hand, electronic excitation may be of primary importance in nonmetals; however careful consideration of the specific mechanism for the specific material must be taken (Goland 1976). Hobbs (1979), identifies two criteria for the observance of radiation damage in nonmetallic solids: (1) available energy and (2) localization. Certain nonmetallic solids will not undergo displacement damage via electron excitation because the dominant excitations involve valence electrons which correspond to excitation energies of the order of the band gap, too low to couple to displacements. Narrow gap semiconductors therefore fail the available energy criterion. Collective excitations of the valence or conduction electrons (plasmons) fail to cause displacements in most cases because, although sufficiently energetic at 15 to 25 eV, they are not sufficiently localized except at the surface. Shown in Table 2.2 is a compilation of defect formation energies, band gaps, and mean ionization energies for a select group of oxides. From these considerations, it appears that wide gap semiconductors (e.g., TiO_2) and insulators (e.g., Al_2O_3, MgO) are the prime candidates

for ionization damage. Specific ionization damage mechanisms in these materials are discussed in Chapter 3.

TABLE 2.2

Defect formation energy, ΔH_f, versus mean ionization energy and band gap in oxides.

Oxide	Defect (eV per pair) $\Delta H_{f(S)}$	$\Delta H_{f(AF)}$	$\Delta H_{f(CF)}$	Mean Ionization Energy (≈ 8.8 Z) in eV	Band Gap (eV)
CaF_2	$\approx$ 5.5 (a)	2.3-2.8 (b)	$\approx$7 (c)	176.0 (Ca), 79.2 (F)	10.0
α-Al_2O_3	10.0	14.0	20.0	114.4 (Al), 70.4 (O)	9.5
MgO	7.72	17.2	13.0	105.6 (Mg), 70.4 (O)	7.8 (op) 7.3 (e)
CaO	6.8	12.4	10.4	176.0 (Ca), 70.4 (O)	6.6
UO_2	10.4	5.4	18.4	809.6 (U), 70.4 (O)	5.5 (op) 1.3 (e)
MnO	6.0	12.8	12.4	220.0 (Mn), 70.4 (O)	3.7
NiO	7.37	13.0	12.6	246.4 (Ni), 70.4 (O)	3.7
MoO_3	-----	-----	-----	396.6 (Mo), 70.4 (O)	3.75 (op) 1.4 - 1.7(e)
Nb_2O_5	-----	-----	-----	360.8 (Nb), 70.4 (O)	3.99 (e) 2.21 (e)
SnO_2	-----	-----	-----	440.0 (Sn), 70.4 (O)	3.53 (e)
ZnO	6.0	6.0	3.8	264.0 (Zn), 70.4 (O)	3.4
TiO_2	-----	-----	-----	193.6 (Ti), 70.4 (O)	3.03 (e)

TABLE 2.2 (continued)

Oxide	Defect (eV per pair) ΔH_f (S)	ΔH_f (AF)	ΔH_f (CF)	Mean Ionization Energy (≈ 8.8 Z) in eV	Band Gap (eV)
α-Fe_2O_3	7.8	10.0	10.0	228.8 (Fe), 70.4 (O)	2.3
ZrO_2	-----	4.1	-----	352.0 (Zr), 70.4 (O)	2.0 (e)
WO_3	-----	-----	-----	651.2 (W), 70.4 (O)	2.2 - 2.5(e)
Y_2O_3	-----	-----	-----	343.2 (Y), 70.4 (O)	1.70 (e)
V_2O_5	-----	-----	-----	202.4 (V), 70.4 (O)	0.5 (e)

Band gap: (e) = electronic, (o) = optical

ΔH_f (S) = Schottky pair formation energy

ΔH_f (AF) = anion Frenkel pair formation energy

ΔH_f (CF) = cation Frenkel pair formation energy

NB: The formation energy for Schottky and Frenkel defects is calculated as the sum of the energies to form the isolated vacancies and interstitials by removing the cations or anions to infinity, but reduced by the energy regained on returning the removed ions to the crystal surface (equal to the cohesive energy).

(a) for the reaction: null $\Leftrightarrow V_{Ca}^{''} + 2V_F^{\circ}$

(b) for the reaction: $F_F \Leftrightarrow V_F^{\circ} + F_i^{'}$

(c) for the reaction: $Ca_{Ca} \Leftrightarrow V_{Ca}^{''} + Ca_i^{\circ\circ}$

References: (Mackrodt 1984; Sangster and Rowell 1981; Kingery, Bowen, and Uhlmann 1960; Davis 1981; Dienes et al. 1975)

In summary, energetic charged particles - whether electrons or ions - will impart damage energy to the lattice via electronic excitations and nuclear collisions. Despite the fact that the mechanisms leading to the final damage event are uniquely different, both lead to permanent atomic displacements or expulsion from the surface. An important point is that both can be treated using probabilistic arguments. The bounding energy regimes and the relative contribution of nuclear versus electronic energy transfer can be evaluated from the appropriate cross sections and stopping power, dE/dx, for these processes.

2.1.2 - A COMPARISON OF MECHANISMS

Regardless of the type of interaction or beam, radiation damage occurs when enough energy is deposited into the specimen such that an atom is permanently displaced. Both ion and electron irradiations transfer energy for displacements primarily via Coulombic-type nuclear and electronic interactions and are treated similarly in theory with the exception of two significant differences: the electron carries a constant charge and has a very small mass. Both features give rise to differences in the interaction behavior with matter. Other energy transfer mechanisms also exist (e.g., bremsstrahlung, Compton scattering, pair production), however they are either not significant in the energy regimes of this study or they do not result in permanent damage to the lattice and therefore will not be described here.

As will be shown in the next section, nuclear and electronic processes are generally not effective at the same time. They rather dominate in different energy regimes for different incident particles as was alluded to in the introduction. For ion irradiation, displacement damage due to nuclear collisions dominates in the low energy regime,

whereas at extremely high energies the energy loss is dominated by electronic processes. This is illustrated in Figure 2.2 where the theoretical rate of energy loss is plotted against incident ion energy. E_Z and E_T represent limiting energies and are described in section 2.2.5. Ion irradiations are generally in the non-relativistic regime, losing a majority of the incident particle energy through nuclear collisions where large discrete amounts of energy may be transferred and multiple displacements per given collision may occur.

For high energy electron irradiation such as in the electron microscope, nearly the opposite is true. As will be shown in section 2.2.5, a majority of the incident energy that is lost goes into electronic interactions, processes which give rise to much smaller energy losses per collision. The energy loss rate for fast electron irradiation is shown in Figure 2.3 (Hobbs 1979). Displacement damage due to nuclear collisions only becomes significant when the energy transferred exceeds a certain threshold energy. Any sub-threshold damage is usually attributed to ionization processes and radiolysis. For electron irradiation in general, the amount of energy that goes into ionization energy loss dominates that which goes into collisional energy loss. In the electron microscope, for example, a majority of incident electrons (> 95%) travel through the crystal with essentially no loss of energy due to the thinness of the sample. Of the incident particle energy dissipated by energy loss encounters, most is dissipated in electronic excitations, with a only small fraction (0.1%) being expended in nuclear collisions (Seitz and Koehler 1958). Thermal effects are generally neglected by TEM studies, the validity of which is examined in section 2.4 of this chapter.

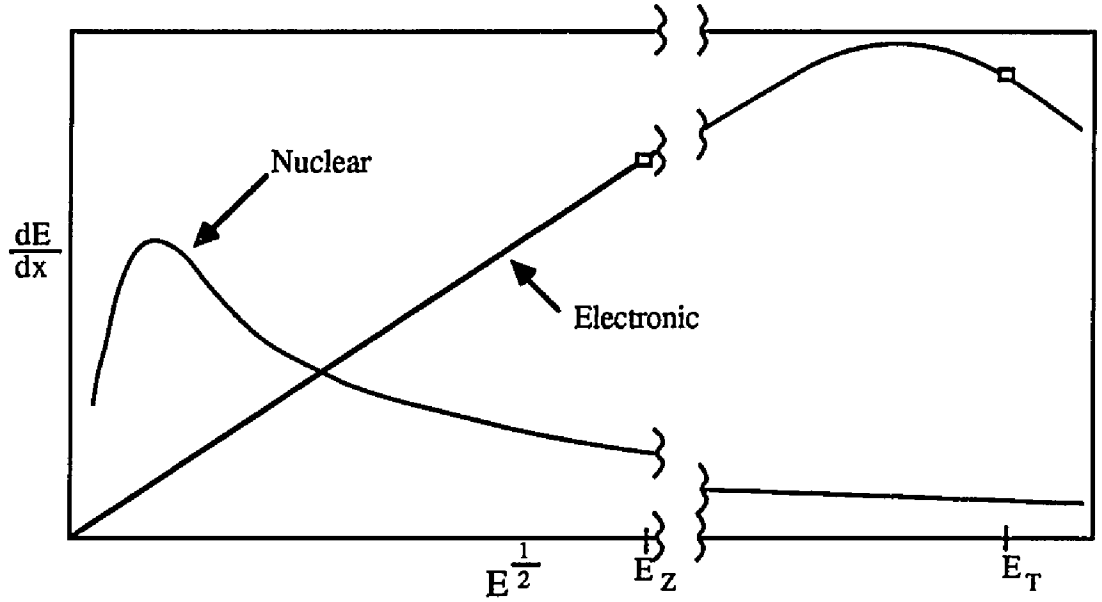

FIGURE 2.2 Theoretical energy loss rate, dE/dx, according to Lindhard, Scharff, and Schiott (1963). The energy loss rate increases with $E^{1/2}$ at low energies, but eventually peaks and falls off as E^{-1} in the high energy Rutherford range.

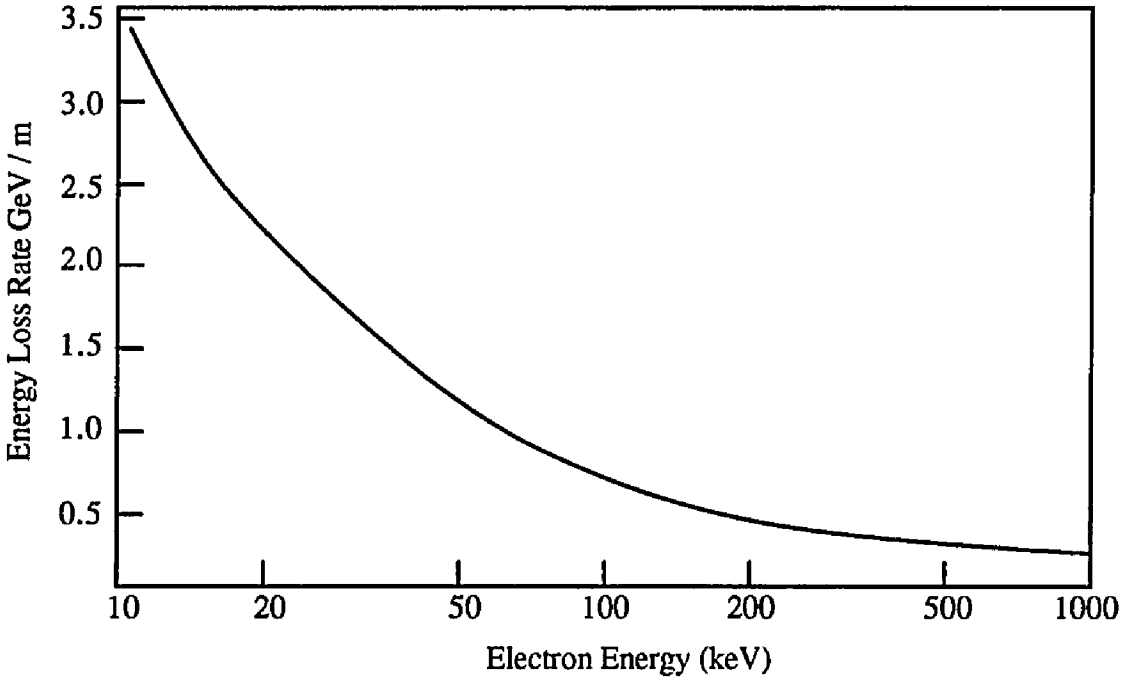

FIGURE 2.3 Theoretical energy loss rate according to the Bethe-Bloch expression (equation 2.33) for fast electron irradiation (Hobbs 1979).

2.2 - THEORETICAL 'TOOLS' AND CONSIDERATIONS

How does the irradiating particle type and energy affect the radiation damage process? What are the relative contributions of nuclear versus electronic processes to the total energy loss? We can begin to answer these questions by considering the theoretical concepts of cross section, $\sigma(E)$, interatomic potentials, $V(r)$, energy transfer from classical collision theory, and stopping power, dE/dx.

2.2.1 - CROSS SECTIONS

The theoretical treatment of beam-solid interactions can be traced to individual collisions between two particles, for example a bombarding ion and an atom of a solid. To fully describe these two-body collisions it is necessary to specify the relevant physical quantities such as mass, position, velocity and force between the two particles. The fate of the final particle (e.g., its momentum and energy) is completely determined by the initial momentum, the impact parameter, b, and the interaction potential of the two particles. In irradiation experiments, a large number of incident projectiles as well as target particles must be dealt with. There will be a wide variation in impact parameters, and thus deflection angles and energies. Although it is virtually impossible to keep track of each individual scattering event, one can derive a relation between the distribution of impact parameters and the distribution of scattering angles θ, and thus energies E, by means of an interaction cross section, $\sigma(\theta)$ or $\sigma(E)$.

Treatment of the problem is greatly simplified if we consider a homogeneous parallel beam of identical monoenergetic particles. Consider, for example, a single projectile passing through a solid consisting of N target particles per unit volume (Figure 2.4). If the incident particle strikes the front face of the dx-thick slice within any

of the projected areas, σ, a collision occurs. The probability of a collision between an incident particle of energy, E_1, with a target particle is given by $N\sigma(E_1)dx$. $\sigma(E_1)$ is the total interaction cross section for an incident particle of energy E_1, and is a measure of the probability of occurrence of a particular type of collision (energy transfer) between beam and solid.

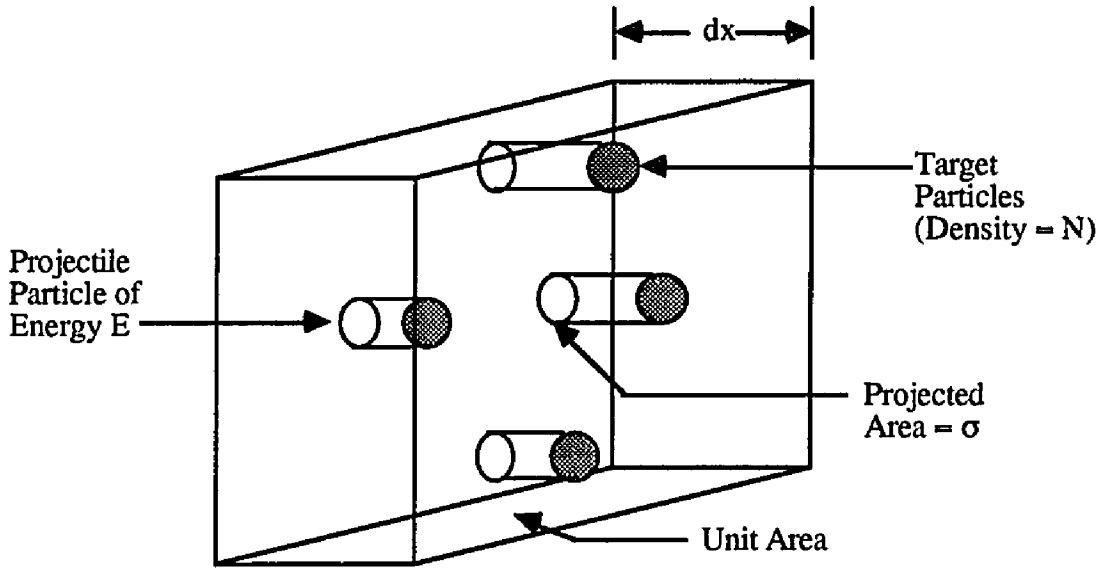

FIGURE 2.4 A projectile passing through a solid consisting of N target particles per unit volume, illustrating the concept of collision cross section (Olander 1976).

It is often more convenient to define a differential energy transfer cross section, $\sigma(E_1,T)$ by:

$$N\sigma(E_1,T)dTdx = \text{probability of a collision in the distance dx which transfers energy in the range (T,dT) to the target particle.} \quad (2.1)$$

where the total and differential cross sections are related by:

$$\sigma(E_1) = \int_{T_{min}}^{T_{max}} \sigma(E_1,T)\, dT \qquad (2.2)$$

with T_{min}, T_{max} the minimum and maximum energy transfer.

Integration of $\sigma(E_1,T)$ to yield the total probability, $\sigma(E_1)$, is usually a divergent quantity in classical collision theory. This divergence is usually immaterial, however, since the measurable quantities such as the number of displacements per atom (dpa) do not depend on the total cross section but on integration of the differential cross section from a minimum threshold energy to the maximum energy transfer. T_{max} and T_{min} are evaluated for both ion and electron irradiation in section 2.2.4.

2.2.2 - INTERATOMIC POTENTIALS

σ is uniquely determined by the interaction potential function, V(r), through the relation $d\sigma = 2\pi pdp$, although the connection is not easily evaluated. The momentum, p, can be evaluated in a number of ways, such as by utilizing the impulse approximation with the force equal to -dV(r)/dr.

Rutherford scattering is generally used to describe interactions where the energies are high enough such that the scattering is determined by the Coulomb repulsion between the nuclei, valid for all types irradiation considered in this study. Potential functions describing the scattering event may be considered purely repulsive and thus determined mainly by the inner shell electrons. Outer shell ionization has little influence on the scattering potential, thus it is assumed that there are negligible differences between atom

or ion irradiation. The appropriate potential to use depends essentially on the distance of closest approach, which in turn is dependent on the kinetic energy of the incident particle.

Unfortunately there is no single analytical form of an interatomic potential available for Rutherford scattering that is valid for all distances, r, between two colliding particles. Interatomic potentials for energies below approximately 200 eV are also not well known (Wedepohl 1969). A number of potential functions have been derived, but are applicable to only limited ranges of r, specific energy regimes, and specific interaction conditions. In principle, it is possible to transform any of the potential functions into a differential cross section. However, full analytical solutions to $\sigma(E_1,T)$ have been given for only the Coulomb and inverse square potential functions (Townsend, Kelly, and Hartley 1976).

Theoretical efforts generally treat statistical models of the atom, most notably the Thomas-Fermi model (Lehman 1977). This model treats the atom as a positive nucleus surrounded by a continuous distribution of atomic electrons; the distribution derived from quantum statistics and the Pauli principle. It is more accurate the higher atomic number, that is, the higher number of atomic electrons.

When the Rutherford interaction between two particles is such that the interaction distance is smaller than the radius of the inner shell electrons (such as the case for electron and high energy ion irradiations), the principle contribution to the total potential energy of the system is due to the electrostatic force between the stripped nuclear or electron charges. This situation is best described by the Coulomb potential:

$$V(r) = Z_1 Z_2 \frac{e^2}{r} \qquad (2.3)$$

For ion irradiations of intermediate energies, where screening by inner shell electrons occurs, a screened Coulomb potential of some form must be used. Here, the Thomas-Fermi model has been successfully applied by a number of theorists. The advantage of this approach, as was first treated by Firsov (1957, 1958a, 1958b) is that it yields a universal interaction potential between any two atoms. The form of the potential is:

$$V(r) = \frac{Z_1 Z_2 e^2}{r} \phi\left[\frac{-r}{a_p}\right] \tag{2.4a}$$

$$\text{with } a_p = \left(\frac{9\pi^2}{128}\right)^{1/3} \frac{a_B}{\left(Z_1^{1/2} + Z_2^{1/2}\right)^{2/3}} \tag{2.4b}$$

a_B = Bohr radius (0.529 Å) and r = internuclear distance.

The above relation essentially describes a screened Coulomb potential, with $\phi(r/a_F)$ being the Thomas-Fermi screening radius and a_F, Firsov's characteristic screening length. Values of $\phi(x)$ with $x = r/a_F$ have been given by:

Wedepohl (1968): $\phi(x) = Axe^{-kx^{1/4}}$; $0.3 \le x \le 16$, $A = 317$, $k = 6.62$ (2.5a)

Lindhard et al. (1968): $$\phi(x) = 1 - \frac{x}{\left(x^2 + 3\right)^{1/2}} \tag{2.5b}$$

Sommerfeld (1932): $$\phi(x) = \left\{1 + \left(\frac{x}{\alpha}\right)^{\beta}\right\}^{-\gamma};\ \alpha = 5.2,\ \beta = 0.8,\ \gamma = 3.7 \tag{2.5c}$$

To date, the Thomas-Fermi type of potential yields the best description of

interaction between not too light atoms in the regime of internuclear separations of interest to most irradiation conditions ($r \leq 1$ Å). Lindhard and coworkers (Lindhard et al. 1968), did a comprehensive study of scattering by screened Coulomb potentials and matched such potentials to inverse power law potentials $V(r) = C/r^m$ over limited intervals of r. Sigmund (1969a), expanded on this concept to delineate three regimes: high energies where m=1, medium energies where m=1/2, and very low energies where m=0. (These regions were illustrated in Figure 2.2). The advantage of this treatment is that an analytical solution for the entire energy range can be obtained for $\sigma(E,T)$ as will be shown in section 2.2.4.

2.2.3 - ENERGY TRANSFER FROM CLASSICAL COLLISION THEORY - UPPER AND LOWER BOUNDS

The classical ballistic transfer of energy between a moving and a stationary charged particle depends only on the mass and charge of the two point particles, and the moving particles' initial speed and direction. While the moving charge passes, the stationary particle recoils and absorbs energy. The moving particle is deflected and the final velocities and trajectories can be found from the conservation of momentum and energy of the system. Depending on the type of irradiating particle - ions, neutrons, or electrons - the maximum energy transferable and the transferred energy spectrum for ballistic collisions may vary significantly. The differences for electrons arise primarily because of relativistic effects. And although T_{max} is identical for ions and neutrons, neither the average energy nor the energy spectra coincide.

UPPER BOUNDS

The general form of the equation for energy transfer due to nuclear collisions between an incident particle of mass M_1 moving with a non-relativistic velocity, v, and kinetic energy $E_1 = mv^2/2$, and a stationary particle of mass M_2, is:

$$T = \frac{4M_1M_2}{(M_1 + M_2)^2} E_1 \sin^2\left(\frac{\theta}{2}\right) \tag{2.6}$$

where θ = scattering angle in the center of mass coordinate system. It can be seen that the maximum energy transfer is for the head-on collision given by:

$$T_{max} = \frac{4M_1M_2}{(M_1 + M_2)^2} E_1 \tag{2.7}$$

The above equations are normally valid for all ion irradiations, since they usually occur under nonrelativistic conditions where incident ion velocities, v, much smaller than the speed of light, c. (For convenience of calculation, the system coordinates are often transformed from the lab system to the center-of-mass system.)

The above relations are not applicable for all electron irradiations, for which relativistic effects must be considered when electron velocities, v, approach the speed of light, c, (above approximately 100 keV). For relativistic electrons, equations (2.6) and (2.7) become:

$$T = \frac{2(m_e v)^2}{M} \sin^2\left(\frac{\theta}{2}\right) \tag{2.8}$$

with a maximum transferred energy, T_{max}, for a head-on collision of:

$$T_{max} = \frac{2E_1(E_1 + 2m_ec^2)}{M_2c^2} \tag{2.9}$$

Equation 2.9 is obtained by using conservation of momentum and energy principles, which give:

$$T_{max} = \frac{2(p_1c)^2}{m_2c^2} \tag{2.10}$$

where p_1 is the momentum of the incident electron and is evaluated from the total energy relation for the electron:

$$E_{tot} = E_1 + m_ec^2 \text{ and } E_{tot}^2 = (p_1c)^2 + m_e^2c^4 \tag{2.11}$$

The center of mass coordinate system is essentially the same as the laboratory system in this case. Plotted in Figure 2.5 are values of T_{max} versus E_1 for various elements. Later it will be shown that in order for ballistic displacements to occur, T_{max} must exceed the threshold displacement energy E_d.

For collisions of incident ions with atomic electrons, the maximum energy transfer is given by equation (2.7) with m_e replacing M_2:

$$T_{max} = 4\frac{M_1m_e}{(M_1 + m_e)^2}E_1 \approx 4\frac{m_e}{M_1}E_1 \tag{2.12}$$

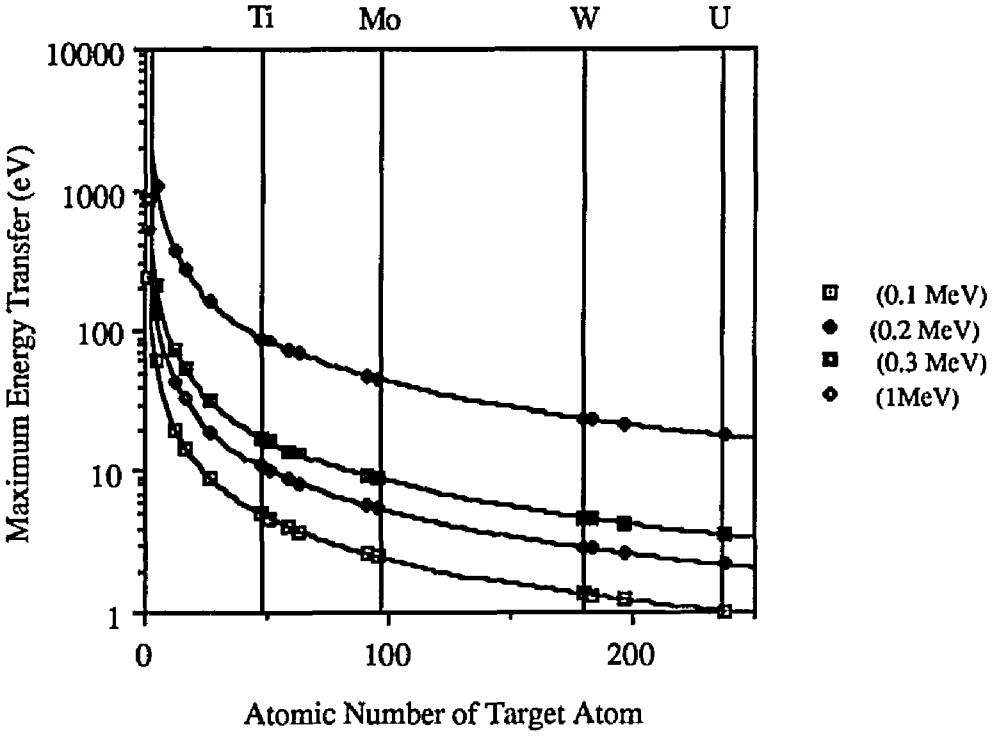

FIGURE 2.5 Maximum energy transfer (Eqn. 2.9) vs. atomic number of target atoms, at incident electron energies of 100, 200, 300 keV and 1 MeV.

In contrast, the maximum energy transfer for incident electrons to atomic electrons (Heitler 1954) is generally approximated by:

$$\frac{1}{2}(E_{tot} - m_e c^2) \text{ or } \frac{E_k}{2} \tag{2.13}$$

with E_k the kinetic energy of the incident electron.

LOWER BOUNDS

T_{min} for nuclear interactions can theoretically be as small as 10^{-2} eV (phonon energy) but is usually set at E_d, the threshold displacement energy or the minimum ballistic energy transfer required to cause a displacement event. For any collisions other than head-on, the resulting trajectories of both particles move at some angle to the incident particle particle trajectory with some energy transfer less than T_{max}. As shown in the preceding section, the probability for all such collisions can be expressed in terms of the differential cross section $\sigma(E_1,T)$. For nuclear collisions, integration of this differential probability between a T_{min} equal to E_d and T_{max} gives an overall probability expressed as the displacement cross section, $\sigma_d(E_1)$. Experimental determinations of E_d are presented in section 2.3.

The minimum energy transfer to atomic electrons is dependent on the type of interaction. General treatments by Bloch (1933) and Fano (1963) have equated T_{min} to I, the mean ionization potential which can be approximated by the range 8.8 Z_2 to 13.5 Z_2 (in eV). There is, however, considerable variation in evaluating the lower limits for electronic interactions (Sosin and Bauer 1969). In metals, a first order approximation for T_{min} can be given as 1/2 E_F, E_F being the Fermi energy. In nonmetallic solids, the

bandgap energy E_g is also used as an approximation to T_{min}.

2.2.4 - CROSS SECTIONS FOR NUCLEAR INTERACTIONS, $\sigma_n(E)$

Using the concept of cross section and having defined the boundaries of the energy transfer, we can now determine the interaction probability distributions $\sigma_n(E_1,T)$ for both ion and electron irradiations. As has been previously stated, nuclear scattering of nonrelativistic charged particles by the Coulomb field of a point nucleus was first treated by Rutherford. The differential scattering cross section for classical Rutherford scattering is given by:

$$\sigma(E_1,T) = 2\pi pdp = \frac{\pi b^2}{4}\cos\left(\frac{\theta}{2}\right)\csc^3\left(\frac{\theta}{2}\right)d\theta = \frac{\pi b^2}{4}T_{max}\frac{dT}{T^2} \qquad (2.14)$$

where p is the momentum, b is the classical distance of closest approach and defined by:

$$\frac{|e_1e_2|}{b} = \frac{\mu v^2}{2} \qquad (2.15)$$

with: e_1e_2 = charges of the interacting particles

μ = reduced mass of the system; $\mu = (M_1M_2)/(M_1+M_2)$

v = velocity of the incident particle

ELECTRON IRRADIATION

Evaluation of relation (2.14) yields the general forms of $\sigma_n(E_1,T)$ and $\sigma_n(E_1)$. For non-relativistic incident electrons of mass m_e, the nuclear cross sections are given by:

$$\sigma_n(E_1,T) = \pi Z^2 e^4 \left(\frac{m_e}{M_2}\right)\left(\frac{1}{E_1 T^2}\right) \tag{2.16}$$

$$\sigma_n(E_1) \approx \pi Z^2 e^4 \left(\frac{m_e}{M}\right)\left(\frac{1}{E_1 T_{min}}\right) \tag{2.17}$$

with T_{max} given as $4(m_e/M)E_1$.

A relativistic treatment of electron scattering was first considered by Darwin (1913). The differential nuclear scattering cross section for relativistic electrons differs from the Rutherford cross section by replacement of m_e with the relativistic mass $m_e/(1-\beta^2)^{1/2}$, where $\beta = v/c$, and is given by:

$$\sigma_n(E_1,T) = 4\pi\left(\frac{Ze^2}{2m_e v^2}\right)^2\left(1-\beta^2\right)\left(\frac{T_{max}}{T^2}\right) \tag{2.18}$$

The full relativistic extension (valid for electron irradiations in the electron microscope) was made by Mott (1929). Mott and Massey (1965) also derived a more rigorous solution for $\sigma_n(E_1)$ by expressing the scattering between a point nucleus and an electron as an infinite series of Legendre expansions. Simpler approximations for the Mott series solution have been presented, most notably by McKinley and Feshbach (1948):

$$\sigma_n = Z^2 4\pi a_H^2 U_R^2 \left(\frac{1-\beta^2}{m_e^2 c^4 \beta^4}\right)\left\{\left(\frac{T_{max}}{T_{min}}\right) + 2\pi\alpha\beta\left(\frac{T_{max}}{T_{min}}\right)^{1/2} - \left(\beta^2+\pi\alpha\beta\right)\ln\left(\frac{T_{max}}{T_{min}}\right) - \left(1-2\pi\alpha\beta\right)\right\} \tag{2.19}$$

where a_H = Bohr radius (52.9×10^{-12} m)

U_R = Rydberg energy (13.6 eV)

Z = Atomic Number

α = Z/137

β= v/c

The McKinley-Feshbach approximation is sufficiently accurate for light elements ($Z \leq 29$), but for heavy elements, the full Mott expression for $\sigma_n(E)$ is required. The total Mott cross sections have been evaluated by Bradley (1988) for all naturally occurring elements up to Z=92 at displacement energies of one, two, four, and five times the sublimation energy and for typical TEM accelerating voltages.

ION IRRADIATION

For an incident ion of mass M_1 moving with a non-relativistic velocity, v, and energy, E_1, and a stationary particle of mass M_2, the differential cross section is given by:

$$\sigma_n(E_1,T) = \pi(Z_1Z_2e^2)^2\left(\frac{M_1}{M_2}\right)\left(\frac{1}{E_1T^2}\right) \qquad (2.20)$$

$$\sigma_n(E_1) \approx \pi(Z_1Z_2e^2)^2\left(\frac{M_1}{M_2}\right)\left(\frac{1}{E_1T_{min}}\right) \qquad (2.21)$$

where Z_1e and Z_2e are the nuclear charges of incident particle and target respectively.

As was illustrated in Figure 2.2, there are three distinct regions of interest. In region 1, the high energy Rutherford scattering regime, relations (2.20) and (2.21) for ion irradiation are valid. Sigmund (1981) further described this region as the energy range where $\varepsilon >> 1$, with ε given by:

$$\varepsilon = \left(\frac{(M_2E_1)}{(M_1 + M_2)}\right)\left(\frac{a}{(Z_1Z_2e^2)}\right) \tag{2.22}$$

where a is the screening radius given by equation 2.25 below.

In regions 2 and 3, at lower ion energies ($\varepsilon \leq 1$), screening of the Coulomb interaction becomes significant and the differential cross section can be approximated using the Thomas-Fermi inverse square potential (Sigmund 1969a):

$$\sigma(E_1,T) \approx C_m E^{-m} T^{-(1-m)} \tag{2.23}$$

$$\text{with} \quad C_m = \left(\frac{\pi}{2}\right)\lambda_m a^2 \left(\frac{M_1}{M_2}\right)^m \left(\frac{2Z_1Z_2e_2}{a}\right)^{2m} \tag{2.24}$$

$$a = 0.885a_H(Z_1^{2/3} + Z_2^{2/3})^{-1/2} = \text{screening radius} \tag{2.25}$$

a_H = Bohr radius (0.529 Å for the above equation)

The three energy regimes can be described quite adequately by the fitting parameter, m. This parameter varies slowly from m=1 at high energies (approaching the Rutherford scattering regime) to m = 0 at very low energy encounters. λ_m is a dimensionless function of m which varies from $\lambda_1 = 0.5$ to $\lambda_0 = 24$. Shown in Table 2.3 is a summary of the behavior of $\sigma(E_1,T)$ in the three energy regimes.

TABLE 2.3

Form of the energy dependence of $\sigma_n(E_1,T)$ and $\sigma_e(E_1,T)$ for ion irradiations.

Energy Range	m	λ_m	Energy Dependence
high energy ($\varepsilon>>1$)	1.0	0.5	$E^{-1}\,T^{-2}\,dT$ (approaching the Rutherford range)
medium energy ($\varepsilon\approx1$)	0.5	0.327	$E^{-1/2}\,T^{-2/3}\,dT$
very low energy ($\varepsilon<<1$)	0.0	24	$T^{-1}dT$

2.2.5 – CROSS SECTIONS FOR ELECTRONIC INTERACTIONS, $\sigma_e(E)$

In a similar fashion, the Rutherford differential cross section for an ion or electron beam interaction with Ze free electrons at rest can be used to evaluate the probability of electronic interactions.

ION IRRADIATION

For ion irradiations, the same energy criteria as for the nuclear cross section apply. In Region 1 ($\varepsilon >> 1$), energy loss is primarily by electronic excitations. The irradiating particle is essentially stripped of its outer shell electrons and its bare nucleus of charge Z_1e interacts with the target electrons via a Coulomb potential (Rutherford scattering). Including an extra factor of two due to a quantum mechanical correction, the differential electronic cross section is given by:

$$\sigma_e(E_1,T) = 2\pi(Z_1e^2)^2\left(\frac{M_1}{m_e}\right)\left(\frac{1}{E_1T^2}\right) \tag{2.26}$$

$$\sigma_e(E_1) \approx 2\pi(Z_1e^2)^2\left(\frac{M_1}{m_e}\right)\left(\frac{1}{E_1T_{min}}\right) \tag{2.27}$$

At lower incident ion energies, the probability of capturing an electron from the medium increases. That is, screening of the Coulomb potential is occurring and can be treated in essentially the same manner as for $\sigma_n(E)$ at lower energies (Table 2.3) with the appropriate bounding energies.

ELECTRON IRRADIATION

In the non-relativistic regime, $\sigma_e(E_1)$ for electron irradiation can be approximated by:

$$\sigma_e(E_1) = Z(\pi e^4)\left(\frac{1}{E_1T_{min}}\right) \tag{2.28}$$

where all variables have the same meaning as previously stated except T_{min}, which in this case is the minimum excitation energy for bound or quasi-bound electrons as discussed in section 2.3.2 and the maximum energy given by $T_{max} = (1 / 2)E_1$.

Useful comparisons can be made by evaluating the nonrelativistic versions of interaction cross sections as given by (2.18) and (2.19) for electron irradiation (for target of atomic number, Z, and atomic mass, M):

$$\sigma_n(E_1) \approx (3.57\text{x}10^{-18})\frac{Z^2}{ME_1} \text{ in}(cm^2) \tag{2.29}$$

with: E_1 in eV, $T_{min} = 10\,eV \approx E_d$

$$\sigma_e(E_1) \approx (3.26\times10^{-14})\frac{Z}{E_1} \text{ in } (cm^2) \qquad (2.30)$$

with: E_1 in eV, $T_{min} = 2\,eV$

Although only the non-relativistic cases are being considered here, a number of features can readily be seen. First is that σ_e is of the order of 10^5 times larger σ_n, illustrating that most of the energy lost by fast electrons in a solid is due to electronic excitations. A comparison of more rigorous evaluations of $\sigma_n(E_1)$ and $\sigma_e(E_1)$ was presented in Corbett and Bourgoin (1975) and Corbett (1979), reproduced in Figure 2.6(a-b) to verify that neglecting the relativistic effects in the simple treatment above has not affected the form or the comparison of the two cross sections, only their absolute magnitudes. It is also interesting to note how $\sigma_n(E_1)$ is affected by different choices of displacement threshold energy.

McGuire (1977) performed a more detailed calculation of $\sigma_e(E)$ than what is presented here for electron energies up to 10 keV in a number of elements. These results are presented in Figure 2.7 to illustrate the general energy dependence of $\sigma_e(E_1)$. In addition, Drinkwine and Lichtmann (1977) determined that for a given system the total cross-sections for electron-stimulated processes are generally of the order of 10^{-18} cm^2 and do not vary by more than a factor of four for the energy range 50 to 50,000 eV. The points to note are that the cross sections for electronic interactions are significantly larger than for nuclear interactions and they are predominantly decreasing with increasing electron energy in the range of TEM applications.

In reality, the Z and E dependence of $\sigma_e(E)$ is irregular due to the interplay of various types of electronic excitations. Therefore a simple relation for this value as a function of energy is difficult to derive especially in the relativistic range. A rigorous approach to the problem has been presented by Inokuti et al. (1978). For the purposes of this study, however, the interaction cross sections as presented above are adequate to illustrate the relative contributions of nuclear and electronic interactions and their energy dependence.

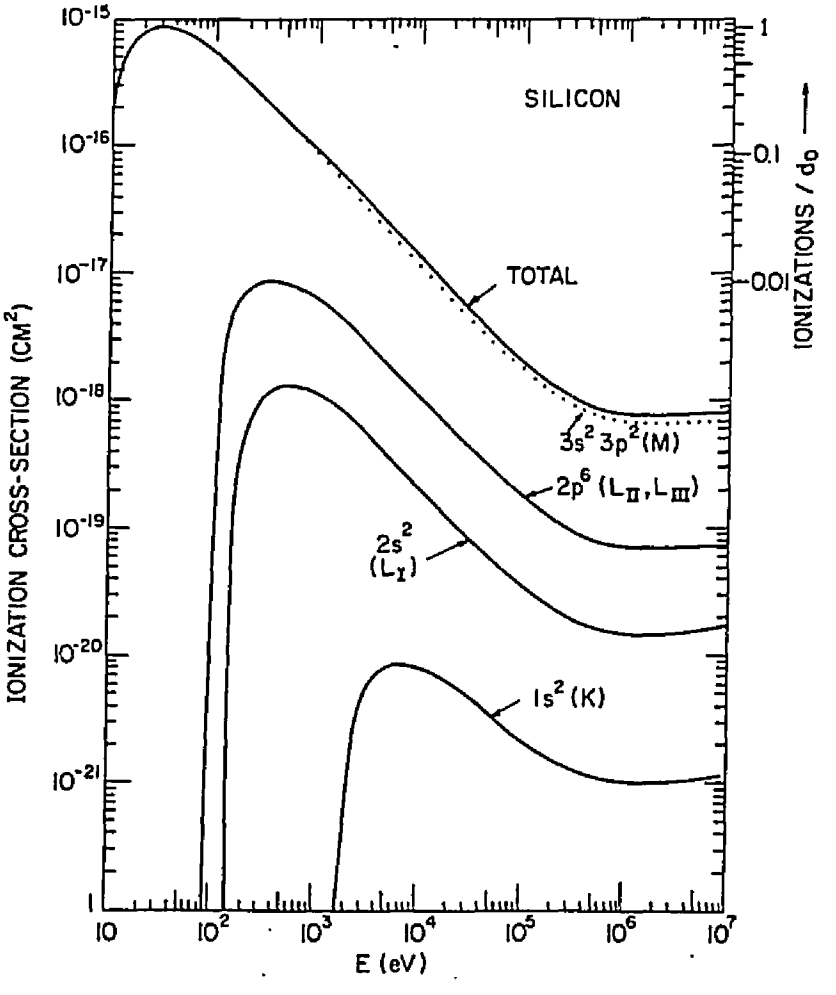

FIGURE 2.6 a) Ionization cross-section per atom (cm^2) for various atomic shells versus incident electron energy in Si (Corbett 1979).

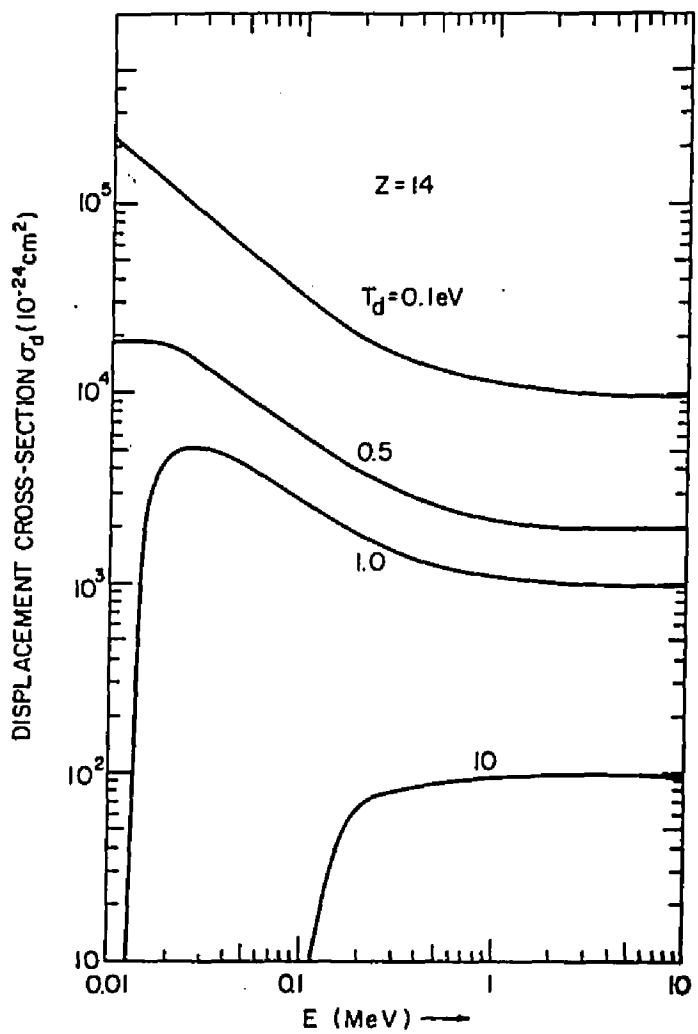

FIGURE 2.6 b) Displacement cross-section per atom (cm^2) for various displacement threshold energies, E_d, versus incident electron energy in Si (Corbett 1979).

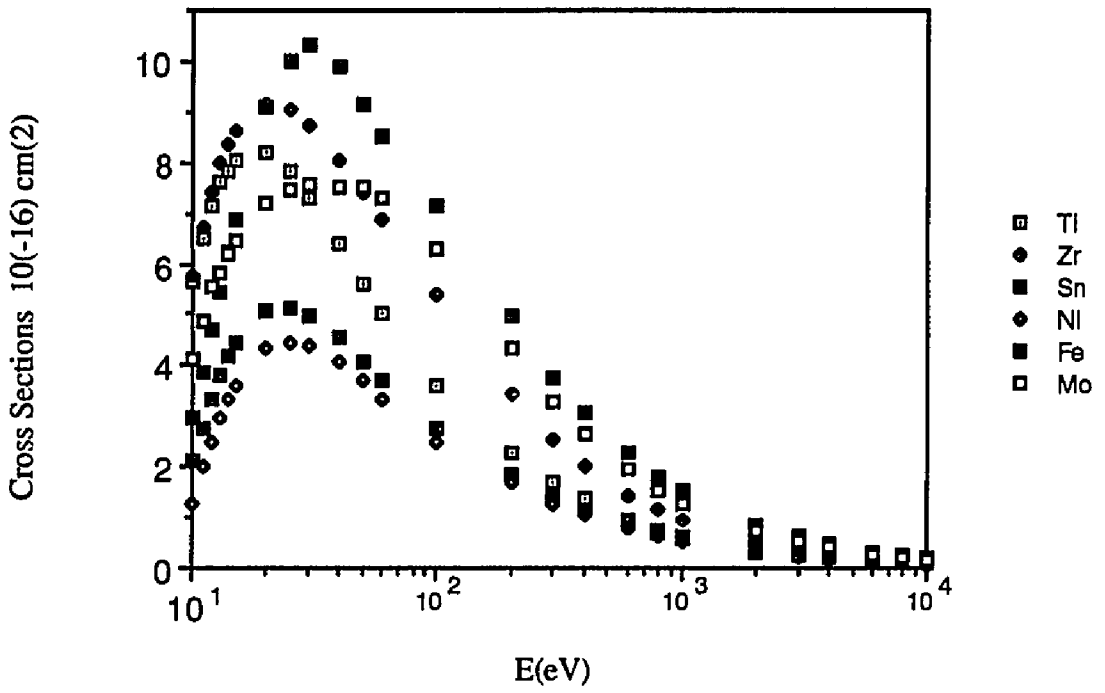

FIGURE 2.7 Theoretical ionization cross sections of various elements versus incident electron energy from McGuire (1977).

2.2.6 - STOPPING POWER

What is misleading is that we have not yet taken to account the average rate of energy loss, –(dE/dx), which is known as the stopping power. It is indicative of how much energy is deposited into a specimen and subsequently how much transferred energy is available for either heating up the solid or causing atomic displacements. Once the cross sections are determined, the stopping power can be evaluated for a solid of density N_o atoms/cm^3 by the following relation:

$$-\left(\frac{dE}{dx}\right) = N_o \int T\sigma(E_1,T)dT \tag{2.31}$$

Realistically, the total stopping power is determined primarily by **nuclear** and **electronic** interactions:

$$\left(\frac{dE}{dx}\right)_{total} = \left(\frac{dE}{dx}\right)_{nuclear} + \left(\frac{dE}{dx}\right)_{elec} \tag{2.32}$$

$-(dE/dx)_{nuclear}$ and $-(dE/dx)_{elec}$ can also be further broken down into the numerous energy loss channels; some displacive, while others self-healing. For electron irradiation, $(dE/dx)_{elec} >> (dE/dx)_{nuclear}$. Thus, the amount of energy which goes into electronic energy loss dominates that which goes into ballistic energy loss. $(dE/dx)_{elec}$ has an essentially inverse relationship with incident electron energy, E_1, and is given by the Bethe-Bloch expression (Bethe 1933) for relativistic electrons:

$$-\left(\frac{dE}{dx}\right)_{elec} = \frac{2\pi e^4}{m_e v^2} N_2 Z_2 \left\{ \ln\left(\frac{m_e v^2 E}{2I^2(1-\beta^2)}\right) - \left[2\left(1-\beta^2\right) - 1 + \beta^2\right]\ln 2 + \left(1-\beta^2\right) + \frac{1}{8}\left[1-\left(1-\beta^2\right)^{1/2}\right]^2 \right\} \tag{2.33}$$

In summary, electron irradiations deposit more energy into the specimen via electronic energy loss than in nuclear collisions, and the rate of energy loss, $-(dE/dx)_{elec}$ increases as the incident electron energy is lowered. Nuclear energy loss only becomes significant when the energy transferred exceeds the displacement threshold energy, which occurs at incident electron energies exceeding approximately 100 keV.

The above statements do not hold for ion irradiations for which the cross sections vary more dramatically with incident energy, depending on the energy regime of interest

as was illustrated in Figure 2.2. The regions are analogous to those described in sections 2.2.4 and 2.2.5 for determining the differential cross sections and are described as follows:

In region 1, the energy loss is primarily by electronic excitations. The Bethe-Bloch relation is valid in this regime. $-(dE/dx)_{elec}$ varies as $(E_1)^{-1}\ln(E_1)$ and is given by:

$$-\left(\frac{dE_1}{dx}\right)_e = N_o 2\pi (Z_1)^2 Z_2 e^2 M_1 \frac{1}{(m_e E_1)} \ln\left(\frac{4m_e E_1}{M_1 I}\right) \tag{2.34}$$

with: $T_{min} = I$ (the mean ionization potential)

$T_{max} = 4\,(M_1/m_e)\,E_1$

In region 2, screening effects become significant. $-(dE/dx)$ now varies as $\ln(E_1)$ and is given by:

$$-\left(\frac{dE_1}{dx}\right)_e = N_o 4\pi (Z_1)^{2/3} Z_2 \bar{h}^2 \frac{1}{(m_e)} \ln\left(\frac{4m_e E_1}{M_1 I}\right) \tag{2.35}$$

In region 3, energy loss is primarily by nuclear collisions as the electronic excitations are not sufficiently energetic to remove bound electrons. $-(dE/dx)_{elec}$ due to electronic losses - predominantly in the form of valence excitations - varies linearly with $\sqrt{E_1}$ and is given by:

$$-\left(\frac{dE_1}{dx}\right)_e = N_o 3.22\pi (Z_1+Z_2) \bar{h}^2 a_o \sqrt{\frac{E_1}{M_1}} \tag{2.36}$$

Estimates can also be made on limiting energies (Olander 1976) given in the

diagram as E_T and E_Z. E_T is the energy above which no screening effects are felt. It is also the energy above which the Bethe-Bloch equation is valid and can be approximated by:

$$E_T \approx \frac{2\pi^2(M_1 e^4)}{h^2} Z_1^{4/3} \tag{2.37}$$

In addition, there exists an incident ion energy, E_Z, below which an incident ion cannot transfer enough energy to remove a bound electron. Thus electronic energy loss, occurring only as weak valence excitations below E_Z, is assumed to be negligible below this value. The order of magnitude of E_Z is given by:

$$E_Z \approx \frac{(M_1)}{4m_e} T_{min} \tag{2.38}$$

where T_{min} in this case is the minimum threshold energy to remove an electron (not the displacement threshold energy, E_d). As was previously stated, T_{min} is dependent on the specific energy loss process. For metals, T_{min} may be approximately $1/2E_f$ (E_f = Fermi energy). For ionic solids and semiconductors, T_{min} may be approximated as the mean ionization potential (which varies from approximately 8.8 Z to 13.5 Z) or the energy needed to bridge the band gap, E_g.

Some representative values of E_Z and E_T are given in Table 2.4. What can be concluded is that for ion irradiations in realistic energy ranges pertaining to this study (< 5 keV), the energy loss is predominantly via ballistic processes.

TABLE 2.4

Representative values of the limiting incident particle energies: E_T - the energy above which electronic processes dominate, and E_Z - the energy below which nuclear processes dominate.

Incident Ion	E_Z (keV)	E_T (MeV)
H	4	2.5×10^{-2}
He	32	2.5×10^{-1}
Ne	810	1.1
Ar	2,900	46.7
Kr	12,000	247
Xe	28,000	664

2.3 - DISPLACEMENT THRESHOLD ENERGIES PREDICTIONS VERSUS EXPERIMENTAL DATA

Whether the energy transferred to a solid is sufficient to knock an atom from its lattice site in the bulk or on the surface depends primarily on the type of specimen: the nature of the bonding in the solid, the space available for accommodating an interstitial atom in the structure, the form of the interstitial, the masses of the constituent atoms, the crystal structure and orientation relative to the beam, among other factors. A displacement threshold energy, E_d, which is dependent on all of the above mentioned factors, defines the minimum energy transfer necessary to cause permanent atomic displacements and is used as the lower limit to $\sigma_d(E)$.

The displacement threshold energy, E_d, is intimately related to the details of interatomic bonding, since several bonds must be broken and others seriously perturbed in order to displace an atom into a normally unoccupied site. Bond energies vary with the solid type, with some typical values given in Table 2.5.

TABLE 2.5

Typical bond energies in various types of solids (Hobbs 1979)

Solid Type	Range of Bonding Energy
Van der Waals	0.1 - 1 eV
metallic	1 - 3 eV
covalent	4 - 8 eV
ionic	8 - 100 eV

Displacement energies will be of this order and most probably larger as the displacement process is highly adiabatic and considerably more energy than just due to the broken bonds is dissipated. In addition for compact solid types such as metals, the displacement event requires the perturbation of significantly more than just the nearest neighbors to accommodate the displaced atom.

2.3.1 - H_S APPROXIMATION

Estimates of E_d in tightly bounds solids such as metals have been made based on the sublimation energy, H_S. Surface binding energies of the elements vary with H_S, and are often equated with that value or some factor multiplied by it (depending on the number of broken bonds required). The argument is that since atoms sublime from the surface, where approximately half of the binding forces compared to the interior are operative, it can be concluded that the energy required to reversibly remove the typical atom or ion from an interior site should be of the order of one half the Coordination Number (CN) multiplied by H_S. If, however, the atom is removed and forced into the the lattice in a highly irreversible way, an energy of at least of the order of 4 H_S should be required (Seitz 1949). Based on this kind of reasoning threshold energies on the order of 25 eV should be required to permanently displace an atom from a stable bulk lattice site and around half of this value for a surface site. Values of H_S, estimates of E_d, and the threshold incident electron energies required for various elements are presented in Table 2.6 from the data of Bradley (1988). The approximate sputtering regime is between H_S and $2H_S$, whereas the bulk displacement regimes are thought to lie between 4 H_S and 5 H_S. For metals, experiments have indicated that this criterion has yielded the proper order of magnitude for the threshold energy (Goland 1976).

TABLE 2.6

Values of the sublimation energy, H_S, and the corresponding threshold incident electron energies, E_{th}, required for displacement in various elements based on estimates of E_d being proportional to H_S.

Element	Sublimation Energy, H_S (in eV)	Threshold e- Energy at H_S (keV)	Threshold e- Energy at $2H_S$ (keV)	Threshold e- Energy at $4H_S$ (keV)
C	7.43	39.2	75.7	142.7
Al	3.42	40.4	78.1	147.0
Ti	4.86	96.9	180.3	322.5
V	5.33	111.5	205.9	364.7
Mn	2.94	68.9	130.5	238.6
Fe	4.31	99.9	185.6	331.3
Co	4.44	107.8	199.5	354.1
Ni	4.46	107.9	199.6	354.3
Cu	3.50	92.9	173.3	310.8
Zn	1.35	38.7	74.9	141.3
Zr	6.31	216.4	381.8	643.6
Nb	7.48	253.6	442.0	736.1
Mo	6.81	240.9	421.5	704.7
Pd	3.9	163.0	293.7	505.8
Sn	3.13	147.9	268.1	465.2
Ce	4.38	228.5	401.5	673.9
Yb	1.58	112.2	207.1	366.7
Hf	6.42	380.4	641.5	1036.6
Ta	8.1	460.3	764.1	1218.4
W	8.81	496.6	819.2	1299.4
Re	8.02	467.0	774.2	1233.2
Au	3.82	270.9	469.7	778.3
Pb	2.02	164.3	295.8	509.1
U	5.46	419.7	702.0	1126.5

2.3.2 - LATTICE ENERGY APPROXIMATION

For highly ionic solids, a more realistic value of the bulk displacement threshold can be determined from the lattice Coulomb energy as an approximation for the bonding energy per ion pair. The lattice Coulomb energy is approximately (neglecting the repulsive term):

$$U_1 = \frac{\alpha(r)(ze)^2}{4\pi\varepsilon r} \approx 8z^2 \text{ (in eV per ion pair)} \qquad (2.39)$$

where $\alpha(r)$ is the Madelung constant, (ze) is the lowest common ion charge, ε is permitivity, and r the characteristic distance used for calculating $\alpha(r)$ which is usually the nearest neighbor distance. Crystal lattice energies and U_1 values for various oxides and the required threshold electron energies are given in Table 2.7.

2.3.3 - ΔH_a APPROXIMATION

Surface binding energies in compounds also vary with the heat of atomization, ΔH_a, and are often equated with that value. The bond strength in covalent solids is comparable to that in univalent ionic solids, however they are usually not close-packed, thus the displacement energies are expected to be closer to the binding energies. Tabulated values of the heat of atomization in a wide range of solid types are given in Table 2.8.

Ionic solids, like metals, are compact therefore the ballistic displacement thresholds can be expected to be high.

TABLE 2.7

Crystal lattice energy, E_l, Coulomb energy, and the corresponding E_{th} (eqn. 2.40) required for displacement based on estimates of E_d being proportional to E_l.

Oxide	Lattice Energy (eV/atom)	Coulomb Energy ($\approx 8z^2$)	E_{th} (surface) (in keV) cation	anion	E_{th} (bulk) (in keV) cation	anion
Ag_2O	31.7	32	517	105	850	194
BaO	32.5	32	629	107	1018	198
BeO	46.9-47.7	32	89	149	166	270
CaO	36.1-37.1	32	264	119	459	219
PbO	37.0	32	918	120	1445	221
SnO	38.4	32	564	107	1032	228
CuO	40.2	32	414	130	693	237
CdO	40.2	32	634	130	1026	237
MgO	40.4-40.8	32	189	131	337	239
MnO	40.2	32	369	130	624	237
NiO	41.9	32	402	135	674	246
CoO	41.9	32	402	134	676	246
FeO	41.9	32	385	134	650	246
ZnO	42.6	32	442	137	736	249
CeO_2	110.3	128	1451	308	2218	529
ZrO_2	116.2	128	1140	322	1767	550
PbO_2	122.0	128	1967	334	2955	570
SnO_2	123.2	128	1402	337	2146	574
TiO_2	126.2	128	780	344	1242	584
MoO_2	128.3	128	1256	348	1935	591
MnO_2	135.7	128	901	364	1419	616
In_2O_3	150.8	288	1559	396	2372	665
Cr_2O_3	157.7	288	961	410	1507	687
Al_2O_3	161.1	288	617	417	1000	697
V_2O_5	---	800	~2609	~1288	~3872	~1982

z = lowest common ion charge.

* Multiply eV/atom by 96.334 to obtain value in kJ/mole.

TABLE 2.8

Minimum heat of atomization criterion for oxides.

Final state is predicted as being the reaction with the lowest heat of atomization, ΔH_a, by comparison of total ΔH_a to partial ΔH_a to lower oxide phases. (ΔH_a values in eV/gas atom.)

Material	final state	ΔHa	alternative final states	ΔHa
TiO_2(l)	Ti_2O_3(s)	5.1	TiO(s)	6.4
			Ti(g) + 2O(g)	6.4
MoO_3(l)	MoO_2(s)	3.8	Mo(s)	5.0
			Mo(g)+3O(g)	5.5
WO_3(l)	$W_{18}O_{49}$(s)	2.9	WO_2(s)	4.7
			W(g) + 3O(g)	6.2
Nb_2O_5(l)	NbO(s)	5.9	Nb(s)	6.3
			2Nb(g) + 5O(g)	6.7
V_2O_5(l)	V_2O_3(s)	4.0	VO(s)	4.8
			2V(g) + 5O(g)	5.6
Ta_2O_5	Ta(s)	6.7	δ-TaO(s)	$\approx$6.7
			2Ta(g) + 5O(g)	7.1
TeO_2(l)	Te(l)	4.2	Te(g)+2O(g)	3.4
NiO(s)	Ni(g) + O(g)	4.8	Ni(s)	5.1
CuO(l)	Cu_2O(s)	3.6	Cu(s)	4.0
CoO(s)	Cu(g) + O(g)	4.7	Co(s)	5.1

TABLE 2.8. (continued)

Material	final state	ΔHa	alternative final states	ΔHa
ZrO_2(s)	Zr(g)+2O(g)	7.7	Zr(s)	8.3
α–Al_2O_3(l)	2Al(g)+3O(g)	6.2	Al(s)	8.0
MnO(s)	Mn(g)+O(g)	5.2	Mn(s)	6.6
MgO(s)	Mg(g)+O(g)	5.2	Mg(s)	8.9
ZnO(s)	Zn(g) + O(g)	3.8	Zn(s)	6.2
BeO(s)	Be(g)+O(g)	6.1	Be(s)	8.8
SnO_2(l)	Sn(g)+2O(g)	4.8–x/3*	SnO(s) Sn(s)	5.5–x* 5.6–x/2*
Cr_2O_3	2Cr(g)+3O(g)	5.5–x/5*	Cr(s)	6.5–x/3*
Bi_2O_3(l)	2Bi(g)+3O(g)	3.3	Bi(s)	4.1

* the enthalpy is written as x/(a+b) eV/atom for the compound A_aB_b.

2.3.4 – EXPERIMENTAL DETERMINATIONS OF E_d

How do these estimates compare with actual threshold displacement energies? Experimental determinations of displacement energies for nonmetallic solids are known for only a limited number of materials. A list of measured E_d values is given in Table 2.9.

TABLE 2.9

Experimentally determined threshold displacement energies.

Material Orientation	E_d(eV)	E_{th}(keV)	Reference
Al	16	169	(Iseler et al. 1966)
Al_2O_3	18 (Al), 72 (O)	187(Al), 394 (O)	(Pells and Phillips 1979)
Ni [100]	21	402	(Bourret 1971)
Ni [110]	38	628	(Bourret 1971)
Ni [111]	>60	867	(Bourret 1971)
Ti	≈ 29	440	(Lucasson, Walker 1962)
Ta	32	1210	(Jung and Schilling 1972)
Mo	34	822	(Jung and Lucki 1975)
V [100]	30	475	(Gittus 1978)
V [111]	34	522	(Gittus 1978)
V [110]	39	577	(Gittus 1978)
W [100]	40-47	1407-1558	(Gittus 1978)
W [111]	53	1678	(Gittus 1978)
Zn	14.5	318	(Maury et al. 1976)
$C_{graphite}$	25	122	(Hayes, Stoneham 1985)
$C_{diamond}$	35-80	165-330	(Hayes, Stoneham 1985)
Mg	10	101	(Faust et al. 1969)
MgO	64(Mg), 60(O)	481 (Mg), 330 (O)	(Hobbs 1979)
UO_2	40(U), 20(O)	1654 (U), 129 (O)	(Hobbs 1979)
Au	33	1300	(Bauer and Sosin 1966)

A useful relation for ballistic displacement damage is the determination of the threshold energy, E_{th}, that will transfer an amount of energy E_d to the solid. E_{th} for electron irradiation can be conveniently calculated from substituting the appropriate values into equation 2.9 to obtain:

$$E_{th} = \frac{\left((104.4 + 0.186AE_d)^{1/2} - 10.22\right)}{20} \tag{2.40}$$

where E_{th} is in MeV and E_d is in eV. For ion irradiations, E_{th} is simply given by:

$$E_{th} = E_d \frac{(M_1 + M_2)^2}{4M_1M_2} \tag{2.41}$$

2.3.5 - ADDITIONAL CONSIDERATIONS

Once the appropriate displacement cross section is evaluated, the number of displacements per atom (dpa) can be calculated using the modified Kinchin and Pease (1955), relation:

$$dpa = \sigma_a \phi t \qquad \text{for } E_d < T_{max} < 2E_d \tag{2.42a}$$

$$dpa = \sigma_a \phi t \left(1 + \ln\left(\frac{T_{max}}{2E_d}\right)\right) \qquad \text{for } T_{max} \geq 2E_d \tag{2.42b}$$

where ϕ is the flux density of the incident radiation and t is the irradiation time. Dpa values are widely used in bottom-line comparisons of different types of irradiations.

Although the above treatment is extremely useful for the study of ballistic damage, the category metals and high energy environments (such as in nuclear reactors), it is of little value for ionization damage. The displacement cross section for radiolysis is not as

easily evaluated as that for ballistic processes, however an approximate relation for high energy electrons can derived from the stopping power:

$$\sigma_I(E) = \zeta \frac{\frac{dE}{dx}}{N_o T_d} \approx 7 \times 10^6 \zeta \frac{Z}{T_d} \quad \text{(in barns)} \tag{2.43}$$

with T_d, the threshold energy for a given ionization process (in eV). ζ is the radiolytic efficiency. N_o is the atomic density of the solid (approximated here as 5×10^{22} atoms/cm^3). Radiolytic efficiencies are typically quite high, ranging from $z = 10^{-4}$ for silicates to $z \geq 0.1$ for halides (Hobbs 1987). Given $\zeta = 1$, ionization processes in comparison to ballistic processes may be as much as 10^5 times more probable under typical electron microscopy conditions. The conclusion is that where radiolytic processes are even marginally likely, ionization will dominate direct displacement processes, and will always dominate for subthreshold ($E_1 < E_{th}$) irradiations.

2.4 - TEMPERATURE RISE IN THE ELECTRON MICROSCOPE THEORETICAL CONSIDERATIONS

It has been shown that high energy electrons transfer energy to the lattice through both nuclear and electron interactions. Both of these are capable of converting the transferred energy to heat via lattice and plasma vibrations respectively. The amount of energy converted to heat and thus specimen temperature rise in the electron microscope is an extremely difficult measurement to make, however theoretical estimates have been made which provide worst case limiting scenarios.

Gale and Hale (1961), provided the heat transfer model to the specific TEM specimen geometry. Fisher (1970), related this model to the Bethe-Bloch energy loss rate

(equation 2.33) and an approximation to the temperature rise in the sample. The following arguments are valid for the energy range 100 keV to 1 MeV. Again, it is assumed that electronic interactions dominate in this regime.

A number of assumptions are made in the Gale and Hale model: 1)The energy loss rate, $(dE/dx)_{elec}$, is constant through the foil. This is the thin foil criterion and is valid for samples thicknesses, d, of less than 1000 nm (10^{-4} cm). 2) As illustrated in Figure 2.8, the geometry is set up such that the specimen is bounded by a circular conductor of radius, b, which has infinite conductivity and is held at a fixed temperature, T_o. b is effectively the maximum distance from any point in the specimen to the conducting sink. 3) The irradiation intensity is symmetrical about the boundary and beam center, with a beam diameter of a. 4) The heat transfer is by conduction only. (It is assumed that the heat conducted away from the irradiated area is greater than the heat radiated, which is valid especially for large b/a. 5) It is assumed that b/a is greater than 1, which is not always the case - especially for the geometries used for surface profile imaging. Larger b/a ratios correspond to a larger temperature rise, thus for the geometries used in this study, this evaluation serves the purpose of a worst-case scenario. 6) It is assumed that all the energy loss goes into heat. This is highly unrealistic, but again, it serves to define the worst-case scenario. It should be noted that alternative processes which do not contribute to the temperature rise - such as radiative emission - account for a significant portion of the energy loss of the incident beam.

The geometrical configuration of this model – while not adequate for small particles anchored to a conducting grid – should be closer to realistic conditions for a thin film supported on a conducting ring. Measurements by Luzzi (1986), however, show that even for this worst-case thin film geometry (with large b/a) that for medium and low

conductivity materials the theoretical predictions largely overestimate observed temperature excursions. With that in mind, it can be safely predicted that if the theoretical predictions show a negligible or low temperature rise, then thermal effects will play a only a secondary role in the radiation damage process.

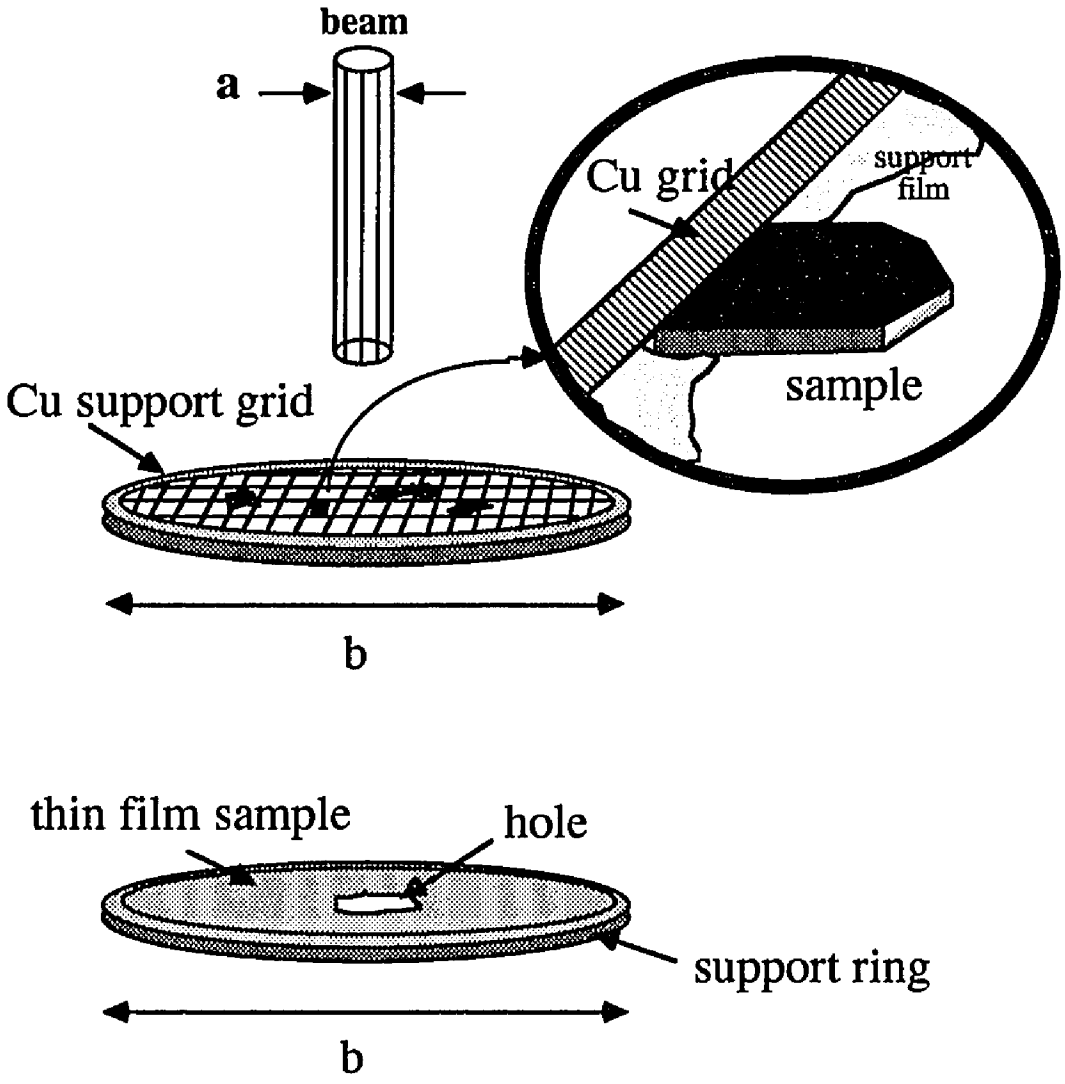

FIGURE 2.8 A comparison of the sample geometries used in this study (top and bottom) and the sample geometry used for the theoretical calculations of temperature rise in the electron microscope (bottom).

The temperature rise in a thin TEM sample is determined from the two-dimensional heat conduction equation:

$$\frac{1}{r}\frac{\partial}{\partial r}\left(r\frac{\partial T}{\partial r}\right) + \frac{1}{\kappa}H(r) = \frac{2\sigma}{\kappa d}\left(T^4 - T_o^4\right) \tag{2.44}$$

where κ is the thermal conductivity of the sample, σ is Stefan's constant, and H(r) is the rate of generation of heat per unit volume, assuming it is independent of the depth of penetration of the beam. The solution to this equation is:

$$(T_{max} - T_o) = \frac{H_o a^2}{\kappa}\left[\nu_o + \ln\left(\frac{b}{a}\right)^2 - E_i\left\{-\left(\frac{b}{a}\right)^2\right\}\right] \tag{2.45}$$

where ν_o is Euler's constant, E_i are standard exponential integrals, H_o is the maximum heat flux. b and a are the radius of conductor and beam, respectively. $T_{max} - T_o = \Delta T$ is the temperature rise, where T_o will be assumed to be room temperature.

The heat flux can be expressed as:

$$H_o = \frac{I_o \Delta E}{d} \quad \text{where } I_o \text{ is the beam flux at the specimen.} \tag{2.46}$$

Also, the E_i functions are negligible for values of b > a compared to the other terms in the expression. Thus, the temperature rise can now be written as:

$$(T_{max} - T_o) = \frac{I_o \Delta E\, a^2}{4\kappa d}\left[\nu_o + \ln\left(\frac{b}{a}\right)^2\right] \tag{2.47}$$

ΔE is obtained from the $-(dE/dx)_{elec}$ expression in a constant thickness, d, and reduces to:

$$\Delta E = 0.153\ \rho \left(\frac{Z}{M}\right) \beta^{-2} \{\text{relativistic correction}\}\ d \qquad \text{in MeV} \tag{2.48}$$

ρ is the density of the sample, given in g/cm^3. Z and M are the atomic number and atomic mass respectively. It can be seen that the temperature rise varies with I_o and ρ, and inversely with the thermal conductivity. Values of ΔT are given in Table 2.10 for a sampling of oxides for three flux conditions used in this study: low flux ($I_o \leq 6.2 \times 10^{19}$ e–/cm^2s or 10 A/cm^2), medium flux ($I_o = 1.0 \times 10^{20}$ e–/cm^2s or 16 A/cm^2), and high flux ($I_o = 6.2 \times 10^{20}$ e–/cm^2s or 100 A/cm^2).

TABLE 2.10

Temperature rise in the TEM as a function of beam energy (in keV), beam flux, and sample geometry (b/a ratio).

Oxide	Beam Energy(keV)	Beam Flux	ΔT (°K) at b/a=1	ΔT (°K) at b/a=10	ΔT (°K) at b/a=250
NiO	100	low	12	--	249
NiO	100	medium	20	--	399
NiO	100	high	124	--	2490
NiO	300	low	7	63	141
NiO	300	medium	11	101	226
NiO	300	high	70	629	1410
TiO_2	100	low	11	102	228
TiO_2	100	medium	18	163	365
TiO_2	100	high	113	1016	2278
TiO_2	300	low	6	57	128
TiO_2	300	medium	10	91	205
TiO_2	300	high	63	570	1279
UO_2	100	low	31	281	630
UO_2	100	medium	50	450	1010
UO_2	100	high	313	2810	6302
UO_2	300	low	18	163	366
UO_2	300	medium	29	262	587
UO_2	300	high	182	1634	3663
UO_2	1000	low	--	--	233
UO_2	1000	medium	--	--	374
UO_2	1000	high	--	--	2334

CHAPTER 3
RADIATION DAMAGE PROCESSES AT OXIDE SURFACES

Chapter 3 is dedicated to a review of radiation-induced defect production mechanisms in oxides and other nonmetallic solids due to electron and ion bombardments. First, the types of defects which occur naturally and/or are radiation-induced in these materials is reviewed. Secondly, an introduction to sputtering processes is presented. A review of damage mechanisms and a survey of radiation-induced structural and chemical modifications are made with respect to considerations of electronic versus ballistic types of behavior. Finally, the role of thermal effects in the radiation damage process is considered.

3.1 - NATIVE AND RADIATION - INDUCED DEFECTS

Under electron or ion irradiation, the concentration of point defects may be far from thermodynamic equilibrium. Defects may be present which are not found under normal conditions. These include transient defects - which only last during the irradiation, or permanent defects - which survive for extended periods but may always be annealed out by heating the sample. This is in contrast to equilibrium native defects, the concentrations of which usually rise with increasing temperature.

Oxides occur in nature with varying degrees of nonstoichiometry as is shown in Table 3.1. Native defects are generally of the Frenkel type (vacancy + interstitial either on the cation or anion sublattice), or Schottky type (cation + anion vacancy pair). Schottky disorder is common in oxides where the cation and anion radii are comparable in size, such as in the alkaline earth oxides. Frenkel disorder is more common in oxides where a large difference in ionic radii exists, such as in UO_2. Descriptions of commonly

occurring defects - both native and radiation induced - are given Table 3.2 and Figure 3.1.

TABLE 3.1

Degree and type of nonstoichiometry in oxides.

(Matzke 1981; Mandelcorn 1964)

Oxide	Ideal(O/M)	$(O/M)_{min}$	$(O/M)_{max}$	Δ(O/M)	Deficiency
MgO	1/1	1/1	1/1	$<10^{-4}$	*
Al_2O_3	3/2	3/2	3/2	$<10^{-4}$	*
SiO_2	2/1	2/1	2/1	$<10^{-4}$	*
NiO	1/1	1.000	1.001	0.001	cation
TiO_2	2/1	1.992	2.000	0.008	anion
Ti_2O_3	3/2	1.501	1.512	0.011	cation
CoO	1/1	1.000	1.012	0.012	cation
α-WO_3	3/1	2.98	3.0	0.2	anion
Fe_3O_4	4/3	1.336	1.381	0.045	cation
MnO_2	2/1	1.93	2.0	0.07	anion
ThO_2	2/1	1.9	2.0	0.1	anion
PbO_2	2/1	1.87	2.0	0.13	anion
NbO	1/1	0.9	1.04	0.14	both
Nb_2O_5	5/2	2.35	2.5	≤0.15	anion
FeO	1/1	1.045	1.2	0.155	cation
MnO	1/1	1.00	1.18	0.18	cation
VO_2	2/1	1.8	2.0	0.2	anion
CeO_2	2/1	1.78	2.00	0.22	anion
VO	1/1	0.9	1.20	0.3	both
ZrO_2	2/1	1.67	2.004	0.33	both
VO	1/1	0.80	1.30	0.5	both
TiO	1/1	0.65	1.25	0.6	both

* shows minimal deviation from stoichiometry.

TABLE 3.2

Types of natural or irradiation-induced point defects in oxides and other non-metallic solids.

Defect	Description
Frenkel defect	vacancy + interstitial on the cation or anion sublattice
Schottky defect	cation vacancy + anion vacancy
F-center	electron trapped on the site of an anion vacancy
H-center	an anion split-interstitial + hole; an X_2^- molecular ion sharing one anion site
V_K center	a self-trapped hole; an X_2^- molecular ion sharing two anion sites
F-H pair	defect complex involving F and H center; a close F-H pair may be considered a self-trapped exciton
e-	electron
h°	hole
e-h	exciton or bound electron-hole pair

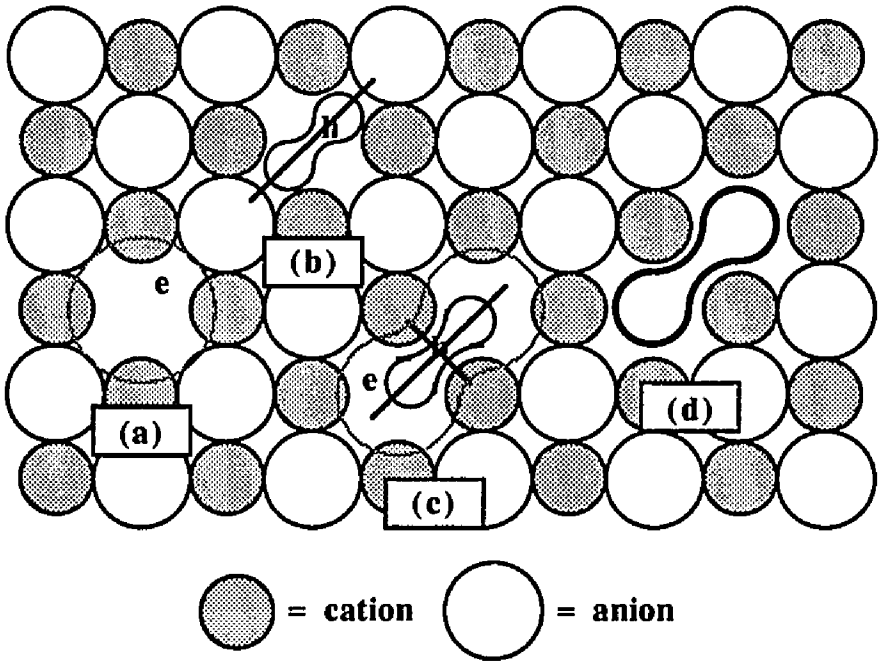

FIGURE 3.1 Commonly occurring radiation-induced defects in non-metallic solids. a) F-center; b) H-center; c) self-trapped exciton; d) V_k center.

In contrast to metals, oxides exhibit a variety of behavior towards irradiation: 1) Knock-on damage can be selective. Different defect species occur depending on which sublattice is involved. 2) Defects of various charge states can occur. Electronic disorder is not uncommon in these solids. Moreover, charge conservation and charge compensation are generally very important in determining radiation damage in ionic solids since long range Coulomb forces can overwhelm elastic interactions. 3) Focused RCS collisions tend to occur only on rows containing a single species and diffusion may be by processes involving only a single type of ion. Consequently, damage initiated on one sublattice tends to stay on that sublattice and radiation-induced defect production may be highly anisotropic (Hayes and Stoneham 1985; Townsend et al. 1976a). 4) Finally, excited states of defects are important in the radiation damage process as well since they

alter displacement thresholds and defect mobilities.

Purely ballistic damage would be affected directly by 1) above, however as the defect's charge state and orientation affects its binding energy, one would also expect differences in the threshold displacement energy. On the other hand, the decay of electronic energy following excitation is a complex process. The energy supplied must be greater than the sum of the formation energies of the defects. There must also be some significant reaction after excitation to inhibit total recombination. This can be achieved in two ways: 1) There may be a local barrier to recombination. 2) There may be a RCS to take the interstitial far enough away from the vacancy to stabilize the defect. Given in Table 2.2 (Chapter 2) were some characteristic defect formation energies compared to various sources of defect energy.

It is well established that the primary electronic defects produced in non-metallic solids by electronic excitation are electrons, holes, and plasmons; all of which are characterized by delocalized wave functions (Hayes and Stoneham 1985). Secondary products - such as self-trapped or relaxed excitons, phonons, or Frenkel pairs - all are formed within time periods of approximately 10^{-12} second, with subsequent decay into nonradiative or radiative channels determining whether permanent damage results or the excitation 'heals' itself. In a number of materials, the alkali halides in particular, an important intermediate stage along the damage channel involves the self-trapped exciton.

Research on color center formation has shown that the final displacement defects produced in alkali-halides by electron bombardment are mainly of the Frenkel type on the anion sublattice (Itoh 1982). It is the relative ease with which anions bond to form molecular ions (H-centers) and the unwillingness for cations to do so which causes preferential damage via an exciton mechanism to the anion sublattice. Oxides differ from

alkali halides in two major respects. First, unlike alkali halides where the reaction X^- + X^o -> X_2^- reaction is exothermic, the reaction O^{2-} + O^- -> O_2^{3-}, in oxides is endothermic. This type of excitonic (H-center) displacement process is therefore not an efficient damage mechanism and would only occur when either the Coulomb repulsion can be reduced or bypassed - such as on the surface. It can be concluded that if radiation damage in oxides proceeds by similar exciton mechanisms as those which occur in alkali-halides, it is most likely limited to the surface region. The specific mechanisms by which radiation-induced defects finally couple to atomic displacements is discussed in section 3.2.3.

3.2 - SPUTTERING PROCESSES

Bombardment of oxide surfaces with both ions and electrons has lead to compositional changes. These changes can be attributed to an interplay of mass-dependent effects, chemical bonding, electronic processes, and diffusion. A number of mechanisms may be operative, ranging from ballistic sputtering and thermal evaporation to electron-stimulated desorption (ESD) processes.

The total erosion due to sputtering is measured by the sputtering yield S, defined as the mean number of atoms removed from the surface of a solid per incident particle. Physically, the sputtering yield depends on three primary factors, the stopping power dE/dx, the surface binding energy E_b, and a factor α: $S = (dE/dx)(1/E_b)(\alpha)$. For purely ballistic sputtering, α depends on the mass ratio of incident and target particle and the angle of incidence of the collision; but for thermal or electronic sputtering, α is not well characterized.

Under many circumstances - e.g., in the TEM - the various sputtering

mechanisms may be operating concurrently. From consideration of the relevant energy transfer mechanisms, the major contributions to the sputtering yield, S, are: $S_{ballistic}$ - that due to ballistic collisions; S_{elec} - that due to electronic excitations; and $S_{thermal}$ - that due to one or more of a number of thermally related effects in combination with either ballistic or electronic mechanisms. These include thermal spike phenomena, dissociation with subsequent vaporization from the impact region, and diffusional processes. The synergistic operation of these processes may result in accelerated erosion or surface reaction beyond what would be predicted by any singular process.

3.2.1 - BALLISTIC SPUTTERING

Ballistic sputtering includes all elastic collisions in which atoms or ions are displaced due to momentum and energy transfer from incident particles. As in the bulk, point defects are created as the energy transferred exceeds a characteristic displacement energy, E_d.

There is no unique mechanism or model for calculation of ballistic or collisional sputtering yields as they depend on specific types of trajectories, which are statistical in nature. A calculation of this type would consist of a number of steps: 1) determining the amount of energy deposited by the incident particles at and near the surface; 2) converting this energy into a number of recoil atoms; 3) determining how many of these atoms come to the surface; and 4) selecting those atoms that have sufficient energy to overcome the surface binding energy. This has been done for a number of specific cases of ion irradiation by Sigmund (1972).

What can be expected from the theoretical considerations is that **ion irradiations** should result primarily in ballistic sputtering. Ion irradiations normally

lead to the formation of Frenkel-type defects, replacement collision sequences, and a large number of displaced atoms if the bombarding particles are sufficiently energetic. Sputtering takes place when an atom near the surface receives a kinetic energy larger than its binding energy. This type of energy transfer may produce anywhere from one to multiple primary and secondary displacements in what is known as a collisional cascade. According to Sigmund (1969a), the sputtering yield at perpendicular incidence of ions with energy E_1 less than E_z (equation 2.34) is given by:

$$S_{coll} = \frac{3\alpha}{\pi^2}\left\{\frac{M_1M_2}{(M_1+M_2)^2}\right\}\frac{E_1}{E_b} \tag{3.1}$$

where M_1 and M_2 are the mass numbers of the incident ion and the target atom respectively, E_b the surface binding energy, and a factor depending on the mass ratio M_2/M_1. The energy spectrum, dS/dE', of ejected particles is of the form:

$$\left(\frac{dS}{dE'}\right)_{coll} \sim \frac{E'}{(E'+E_b)^3} \tag{3.2}$$

Estimates show that for ion irradiations, collision cascades contribute between 50 and 80% of the total sputtering yield (Overeijnder et al. 1978a).

Calculation of a collisional sputtering yield for electron bombardment had not been considered by Sigmund, but it is believed that a similar dependence on mass and energy would exist; thus making the sputtering yield low for electron irradiations. It can be argued that collisional sputtering due to purely ballistic effects is unlikely in the electron microscope except on the extreme surface when the transferred energy exceeds the sputtering threshold energy, E_d. According to the Kinchin-Pease model, the incident

energies used in electron microscopy are well within the range where a maximum of one displacement event occurs per incident electron ($T_{max} \leq 2E_{th}$, i.e.-no cascades). Momentum transfer (via $\sigma(\theta)$) favors perpendicular motion of the struck atom (Pines 1955; Corbett 1966). The possibility of a replacement collision sequence would depend on the sample being favorably oriented, especially when considering ionic materials where RCS focusing rows are strictly defined.

In summary, the ballistic energy transferred to lattice atoms by ions or electrons depends primarily on the energy and mass of the incident particle and the mass of the displaced particle. The value of the sputtering threshold is an experimentally determined quantity which has a dependence on mass, surface binding energy, and crystal orientation. It is argued that sputtering of this type should not occur except on the very surface for electron irradiations and the ballistic sputtering yield should be low ($S << 1$); whereas ion irradiations may result in collision cascades and large ($S > 1$) sputtering yields.

3.2.2 - ELECTRONIC SPUTTERING

It is now well established that non-metallic solids such as oxides, halides, and carbides exhibit changes to surface and near surface regions during subthreshold, low energy electron or photon bombardment. This type of damage can unambiguously be attributed to electronic rather than ballistic sputtering because the maximum energy transfer is far below that required for ballistic processes.

Electronic sputtering includes all indirect mechanisms where electronic excitations are converted to the kinetic motion of atoms. In ionic solids, lifetimes of excited electronic states may be long enough to allow the excitation energy to be transferred to

atomic motion. When in the bulk, this is termed radiolysis and the result is the creation of point defects such as color centers. When on the surface, the result is desorption of neutrals and ionic species and is known as electron-stimulated desorption (ESD).

Fast **electron irradiations** ($10\,keV < E_i < 1\,MeV$) should give rise to primarily electronic energy transfer. Collision cascades are predicted to be energetically unfavorable since T_{max} is highly unlikely to exceed $2E_d$. Furthermore, since $(dE/dx)_{elec}$ varies as 1/E in this range, decreasing the incident energy increases the magnitude of the electronic over the ballistic energy transfer processes. Especially for sub-threshold irradiations (where $T_{max} < E_d$), the primary energy loss mechanism is expected to be via electronic processes. How efficiently this energy transfer couples to displacements or sputtering is not well known and a general analytic expression for S_{elec} would involve a determination of specific cross sections and displacement efficiency factors. Efficiency factors for radiolysis in oxides are for the most part unknown in the energy range of interest to this study. Moreover, electronic sputtering is often associated with thermal effects such as defect migration processes and vaporization as is discussed in section 3.3.

To form a displacement defect or eject a species from the surface, it is necessary for the wave function of the electronic defects to be localized. This is the first question a displacement or desorption mechanism must address. The second question pertains to how the electronic energy is transferred to atomic motion. There are two possible modes: multi-phonon emission and local excitation. Multi-phonon emission can be regarded as a local heating mechanism, where an atom is vibrationally excited upon a non-radiative transition from some higher electronic state to a lower one. Local excitation assumes electronic energy is transferred directly to the reaction mode and lattice relaxation leads to the final displacement process (Itoh 1985).

The electron-stimulated defect formation and/or desorption process considered above can be summarized by the following sequence of events (Tully 1983):

1) The initial electronic excitation: ($\leq 10^{-19}$ sec) from a source such as an electron or photon beam generally within - but not limited to - the 30 - 500 eV range, an energy regime in which direct momentum transfer would barely cause the atoms to rattle around, much less get knocked off the surface. This can be thought of as an impulse applied to the solid's (target's) electron wave function (or electronic configuration).

2) A fast redistribution of electronic energy: ($\leq 10^{-15}$sec). This involves the localization of the wave function for the relevant electronic excitation.

3) A slower displacement of atomic positions: This involves the transfer of electronic energy to atomic motion, resulting in the displacement or ejection of some species. Since the electron configuration has changed, the atoms see a changed potential. This changed potential acts as the driving force for displacement - forcing an atom to an interstitial site in the bulk and desorption of an atom on the surface.

4) A modification of the escaping species as it diffuses in the bulk or moves away from the surface. The detected final electronic state of the desorbed species is not necessarily representative of what was originally created, as there are many opportunities to gain and lose electrons as the atom escapes.

Each of the proposed mechanisms should attempt to account for the details of these events. It has been recognized that the atomic displacement processes caused by electronic excitation in the bulk and on the surface are essentially the same (Knotek 1983). In addition, a number of the electronic excitations which are either not sufficiently energetic or localized to cause displacements in the bulk may be operative at the surface. This has led to a re-examination of bulk defect creation processes due to electronic excitations as they may be applicable to surface and near surface regions.

3.2.3 - ELECTRONIC DAMAGE MECHANISMS

Various mechanisms for defect creation by electronic excitation and electron-stimulated desorption have been proposed in the literature since Seitz (1954), first presented a defect trapping model for alkali halides. As defect creation in alkali halides is perhaps the most well characterized and understood, most of the existing models have been proposed for - but are not limited to - these materials. A summary of the proposed models for alkali halides and other materials is presented in Table 3.3. The prominent models for bulk damage in alkali halides are due to Varley (1954), Klick (1960), Williams (1961), Pooley (1965), and Hersh (1966). Electron-stimulated desorption processes from surfaces have been modeled by Menzel and Gomer (1964), and Redhead (1964), for generalized desorption, Knotek–Feibelman (1978a), for maximum valence oxides, Van Vechten and Tsu (1979), and Itoh and Nakayama (1982), for semiconductors. This study is mainly concerned with the processes which alter the structure of the surface. The purpose of this section, then, will be to discuss in detail these various proposed mechanisms as they pertain to structural changes.

TABLE 3.3

A summary of defect creation and desorption mechanisms induced by electronic transitions.

Name	Model	Bulk/ Surface	Localization	Energy Transfer	Application
Varley	2h	B	multiple excitation	local excitation	alkali halides
Pooley Hersh	1h-1e	B/S	self-trapping	local excitation	alkali halides
MGR	1h-1e	S	self-trapping	local excitation	general, adsorbed gas
Anton-iewicz	1h 1h-1e	S	self-trapping	local excitation	physisorbed gases
K-F	2h	S	multiple excitation	local excitation	max.valency ionic solids
K-W	2h-2e	B	multiple excitation	local excitation	alkali halides
N-I	2h-2e (separately)	S	multiple excitation, Anderson neg. U	phonon emission	dense e-h plasmas
Van Vechten	nh-ne	B/S	-------bond weakening-------		dense e-h plasmas

MGR = Menzel, Gomer, Redhead

K-F = Knotek, Feibelman

K-W = Klick, Williams

N-I = Nakayama, Itoh

Varley (1954) proposed a mechanism of double ionization in the anion sublattice as a mode of defect formation in alkali halides. Unlike the Seitz mechanism, proposed slightly earlier, the defects predicted in this model have been experimentally confirmed (F-centers and F-H pairs). The model requires only that lattice bonding is heteropolar, the recombination time for stripped electrons ($\sim 10^{-12}$ s) is long compared to a lattice vibration ($\sim 10^{-13}$ s), and the cross section for multiple excitation is appreciable. This condition is satisfied if one considers electron bombardment, where the first ionization cross section, $\sigma_1 \sim 10^{-16}$ cm^2, $\sigma_2 \sim 10^{-17}$ cm^2, and $\sigma_3 \sim 10^{-18}$ cm^2.

Using an alkali halide as an example, the mechanism can be described as follows: Incident electrons multiply ionize the halogen ions in the ionic lattice, eventually rendering them positive. Since positive and negative ions in the halogen sublattice are attractive, an instability results. The potential curve shows that the +/- ions are first attractive – following a bonding curve, but transfer to an antibonding curve due to the high Coulombic force. On repulsion, one of the halogen ions may get enough kinetic energy to cause a replacement collision sequence or get displaced itself into an interstitial site. The result is the creation of F-centers or F-H pairs.

Klick (1960) addressed some of the serious objections raised against the Varley mechanism and proposed a modified mechanism which considered double ionization and multiple excitation. This model is illustrated in Figure 3.2. First, electron irradiation may cause a halide ion to lose two electrons. About 10% of the ionization processes result in double ionization of this kind. As proposed by Dexter (1960), in criticism of the Varley model, the doubly ionized halide ion could capture an electron from a neighboring halide so that two neutral halogen atoms are formed. As a result, a large amount of energy is deposited into this defect. Subsequently, electrons from outer halide ions are transferred

to these atoms, that is the holes are repelled outward. The two halogen atoms may also alter their electronic configurations such that a halogen molecule results. The molecule is small and neutral so that its energy is nearly position independent. It may then jump into one of the two neighboring vacancies, allowing a halogen ion to jump into the other vacancy; the whole process occurring at very little energy expense so that back diffusion is less likely.

Williams (1962) estimated time constants for electronic and atomic relaxation processes which lead to a two hole model, illustrated in Figure 3.3. It begins with the creation of a hole in two adjacent halogen ions, thus forming two halogen atoms. The important consideration is the time constant for each positive hole to move an additional interatomic distance in the [110] direction compared to the time constants to form stable molecules or molecular ions. He found that two holes created adjacently should be followed by atomic motion before the holes separate further. The atomic motion most probably forms two negative halogen molecular ions rather than a neutral halogen molecule. Each ion acquires momentum in [110] directions from interaction with the asymmetric crystalline field and by "billiard ball" collisions concurrent with tunneling of the positive hole, thus resulting in the separation of the defects.

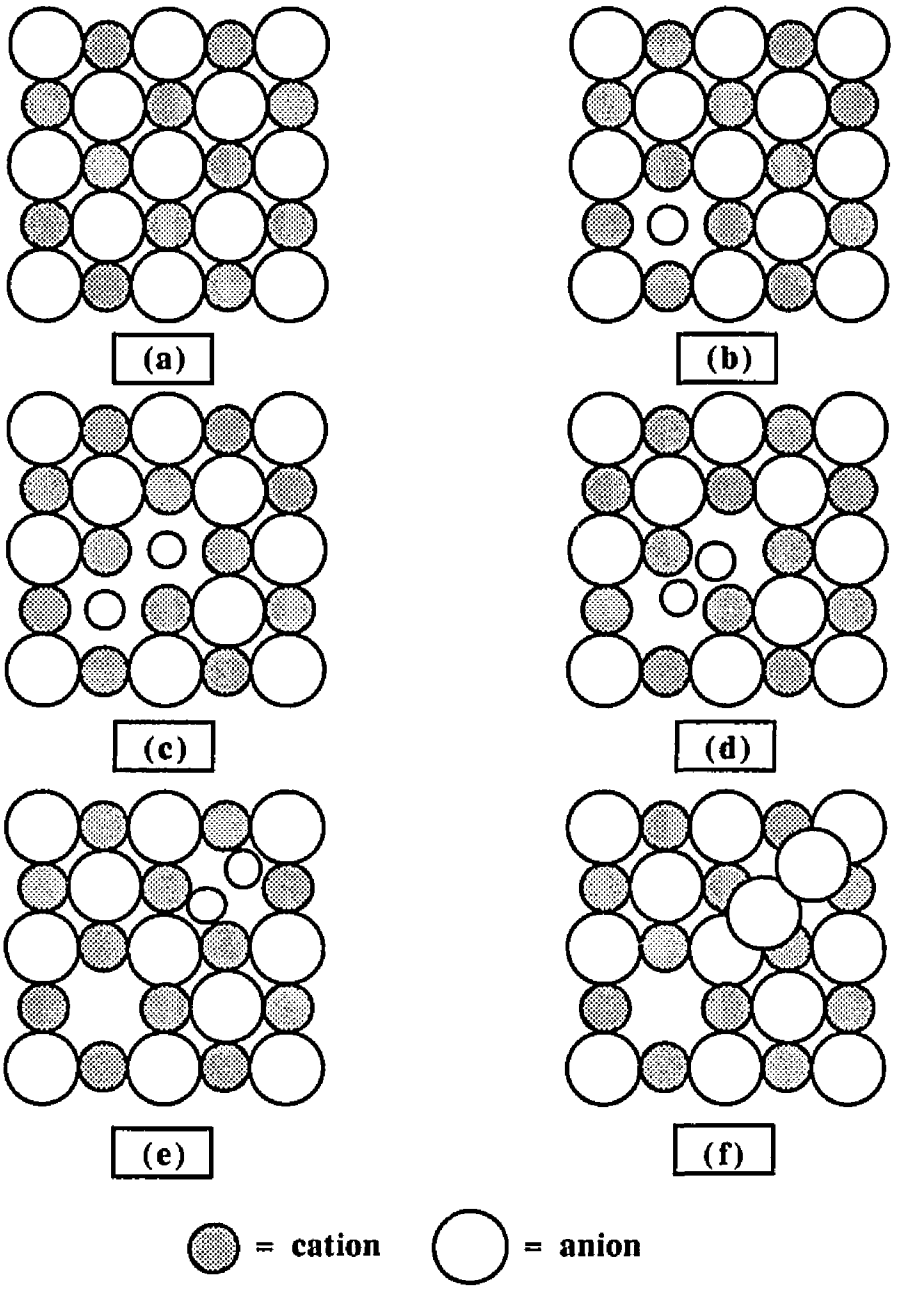

FIGURE 3.2 The Klick model. (a) perfect lattice; (b) after double ionization of a halide ion; (c) after transfer of an electron to the doubly ionized halide ion; (d) formation of a neutral halogen molecule; (e) formation of a vacancy and interstitial halogen by the jump of a halide ion; (f) capture of an electron by the vacancy to form a F-center and electron by the halogen to form a H-center.

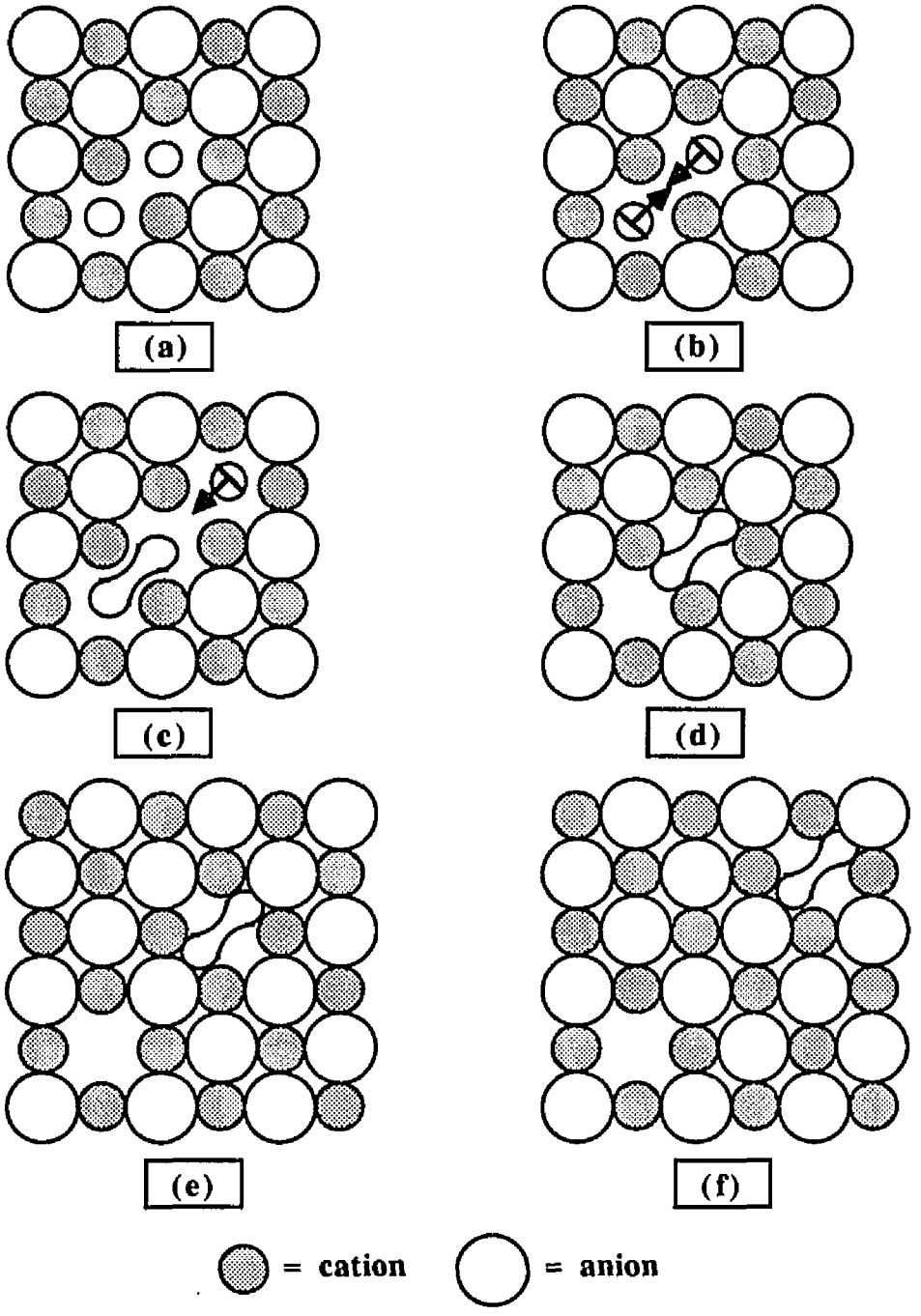

FIGURE 3.3 The Williams model. Sequence of events similar to those described in Figure 3.1, illustrating the dynamics of vacancy-interstitial formation and their separation via the migration of H-centers.

EXCITONIC MODEL (POOLEY-HERSH)

Pooley (1965), and Hersh (1966), described defect production and desorption in alkali-halide systems by a single ionization process beginning with creation of an exciton followed by a non-radiative electron-hole recombination. The conversion of electronic energy to atomic motion can then occur by a non-radiative transition from the lowest state of the exciton to the ground state, emitting phonons of localized modes. This, for example, could be the stretching mode of the two halogen ions forming the molecular ion defect. One of the halogen ions in this defect may subsequently induce a [110] replacement collision sequence, leading to the production of a negative ion vacancy and a negative ion interstitial (F-H pair or Frenkel pair). This is in agreement with experimental observations showing that the prevalent defects in alkali halides are Frenkel defects on the halogen sublattice. In addition, there exists considerable evidence that defect mechanisms in alkali halides begin with the creation of an exciton (Itoh 1976; Avouris and Walkup 1989).

The Pooley-Hersh or excitonic mechanism, shown in Figure 3.4, operates as follows: A halogen electron is excited to a state where it is still bound to the halogen, but in a large orbit. Because this electron is now absent for a large fraction of the time, the halogen relaxes toward one of its halogen neighbors, forming a V_k center. Sometime later, the electron in the large orbit recombines with the hole left behind in the V_k center, and as a result the two halogen atoms that make up the defect suddenly find themselves too close to one another. Coulombic repulsion sends them shooting off in a [110] direction, leading to a replacement collision sequence and a vacancy (F-center) - interstitial (H-center) pair, or an F-center and a desorbing halogen atom. Energy considerations reveal that this process would occur at less energy expense than the Varley

mechanism. Experimental observations of desorbing halogen atoms in [110] directions at low temperatures support this mechanism (Townsend et al. 1976a).

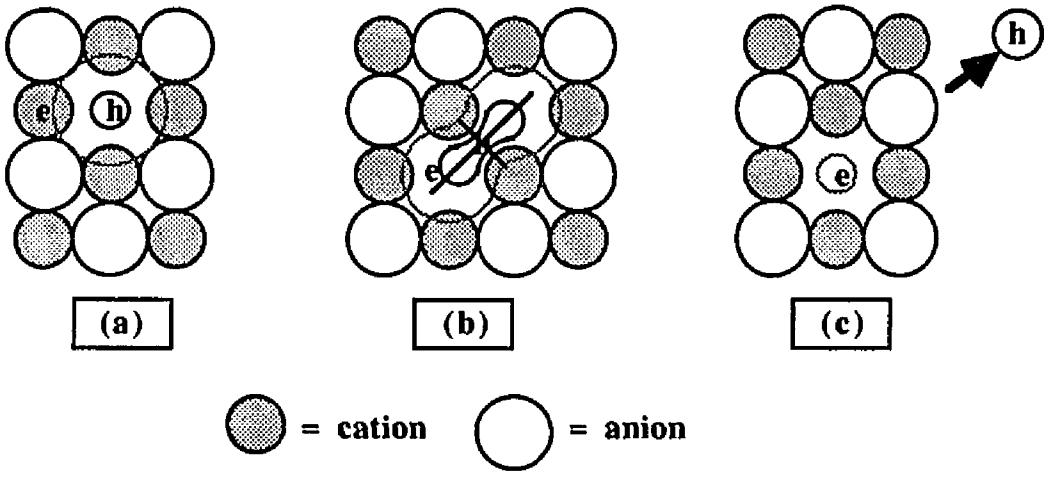

FIGURE 3.4 Pooley-Hersh model; (a) excitation of the halogen; (b) formation of the X_2^- molecular ion; (c) dissociation of the molecular ion with the ejection of a halogen fragment and formation of a F-center.

Toyozawa (1973), and Kabler and Williams (1978), further developed the Pooley-Hersh idea. They differentiate between the self trapped electron/hole pair (S_e:S_h) and the self trapped exciton (S_{ex}), shown in Figure 3.5(A, B) for the NaCl and CaF_2 structures respectively. It is noted that in alkali-halides (NaCl structures) both (S_e:S_h) and (S_{ex}) states are possible and are formed. However, as shown by Williams et al. (1977) the alkaline earth fluorides (CaF_2 structures) only form (S_e:S_h) states because in the (S_{ex}) state, the surrounding atom configuration is not symmetrical and therefore not stable. Consequently, the F_2^- molecular ion is displaced to the (S_e:S_h) state. This orientation is

less favorable for the formation of separated Frenkel pairs compared to the (S_{ex}) configuration along [110] in the alkali halide (NaCl) structures since RCS focusing depends strongly on the crystal structure.

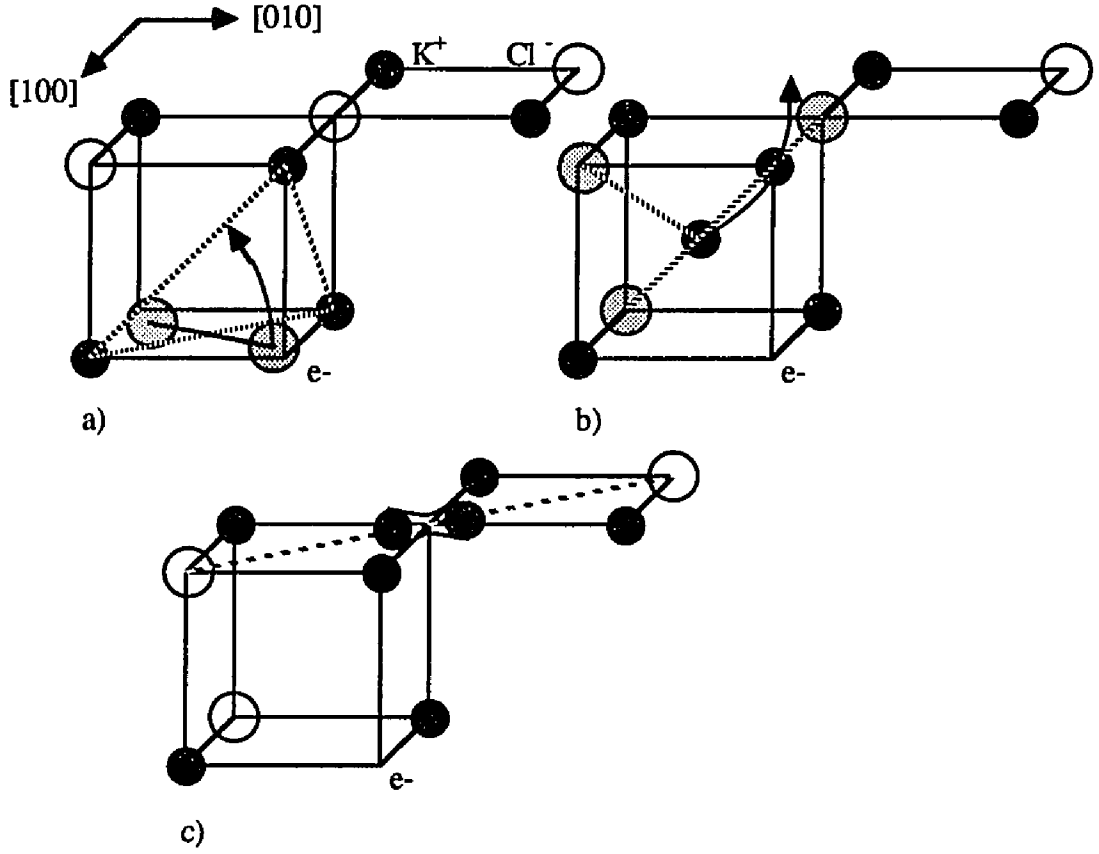

FIGURE 3.5 A. Kabler and Williams model for rocksalt structures. a) KCl with hole localized on a Cl_2^- ion pair. b) A generalized rotation translation places excited halide in position such that the hole is being shared resonantly. (c) Motion to one of the possible nearest-neighbor F-H pairs.

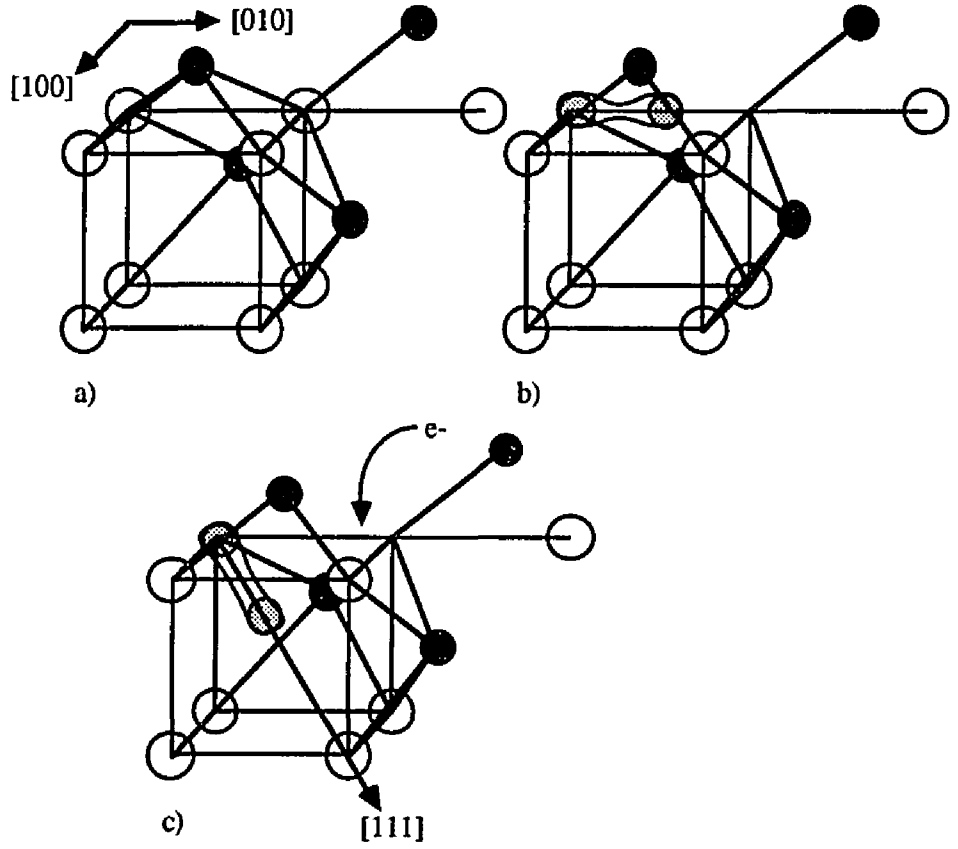

FIGURE 3.5 B. Kabler and Williams model for CaF_2 structures. (a) CaF_2 perfect lattice. (b) Self-trapped hole localized on the shaded ion pair. (c) Final configuration of a nearest-neighbor F-H pair along a [111] direction.

For structures such as rutile or calcium fluorite, there are no suitable focusing rows because the symmetry axis of the defects differ from that of the close-packed row. Their prediction, then, is that defect creation should be much more pronounced in the alkali halides as compared to the alkaline earth fluorides. This has also been experimentally confirmed (Townsend 1973).

THE MGR MODEL

The MGR model proposed by Menzel and Gomer (1964), and Redhead (1964), has become in many ways the traditional way of viewing generalized ESD processes. It proposes a direct two step process of electron–stimulated desorption: a Franck-Condon electronic excitation followed by a delocalization (recapture) of the excitation in competition with desorption. It can be described schematically using potential energy diagrams as shown in Figure 3.6. Electron impact of a compound MA causes a vertical (Franck-Condon) transition from the ground state to the anti-bonding or ionic state. As a consequence of this excitation, the excited complex starts to move along the repulsive potential gradient, with a probability $P = \exp(-\alpha r)$ of staying on the upper (excited) curve. There exists the finite possibility of recapture to the bonding (ground) state. Because of the large density of states, essentially an infinite number of excited state curves exist into which the deexcitation can go. There is also the finite probability that the particle will escape from the solid. The condition for escape (desorption) is that the particle gain sufficient kinetic energy. This translates to its traveling a critical distance along the upper potential energy curve. This can also be seen as the excited state having a (distance dependent) critical lifetime, t_c, for electron-stimulated desorption.

The case of desorption as an ion is described in a similar fashion. Whether the species leaves the surface as an ion or neutral depends on whether a transition occurs along the trajectory of escape. Desorption as an ion requires that no transition occur. Desorption as a neutral or negative ion requires that at least one transition occur. The expected result, then, is that the cross section for ionic desorption is much smaller than for neutral desorption. This has been confirmed experimentally in desorption studies (e.g., articles in DIET II 1984).

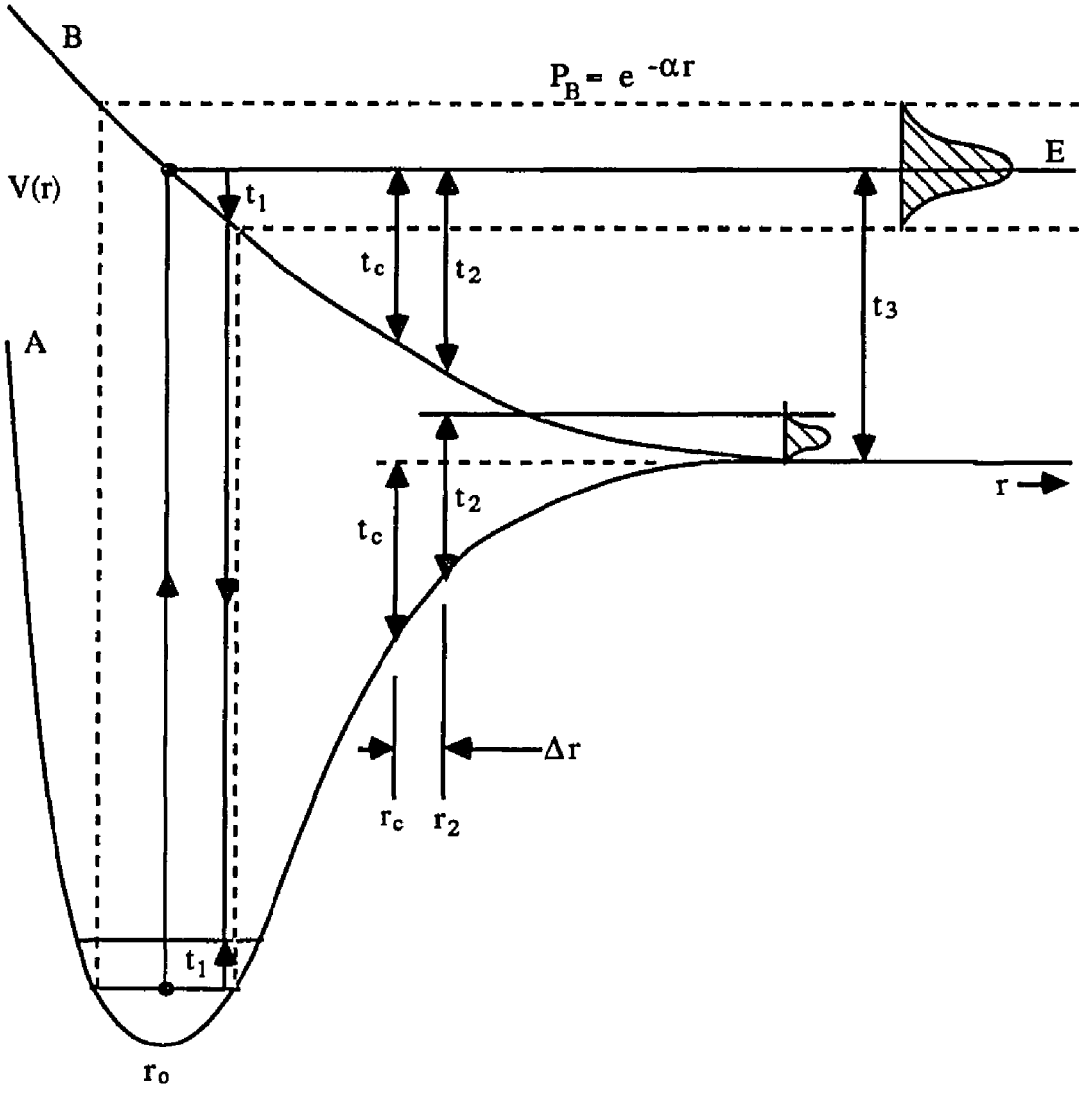

FIGURE 3.6 Potential energy diagram illustrating the MGR mechanism. Excitation to the upper, purely repulsive potential may result in ESD if t_c is exceeded.

The generalized features of this model hold for any desorption mechanism. After an initial electronic excitation there are the competing processes of recapture and desorption, the relative probability of each modeled by characteristic cross sections. Both

deexcitation processes relieve the high energy of the excited configuration. The ESD process, however, is heavily time (t) dependent, relying on the particle being in the excited state long enough to attain sufficient kinetic energy to escape.

The major objections to the MGR model pertain to its oversimplification (one electron, one dimensional), the vagueness with which it describes the details of the desorption process, and discrepancies in the energy distribution of the desorbed particles. (Predicted energies are too high). In addition, it fails to provide any new insight to the understanding of radiation damage processes. Notable modifications of the MGR model have been made by Antoniewicz (1980), and Breunig (1983).

KNOTEK–FEIBELMAN MODEL

In 1978, Knotek and Feibelman reported on ion desorption of O^+ from a titanium dioxide (TiO_2) surface not due to excitation at the valence level, but by excitation of the Ti-3p core level. The fact that oxygen was desorbed in the O^+ state when it normally resides in the O^{2-} state implied at least a three electron transfer leading to desorption. To explain these observations they proposed a model involving a metal core ionization followed by interatomic Auger decay, illustrated in Figure 3.7(a-b).

The K-F model is based on the realization that TiO_2 is a maximum valency ionic solid. Both Ti^{4+} and O^{2-} are ionized to the noble gas configuration. The Ti^{4+} have effectively no valence electrons. Their highest occupied shells are the 3p core levels located ~30 eV below the Fermi level. The important idea here is that if a core hole is created on any ion, it will decay toward the Fermi level (i.e. holes decay "up" to the valence band while electrons decay "down" to the core level) by a single or multiple Auger emission as illustrated in Figure 3.7(a). Because only electrons on the anion are

near the Fermi level, they are selectively stripped. In the case of TiO_2, the O^{2-} loses one electron by decaying into the hole. In approximately 10% of the subsequent adjustment events, two Auger electrons are emitted, leaving the oxygen in an O^+ state. This O^+ sees a reversal in the Madelung potential and is repelled away from the positive Ti cores, as is illustrated in Figure 3.7(b).

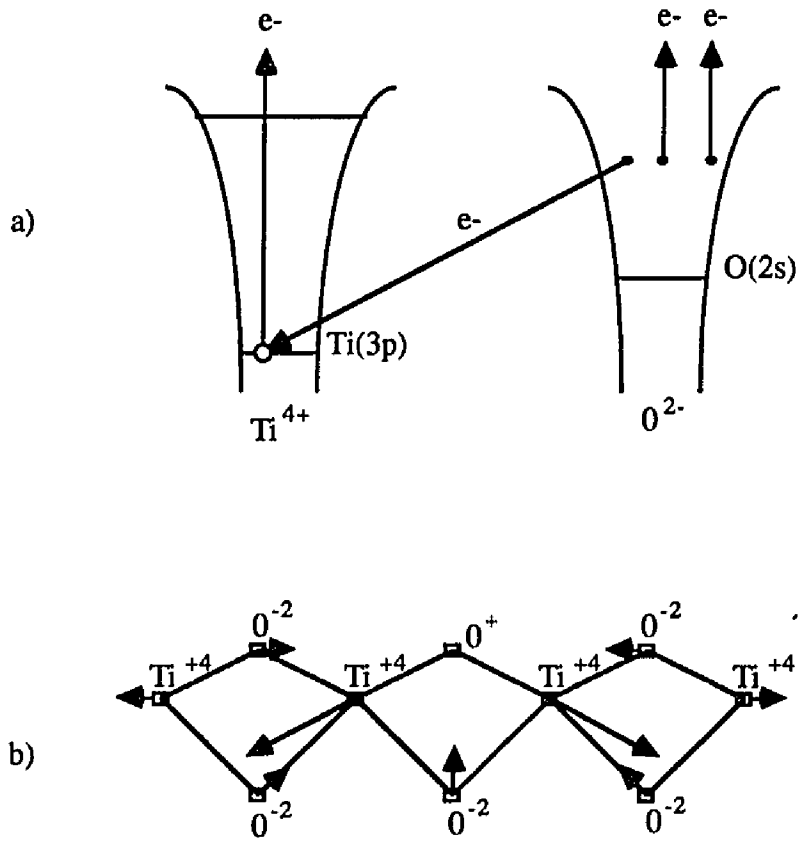

FIGURE 3.7 a) Schematic energy band diagram illustrating the Knotek Feibelman mechanism of desorption initiated by Auger decay.
b) Atomic picture of oxygen (O^+) desorption from the bridging sites of the TiO_2 (110) surface (Avouris and Walkup 1989).

Ions can be desorbed from covalently bonded surface complexes by essentially the same mechanism. The final product of the core hole Auger decay in such system results in a two or three valence hole final state. This can result in a "Coulomb explosion" as reported by Franchy and Menzel (1979).

The K-F model successfully predicts two specific observations which the MGR model cannot: 1) Excitation of core holes can lead to desorption. 2) The multiple Auger process produces sufficient charge transfer to convert O^{2-} to O^{+}. An important prediction comes out of their model: that sub-maximal valency compounds should show less tendency to decompose by desorption via Auger decay. This has been experimentally verified in a limited number of oxides. Maximal valency compounds such as TiO_2, V_2O_5, WO_3, and MoO_3 have shown a strong tendency toward ESD, whereas sub-maximal compounds such as Ti_2O_3, V_2O_3, Cr_2O_3, and NiO have generally shown weak or no desorption (Knotek and Feibelman 1978; Colpaert et al. 1973). For maximum valence transition metal oxides - HREM reports have generally supported the surface science findings of a strong tendency to undergo preferential oxygen loss at the surface during electron irradiation, but under what may be described as uncontrolled experimental conditions (Buckett et al. 1987).

DENSE E-H PLASMA MODELS

Itoh and Nakayama (1982), have described electronic sputtering of semi-conductors by a trapped defect formation mechanism. This model accounts for the high yield of neutral particles from surfaces and their non-Maxwellian energy distribution (evidence of the absence of a temperature excursion). They explain the desorption process in a dense electron-hole plasma in terms of a two hole – two electron (2h2e) state

in which the two holes are localized on the same atom. The premise is that non-radiative recombination in a crystal has a strong electron-lattice coupling which causes the generation of local mode phonons. The resultant sputtering of (neutral) atoms in a dense e–h plasma is caused by a phonon-assisted recombination at the surface. The extra "kick" of energy to the ejected atoms is transferred by the recombination process. Thus, lattice temperature may be much lower than the melting point, while sputtered atoms are fairly energetic.

The process occurs as follows: In a dense electron-hole plasma, when two holes on the surface approach each other, they can be attracted on a single anion, for example O^{2-}, resulting in a neutral O atom sitting on the surface. The O atom is then desorbed as a manifestation of the Anderson negative U interaction (Anderson 1975). In this process, two holes are attractive when the gain in lattice relaxation energy exceeds the Coulomb repulsion. The lattice relaxation is such that the O atom is ejected. Subsequently, two electrons become bound by the vacancy and the binding energy released in this process gives the ejected species a little extra kinetic energy.

Van Vechten and Tsu (1979), have suggested a bond-weakening model – also called the plasma annealing model – as an alternative to thermal melting in dense electron-hole plasmas. This mechanism is described as follows: If more than a critical number of electrons ($\sim 8 \times 10^{21}/cm^3$) are excited out of bonding states in the valence band to antibonding states in the conduction band, a second order phase transformation occurs. The bond weakening will be such that they will no longer be able to stabilize the thermal annealing phonon mode, and the crystal essentially becomes fluid. This fluid is not the same as the normal molten fluid because it is not driven by temperature (a first order type of phase transformation). This process should be reversible assuming the resulting

surface is once again below its crystallization temperature. The covalent bonding should reappear, forming a single crystal recrystallized epitaxial layer on the surface because this is the state of lowest energy.

Criticism of this mechanism lies in the fact that it predicts a Maxwellian energy distribution of ejected particles, which is contrary to experimental evidence. Further support of this and the Nakayama and Itoh model over local thermal melting lies in the observed crystalline to (4-fold) amorphous transformation of Si under low energy laser pulses (Liu et al. 1979). After irradiation, the glassy Si retained its 4-fold symmetry. If the Si were to have melted, a 6-fold symmetry would have resulted, as molten Si has coordination of 6 or greater and the quenched glassy phase would have retained this coordination.

In summary, electronic sputtering of oxides may be categorized into three possible modes: (1) Direct interaction of the incident particles with surface oxygen such that the latter is either neutralized or rendered antibonding and is subsequently ejected. (2) Interatomic Auger decay in maximum valence oxides can lead to the expulsion of both neutrals and of positive oxygen ions. (3) Creation of defects which can diffuse to the surface and bring about neutralization, possibly with expulsion due to the internal energy of the defect itself or possibly by a thermally-assisted process.

3.3 - THERMAL EFFECTS IN SPUTTERING

During electron irradiation, thermal effects certainly cannot be ignored in the consideration of sputtering or desorption from surfaces. Thermally-assisted sputtering occurs by vaporization at the surface either with or without the aid of a temperature excursion. Up until this point, thermal effects and their role in bulk radiation damage

have been neglected mainly because they are not a primary damage mechanism. Thermal effects will, however, play a large role in secondary processes – migration of defects – especially at or near the surface.

At least three aspects of sputtering phenomena have been attributed to thermal effects: prompt thermal sputtering, slow thermal sputtering, and thermally-induced diffusion of defects. Each of these effects show characteristic behavior; so much so that a number of criteria have been determined to categorize them. These are discussed in detail in the next sections.

3.3.1 - PROMPT THERMAL SPUTTERING

The first thermal effect is the observance of prompt thermal sputtering (Kelly 1977): vaporization from the impact region in accordance with a briefly lived ($t = 10^{-11\pm1}$ s) temperature spike on the order of 3000°K, the increase in temperature varying directly with the rate of energy dissipation and inversely with the heat capacity of the target. The localized, briefly-lived temperature excursion – or thermal spike – may take place if a primary ion dissipates its energy to the lattice at such a high rate that nearly all particles within a small volume of the collision cascade can be in motion and interacting with each other. The thermal spike, or hot region in the crystal, may contribute to sputtering if the time constant τ of the spike is of the order of the slowing down time τ_o of the projectile(s) and if the energy density in the spike is of the order of the binding energy of the target, which can be approximated by either the sublimation energy or heat of atomization. Spike temperatures have been measured to be in the range 1500-3000°K (Good-Zamin et al. 1978). A mean energy per atom in the spike can be estimated as $\varepsilon_{spike} = 3/2kT_{spike}$ (Overeijnder et al. 1978a). There is a tendency in such a

system to reach local equilibrium and consequently a Maxwellian distribution describes the energy spectrum of sputtered particles from the spike area:

$$\left(\frac{dS}{dE'}\right)_{\text{thermal spike}} \sim E' \exp\left(\frac{-E'}{kT_{\text{spike}}}\right) \tag{3.3}$$

This is known as prompt thermal sputtering. It is a thermal effect which should be more sensitive to the nature of the chemical bonds (through E_b) rather than mass.

A number of models based on the concept of a thermal spike have been proposed which attempt to explain the different response of similar oxides to ion bombardment. In accordance with a thermal spike model, Naguib and Kelly (1975), could predict with reasonable success whether oxides would amorphize or remain crystalline based on either a temperature ratio criterion or a bond-type criterion. The first criterion is the crystallization temperature-to-melting temperature (T_c/T_m) ratio. If this ratio is greater than approximately 0.3 the oxide will become amorphous during ion bombardment; whereas oxides with T_c/T_m less than 0.3 will remain crystalline.

The bond-type criterion based on ionicities is also quite successful in predicting whether a material will become amorphous during ion bombardment. With few exceptions, oxides with ionicities greater than approximately 0.63 will remain crystalline, whereas oxides with ionicities less than approximately 0.59 become amorphous under ion impact. Results based on both these criteria are given in Table 3.4.

Another simple criterion for the occurrence of prompt thermal sputtering has been evaluated by Kelly (1979), based on the vaporization model and the requirement of $S_{\text{thermal}} \geq 1$. At an assumed spike temperature ΔT of 3000 – 4000°K for oxides it is proposed that oxygen is preferentially lost if the decomposition pressure is near to or

greater than the critical value $10^{2\pm1}$ atm (Figure 3.8). The validity of this theoretical prediction is presented in Table 3.5, where a number of experimental observations are compared to vapor pressure data.

TABLE 3.4

Temperature ratio (TC/TM) and bond type (Ionicity) criterion for the observance of prompt thermal sputtering.

Material	Structure	T_C (°C)	T_C/T_M	Ionicity [a,b]	Final Structure [c]
MoO_3	orthorhombic	250	0.49	0.30	A, CS
WO_3	monoclinic	475	0.43	0.34	A, CS
CuO	monoclinic	-----	-----	0.43	CS
SnO_2	tetragonal	≈ 500	≈ 0.41	0.43	A
Fe_2O_3	hexagonal	535	≈ 0.43	0.47	A, CS
NiO	cubic (NaCl)	< 25	< 0.13	0.47	CR, CS
PbO	orthorhombic	-----	-----	0.47	CR
V_2O_5	orthorhombic	310	0.61	0.47	A, CS
Fe_3O_4	cubic	-----	-----	0.49	CR
CoO	cubic (N)	-----	-----	0.51	S
Cu_2O	cubic	-----	-----	0.51	-----
SnO	tetragonal	-----	-----	0.51	-----
MoO_2	monoclinic	-----	-----	0.55	C
Al_2O_3 (alpha)	hexagonal	640-730	≈ 0.43	0.59	A
Al_2O_3 (gamma)	cubic	-----	-----	0.59	C
Cr_2O_3	hexagonal	-----	-----	0.59	-----
Nb_2O_5	monoclinic	475-590	0.42-0.49	0.59	A, CS
TiO_2	tetragonal	480	0.35	0.59	A, CS

TABLE 3.4 (continued)

Material	Structure	T_C (°C)	T_C/T_M	Ionicity [a,b]	Final Structure [c]
BeO	hexagonal	300	0.21	0.59	C
NbO	cubic(≈NaCl)	-----	-----	> 0.59	C, disorders
ZnO	hex./cubic	-----	-----	0.62 (b)	C
Ta_2O_5	tetragonal	550-715	0.38-0.46	0.63	A, CS
Ti_2O_3	hexagonal	-----	-----	0.63	C
V_2O_3	monoclinic	-----	-----	0.63	C
ZrO_2	monoclinic, cubic(CaF_2)	530	0.27	0.63	C
VO	cubic (≈NaCl)	-----	-----	> 0.63	C, disorders
HfO_2	cubic (CaF_2)	≈ 500	≈ 0.25	0.67	C
MnO	cubic (NaCl)	-----	-----	0.67	S
TiO	cubic (NaCl)	-----	-----	0.67	C
UO_2	cubic (CaF_2)	675	0.30	0.67	C
MgO	cubic (NaCl)	≈ 200	≈ 0.15	0.73	C
CaO	cubic (NaCl)	≈ 350	≈ 0.22	0.79	C
CaF_2	cubic (CaF_2)	< 25	< 0.18	0.89	C
BaF_2	cubic (CaF_2)	< 25	< 0.19	0.91	C
[LiF,KBr, KCl, KI, NaCl]	cubic (NaCl)	none	0.0	0.92-0.95 (b)	C

(a) Pauling Ionicity = $1 - \exp[-0.25(X_A - X_B)^2]$), X = electronegativity

(b) Phillips Ionicity = C^2/E_g^2 where C = ionic contribution to bonding, E_g = band gap

(c) Final Structure is: (A = Amorphous, CS = changes Stoichiometry, S = remains Stoichiometry, C = remains Crystalline) after ion impact doses exceeding 10^{17} ions/cm^2.

References: (Pauling 1939; Phillips 1970; Hotop et al. 1975)

TABLE 3.5

Prompt thermal sputtering of oxides.

A) Groups of structurally and chemically similar oxides which show differing responses to ion bombardment (Kelly 1979).

Category	Oxides preferentially lose oxygen	Oxides sputter congruently
1	CuO, NiO*	TiO, VO, MnO, FeO, CoO, NiO*
2	CdO	ZnO
3	PdO	NbO
4	Fe_2O_3, Fe_3O_4, Co_3O_4	Ti_2O_3, V_2O_3, Cr_2O_3
5	WO_2	MoO_2, UO_2,
6	PbO, PbO_2	SnO, SnO_2
7	TiO_2	ZrO_2, HfO_2, ThO_2
8	V_2O_5, Nb_2O_5, Ta_2O_5	
9	MoO_3, WO_3	

*The experimental observations of sputtering in NiO have produced contradictory results.

B) Predictions of the decomposition pressure model:

$p << 10^2$ atm at T=3333°K	$p \approx 10^2$ at T=3333°K	$p << 10^2$ atm at T=3333°K
ZrO_2	NiO	MoO_3
Al_2O_3	V_2O_5	SnO_2
TiO_2	ZnO	CdO
MgO	WO_3	PbO
BaO	SiO_2	GeO_2
Nb_2O_5		
UO_2		

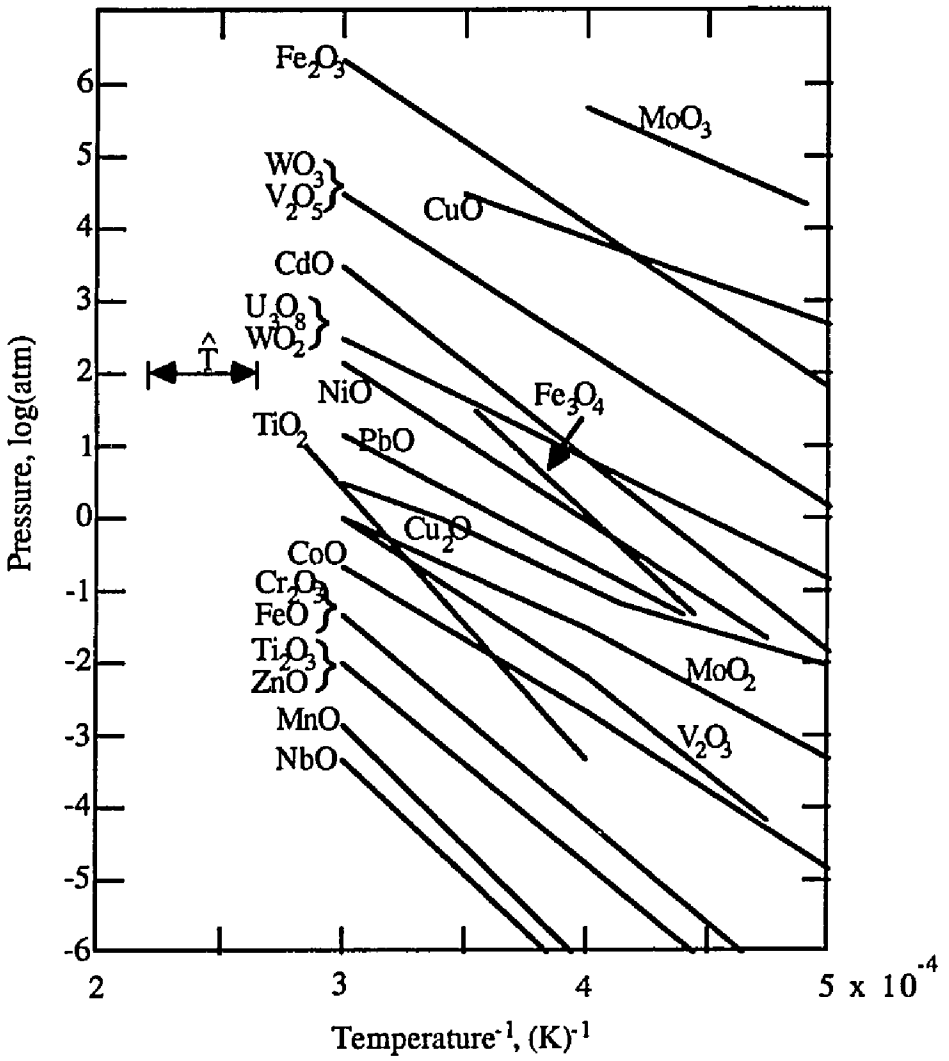

FIGURE 3.8 Vapor pressure verses 1/T at high temperatures. Oxides which exceed approximately 10^2 atmospheres meet the prompt thermal sputtering criterion for preferential loss of oxygen.

The question of whether the constituents will sputter congruently or preferential loss of oxygen will occur was also investigated by Kelly (1980). Their vaporization model postulates that the thermal spike associated with each ion impact permits processes

such as the following to occur:

$$2\,TiO_2(am) \rightarrow Ti_2O_3(am) + 1/2\,O_2(g) \qquad (3.4)$$

In principle, the state of the initial and final components should be consistent with those experimentally observed, in this case the TiO_2 goes amorphous before the final Ti_2O_3 is observed. The final phase is also assumed to be amorphous initially due its formation at high temperature, with its recrystallization being determined by its crystallization temperature. This criterion simply compares the total heat of atomization, $(\Delta H_a)_{tot}$, to partial heats of atomization to lower oxides as an extension to the surface binding energy arguments described in Chapter 2. The reaction with the lowest ΔH_a determines the final phase observed. Predictions based on this criterion were given in Table 2.8 (Chapter 2). For ion irradiations, it is quite successful.

3.3.2 - SLOW THERMAL SPUTTERING

Slow thermal sputtering describes the loss of the metal component in non-metallic solids by vaporization without the aid of a thermal spike. Such vaporization is recognized to occur in conjunction with the accumulation of metal on a surface following the loss of halide or oxygen via some reduction mechanism, e.g., ESD, during irradiation. It will occur only if the metal has sufficiently high vapor pressure at the temperature of the substrate. The energy distribution of the sputtered yield in this case is described by: $(dS/dE')_{thermal} \alpha (E')^{1/2} \exp[-E'/kT]$. The characteristic $E^{1/2}$ Maxwellian distribution is a deviation from the ideal gas distribution and has been attributed to thermal evaporation acting in cooperation with non-thermal mechanisms and the limitations in the motion of

the two-dimensional gas at the surface.

This category is believed to be of importance for the case of electron irradiation in the absence of thermal spikes as two types of sputtering are often observed. The first type shows that the anion is lost to directional electronic sputtering, while the metal atoms accumulate (Townsend et al. 1976b). Surface sputtering finally ceases due to encapsulation by a metallized layer. The second shows that one component is lost due to electronic sputtering, while the other is sufficiently volatile at the target temperature that it undergoes vaporization (Kelly 1981). The occurrence of one over the other of these processes would depend on the relative rates of metal vaporization and electronic sputtering.

3.3.3 - DIFFUSING DEFECT MODEL

Lastly, an interpretation of desorption based on slow thermal sputtering and the creation of defects which can diffuse to the surface and bring about neutralization. Assuming that a differential concentration of defects, $C_d(t)$ are created within the first few layers of the surface, they have a finite probability of diffusing to – and being ejected from – the surface. Under a diffusing defect type of mechanism, a sputtering yield (S_{elec}) may be approximated by:

$$S_{elec} \approx \frac{E_1 C_d(0) (D\tau)^{1/2}}{\Delta E} \qquad (3.5)$$

E_1 is the incident electron energy, D is the diffusion coefficient for the appropriate defect, τ is the lifetime of the defect, and ΔE is the energy consumed per relative defect. In some cases (e.g., diffusing electrons, holes and e-h pairs), $(D\tau)^{1/2}$ is equivalent to L_D, the

diffusion length for trapping. Note that this process is not specific to a particular defect creation mechanism, only that the subsequent defect can get to the surface. This mechanism predicts small kinetic energies of ejected particles as are observed experimentally, and should have a slightly different energy dependence of the sputtering yield than that due to surface excitations.

There have been a number of studies which have considered sputtering from a diffusing defect point of view as described above (Overeijnder et al. 1978b). A review of the sputtering of halogen atoms finds three possible diffusional mechanisms: 1) a focused RCS penetrating the surface, 2) diffusion of an interstitial (H-center) to the surface, or 3) diffusion of an exciton to the surface. They can all be described by Pooley-Hersh type processes, for example: an exciton in the bulk migrating to the surface where it undergoes a radiationless transition, giving rise to emission of an energetic halogen (Townsend 1973); or an exciton decaying in the bulk and starts a focused replacement collision sequence (Townsend et al. 1976b) followed by thermal migration of an H-center (Itoh 1972).

Mechanism 1 (focused RCS) will lead to high energy sputtered particles, in the range of 5 to 7 eV after the atom has overcome the surface binding energy. Experimentally observed energies in alkali halides are in the range of 1.5 eV, therefore it is unlikely that this mechanism is occurring. A focused RCS is also unlikely to reach the surface unless it initiates less than ~5 steps away at 200°K (Dienes and Smoluchowski 1976). Also, thermal defocusing will make this even less likely. Migrating H-centers, on the contrary, have long lifetimes (~10^{-6} s) and consequently long ranges (~10^{5} steps). The activation energy for migration is approximately 0.09 eV. A migrating H-center also has a stored energy of ~2.5 eV per atom (Itoh 1976). At the surface, this energy can be

used to break the X_2^- bond and to overcome the surface binding energy. The excess energy is then released in the form of kinetic energy of the escaping halogen (~0.5 to 1.0 eV).

Overeijnder et al. (1978b), have considered the sputtering of halogen and alkali atoms under electron bombardment and under varying temperatures. The energy distribution of the halogen atoms showed both thermal and athermal components, the low energy non-thermal component presumably due to electronic excitation. A definite cut-off was observed, above which only thermal effects were observed (~150 to 200 °C). The athermal component was not temperature dependent. It is suggested that this slow thermal sputtering is connected to the thermal migration of H-centers created by any appropriate electronic mechanism.

This can be explained quite adequately by using the geometrical treatment of Elliot and Townsend (1971), to predict which materials can have a focused RCS (and thus form F-H pairs). It is described as follows: Sputtering of halogen atoms above 150°C is considered to be dominated by diffusion of interstitial halogen atoms or by diffusion of holes, followed by thermal evaporation. Below 100°C, halogen atom desorption is partly thermal and partly enhanced by electronic defects, presumably H-centers. According to their model, sputtering can be divided into two cases: whether materials have S/D > 1/3 or S/D < 1/3; where S is the space between anions in the <110> direction and D is the diameter of a halogen atom, as shown in Figure 3.9. The S/D criterion essentially tests the Pooley-Hersh model as an efficient displacement defect mechanism. It measures both the ease of forming V_K centers (small S) and the ease of initiating a focused RCS (small D). By considering the available space involved in a Pooley-Hersh type of mechanism, they predict that for materials with S/D < 1/3, H-centers cannot easily be

formed, thus the non-thermal component of sputtering (via migrating electronic defects such as H-centers) should not exist. Correspondingly, for S/D > 1/3, there could be a considerable contribution of migrating H-centers via RCS processes and thermal migration. Experiments have shown that materials with S/D > 1/3 exhibit enhanced sputtering yields due to non-thermal halogens, while samples with S/D < 1/3 do not (Overeijnder et al. 1978b).

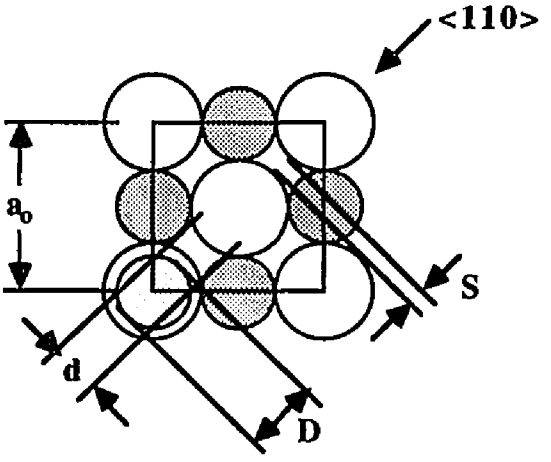

Figure 3.9 Geometrical picture of the S/D criterion. S represents the space between cations in the [110] direction. D is the diameter of the halide atom (vs. ion).

A summary of these results is presented in Table 3.6. The experimental results also show that alkali atoms are only evaporated thermally, a process which is vapor pressure related. At sufficiently low temperatures, no metal atoms should leave the surface, as is observed in these materials. This model also predicts the correct energy range of emitted particles.

TABLE 3.6

S/D criterion for the observance of non-thermal sputtering.

(Overeijnder et al. 1978)

Material	S/D	Non-thermal sputtering observed?
CsI	0.17	no
NaI	0.18	no
NaBr	0.29	no
CsBr	0.30	no
KI	0.33	yes
RbI	0.40	yes
KBr	0.47	yes
RbBr	0.55	yes
RbCl	0.73	yes

In summary, thermal effects in sputtering involve a complicated interplay of vaporization, diffusion, binding energies, and defect formation by alternative processes. It is argued that direct thermal sputtering (local melting) as a result of a beam induced thermal spike is unlikely for electron irradiation, but slow thermal sputtering is certainly possible. For the case of heavy ion bombardment, prompt thermal sputtering may be significant and criteria based on temperature ratio, bond type, and the heat of atomization have proven successful in predicting structure, stoichiometry, and composition changes. Whether or not these same criteria hold for electron bombardment has been investigated by this study and will be discussed in Chapter 6.

These are but a small sampling of the current state of understanding of defect creation mechanisms and their relation to sputtering/desorption processes. Renewed interest in the area of electron-stimulated desorption has been ignited by recently

discovered examples of surface desorption (Knotek 1984). In particular, new questions have arisen on the concepts of bonding in solids and on surfaces. There has also been interest in this phenomenon as an analytical probe of the atomic and electronic structures of surfaces.

The discussion of electronic damage mechanisms given here is admittedly only a limited cross section of a vast literature on the subject. The emphasis was strictly confined to only those mechanisms for which predictions of resulting structural changes could be made. As will be shown in Chapters 6 and 7, it is from these structural predictions where the electron microscopy studies begin.

The importance of electron-stimulated processes in causing radiation damage has yet to be fully explored. Electron microscopy investigations can further the understanding of surface radiation damage processes by monitoring the structure left behind and the extent to which the damage front progresses into the bulk. The resulting state of the surface, erosion rate, and consequent penetration of damage into the bulk are some of the most critical aspects of material degradation and – to date – are the aspects for which the least amount of information is available. Studies of this type would yield complementary information to the existing surface spectroscopy studies, where the understanding of desorption has been based primarily on the examination of desorbed species: namely their identity, charge state, angular and energy distributions, and electronic and vibrational distributions.

CHAPTER 4
EXPERIMENTAL DETAILS

4.1 - AN INTRODUCTION TO HREM

The technique of high resolution electron microscopy (HREM) for providing real space images of atomic structure is well established (Spence 1981). In interpreting HREM images, it is important to understand the relationship between the final image and the projected crystal structure. The microscope itself can be viewed as band pass filter of spatial frequencies, with the desired result being a one-to-one mapping of the crystal periodicities and the experimental image.

A generalized view of HREM image formation is illustrated in Figure 4.1. According to Abbe's theory (Hirsch et al.1977), the diffraction pattern which appears at the back focal plane of an objective lens is actually a mapping of the Fourier transform of the specimen. Maximum information about the specimen should therefore be obtained by allowing all of these diffracted beams to interfere and form an image, which involves another Fourier transform. In principle, this is what is contained in an HREM image. Retention of the full information, however, is only possible in the idealized case of a perfect lens and infinite objective aperture. Real lens systems introduce modifications to both the amplitude (because of finite aperture size) and phase (due to lens aberrations) of the intensity distributions in the back focal plane. These problems can be dealt with using standard contrast transfer theory.

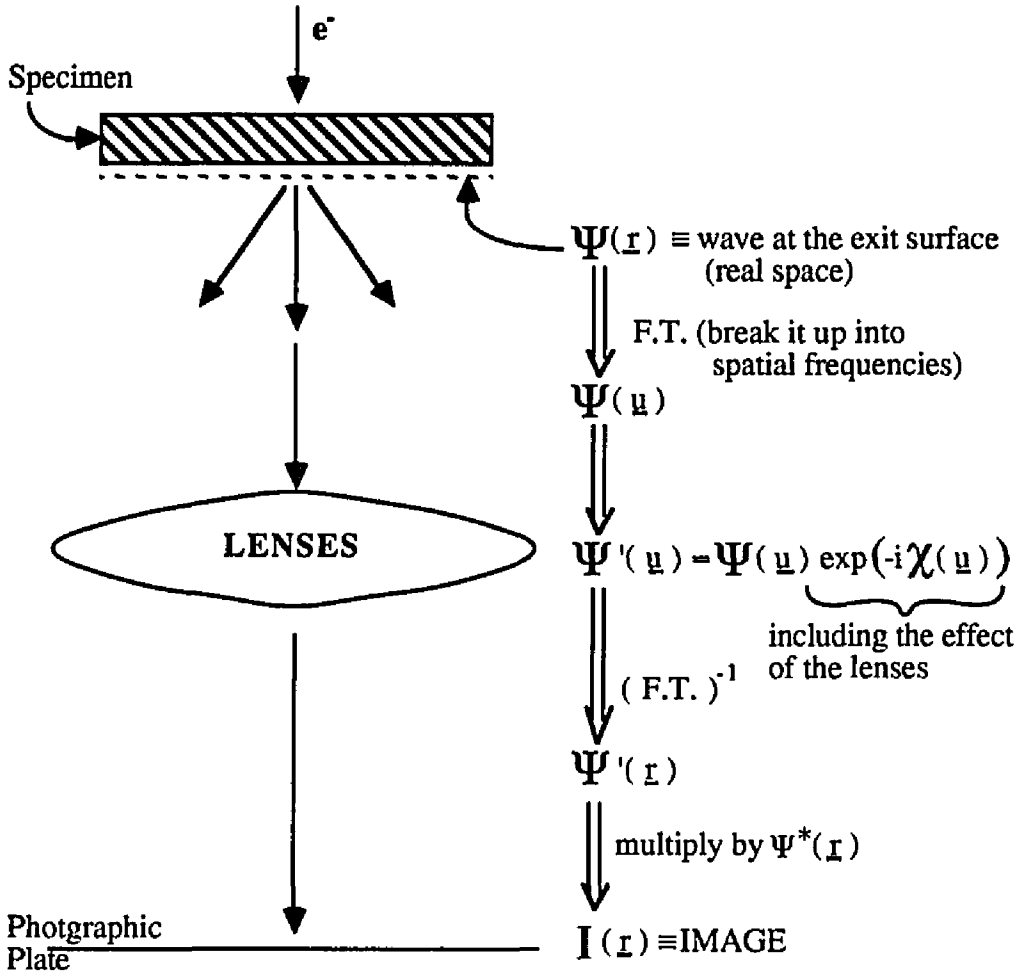

FIGURE 4.1 General view of HREM image formation in the electron microscope.

In standard contrast transfer theory, the interaction of the incident wave with the crystal and the action of the lenses are generally treated separately. The exit surface wave is generally represented by a transmission function, which carries the information about the projected potential of the crystal. The effects of objective lens defocus and sphericalaberration, chromatic aberration, and the effect of a finite objective aperture size are generally combined into a single contrast transfer function, T(u), which operates at the

back focal plane on the spatial frequencies, u, and is given by:

$$T(u) = A(u) \exp(i\chi(u)) \tag{4.1}$$

where A(u) is a step function representing the information cut-off by the objective aperture. $\chi(u)$ represents the phase distortion and is given by:

$$\chi(u) = \frac{2\pi}{\lambda}\left(C_s\frac{\lambda^4 u^4}{4} - \Delta z\,\frac{\lambda^2 u^2}{2}\right) \tag{4.2}$$

where λ is the incident electron wavelength, Δz is the lens defocus, and C_s is the spherical aberration coefficient. The effects of chromatic aberration and limited coherence may further be represented in T(u) by an envelope function which attenuates higher spatial frequencies (Ishizuka 1980).

The important result is that in order to faithfully transfer spatial information from the crystal to the image, $\exp(i\chi(u))$ should be near unity. For the specific case of surface profile imaging, an added constraint is one of image localization such that the transfer function is well-behaved at the spatial frequency of interest.

4.2 - THE NEED FOR UHV MICROSCOPY

With the development of better vacuum systems and better than 1.8 Å resolution instruments, HREM has recently entered the surface science arena as a complementary surface characterization technique. Various HREM techniques using modified conventional instrumentation have already been applied to surfaces with considerable success - but in a limited number of systems. The major reason for this has been the inability to do the experiments under surface science equivalent conditions. Conventional

microscopes operate in the 10^{-6} to 10^{-7} Torr range, making it virtually impossible to control the ambient atmosphere above the specimen. There are also no means to provide in-situ cleaning and/or annealing of the initial surface. For surface studies in particular, conventional instrumentation is inadequate to provide meaningful and consistent results, as the controversy in the early microscopy literature on oxide surfaces shows quite overwhelmingly (see Chapter 6).

At the outset of the present study, it was recognized that HREM contributions to surface studies of ESD or ESR could only be considered valid if performed under surface science conditions or at least in controlled environments. The approach of our group at Northwestern University has been to set up a UHV microscope and side transfer chamber (STC) system shown schematically in Figure 4.2. This concept allows the study of both species coming off the surface and the structure left behind, with initial surface preparation of the sample performed in-situ. Our group has developed an ultra high vacuum microscope operating in the 10^{-10} Torr range with an attached surface science chamber - the UHV-H9000 model manufactured by Hitachi Corporation - which allows for control of the surface environment, sample cleanliness, and also provides the ability to investigate other types of ionizing radiation such as ion and laser beams.

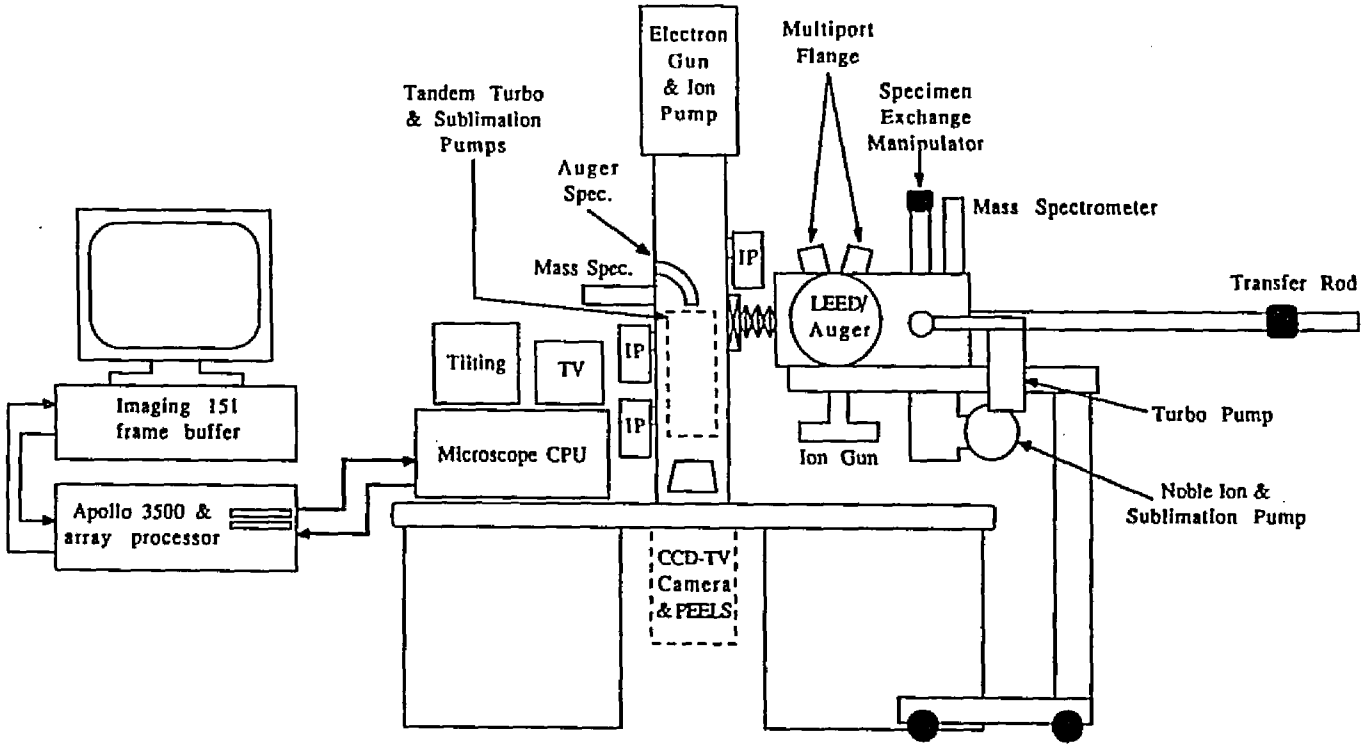

FIGURE 4.2 Schematic Diagram of the UHV-H9000 Microscope

4.3 - ANALYTICAL INSTRUMENTATION OF THE UHV-H9000

Unlike previous systems where an existing microscope was modified to accommodate UHV, the UHV-H9000 system was designed at the outset to be a surface analytical instrument. It is equipped with various analytical capabilities: parallel electron energy loss spectroscopy (by means of a Gatan 666 PEELS system), Auger electron spectroscopy (a modified Comstock model AC-901 AES system), and a mass spectrometer port are located on the microscope column; with low energy electron diffraction (LEED), Auger electron spectroscopy (AES), and various other analytic capabilities still under development in the STC. The AES system in the microscope column has only recently come on-line and was therefore not utilized for this study.

The STC houses a Perkin-Elmer ion gun which is capable of operation at energies between 500 eV and 4 keV, an optical annealing source, a UHV gas inlet valve, an evaporation source, a chemical dye laser source, and an Ametek quadrapole mass spectrometer. In addition, a Kimball Physics electron gun (with a variable voltage range of 0-10 keV) has been installed to perform low energy electron irradiations. Specimens can be transferred into the STC without fully breaking vacuum by means of a specimen transfer mechanism designed by John Bonevich.

The UHV-H9000 system is capable of operation at pressures in the low 10^{-10} to high 10^{-11} Torr range. In comparison, the conventional H-9000 operates in the 1×10^{-7} to 1×10^{-6} Torr range. The UHV microscope column is differentially pumped with three 20 l/s diode ion pumps, one each in the condenser lens, objective lens, and projector lens regions. The specimen area is additionally pumped by a 420 l/s tandem turbo-molecular pump. To offset potential vibration problems, the turbo pump is magnetically levitated and shock isolated. There is also a 1000 l/s titanium sublimation pump located at the

backside of the column, however UHV is regularly achieved without having to use it. The microscope column is generally fully bakeable. Baking of the objective lens region, however, is limited to 200°C and is accomplished by two quartz halogen lamps located in the column.

The STC is equipped with a 60 l/s noble pump and a 400 l/s titanium sublimation pump. It also houses a turbo molecular pump which serves a number of functions: 1) it rough pumps the STC and assists in the bake-out, 2) it can be used to differentially pump the ion gun, and 3) it is used to evacuate the specimen transfer mechanism. A mechanical pump, sufficiently filtered for back-streaming of contaminants into the chamber, is attached to the turbo pump and also serves to rough pump the gas line to the UHV gas-inlet valve. The STC is fully bakeable.

4.4 - OPERATING CHARACTERISTICS OF THE UHV-H9000

Both the H-9000 and UHV H-9000 are high resolution instruments, with point-to-point resolutions better than 2.0 Å, r..m.s. focal spread of 80 cm-Å, convergence between 0.8 and 1 mR, and spherical aberration coefficient (C_s) of 0.9 mm. The instrumentation is essentially identical for both microscopes. Incident electron energies can be varied from 50 keV to 300 keV in steps of 0.5% of the full voltage scale.

The incident flux can be varied from a few A/cm^2 to over 100 A/cm^2, which is of the order of 10^{12} times the typical electron flux in space. Flux was measured using a Faraday cage located in the viewing chamber and calibrated to the film sensitivity meter of the microscope. Once calibrated, the film sensitivity meter could be used to obtain the desired incident flux.

In addition to conventional TEM film recording, videotape and direct computer

image acquisition are available via an on-line TV camera. An Imaging Technologies 151 framestore device was used to "grab" and store digital images. This device is fully integrated into an Apollo minicomputer, and is set up so that images could be directly transferred to disk within the SEMPER image processing software system. The advantage is that surface radiation damage processes can be monitored by dynamic observation of the structural and chemical changes. Image processing could then be done either on-line or on the workstation ring.

4.5 - SAMPLE PREPARATION

The oxides used in this study were provided in single crystal, polycrystalline, or powder form from various sources as given in Table 4.1. An effort was made to obtain samples with the lowest possible impurity levels and a well-characterized structure and composition. For example, NiO samples used for this study were high purity bulk single crystals provided by Argonne National Laboratory courtesy of Dr. K. Merkle. The composition of these crystals was $Ni_{1-x}O$, with x being 0.0001. The oriented [001] single crystal TEM samples were prepared by John Reddy of Argonne National Laboratory. Samples from M. Gardos, K. Persels, and M. Radler were those used in their own research and are well-characterized in terms of structure and impurity levels. It was found that the least reliable samples were those in powder form due to the large surface area and consequent contamination problems. For at least one of the oxides (TiO_2) the powder form was unacceptable for use in the TEM due to inherent contamination problems. When possible, the effect of starting form of the sample (single crystal, polycrystal, or powder) was investigated. In all cases except TiO_2, the starting form had no effect on the subsequent experimental observations.

TABLE 4.1

Sources of materials used in this study.

Material	Form	Source
NiO	single crystal	Dr. K. Merkle, Argonne National Laboratory
CoO	single crystal	Dr. K. Persels, Argonne National Laboratory
MnO	single crystal	Dr. K. Persels, Argonne National Laboratory
TiO_2	single crystal	Atomergic Chemicals Corporation
TiO_2	polycrystalline	Dr. M. Gardos, Hughes Aircraft Corporation
TiO_2	powder	Johnson Mathey
MnO	powder	Dr. M. Radler, Northwestern University
FeO	powder	L. Cooper, Northwestern University
ZrO_2	polycrystalline	Johnson Mathey
Nb_2O_5	powder	Johnson Mathey
CeO_2	powder	Johnson Mathey
PbO	powder	Johnson Mathey
$LiNbO_3$	single crystal	Dr. R. Jarmon, Amoco Research Corporation

TEM samples were generally prepared by crushing the bulk crystal with an agate mortar and pestle immediately before insertion into the microscope. Optimum particle sizes ranged from 5 to 10 μm in diameter and roughly 30 to 100 Å thick at the profile edge of the particle.

The question of sample contamination from the agate mortar and pestle was evaluated by crushing some NiO samples in nickel foil for comparison. Essentially no difference was noted with these two preparation techniques. For the NiO and TiO_2 samples, a mortar and pestle was dedicated to that particular material only. Samples were both dry crushed, and crushed under high purity methanol. Again, essentially no difference was noted with these two preparation conditions; however a better particle size distribution was obtained with the wet crushing method. In this case, the suspension was ultrasonically mixed and a droplet of the solution was typically placed on a holey carbon

film supported on a Cu grid. For the UHV experiments, a SiO support film was used.

4.6 EXPERIMENTAL PROCEDURES

Samples were examined in a conventional Hitachi H9000 microscope typically operating at approximately 3×10^{-7} Torr and in a UHV-H9000 microscope operating at approximately 1.5×10^{-10} Torr. UHV samples were typically baked in-situ under vacuum for approximately 12 hr. at 250°C and in an O_2 atmosphere for short time periods (typically 15 minutes) during optical annealing. For the single crystal NiO samples, clean surfaces were achieved by a combination of sputtering with 2.1 keV Xenon ions and annealing in an oxygen atmosphere ranging from 10^{-6} Torr to a few millitorr. (Sputtering was not possible on the particles supported on the SiO films.)

ELECTRON ENERGY LOSS SPECTROSCOPY

Electron energy loss spectroscopy, a technique which measures the angular and energy distribution of electrons which have been scattered by the specimen, was used in the UHV microscope to monitor the initial contamination level as well as the changing chemical state of the surface during irradiation. For this, the inner-shell "core loss" spectra from characteristic ionization edges were generally monitored. For example, the carbon K-edge appeared in the PEELS spectrum when sample surface was contaminated. Chemical shift information could be obtained by monitoring the shape as well as the onset and maximum positions of the core loss edge (Egerton 1986).

DOSING EXPERIMENTS

A series of experiments were performed in which a clean NiO surface was

exposed to O_2 and CO gases respectively. High purity gases were inlet through a UHV-to-atmosphere leak valve. The gas-inlet line was equipped with filters for the trapping of particulates and H_2O. Prior to the opening of the valve, the gas line was alternately pumped with the gas of interest and flushed into the trapped roughing pump approximately 10 to 15 times.

4.7 - METHODS OF HREM SURFACE IMAGING AND ANALYSIS

The primary microscopy techniques used in this study include HREM imaging and diffraction as well as conventional bright field and centered dark field imaging, illustrated in Figure 4.3. Bright field images are simply those where the transmitted beam contributes to the final image, usually with some or all of the diffracted beams excluded. Centered dark field images are simply those in which the transmitted beam is excluded and the diffracted beam of interest is placed on the optic axis in order to minimize the lens aberrations.

The images shown in Chapters 5 and 6 are generally HREM images of the surface profile, diffraction patterns, and computer image simulations, as illustrated in Figure 4.4. Surface profile imaging involves the observation of a crystal edge under localized imaging conditions such that a one-to-one mapping of the projected arrangement of atomic columns at the surface is achieved (Marks 1984). Each sample was irradiated by centering the focused electron beam at the profile edge. Structural changes were observed in projection as they progressed inward from the profile surfaces. For the remainder of the text, brackets [ ] will be used to indicate the crystallographic zone being described. The notation [zone]/(profile plane) will be used to indicate specific profile surfaces.

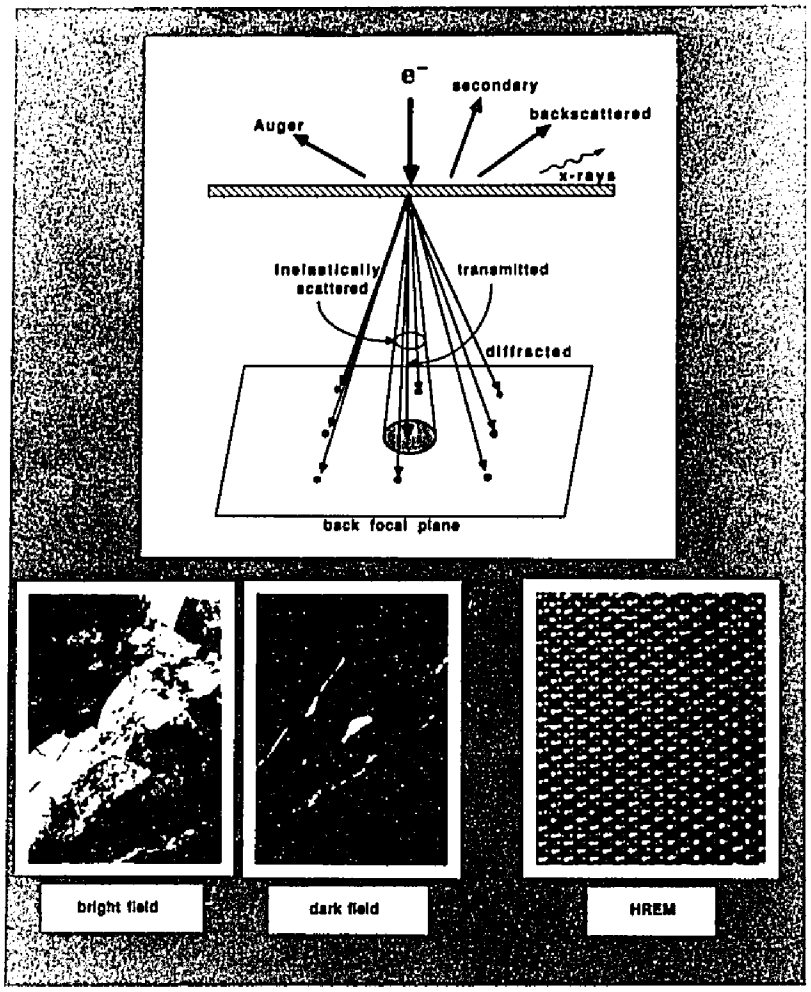

FIGURE 4.3 (top) The variety of processes which occur when an electron beam impinges on a sample. (bottom) Examples of microscopy techniques used in this study.

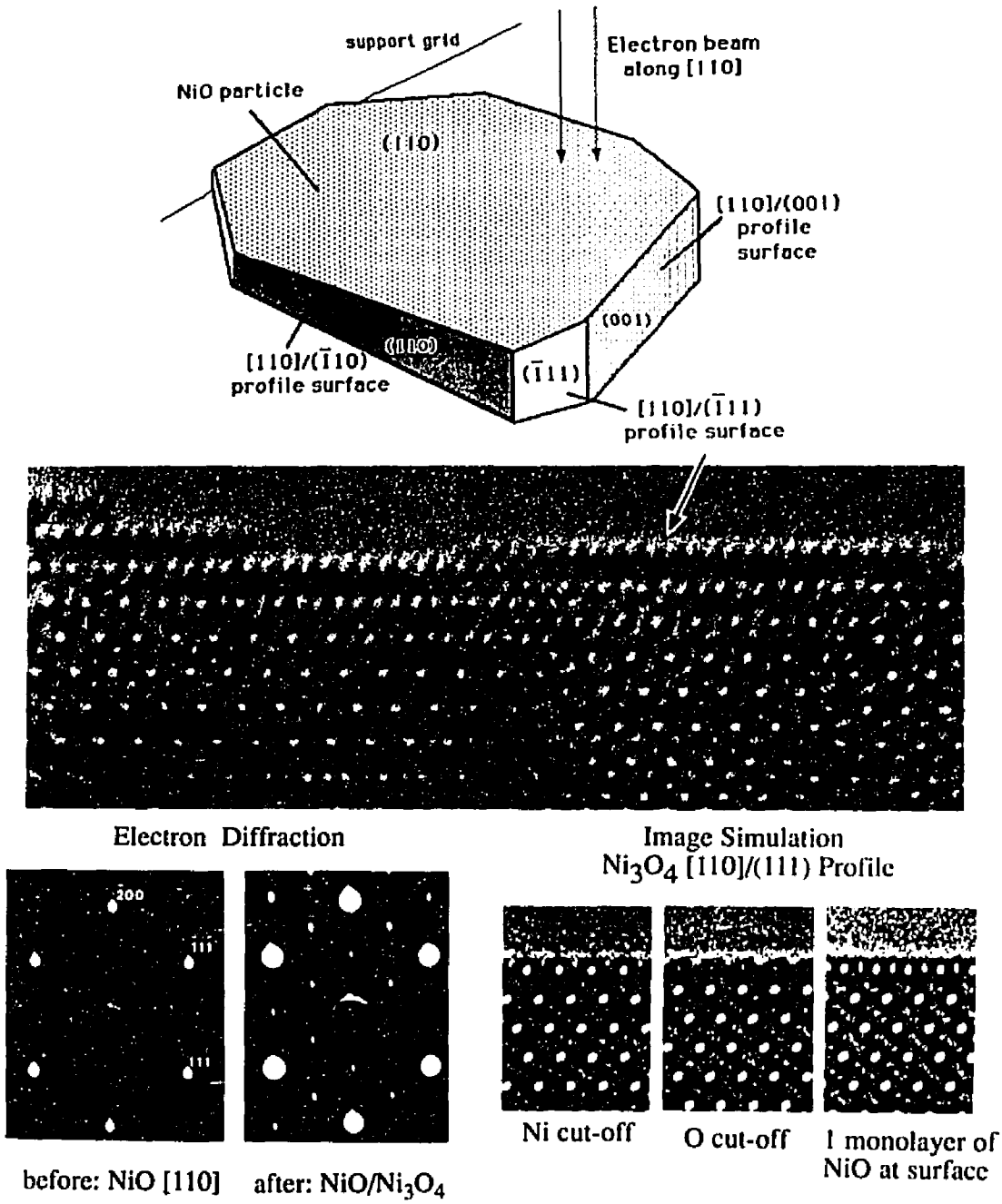

FIGURE 4.4 (top) Schematic diagram of the experimental sample configuration used for surface profile imaging. (bottom) Examples of HREM imaging and simulation techniques used in this study.

For structure identification, electron diffraction and through-focal experimental images are used. The experimental surface profile images are compared with computer calculations using the standard Multislice algorithm (Cowley and Moody 1967), which is the most efficient for large unit cell structures and thin specimens. This method, shown schematically in Figure 4.5 operates under the assumption that the crystal may be sliced plane-by-plane relative to the incident beam direction. In the planes of the atoms (positions 1, 3, and 5) the incident wave is multiplied by a phase grating function, which includes the crystal potential projected in the z direction. Between the atomic planes (positions 2 and 4), the resultant wave is acted upon by the Fresnel propagator function. This iteration continues for the entire crystal thickness in the z-direction. The Multislice algorithm is actually only a combination of two Fourier transforms and two multiplications as is shown in Figure 4.6.

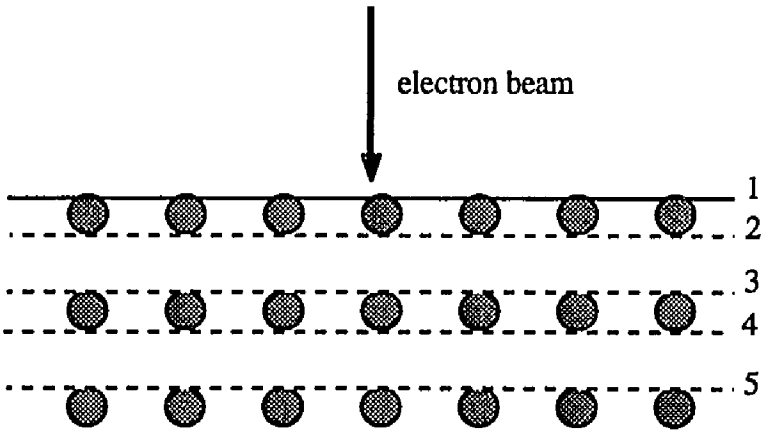

FIGURE 4.5 Schematic illustration of the Multislice method.

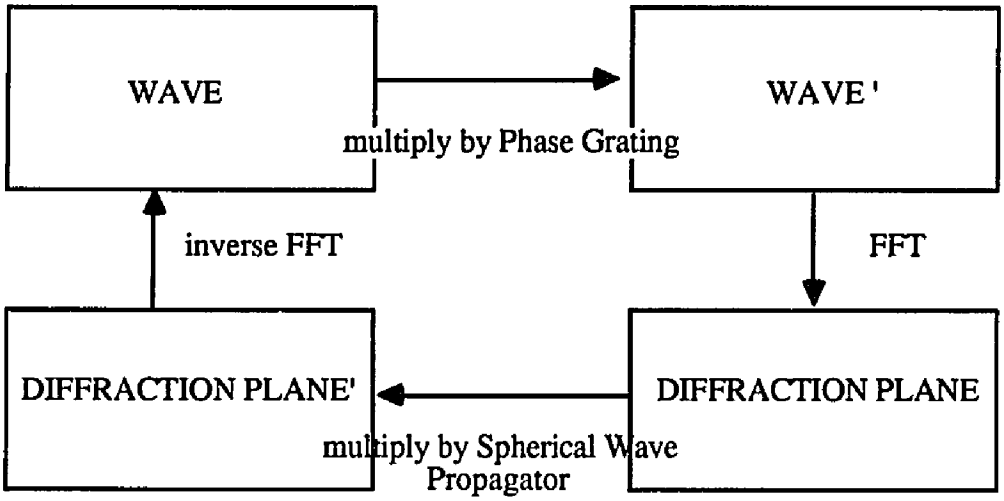

FIGURE 4.6 The Multislice algorithm.

A special consideration in using the Multislice method for surface calculations is that they must be set up to prevent unwanted interference which arises because the numerical Fast Fourier Transforms (FFT) used in the calculations implicitly extend the unit cell periodically. A surface calculation must therefore be set up such that the unit cell dimension parallel to the surface is large enough to prevent aliasing. One further problem is that the calculations of certain high index surfaces or surfaces in complex non-cubic systems sometimes require choosing non-orthogonal axes and/or the use of extended unit cells. Care must be taken such that the transformed unit cell correctly reproduces the atom positions, and also that is does not produce a skew in the z direction.

4.8 - CROSS CORRELATION ANALYSIS OF HREM IMAGES

Typical HREM structure images contain a large amount of intensity information which is masked by both statistical and amorphous noise. In the interest of finding reliable methods for which to recover the maximum amount of information from such

images, the use of correlation techniques in image processing was investigated (Saxton 1978; Frank 1980).

SEMPER correlation averaging routines were used to test the use of cross correlation in recovering position and intensity information from noisy images. A number of image conditions were tested using simple Gaussian functions assuming a 5 pixel/Angstrom resolution. The goal was to evaluate how well the cross correlation worked under various levels of noise and motif configurations.

The cross correlation function simply provides the statistical comparison between two images. Two quantitative measurements may be obtained: 1) the position of maximum correlation (r_j); and 2) the peak heights (α_j) - corresponding to the degree of alignment and similarity of two functions.

To simulate typical HREM images a linear array of Gaussian functions was produced, using a single Gaussian as the motif. The use of a windowed motif (chopped Gaussian at FWHM) was also investigated to ascertain whether better resolution in the cross correlation function could be obtained.

With respect to HREM images, the problem can be considered as a least squares fit requiring the minimization of the error parameter, R, given as:

$$R = \int \left\{ I(\bar{r}) - \sum_j \alpha_j m(\bar{r} - \bar{r}_j) \right\}^2 d\bar{r} \qquad (4.3)$$

where $I(\bar{r})$ is the image, and $m(\bar{r} - \bar{r}_j)$ is the motif. The unknowns are the positions, $\bar{r}_j$, of the motifs and their peak heights, α_j. The aim is decompose the total image into separate motifs, each characterized by positions $\bar{r}_j$ and peak heights α_j. One standard approach is

to expand the error parameter:

$$R = \int \left\{ I^2(\bar{r}) - 2\alpha_j I(\bar{r}) \sum_j \alpha_j m(\bar{r}-\bar{r}_j) - \sum_{j \neq k} \alpha_j \alpha_k m(\bar{r}-\bar{r}_j) m(\bar{r}-\bar{r}_k) + \sum_j \alpha_j^2 m^2(\bar{r}-\bar{r}_j) \right\} d\bar{r} \tag{4.4}$$

and look for the peaks (or maxima) in the cross correlation function (XCF):

$$XCF(\bar{\bar{r}}_j) = \int I(\bar{r})\, m\,(\bar{r}-\bar{r}_j)\, d\bar{r} \tag{4.5}$$

This would result in the minimization of R, provided that the cross term is negligible.

For the model HREM examples, two limiting cases were found: 1) where the motif positions are well separated and the cross term is negligible, and 2) where motif or peak overlap occurs and the cross term is non-negligible. In the first case the cross correlation plus a peak search will give peak position $\bar{r}_j$ and peak height α_j directly. In the second case, the situation becomes more complicated. There are a number of approaches one could take such as solving the equation explicitly, windowing the motif, or using an iterative approach. The iterative approach involves: 1) making a first guess of certain motif positions $\bar{r}_k$, 2) subtracting the motif at these positions from the image to form a new image I', and 3) cross correlate the motif with I', and reiterate until the result converges as illustrated in Figure 4.7.

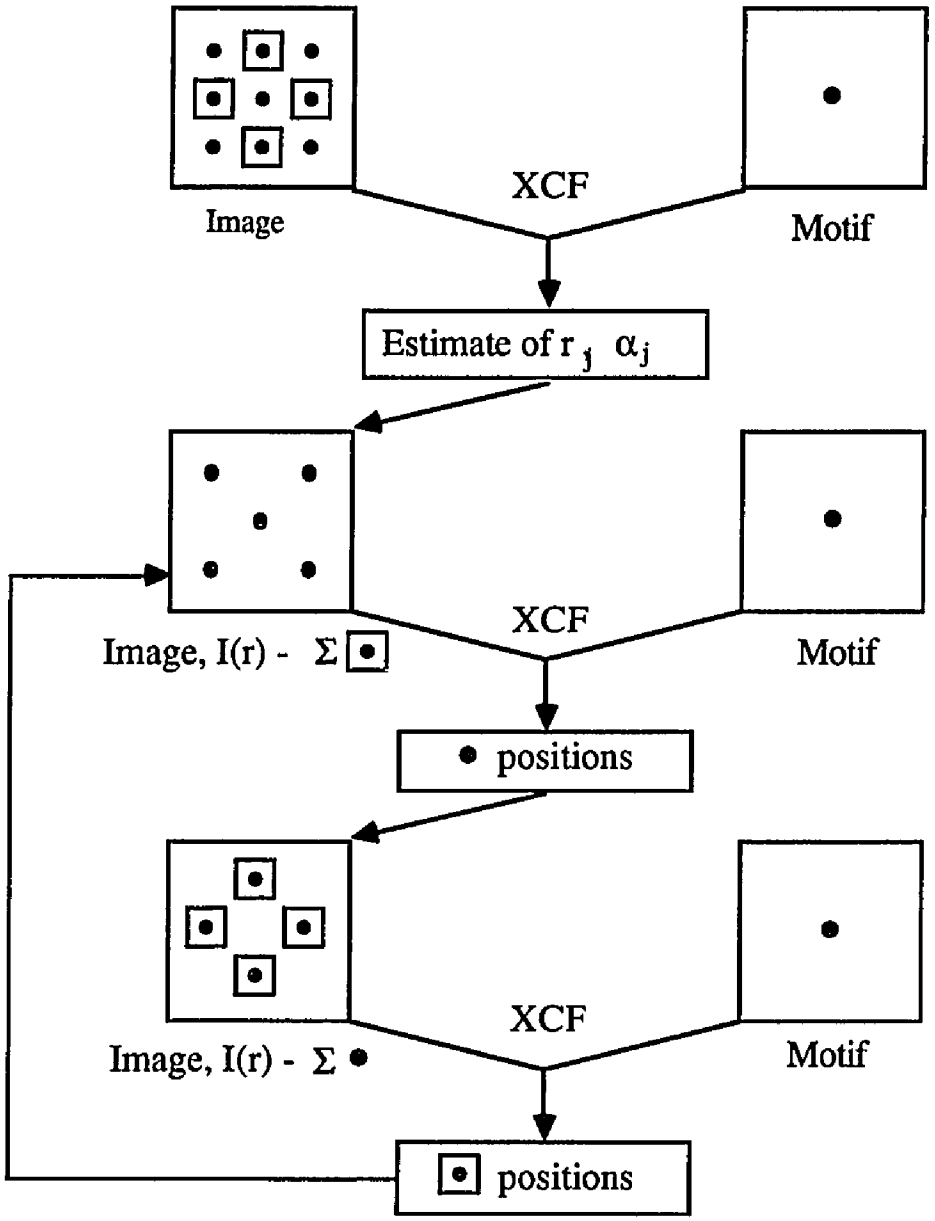

FIGURE 4.7 Iterative procedure to determine peak positions of overlapping motifs using cross correlation (XCF).

To monitor the accuracy of this technique, statistical data on peak position error and peak height standard deviation were compiled, varying both noise levels and motif separations. When the motifs are well separated, the cross correlation function could detect positions without fail, however rapidly failing when the radius of the motif was comparable to the peak separation.

As long as the motif positions are well separated, with spacing greater than twice the full width half maximum of motif, the XCF technique could detect positions with extreme accuracy, regardless of noise level (up to the chronic case of a 25 electrons/Å^2 dose when 10^4 electrons/Å^2 are generally required for HREM imaging). The peak height could be characterized even in this chronic case with a standard deviation of better than 4%.

When the motif positions were not well separated, the motif positions could be located to within an error of 10% with a standard deviation comparable to the first case by masking the motif. Using the iterative approach, the error in position could again be improved to within a maximum error of just over 4% in the chronic case.

Use of this technique provided an alternative means for the quantification and analysis of HREM images with simple well-defined motifs. Further development of this technique, however, is still required for the case of complex motifs.

4.9 SAMPLE THICKNESS DETERMINATIONS

The sample thickness was generally determined by the comparison of through-focal and through-thickness image simulations, illustrated in Figures 4.8 and 4.9 respectively for the Ni_3O_4 spinel phase. This phase proved to be quite sensitive to crystal thickness and objective lens defocus. Comparison of the surface calculations reveal that

thickness deviations as small as 10 Å can be apparent in the image.

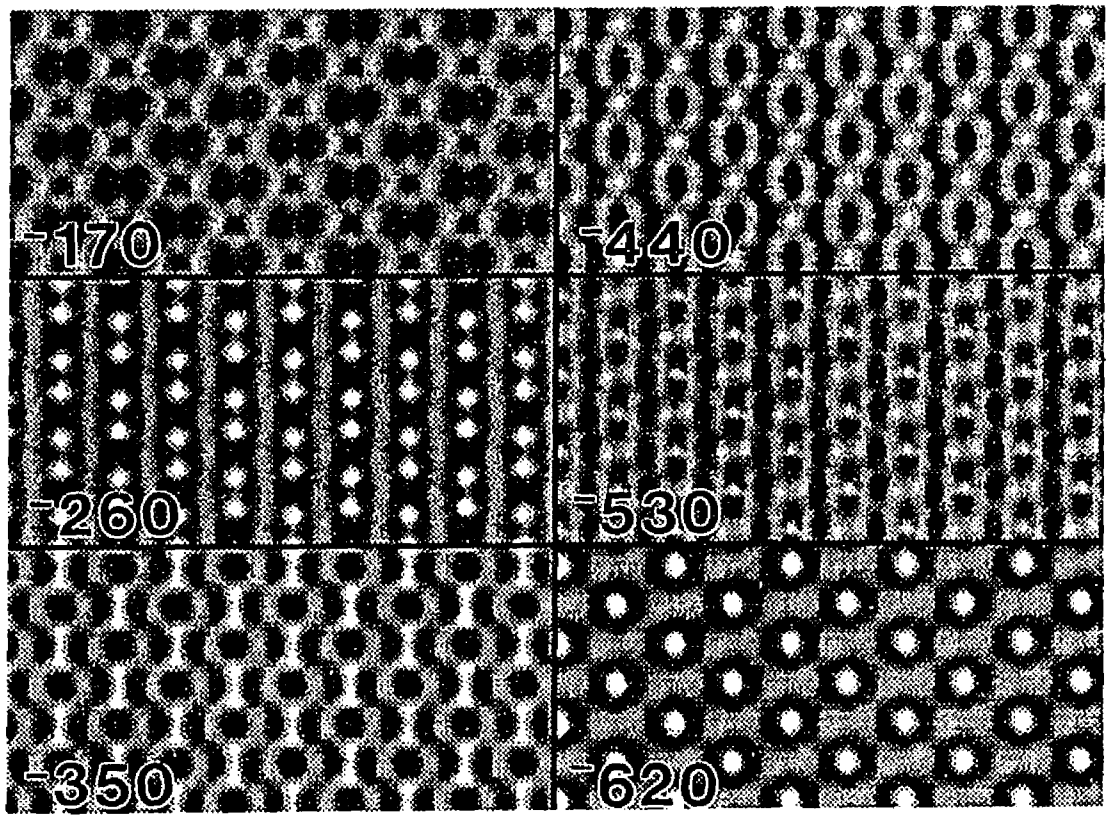

FIGURE 4.8 a) Example through-focal image calculations for Ni_3O_4. Focus step is 90 Å. Sample Thickness = 30 Å.

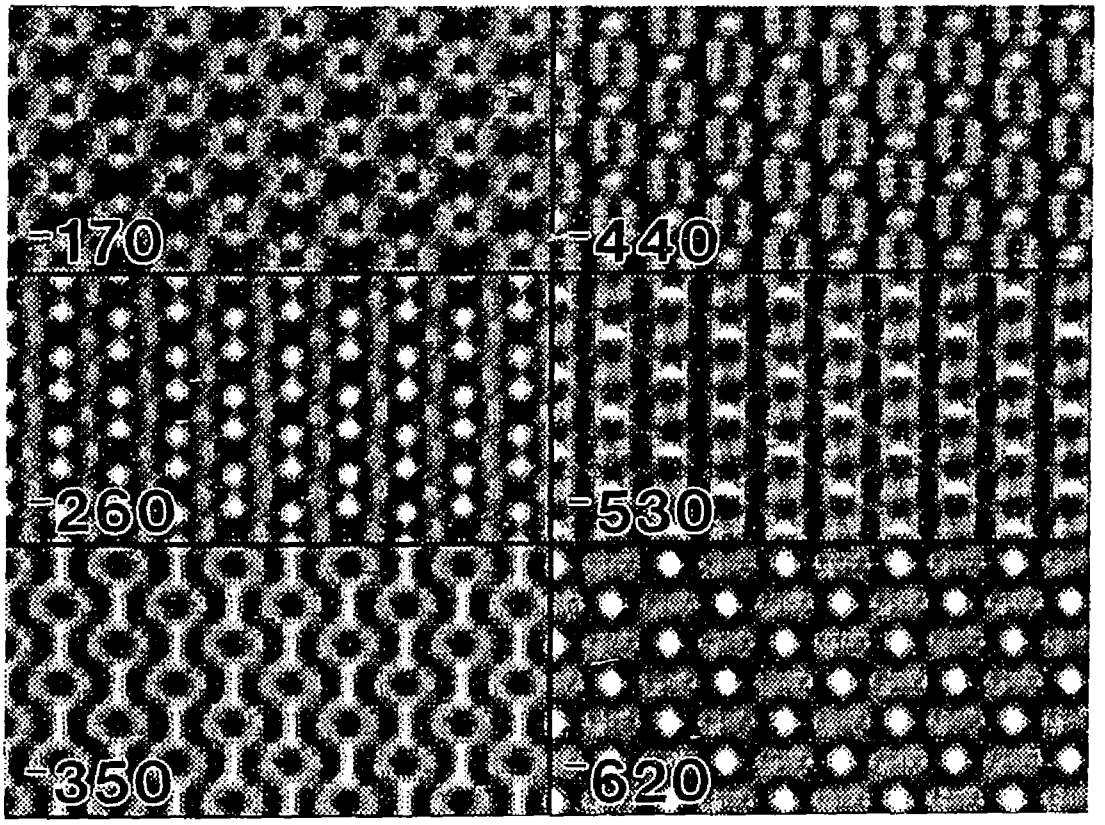

FIGURE 4.8 b) Example through-focal image calculations for Ni_3O_4. Focus step is 90 Å. Sample Thickness = 40 Å.

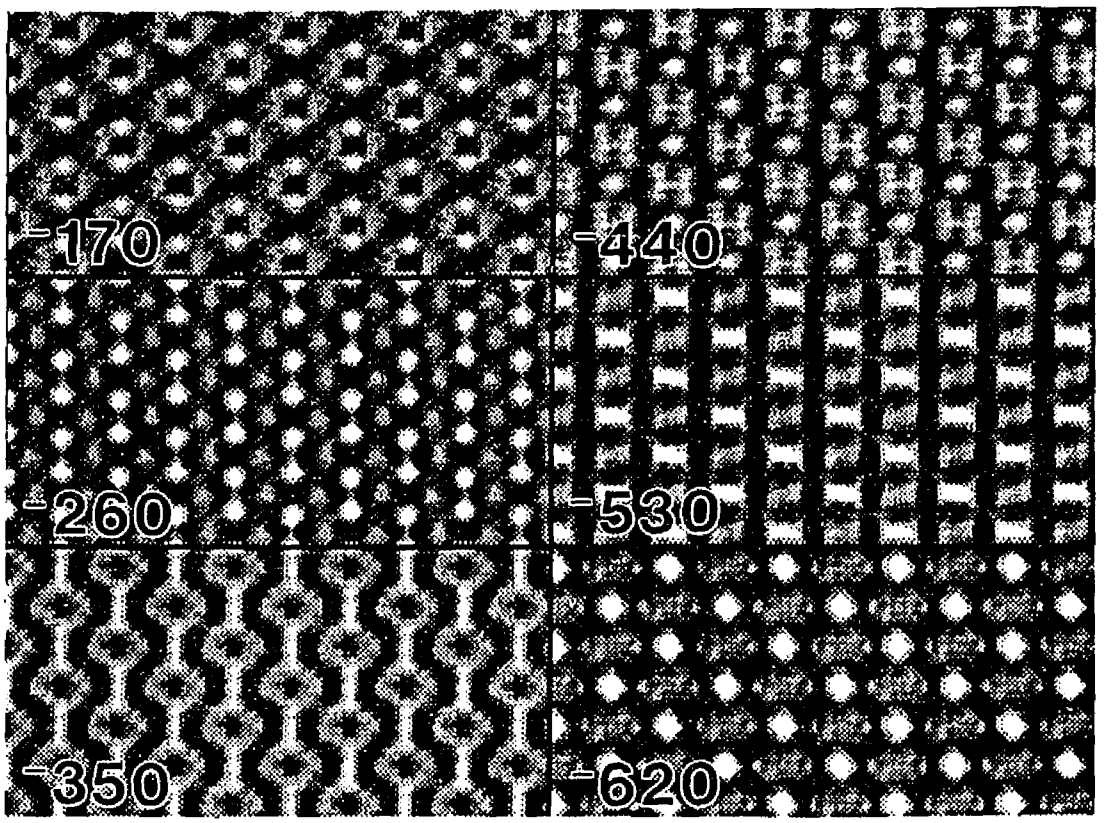

FIGURE 4.8 c) Example through-focal image calculations for Ni_3O_4. Focus step is 90 Å. Sample Thickness = 50 Å.

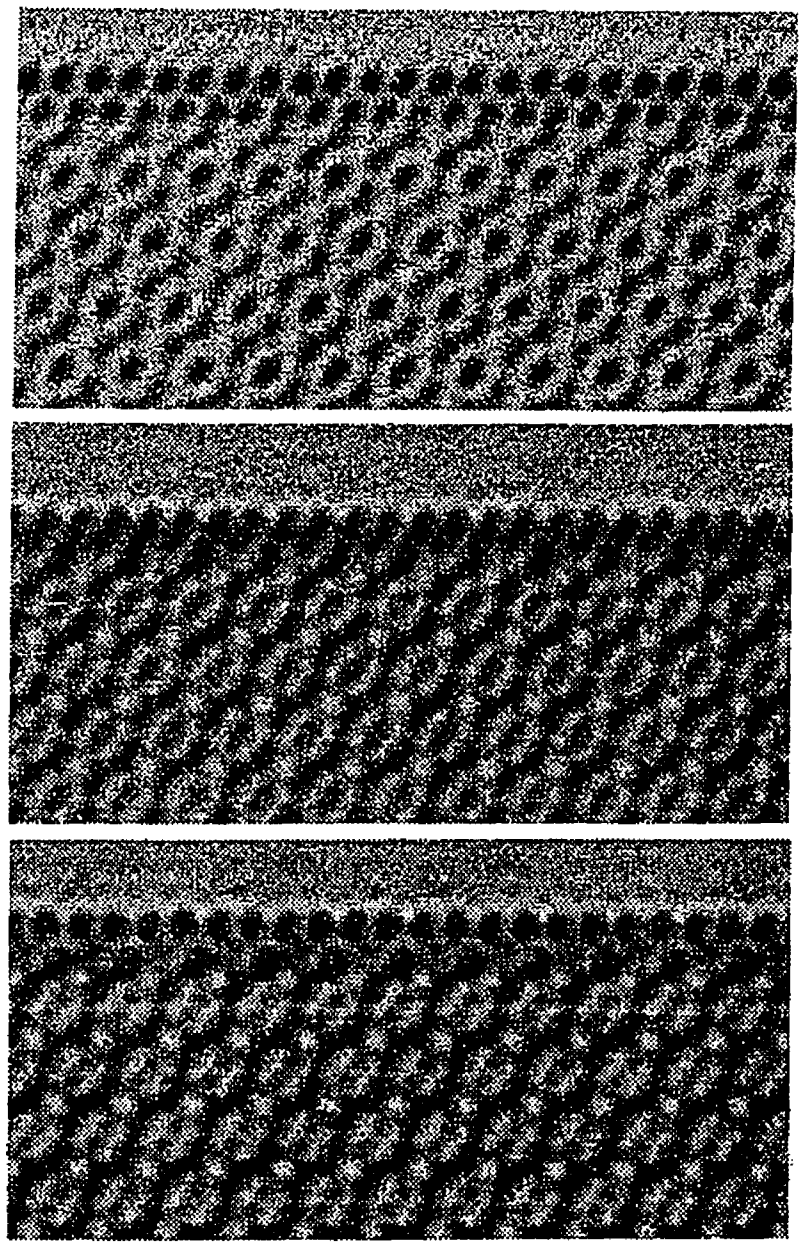

FIGURE 4.9 Example through thickness calculations for Ni_3O_4. Lens defocus is –440 Å. Sample thicknesses are 30, 40 and 50 Å from top to bottom.

In addition to the image calculations and in samples too thick to obtain a HREM image, the technique illustrated in Figure 4.10(a-b) was utilized. This technique simply maps out the projected image of a defect such as a dislocation from its projected image on the film. For example, the sample shown is a NiO [001]/(001) thin film. Dislocations in NiO generally run in [110] types of directions in (110) planes. This is what is illustrated in Figure 4.10(b). Once the crystal (hkl) orientation is determined, one can then calculate the angle θ between the surface and the slip plane of the dislocation. By measuring the projected distance (x), the thickness (t) may be determined as shown. The sample thickness in this case was determined to be 310 nm.

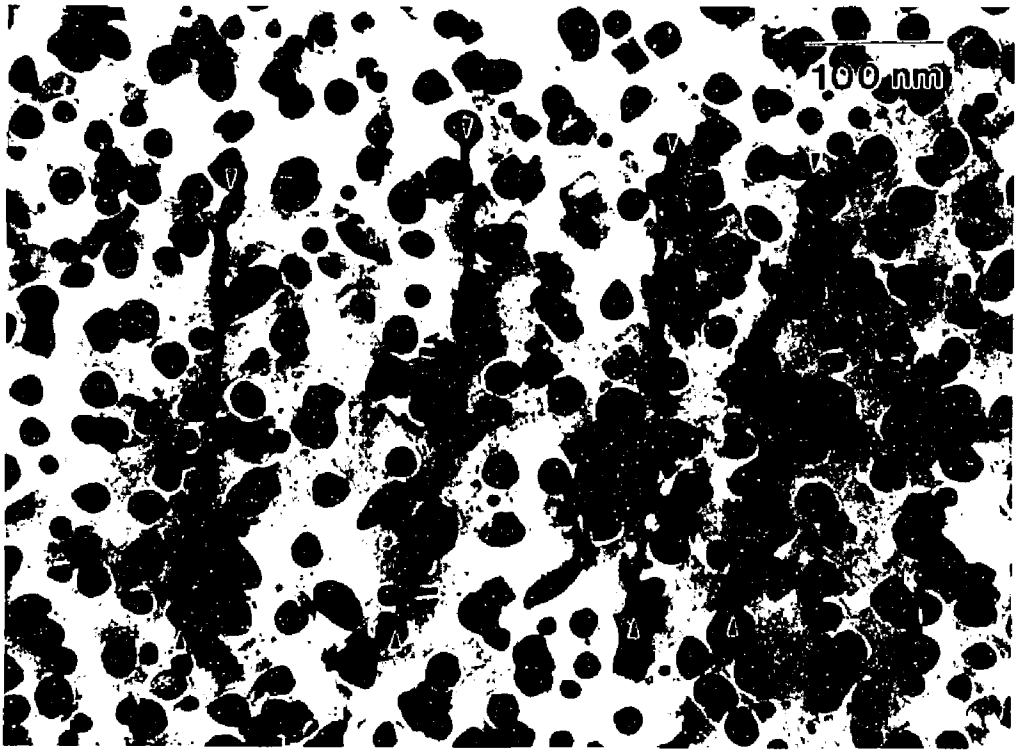

a)

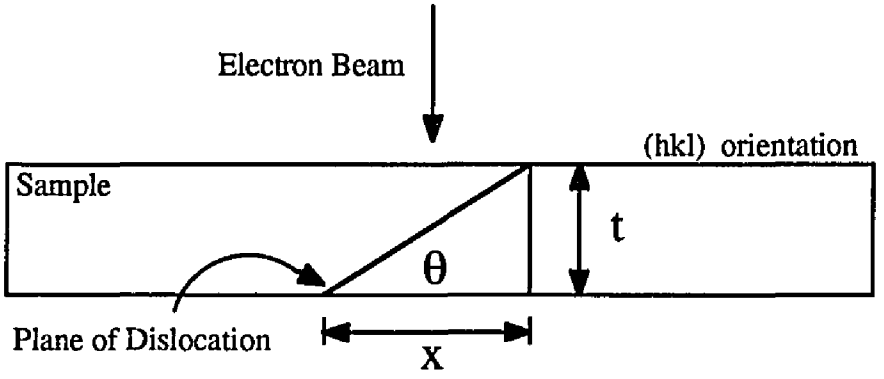

b)

FIGURE 4.10 a) Image of a NiO [001]/(001) crystal showing dislocations running from top to bottom. b) Schematic diagram of the sample geometry in (a). θ in this case = 45°.

CHAPTER 5
ELECTRON IRRADIATION DAMAGE IN NiO AND OTHER METAL MONOXIDES IN THE GROUP VII-VIII SERIES

5.1 - INTRODUCTION

The transition metal oxides span as broad a range as any class of materials. They lie between the extremes of ionic and covalent bonding behavior, and in terms of electrical behavior they range from insulating to metallic. Structurally they are just as diverse, as is illustrated in Table 5.1 which shows a classification of the oxides of the transition metal series. The crystal structures are often classified by considering a cubic or hexagonal close-packed lattice of one set of ions with the other set filling the octahedral and tetrahedral interstices. Actual structures generally deviate from this ideal packing due to distortions caused from the different sized ions. Since d-electron bonding levels are involved, the cations may exist in various valence states and thus give rise to multiple structure types.

NiO, CoO, MnO, and FeO - oxides of the group VII-VIII series - are a subset of the first transition metal series of monoxides (TiO through NiO) which exhibit the rocksalt (NaCl) structure. The oxides of the early end of this series (e.g. TiO and VO) tend to behave as metallic conductors since the lower effective nuclear charge enables the cation d orbitals to collectively penetrate from one unit cell to another. This type of behavior has been shown to stabilize gross deviations on either side of stoichiometry (Smeltzer and Young 1975). In comparison, oxides of the later end (e.g. CoO and NiO) behave as p-type semiconductors with conduction arising from the effects of the localized d electrons, and consequently show only very small deviations from stoichiometry (see Table 3.1, Chapter 3).

TABLE 5.1

Classification of oxides of the transition metals.

Metal	Sc	Ti	V	Cr	Mn	Fe	Co	Ni	Cu	Zn
	Y	Zr	Nb	Mo	Tc	Ru	Rh	Pd	Ag	Cd
	Lan.	Hf	Ta	W	Re	Os	Ir	Pt	Au	Hg
Oxide									M_2O	
		MO	MO	MO	MO	MO	MO	MO	MO	MO
					M_3O_4	M_3O_4	M_3O_4			
	M_2O_3	M_2O_3	M_2O_3	M_2O_3	M_2O_3	M_2O_3	M_2O_3	M_2O_3	M_2O_3	
		MO_2	MO_2	MO_2	MO_2	MO_2				
			M_2O_5	M_2O_5	M_2O_5					
"Ionic Oxides"										
"Covalent Molecules"				MO_3	MO_3	MO_3	MO_4			
						M_2O_7				

The rocksalt-structured oxides may be considered as the metal monoxide analogies to alkali halides of the same structure. It is known that H-centers are a stable form of electronic defect in these materials (Crawford and Slifkin 1972), causing a <110> distortion similar to a self-trapped hole. But because of the extreme non-equilibrium situation which is set-up, the nature of irradiation defect interactions is not well

established. As was discussed in Chapter 3, electron-stimulated damage mechanisms in these structures involving self-trapped exciton decay would only be energetically favorable at or near the surface. Shown in Table 5.2 is a continuation of Table 3.6, where a comparison of the S/D ratio is made to the observance of nonthermal, nonballistic sputtering processes in the rocksalt structured oxides. The value of d/D is also given, which is a measure of the available space for migration of the H-center. As was illustrated in Figure 3.9, the lower the value of d/D, the easier it is for the H-center to squeeze past the nearest neighbor cations along the [110] directions. As S/D is consistently $< 1/3$ in each case and $d/D > 1$, the model predictions do not show any propensity for these materials to undergo ionization damage in the form of the migration of electronic defects to the surface or decay of excitons at the surface. This type of sputtering has been studied only in a limited number of oxides (Chen and Sibley 1967; Elliot and Townsend 1971; Knotek and Feibelman 1979). The results show that electronic mechanisms do not appear to play a major role in radiation damage of these materials.

From consideration of the above data and the discussion of mechanisms in Chapter 3, certain predictions may be made. Sub(ballistic)-threshold, low temperature irradiation of the transition metal monoxides with rocksalt structure should not result in preferential loss of oxygen. Neither excitonic or Auger types of processes are favored in these oxides. Thermal and ballistic mechanisms may be operative under the conditions of high flux or if the ballistic sputtering threshold is exceeded.

TABLE 5.2

S/D criterion applied to oxides.

$$S = \frac{\sqrt{2}a_o - 4r^-}{2} \qquad d = \frac{\sqrt{2}a_o}{2} - 2r^+$$

Oxide	a_o	cation radius, r+	anion radius, r-	S/D	d/D
TiO	4.17	0.80	1.40	0.113	1.02
NiO	4.1769	0.69	1.40	0.116	1.19
CoO	4.26	0.72	1.40	0.161	1.19
MnO	4.44	0.80	1.40	0.257	1.17
FeO	4.31	0.60	1.40	0.188	1.40
MgO	4.20	0.65	1.40	0.257	1.27
NbO	4.2013	0.70	1.40	0.259	1.19

In light of these predictions, a most interesting response to electron irradiation is found in NiO. NiO surfaces have been extensively studied by conventional surface science techniques; however the findings remain inconclusive regarding electron irradiation effects such as electron-stimulated desorption (ESD) and electron-stimulated reaction (ESR). Conflicting investigations report both oxygen (O^+) Knotek-Feibelman type of ESD similar to that of the maximum valence transition metal oxides (Gerritson et al. 1984; Wang and Verhoeven 1986) as well as no preferential oxygen loss (Knotek and Feibelman 1978; Niehus and Losch 1981). Electron irradiation effects in the NiO system have previously been investigated in the electron microscope, but not under UHV conditions. The HREM studies are inconclusive as well. Reports of surface reduction (Ostyn and Carter 1982; Smith, Bursill, and Jefferson 1986; Liu and Cowley 1987; Luzzi

et al. 1988) as well as stability toward ionization damage have been published (Buckett and Marks 1989). It will be shown here that for NiO – and related metal monoxides of the group VII and VIII series: CoO, MnO, and FeO – the microscope environment itself can have a significant effect on the nature of the damage mechanism.

The initial structure of each materials is the rocksalt structure with space group Fm3m (#225), as confirmed by x-ray and electron diffraction. Crystal structure and diffraction data for the NiO system was obtained from the *JCPDS* (1973) and O'Neill and Navrotsky (1983). These oxides exhibit cation deficient non-stoichiometry and are reported to exhibit antiferromagnetic behavior (Roth 1958). NiO supports the least amount of non-stoichiometry, with increasing deviations from stoichiometry occurring in CoO, MnO, and FeO in that order. NiO and CoO are physically very similar, except that CoO is thermodynamically unstable with respect to Co_3O_4 spinel phase at room temperature (Dieckmann 1977). The spinel phase occurs as a stable low temperature phase in the Mn-O and Fe-O systems as well (Kofstad 1972).

Profile surfaces were examined in a Hitachi H-9000 high resolution electron microscope with a vacuum of approximately 3×10^{-7} Torr and also in a Hitachi UHV H–9000 microscope with a vacuum of approximately 1.5×10^{-10} Torr, operating at voltages between 90 kV and 300 kV. Initial surfaces were observed to be simple terminations of the bulk structure, in agreement with the surface science literature (Prutton et al. 1979). Optimum particle sizes ranged from 5 to 10 μm in diameter and roughly 30 to 200 Å thick at the profile surface. The [001] and [110] crystal orientations were examined in detail. The [111] orientation was also examined, but was rarely seen and thus only diffraction and qualitative structural information could be obtained. To verify the effect of the surface environment, a series of O_2 and CO dosing experiments were

carried out in the UHV chamber.

Each sample was irradiated by centering the focused electron beam at the specimen profile edge. Three specific electron flux conditions, low (6.2×10^{19} e-/cm^{2}s), medium (1×10^{20} e-/cm^{2}s) and high (6.2×10^{20} e-/cm^{2}s), were used. The incident electron energy dependence was determined by varying the operating voltage of the microscope.

5.2 - RESULTS

Radiation damage processes in NiO fell into three categories: ballistic, surface-initiated oxidation to a Ni_3O_4 spinel phase, and surface-initiated reduction to metallic nickel. A summary of the results is presented in Table 5.3. Ballistic damage was observed at 300 keV but not 100 keV irradiation, and is described in section 5.2.1. Formation of the spinel phase was observed only in the non-UHV environment and was determined to be an electron-stimulated oxidation reaction, as described in sections 5.3.1 and 5.3.2. Metallic nickel was observed only in the presence of amorphous carbon and/or CO, and is described in sections 5.4 and 5.6.2. As outlined in Chapters 2 and 3, careful consideration of the incident energy and flux were taken into account to insure that thermal effects would be kept to a minimum, that bulk displacements would not enter into the analysis, and to insure that the observations made were truly due to surface effects. It was confirmed that the observed processes were surface-initiated because they could be quenched by encapsulation layers formed from surface contamination (see section 5.5).

TABLE 5.3

Summary of electron irradiation damage

in NiO at 300 and 100 keV Under Non-UHV Conditions.

A. Incident Electron Energy =300 keV, Vacuum = 3×10^{-7} Torr

Sample Orientation	Clean		Reactive Carbon Present	
	High Flux	Low Flux	High Flux	Low Flux
[001]	Ballistic surface erosion, scarce traces of Ni_3O_4	Ballistic surface erosion, competing Ni_3O_4 formation	Instantaneous disintegration	Instantaneous reaction to form Ni islands, Recrystallization, Instantaneous disintegration
[110]	Ballistic erosion of surface, scarce traces of Ni_3O_4	Ballistic erosion of surface, competing Ni_3O_4 formation	Instantaneous disintegration	Instantaneous reaction to form Ni islands, Recrystallization, Instantaneous disintegration
[111]	–	Ballistic erosion of surface, competing Ni_3O_4 surface phase formation	–	–

B. Incident Electron Energy =100 keV, Vacuum = 3×10^{-7} Torr

Sample Orientation	Clean		Reactive Carbon Present	
	High Flux	Low Flux	High Flux	Low Flux
[001]	no erosion	–	Recrystallization, Disintegration	–
[110]	no erosion	Formation of Ni_3O_4 surface phase	Recrystallization, Disintegration	–
[111]	–	–	Disintegration	–

C. Only a slow erosion process, characteristic of ballistic sputtering, occurred in UHV.

5.2.1 - BALLISTIC DAMAGE

UHV

During electron irradiation under UHV conditions (2×10^{-10} Torr), the most prevalent structural modification seen in NiO was the slow, ballistic erosion of the surface, as shown in Figure 5.1(a-c). Initial surfaces were determined to be atomically clean by visual examination (Figure 5.1a) and by checking the PEELS spectrum for the presence of the carbon K edge at 283.8 eV. Comparison of experimental initial surfaces to calculated images using a cross correlation analysis showed them to be simple bulk terminations as has been reported in the surface science literature (Netzer and Prutton 1975; Kinniburgh and Walker 1977). Ballistic sputtering appeared to be the primary type of beam damage observed and could be easily monitored, presumably due to cleaner initial surfaces in the UHV instrument (Strane et al. 1988). The accumulation of Ni on the surface (Figure 5.1b,c), as has been reported by other ion irradiation studies of ballistic sputtering, could only be observed after doses of the order of 10^{24} e-/cm^2. The nickel tended not to whet the NiO substrate, but rather form into small clusters on the surface as is shown in Figure 5.1(c). This type of knock-on damage was observed with 300 but not 100 kV irradiation.

PEELS spectra of the UHV sputtering process indicated that mass loss was occurring with no observable change in the chemical state of the surface. Shown in Figure 5.2 are typical PEELS spectrum taken initially and after long duration electron irradiation. The only change noted in the PEELS spectra from initial surface to final surface was a general reduction of the nickel $L_{2,3}$ and oxygen K edges at 854 eV and 532 eV, respectively, with no observable shift in the peak positions or relative change in peak heights.

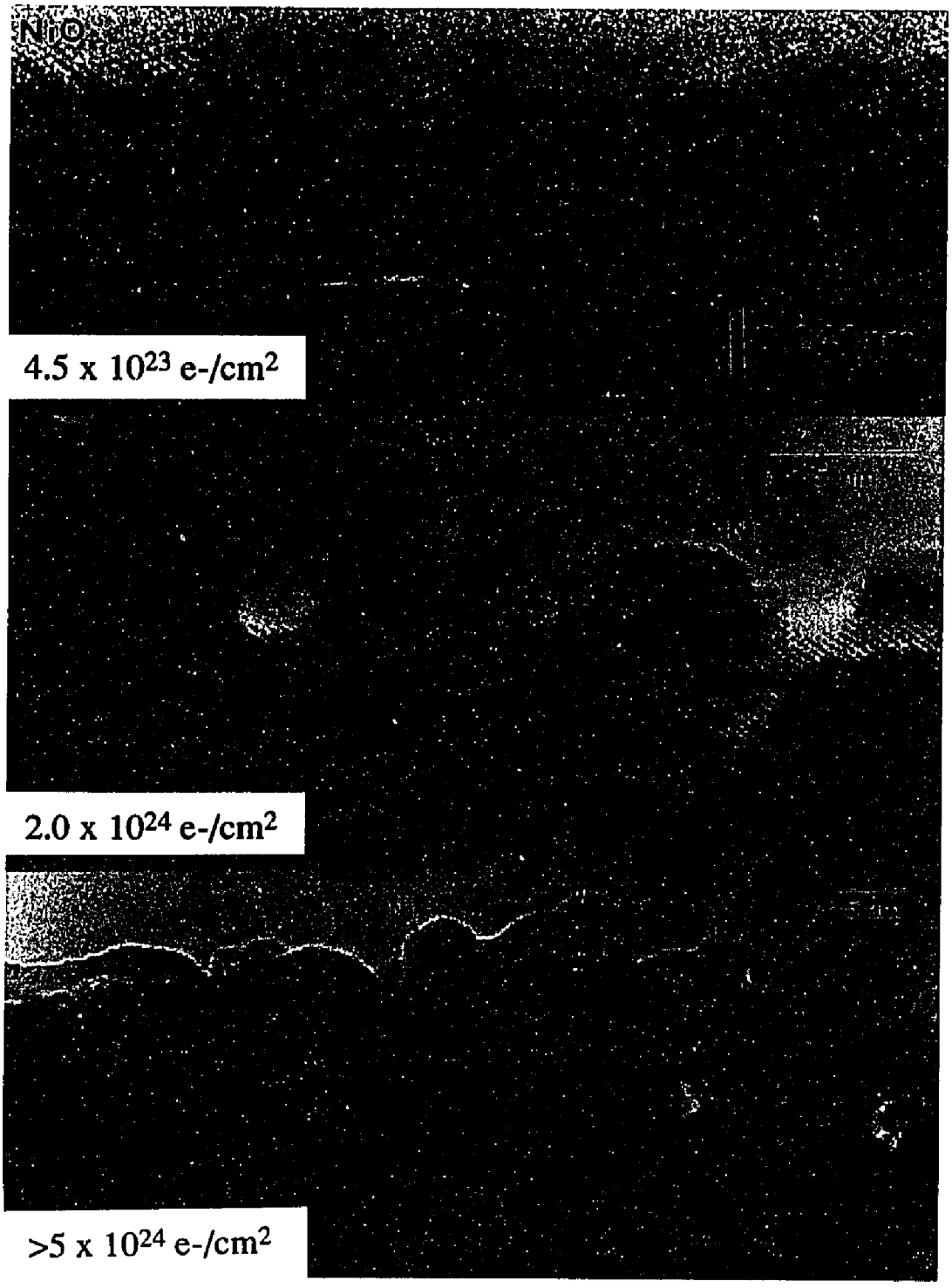

FIGURE 5.1 NiO in the UHV environment (2×10^{-10} Torr).

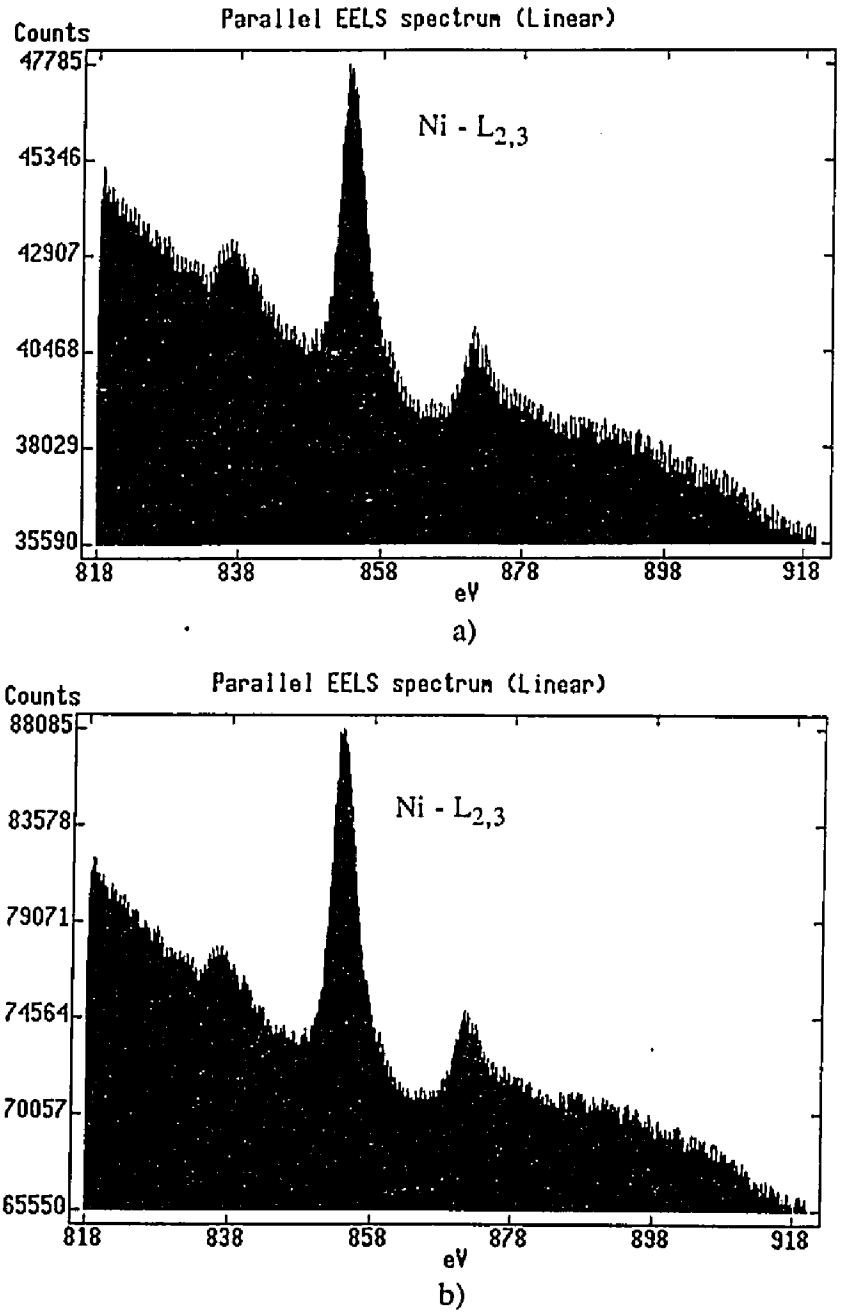

FIGURE 5.2 Example PEELS Spectra for NiO.
a) Initial area. b) After extended electron-irradiation at 300 keV.

In contrast to the non-UHV case (to be described later), neither a doubling of the [110]/(111) profile planes nor faceting was observed under UHV conditions. There was also no drastic orientation dependence of the sputtering process, which supports the view that the formation of electronic defects are not contributing to the sputtering process. (Electronic sputtering of this structure, assuming an excitonic mechanism, would have resulted in preferential damage along the [110] directions due to RCS focusing and other effects.)

Precise measurement of the ballistic sputtering threshold beam energy, E_{th}, for the NiO[110]/(110) orientation was made in the UHV microscope by incrementing the operating voltage in steps of 3.0 keV and irradiating at high flux for 8 to 12 hours at each increment. A value of 103±3 keV was obtained for E_{th} by making a number of measurements in this way. This corresponds to a maximum ballistic energy transfer of approximately 4.3 eV to nickel and 15.7 eV to oxygen atoms.

Recently, Jin Huang and Seidman (1991), have calculated E_d as a function of orientation using a molecular dynamics simulation technique. Their results, presented in Table 5.4, are consistent with the experimental observations of the present study. The experimental determinations are lower than the calculated values, as expected since the qualitative comparison is between surface and bulk phenomena. A more detailed comparison, described below, may be made by considering the specimen geometry of surface profile imaging.

As was discussed in Chapter 2, the threshold energy for sputtering, E_d, lies approximately in the range between ΔH_a and the number of broken bonds (CN/2) multiplied by ΔH_a. For the specific case of surface profile imaging there are distinct sites of varying coordination number, as is illustrated in Figure 5.3. Thus a range of E_d

should be obtained. These E_d values based on the bond breaking model are compared in Table 5.5. In comparison, E_d for oxygen in the (110) orientation measured by surface profile imaging should be approximately 1/2 (surface kink) to 0.833 (surface-mid) times the calculated value, thus between 12.5 and 20.8 eV. Using this bond-breaking analysis, the result of this study, $E_d(O) = 15.7$ eV, is in excellent agreement with the theoretical predictions. There also exists fairly good agreement with experiment and the value predicted using the ΔH_a criterion, but for bulk ($\sim 3\Delta H_a$) rather than surface estimates. The lattice energy, E_l, criterion predicted values significantly higher than both experimental or calculated values.

TABLE 5.4

Molecular dynamics simulation data of Jin Huang and Seidman (1991), showing the orientation dependence of the displacement threshold energy and corresponding incident threshold energy, E_{th}, required for displacement damage in NiO.

Orientation	Knock-on Ion	E_d	E_{th} (keV)
[110]	Oxygen	25	≈ 158
	Nickel	30	≈ 529
[112]	Oxygen	45	≈ 261
	Nickel	50	≈ 765
[100]	Oxygen	125	≈ 581
	Nickel	88	≈ 1122
[111]	Oxygen	> 145	≈ 647
	Nickel	100	≈ 1220

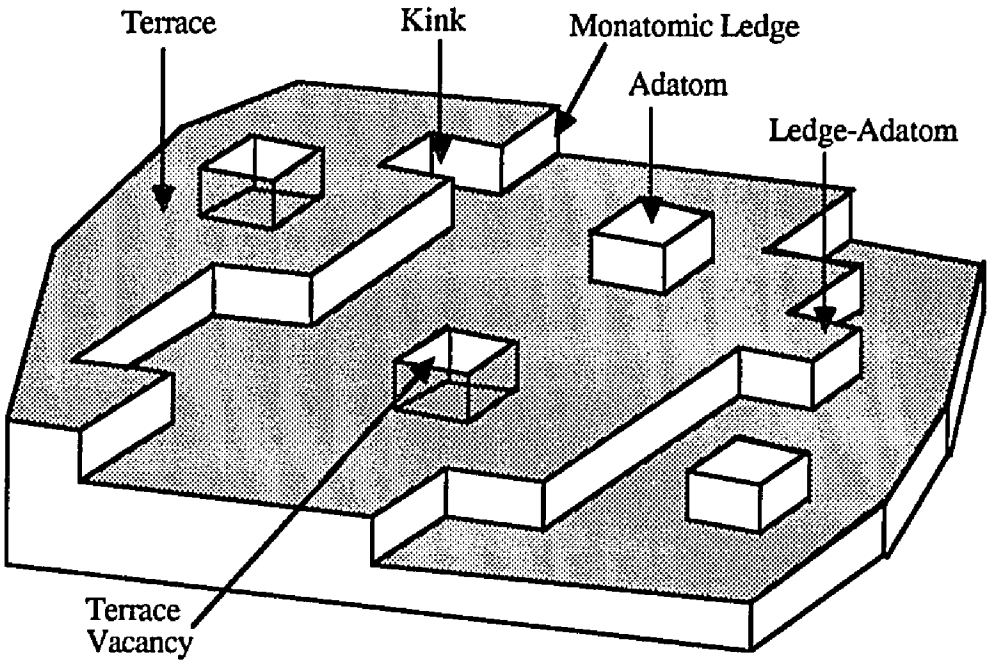

FIGURE 5.3 Schematic diagram illustrating the various types of surface sites.

TABLE 5.5

Values of the site-specific threshold energy in NiO
(Energies E_d in eV, E_{th} in keV.)

Atom Position	# Nearest Neighbors	E_d	Predicted E_d using ΔH_a	Predicted E_d using E_l	Predicted E_{th} using ΔH_a O	Predicted E_{th} using ΔH_a Ni	Predicted E_{th} using E_l O	Predicted E_{th} using E_l Ni
Bulk	6	3.0 ΔH_a	15.3	63.0	101	312	343	896
Surface-mid	5	2.5 ΔH_a	12.8	52.5	86	270	296	791
Surface-ledge	4	2.0 ΔH_a	10.2	42.0	69	223	246	675
Surface-ledge at a kink	3	1.5 ΔH_a	7.6	31.5	52	173	192	548
Ledge adatom	2	1.0 ΔH_a	5.1	21.0	36	122	135	402
Adatom	1	0.5 ΔH_a	2.6	10.5	18	65	71	229

For NiO: $\Delta H_a = 5.1$ eV/atom, $E_l = 42.0$ eV/atom
E_{th} is given by Equation (2.40)

The NiO [001]/(001) orientation was also investigated to lesser extent. At 100 and 200 keV irradiations, no sputtering was observed. At 300 keV, reluctant sputtering was observed, however it occurred so slowly that a sputtering threshold could not be determined under reasonable experimental time frames. These observations can be reasonably explained purely in terms of ballistic effects. The [001]/(001) type sample orientations relative to the beam offers fewer RCS rows compared to the [110]/(110) type orientations for the funneling of ballistic energy transfer. This is illustrated in Figure 5.4, which shows the atom stacking relative to the beam alternating as Ni-O-Ni-O-. . . chains in the [100] type orientations compared to the efficient RCS rows: O–O–O– . . . or Ni–Ni–Ni–. . . chains parallel to the beam for the [110]/(110) type orientations.

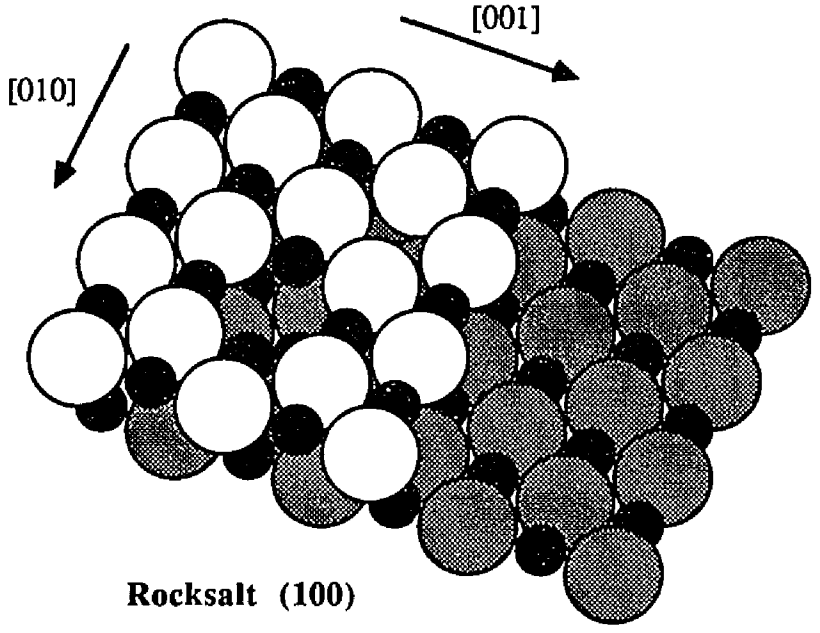

FIGURE 5.4 "Ball-and-stick" model of the NiO [100]/(100) orientation, showing cation and anion surface defects (after Henrich 1985).

NON-UHV

Under non-UHV conditions (3×10^{-7} Torr), surface erosion competed with surface contamination processes, and therefore could only be monitored at an appreciable rate during medium and high flux irradiations. Ballistic surface erosion was observed to be anisotropic in this case. Shown in Figure 5.5(a-c) is a NiO particle in the [110]/(110) orientation, supported directly on a Cu grid (without the carbon support film), and irradiated under high flux at 300 keV. In contrast to the UHV results, the [110]/(110) and [110]/(001) profile surfaces were generally found to be unstable (Figure 5.5(a)). Under irradiation, these surfaces rapidly reoriented into [110]/(111) microfacets and erosion progressed preferentially along these facets. Faceting of the normally polar (111) planes was typically observed in NiO under non-UHV conditions. It is possible that these facets are being stabilized by contamination on the surface.

A doubling of the surface [110]/(111) profile plane spacing was observed very early on and was present throughout the irradiation, most easily seen in Figure 5.5(c). This characteristic feature was also seen at 100 keV irradiation. With further time, the surface cell doubling was seen to evolve into a phase transformation to the Ni_3O_4 spinel phase (Figure 5.5(b)). This surface cell doubling was determined to be a precursor to Ni_3O_4 spinel phase formation; the mechanistics of which are described in further detail in the next section. Finally, ballistic sputtering took over and a characteristic fingerlike structure resulted due to preferential sputtering along the (111) facets (Figure 5.5(c)).

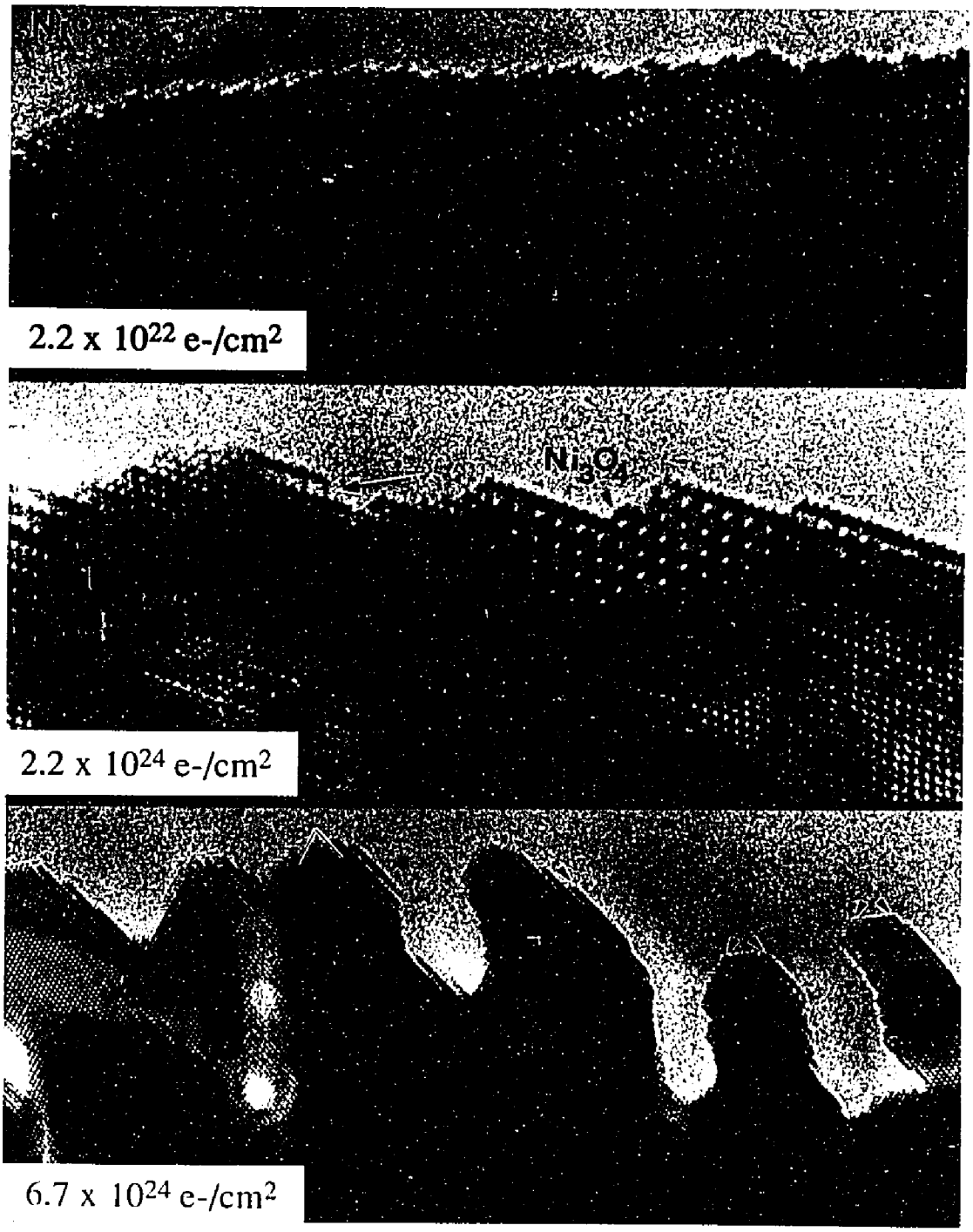

FIGURE 5.5 NiO [110]/(110) in the non-UHV environment (3×10^{-7} Torr).

Shown in Figure 5.6(a-d) are comparisons of spinel phase formation during low (Figure 5.6(a-b)) and high (Figure 5.6(c-d)) flux irradiations in the NiO [001]/(001) and [110]/(110) orientations respectively. Transformation to the spinel phase was extensive under low flux conditions in samples free of observable surface contamination. At high flux, the Ni_3O_4 phase could only be observed during early stages of irradiation. This reaction was eventually taken over by surface erosion with further exposure, but always with the doubling of the surface layer visible. The accumulation of nickel on the surface was not seen under non-UHV conditions and the combined effect of electron-stimulated reaction (ESR) and ballistic sputtering resulted in accelerated erosion behavior.

The NiO [001]/(001) orientation (Figure 5.7(a-c)) also showed surface erosion behavior in the non-UHV environment at 300 keV, which is in contrast to the sluggish erosion behavior in the UHV environment. Shown in Figure 5.7(a) is the surface after 10 minutes of high flux irradiation (essentially unchanged from the initial surface). Figures 5.7(b) and(c) show the surface after 65 minutes and 90 minutes respectively. Ballistic damage was not as highly anisotropic and the sputtering rate was significantly slower than for the [110]/(110) orientation, as would be expected from the structure arguments given earlier. Although neither a doubling of the surface layer spacing nor extensive faceting was observed, evidence of the Ni_3O_4 phase was present. This orientation, however, was found to be non-ideal for observation of the phase due to its similar appearance to the parent NiO phase, as is illustrated in Figure 5.6. In comparison to the UHV results, it appears that the electron-stimulated transformation of the surface region to Ni_3O_4 is not only accelerating the erosion process but lowering the sputtering threshold energy as well.

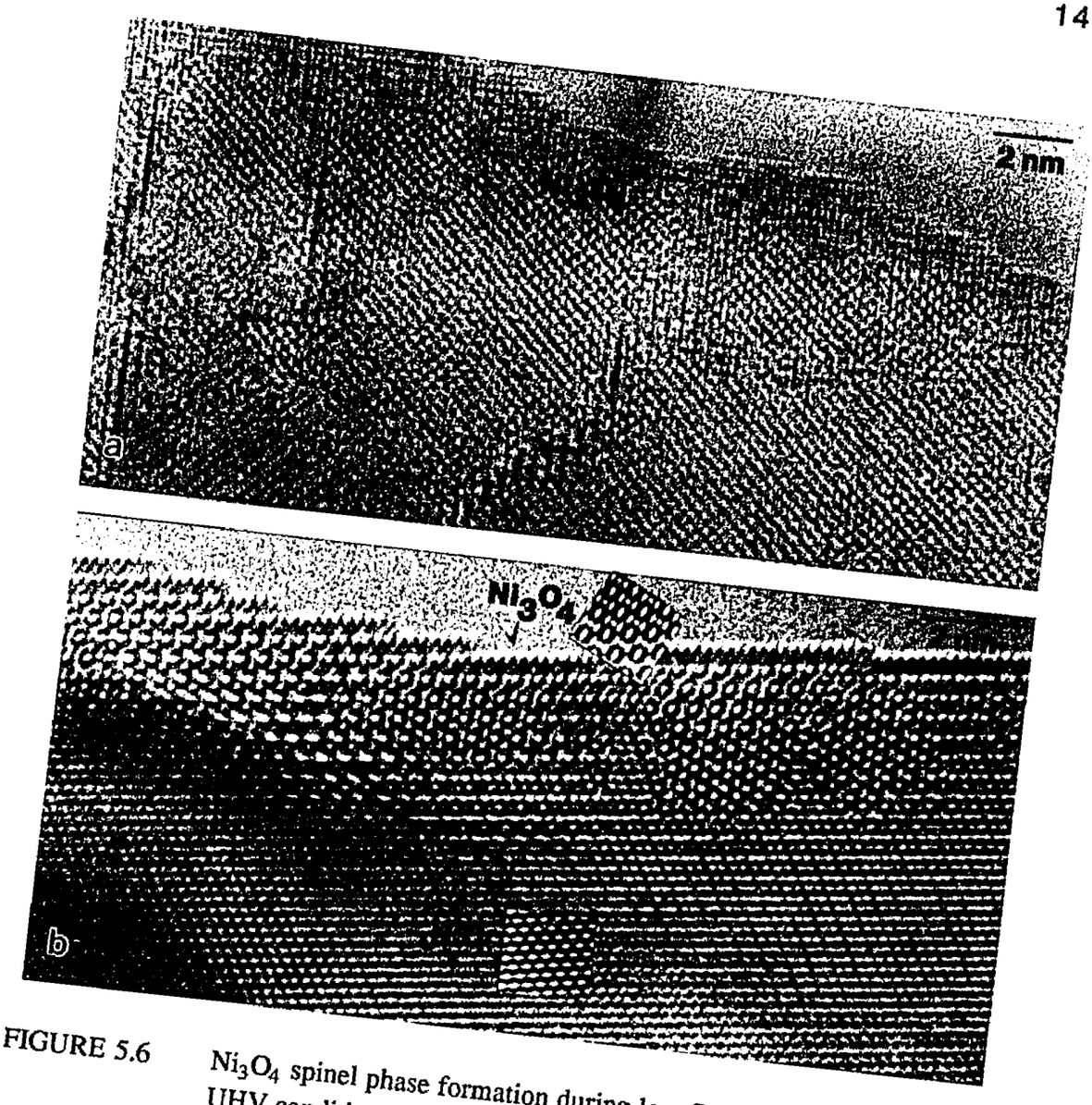

FIGURE 5.6 Ni_3O_4 spinel phase formation during low flux irradiation under non-UHV conditions.

a) NiO [001]/(001)

b) NiO [110]/(110)

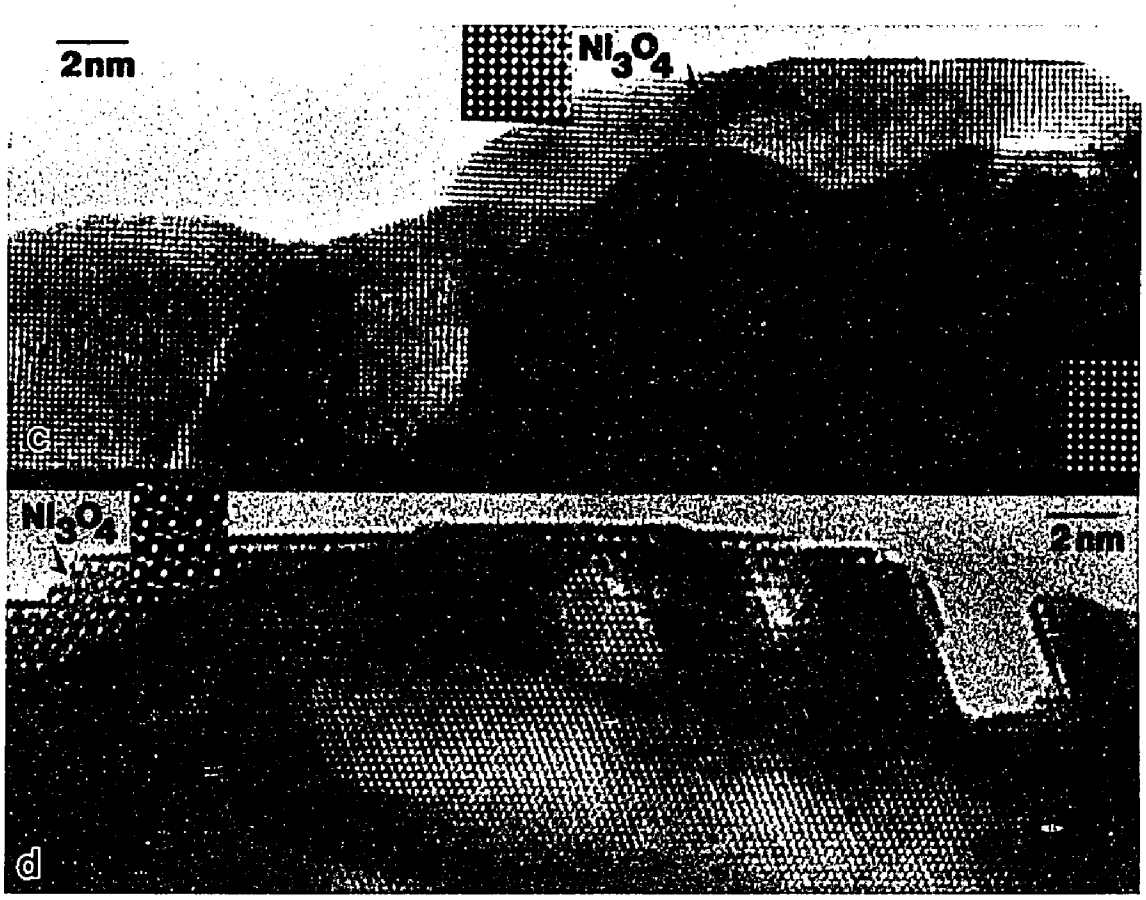

FIGURE 5.6 (con't) Ni_3O_4 spinel phase formation during high flux irradiation under non–UHV conditions.
c) NiO [001]/(001)
d) NiO [110]/(110)

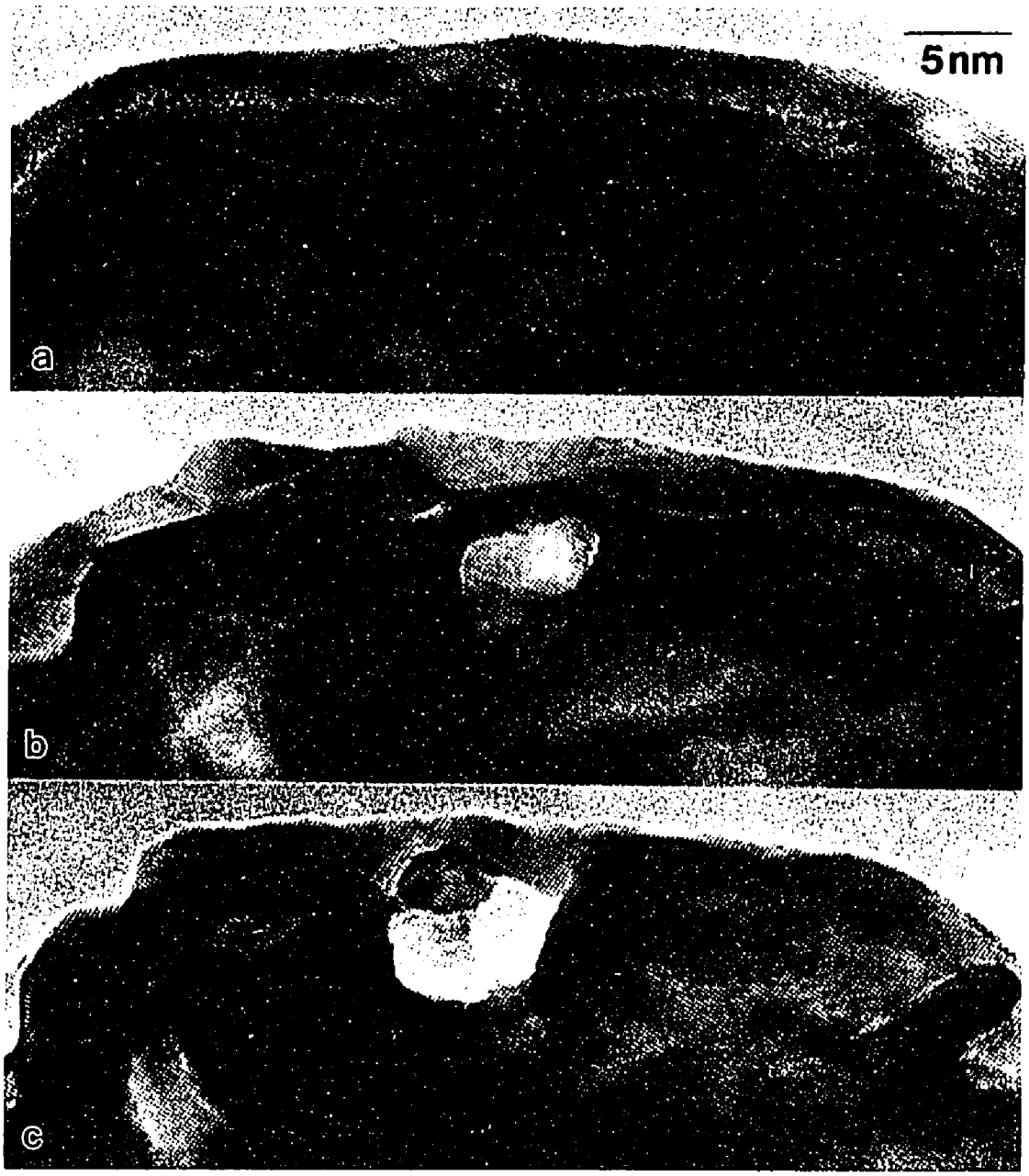

FIGURE 5.7 NiO [001]/(001) in the non-UHV environment (3×10^{-7} Torr).

5.3 - SURFACE-INITIATED OXIDATION

In competition with ballistic knock-on damage under non-UHV conditions, the surface-initiated nucleation of a Ni_3O_4 spinel phase has been described. This phase was identified from diffraction data and from through focal series comparisons of experimental to simulated images in both the [110] and [100] orientations, an example of which is shown in Figure 5.8(a) where the spinel phase has formed at the [110]/(111) profile surface facets. Crystal structure and atom position data for the spinel phase image simulations were obtained from the data of O'Neill and Navrotsky (1983). Shown at the top of Figure 5.8b) is an experimental image matched to a best-fit calculated image (inset) which, in this case, included two monolayers of NiO at the profile surface. Selected area diffraction patterns in three independent orientations (Figure 5.8(b) bottom) showed the spinel structure to have a cube-cube orientation relationship and exactly double the NiO unit cell spacing as well as the required Fd3m symmetry. This beam-induced phase transformation to a spinel phase was also observed in the CoO, MnO, and FeO systems, where the M_3O_4 type spinel structure is an equilibrium phase. In these cases, however, the spinel structures indexed to the known lattice parameters, not a simple doubling of the monoxide unit cell. Further details on these results are presented in the next section.

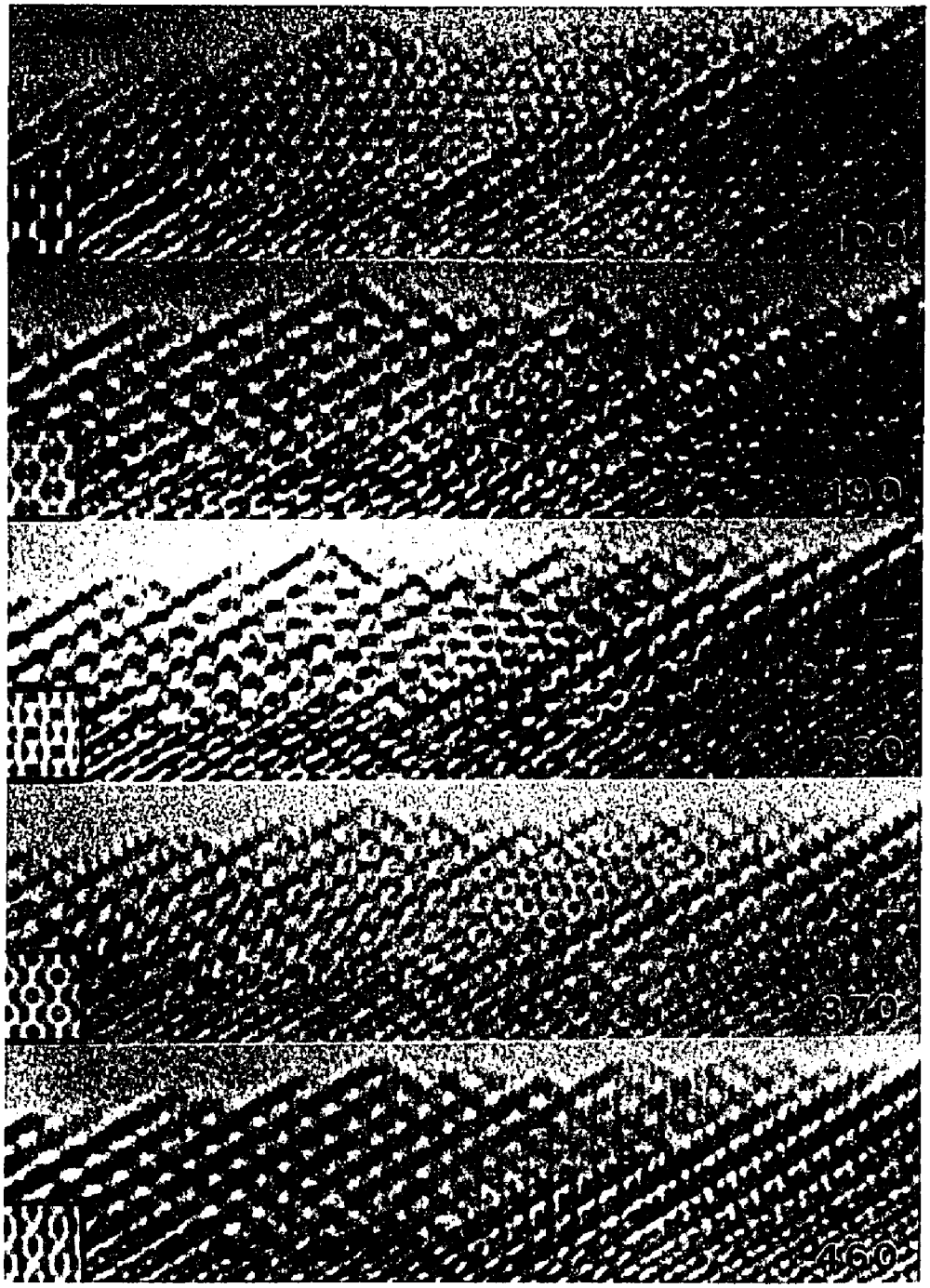

FIGURE 5.8 a) Ni_3O_4 through-focal-series taken during 300 keV irradiation. Calculated images are inset. Defocus values given at the right (in Å).

Ni_3O_4

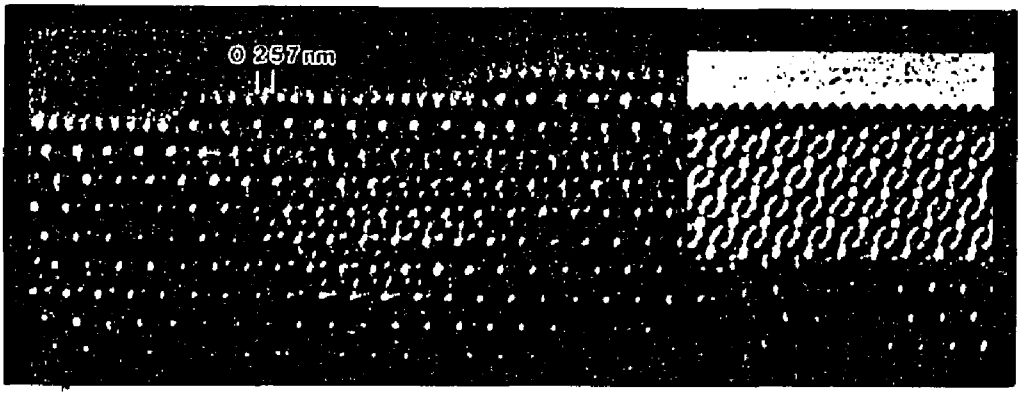

Ni_3O_4 formation at the (111) profile surface. Calculated image is inset (defocus = -440 Å).

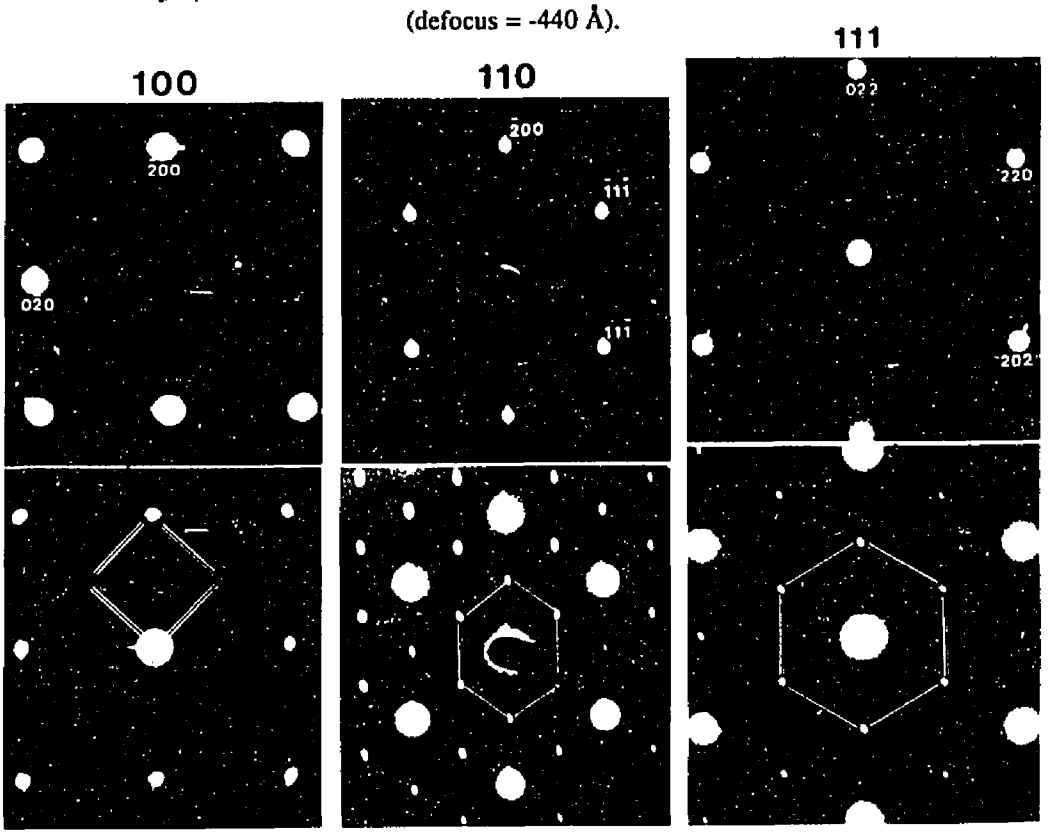

FIGURE 5.8 b) Electron diffraction patterns indicating that Ni_3O_4 forms with a cube-cube epitaxy to the parent NiO. Typical experimental image and simulation are at top.

The Ni_3O_4 phase transformation readily occurred at both 100 and 300 kV and was observed to be reversible. That is, this phase slowly reverted to the original NiO structure when the electron beam was removed. This was contrary to the observations for CoO, MnO, and FeO, where the spinel phase remained after the beam was removed. Neither significant mass loss nor volume expansion were apparent in the NiO sample, however surface rearrangement was clearly observed (e.g., arrows in Figure 5.9). A threshold flux of approximately 1.2×10^{19} e-/cm^{2}s (2 A/cm^2) was required for the onset of this phase transformation. The early stages of this transformation were characterized by a precursor state - the doubling of the [110]/(111) profile planes, as seen in the [110]/(110) orientation of Figure 5.3(d). Formation of this phase contributed to an accelerated and directional sputtering of the NiO surface under non-UHV conditions.

Growth of the spinel phase into the bulk behaved as a diffusion-controlled process. Progression of the growth front inward from the surface could be monitored layer by layer as shown in the time evolution sequence of Figure 5.9. The left-handed arrows mark a fixed position in the sample, while the right-hand arrows illustrate the rearrangement occurring at the surface. The growth was also strongly orientation dependent. It appeared to be limited to diffusion paths along the Ni (111) layers of the structure. For example, diffusion paths along projected <112> directions inward from the [110]/(111) and [110]/(110) profile surfaces were preferred without exception. Migration in NiO is easiest along the [110] directions in the (111) planes. If one assumes that the propagation of the spinel phase into the bulk is via point defect migration (most likely nickel vacancies and holes), all that is required to form the inverse spinel is that some Ni^{3+} defects (trapped holes) migrate into tetrahedral trivacancy (an ordered cluster of Ni vacancies) configurations.

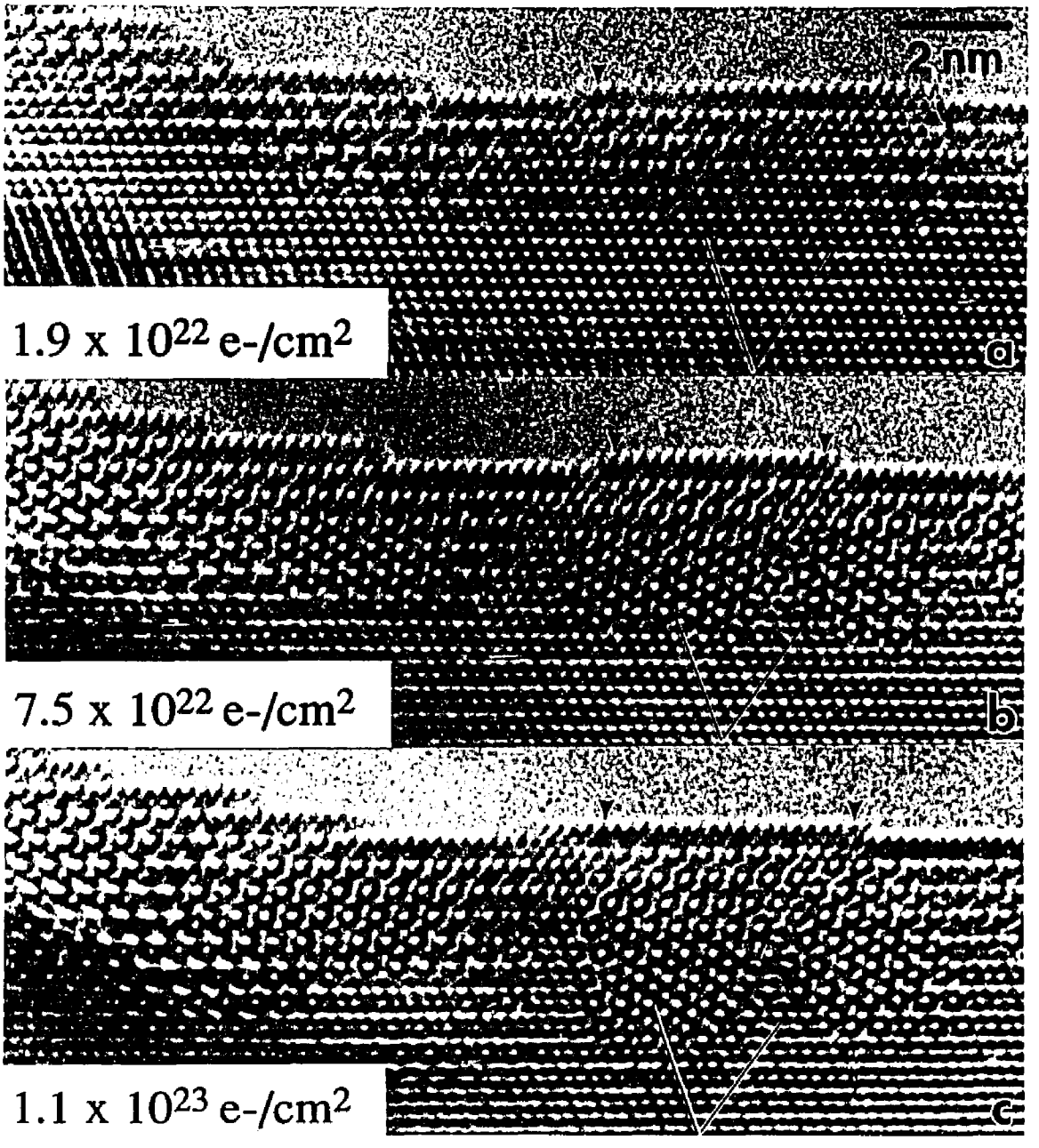

FIGURE 5.9 Time-evolution sequence showing diffusion of the Ni_3O_4 into the bulk during low flux irradiation. a) after 5 min. b) 20 min. c) 30 min. Total dose is given at left. Arrows illustrate surface rearrangements.

Although not previously documented in NiO, this type of defect configuration is known to occur in physically similar oxides. Research on point defect interactions in FeO, CoO, and MnO, have predicted the existence of the tetrahedral trivacancy (4:1) cluster (Anderson et al. 1985), shown schematically in Figure 5.10. Catlow and Stoneham (1981), also showed that such 4:1 and possibly 6:2 clusters should dominate in more grossly nonstoichiometric regions.

NiO is cation deficient; the mobile species in NiO is known to be nickel (Kofstad 1972; Peterson and Wiley 1985), and the ionic radius of Ni^{3+} is approximately 0.58 Å (Shimomura et al. 1956) compared to 0.69 Å for Ni^{2+} (Kingery et al. 1975). The migration energy of cation vacancies in NiO is 2.12 eV (Peterson 1984), while cation interstitials only require 1.08 eV (Mackrodt 1984). Both values are sufficiently low that beam-stimulated migration of these defects is likely.

Three sets of time evolution sequences, with detailed analyses of the thickness and shape of the crystal from through focal series image simulations, were used to determine an effective diffusion coefficient was determined to be approximately 7.5×10^{-17} cm^2/s from the slope of the data plot shown in Figure 5.11. In comparison to the thermodynamic diffusion data of (Monty 1983) and (Kofstad 1972), this diffusion coefficient would correspond to a temperature between 480 and 500°C. In light of the previous arguments, it is not believed that a temperature excursion of this magnitude is occurring, rather a radiation-enhanced diffusion process. The appearance of a low threshold flux supports this conclusion. The model assumed is one where nickel vacancies (and holes) are the mobile defects, propagating along the (111) layers. This type of layer-by-layer growth corresponds quite well to the experimental observations.

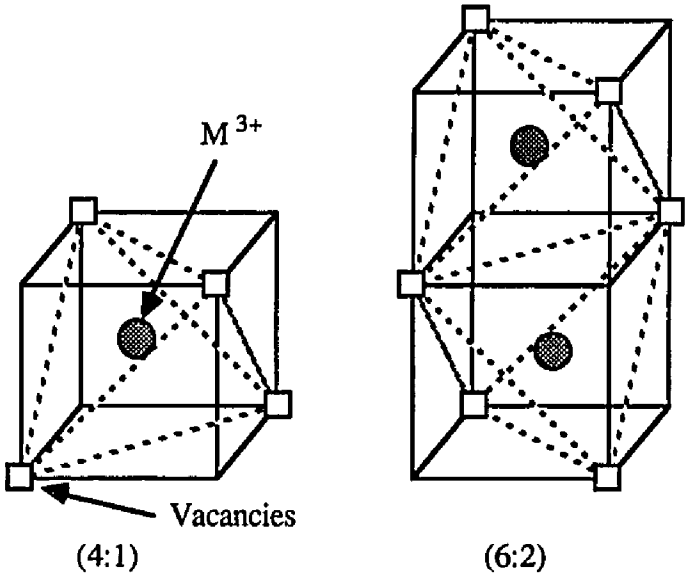

FIGURE 5.10 4:1 and 6:2 vacancy clusters.

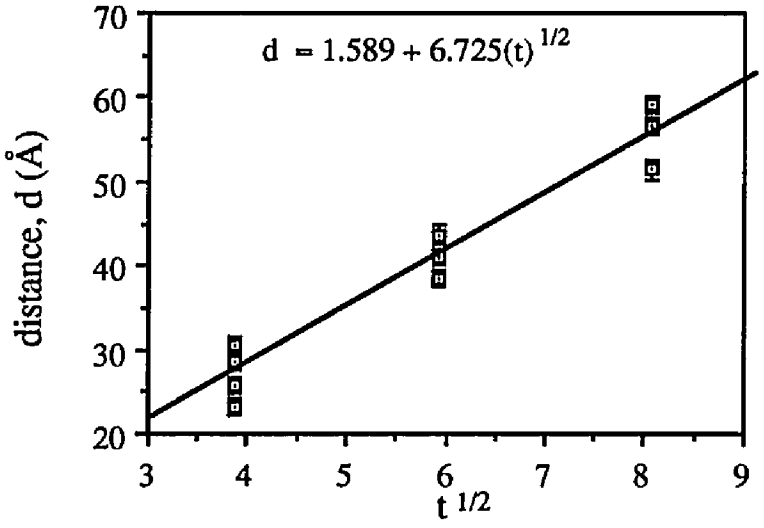

FIGURE 5.11 Plot characterizing the diffusion of the Ni_3O_4 phase from the profile surface into the bulk, with distance given in Å and time (t) in minutes.

5.3.1 - BEAM-INDUCED SPINEL PHASE FORMATION IN CoO, MnO, AND FeO

Because the observance of a spinel phase in NiO has previously not been reported, physically similar oxides were investigated to ascertain if they also underwent this apparent beam-stimulated oxidation reaction.

CoO in UHV

The surface science literature reports that clean CoO surfaces are stable under UHV conditions. The CoO(100) surface, for example, is close to a simple termination of the bulk lattice with a small surface layer contraction of 0 to 3% of a layer spacing (Felton et al. 1979). Electron-stimulated desorption (ESD) of oxygen has generally not been observed and is not believed to occur (Niehus and Losch 1981). Sputtering of the surface with heavier ions such as Ar^+, however, has resulted in a mixture of the original oxide, lower oxides, and metal (Chuang et al. 1978). The effect has been even more pronounced in systems containing hydroxyl groups which are readily destroyed by the ion beam via electron-stimulated damage mechanisms.

Shown in Figure 5.12(a-c) is CoO oxide under UHV conditions (3.5×10^{-10} Torr). CoO showed similar isotropic sputtering behavior to NiO in the UHV environment. No visual evidence of preferential sputtering of oxygen was observed after extended low flux irradiation (Figure 5.12(a,b)). Neither the electron diffraction patterns nor PEELS spectra showed any evidence of structure changes, in agreement with the surface science literature for clean CoO surfaces. However, when a leak of the order of 10^{-8} Torr was introduced into the microscope column (Figure 5.12(c)), the characteristic spinel phase, Co_3O_4, formed at the surface within minutes after the beam was turned on.

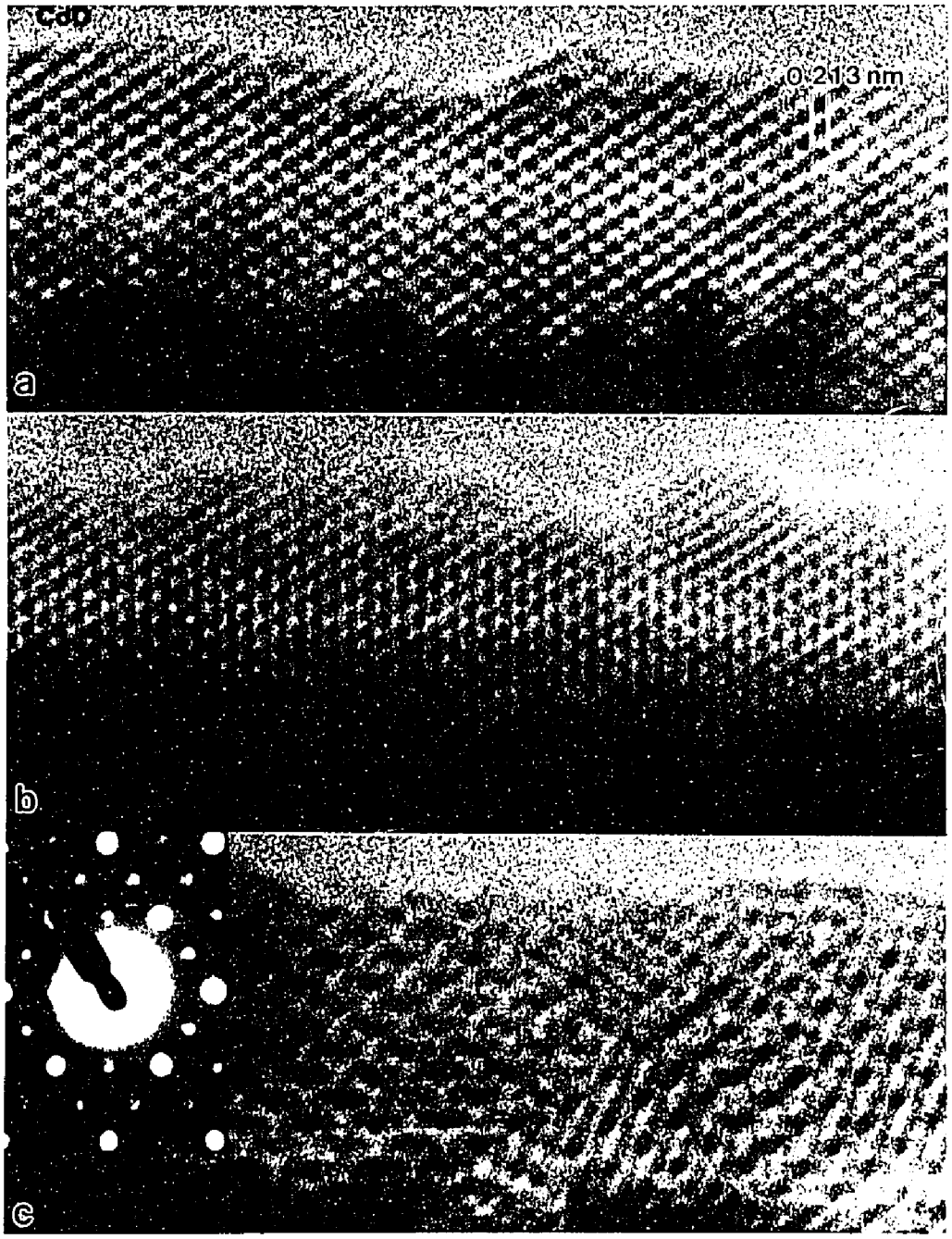

FIGURE 5.12 CoO under UHV conditions: (a) initial surface; (b) after 30 min. of low flux irradiation; (c) after a 10^{-8} Torr leak was introduced.

Non-UHV

In the non-UHV environment, CoO, MnO and FeO were all seen to undergo transformation to their respective spinel phases which competed with ballistic erosion. Surface faceting was only observed in FeO. Shown in figure 5.13(a-d) respectively are the NiO, CoO, MnO and FeO (110) diffraction patterns after oxidation to the spinel phase. Cube-cube epitaxy between the two phases was largely maintained. The onset of the spinel phase transformation was often seen initially in the diffraction pattern as an appearance of half order spots, which corresponded to a simple doubling of the monoxide unit cell as shown in Figure 5.14 for NiO. With time, the (200) type spots were seen to disappear as would be required for the Fd3m-O_h^7 symmetry of the spinel phase. In the NiO samples, the spinel phase indexed to exactly double the NiO unit cell spacing. The 'true' spinel phase diffraction spots which could be indexed to the known M_3O_4 structure appeared with further irradiation in the CoO, MnO and FeO samples, as illustrated in figure 5.15 for MnO.

Shown in Table 5.6 is a comparison of the spinel phase lattice parameters and the volume expansion required for its formation from the parent metal oxide structure. In CoO, MnO and FeO, it was clear that volume expansion and rearrangement of the surface region occurred in conjunction with spinel formation as shown in Figure 5.16 for CoO. Once formed, the spinel phase was stable in all systems except NiO. The stability of the spinel phase in the electron microscope was confirmed by observing a $Co_{0.8}Fe_{2.2}O_4$ spinel, which showed no signs of reactivity except for ballistic sputtering.

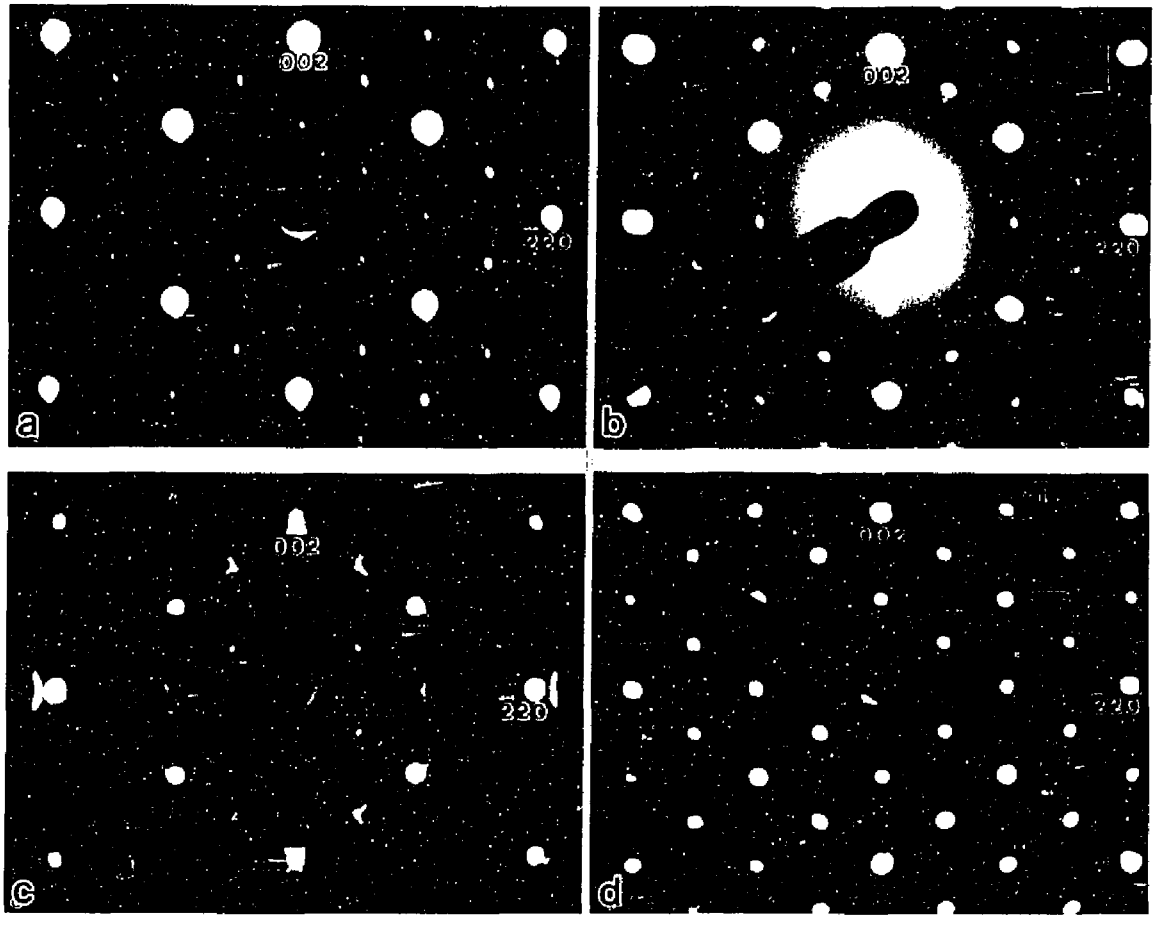

FIGURE 5.13 [110]/(110) diffraction patterns showing the cube-cube epitaxy retained between the parent MO (metal oxide) and resulting M_3O_4 phase. The MO phase is indexed. a) NiO; b) CoO; c) MnO; d) FeO.

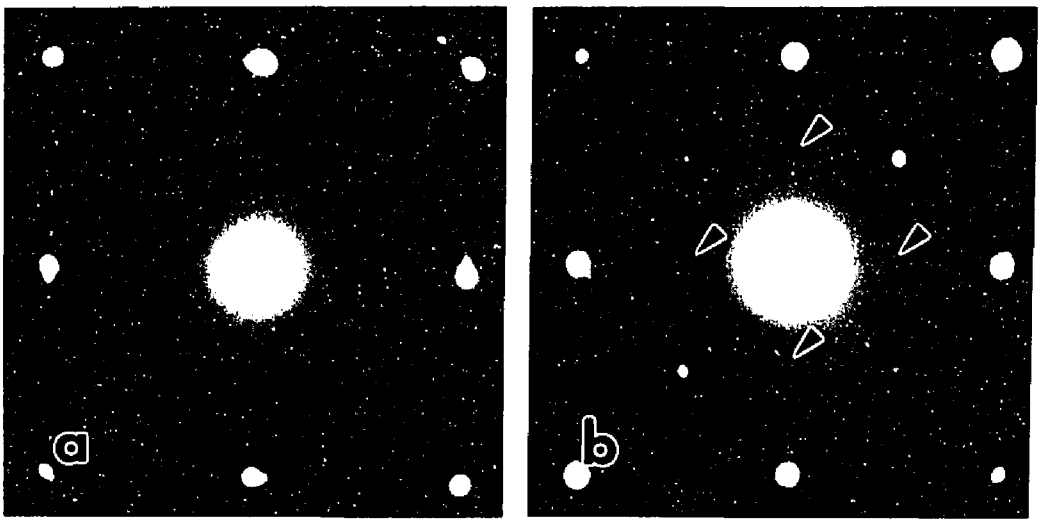

FIGURE 5.14 NiO [001]/(001) diffraction patterns. a) initial surface; b) during initial stages of spinel phase formation. Arrows show a simple doubling of the NiO unit cell. With time, the Ni_3O_4 (200) reflections (marked with arrows) disappear.

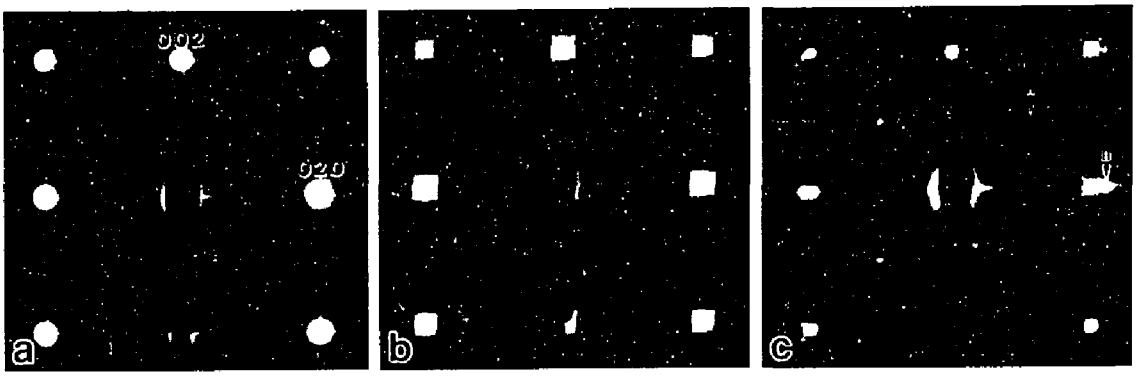

FIGURE 5.15 MnO [100]/(100) diffraction pattern. a) initial surface; b)after the appearance of 1/2 order spots; c) after Mn_3O_4 phase is fully formed. Marks A and B indicate Mn_3O_4 (022) and Mn_3O_4 (040) reflections respectively.

TABLE 5.6

A comparison of spinel phases in NiO, CoO, MnO, and FeO.

Compound	Lattice Parameter (Å)	Space Group	Density	(% Volume increase)
FeO	4.3088	Fm3m (#225)	5.7	
Fe_3O_4	8.3963	Fd3m (#227)	5.18	+9.1%
CoO	4.260	Fm3m (#225)	6.45	
Co_3O_4	8.084	Fd3m (#227)	6.07	+5.9%
MnO	4.4448	Fm3m (#225)	4.32 - 5.46	
Mn_3O_4	8.136	I_{41}/amd (#141)	4.856	+10.6% - 11.0%
NiO	4.177	Fm3m (#225)	6.67	
Ni_3O_4	≈ 8.35	~ Fd3m (#227)	----	+0.0%
$MgAl_2O_4$	8.080	Fd3m (#227)	3.6	

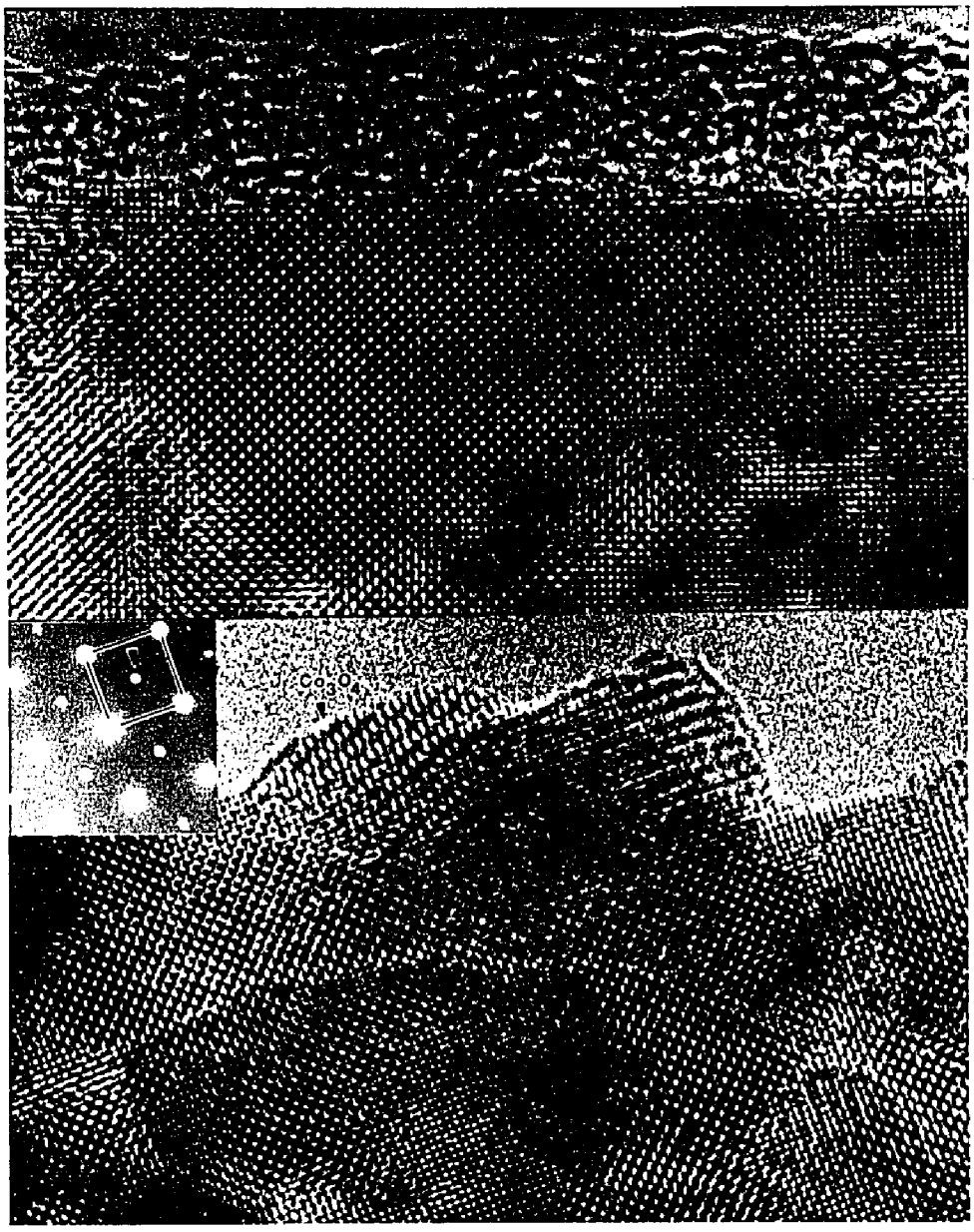

FIGURE 5.16 CoO [001]/(001) after spinel formation. The epitaxial Co_3O_4 is difficult to view in this orientation, however Co_3O_4 growing out from the surface is clearly visible.

5.3.2 - HREM IMAGE SIMULATIONS OF Ni_3O_4

As the Ni_3O_4 spinel phase is not a stable phase in the NiO system, formation of the spinel phase was not as clear-cut as in the other oxides. Therefore, a detailed study involving electron diffraction from three independent orientations and HREM surface profile image simulation was performed to assure that the identification of the phase was correct. The best fit through-focal image simulation of the faceted NiO[110]/(111) profile surface was that of Ni_3O_4 spinel phase with one to three monolayers of NiO at the surface. The experimental image shown in Figure 5.17, for example, can be compared to the surface calculations for one, two and three monolayers of NiO at the surface of Ni_3O_4 (Figure 5.18) to illustrate the monolayer sensitivity of the image simulations; the best-fit in this case being two monolayers.

The simulations also provided an explanation for the apparent doubling of the surface (111) profile planes. As shown in Figure 5.19, by allowing the surface cell (three monolayers) to revert back to the NiO phase, the image often showed an apparent doubling of the surface unit cell. The physical picture is one of a flux of irradiation-induced defects on the Ni sublattice diffusing into the bulk with Ni diffusing out to the surface. The mechanism of this process is discussed further in section 5.7.

Additional support of the existence of the Ni_3O_4 phase is that the structural transformation of NiO (rocksalt structure) to Ni_3O_4 (spinel structure) progressed almost entirely on the nickel sublattice as evidenced by dynamic observation of growth along the NiO [110]/(111) profile planes. If the assumption is that a nickel vacancy is created to maintain charge and site neutrality due to the electron-stimulated addition of oxygen, formation of Ni_3O_4 spinel from four formula units of the parent NiO requires only that one half of the nickel go from Ni^{2+} to Ni^{3+} charge states and that one fourth of the nickel

on octahedral sites move into tetrahedral sites. If Ni_3O_4 is an inverse spinel, then the nickel on tetrahedral sites are Ni^{3+} ions. If it is a normal spinel, then the nickel on tetrahedral sites are Ni^{2+} ions. Consideration of ionic size and the fact that the inverse spinel is the more conductive of the two possible structures, a reasonable estimation would be that the inverse spinel has formed. It should be noted, however, that HREM image simulation may not be a sensitive enough technique to unambiguously differentiate between the two structures. The inverse spinel structure was used for the image calculations.

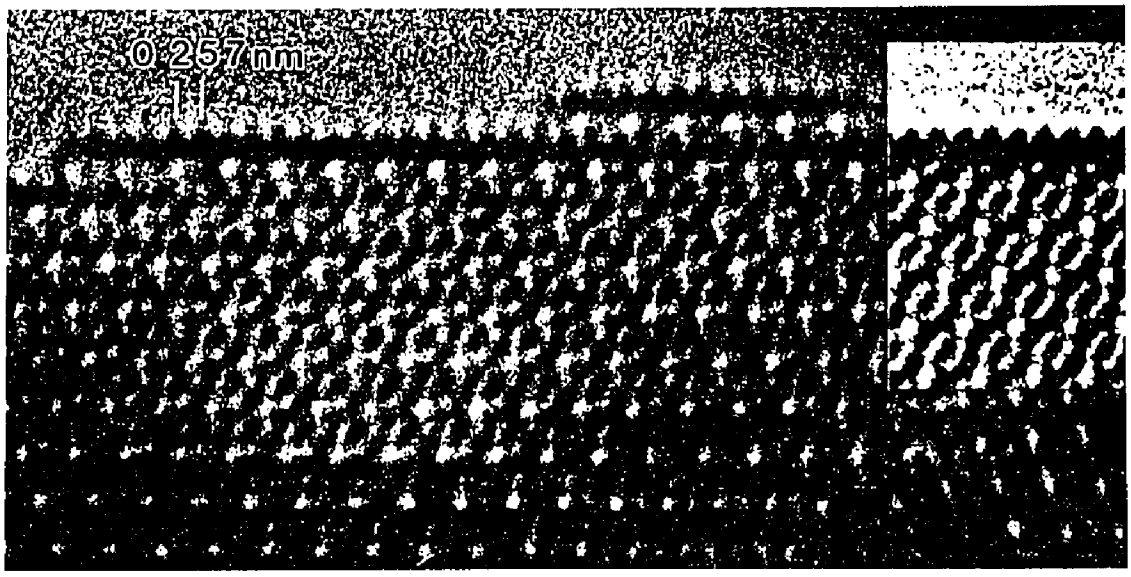

FIGURE 5.17 NiO [110]/(111) profile surface where the Ni_3O_4 has formed. (Lens defocus is -440 Å). The best fit calculated image (shown inset) includes 2 monolayers of NiO at the (111) profile surface.

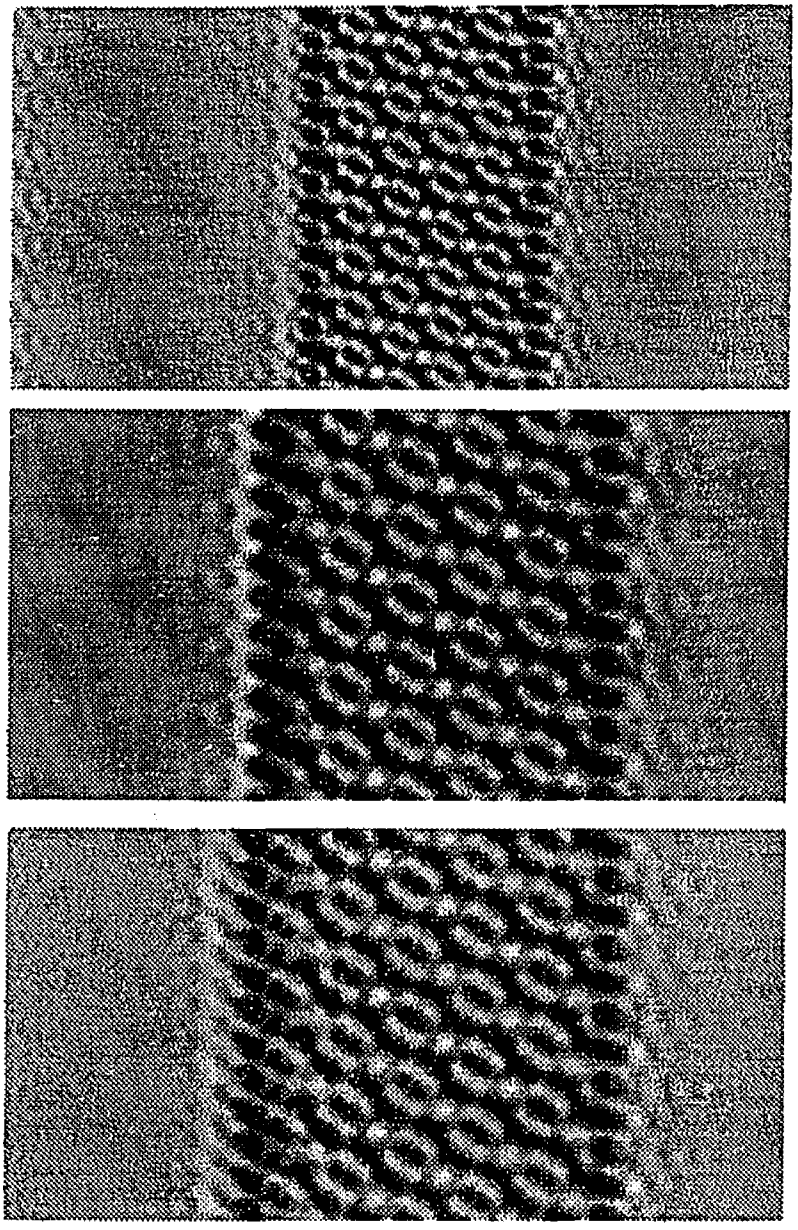

FIGURE 5.18 Calculated images for Ni_3O_4 [110]/(110). Thickness is 40 Å, defocus is –440 Å. Shown from top to bottom are 1, 2, and 3 monolayers of NiO at the Ni_3O_4 [110]/(111) profile surface (left side). Right side shows bulk termination.

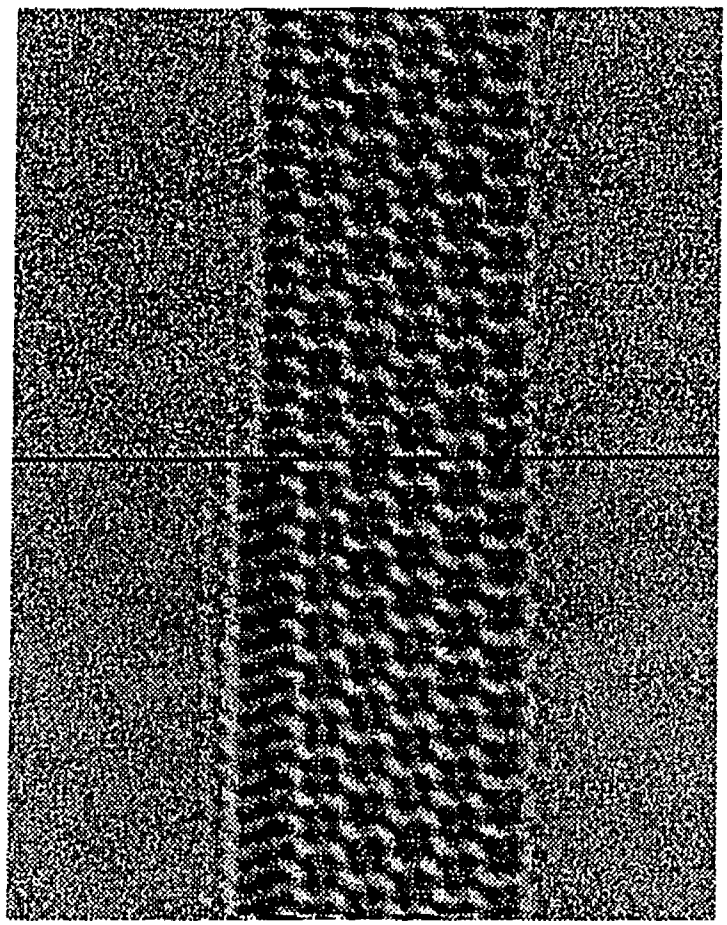

FIGURE 5.19 Calculated images of Ni_3O_4 [110]/(110) with surface cut-off at the [110]/(111) profile surface. Right side surfaces illustrate normal bulk terminations. Top image left side shows 1 monolayer of NiO at the profile surface. Bottom image left side shows 3 monolayers of NiO at the profile surface. Thickness = 40 Å. Defocus = -40 Å.

5.4 · SURFACE-INITIATED REDUCTION OF Ni

In the presence of amorphous carbon contamination on the surface, or CO from the vacuum (see section 5.6.2), a spontaneous reaction occurred which resulted in the reduction of the NiO surface to islands of metallic nickel (Figure 5.20 (A and B)), with a cube-cube epitaxy revealed in the diffraction patterns (inset). The influence of the carbonaceous species was verified by artificially evaporating a small amount of carbon onto NiO particles supported on a holey SiO film and Cu grid. The carbon "islands" were seen to disintegrate into the bulk, leaving behind metallic nickel in the crater left behind, as shown in Figure 5.21. This reaction varied in extent (apparently due to the amount of reactive carbon present) from the formation of nickel islands to more extensive bulk structural changes such as recrystallization, complete disintegration, and/or apparent melting of the sample. Shown in Figure 5.22(a-d) are examples of the varying degrees of structural damage which occurred in the presence of reactive carbon. Figure 5.22(a) shows metallic nickel islands forming during low flux irradiation at 300 keV. The reaction occurred more vigorously at either higher electron fluxes or lower electron energies, characteristic of an electronic rather than a knock-on process. Figure 5.22(b,c) shows a heavily contaminated sample before and after exposure to a high flux electron beam at 300 keV. Figure 5.22(d) shows a similarly contaminated sample which underwent complete disintegration after exposure to a high flux electron beam at 100 keV. Similar findings have been reported in other microscopy investigations under various operating conditions (Ostyn and Carter 1982; Liu and Cowley 1987; Luzzi et al. 1988). In all cases, however, it appeared that the interaction of the electron beam and reactive carbonaceous species caused severe degradation of the NiO surface.

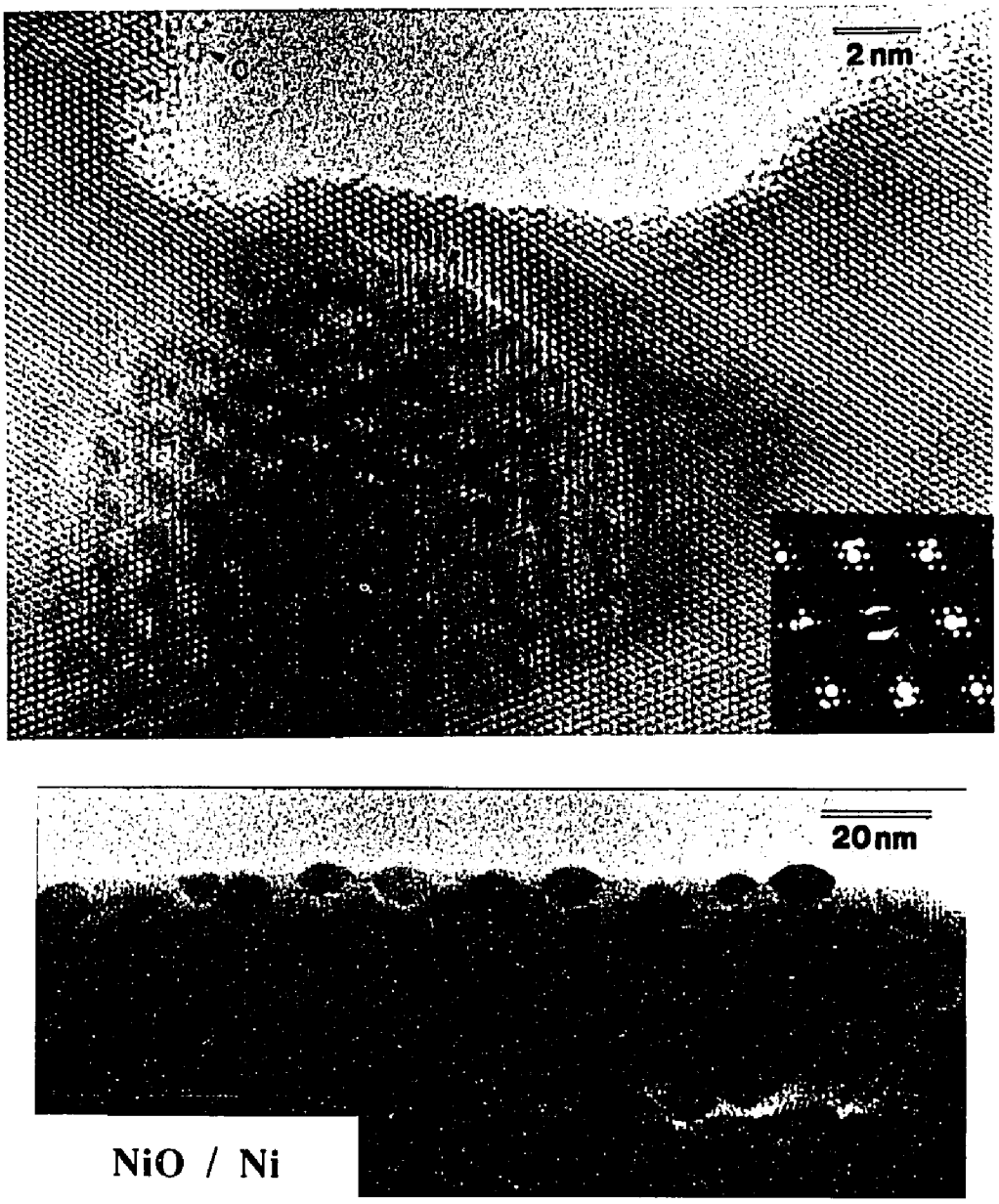

FIGURE 5.20 A) HREM image (top) and low magnification bright field image (bottom) of NiO after electron-stimulated reaction in the presence of carbon (C), which results in the formation of islands of metallic nickel at the surface.

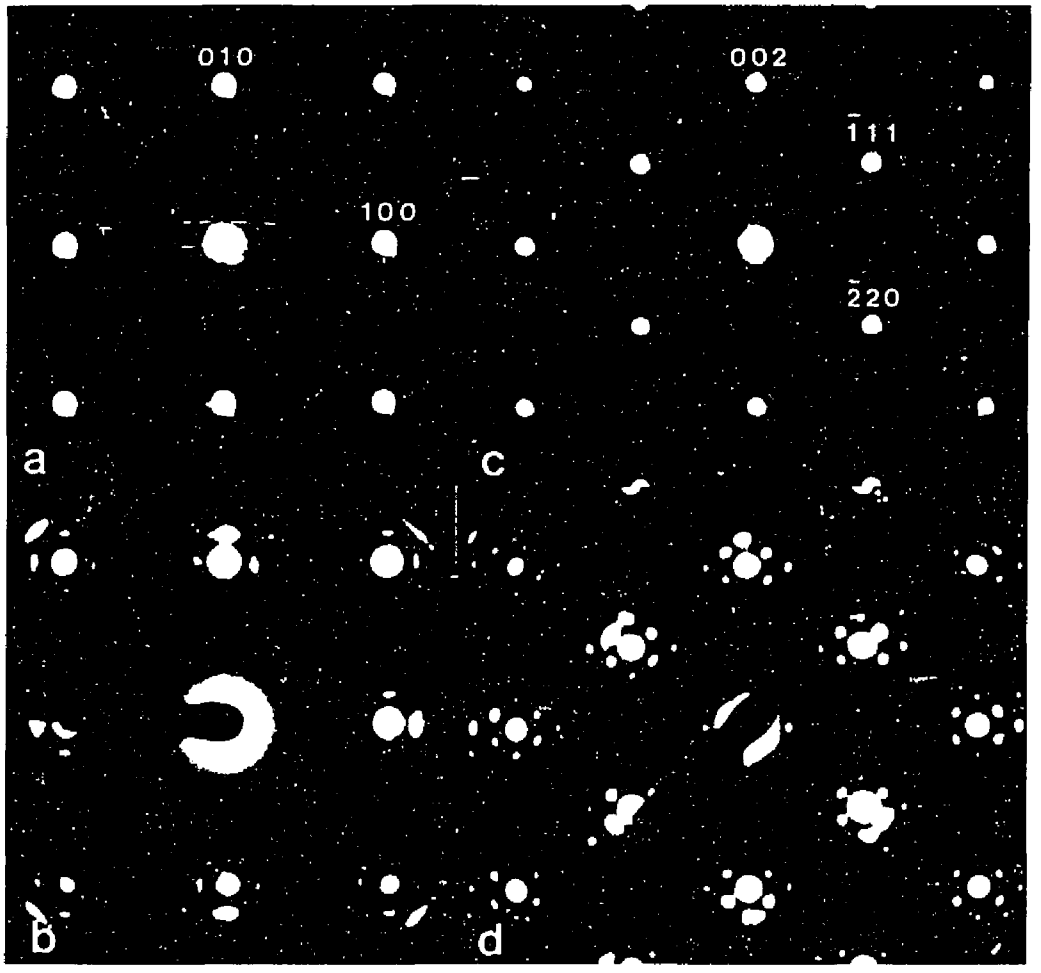

FIGURE 5.20 B) Diffraction patterns before (top) and after (bottom) ESR indicate that the nickel islands form with a cube-cube epitaxy to the parent NiO. (a-b) NiO [001]/(001) orientation ; (c-d) NiO [110]/(110) orientation.

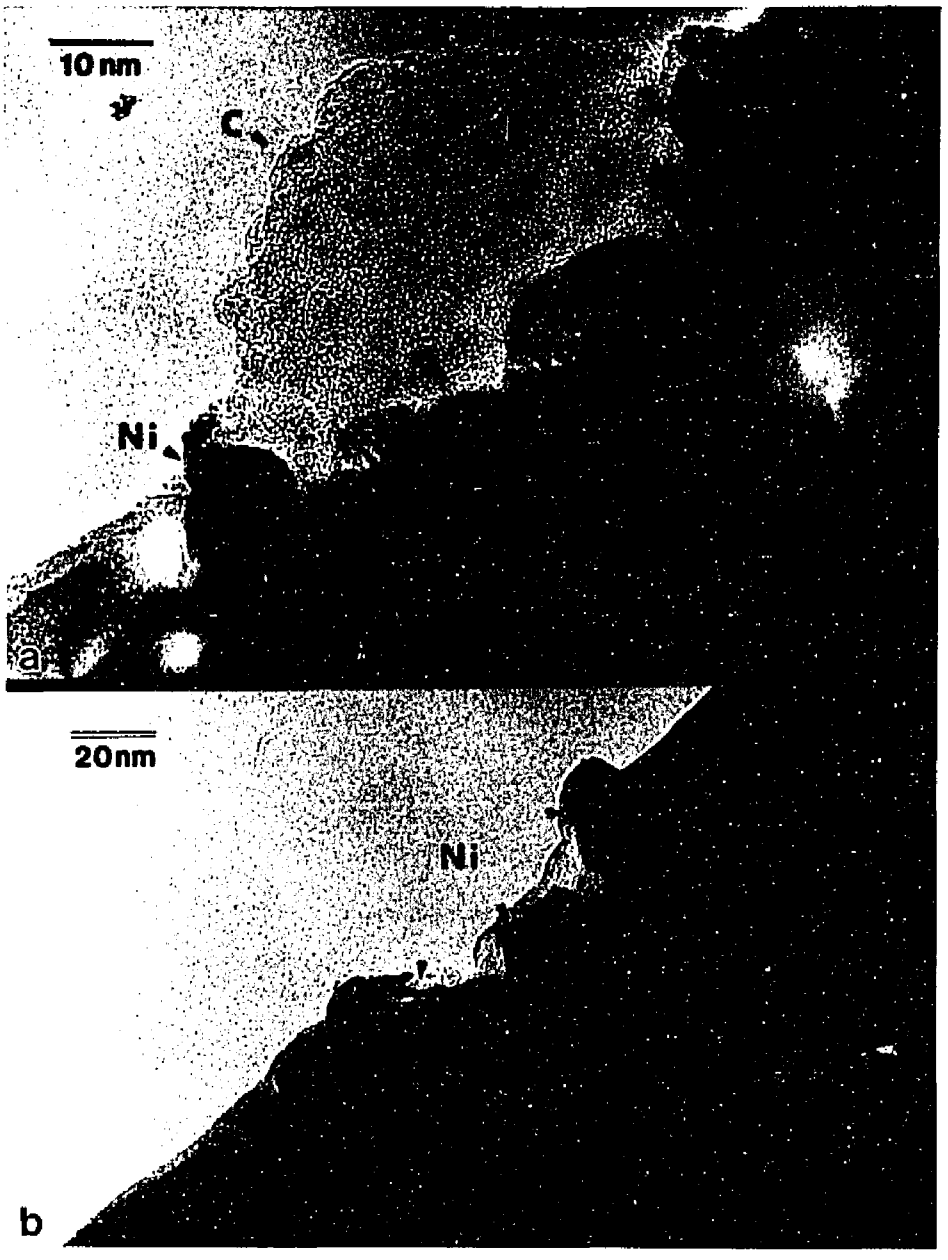

FIGURE 5.21 a) Carbon contamination resting on the NiO Surface. Moire fringes indicate Ni at the Interface. b) After complete disintegration of the carbon.

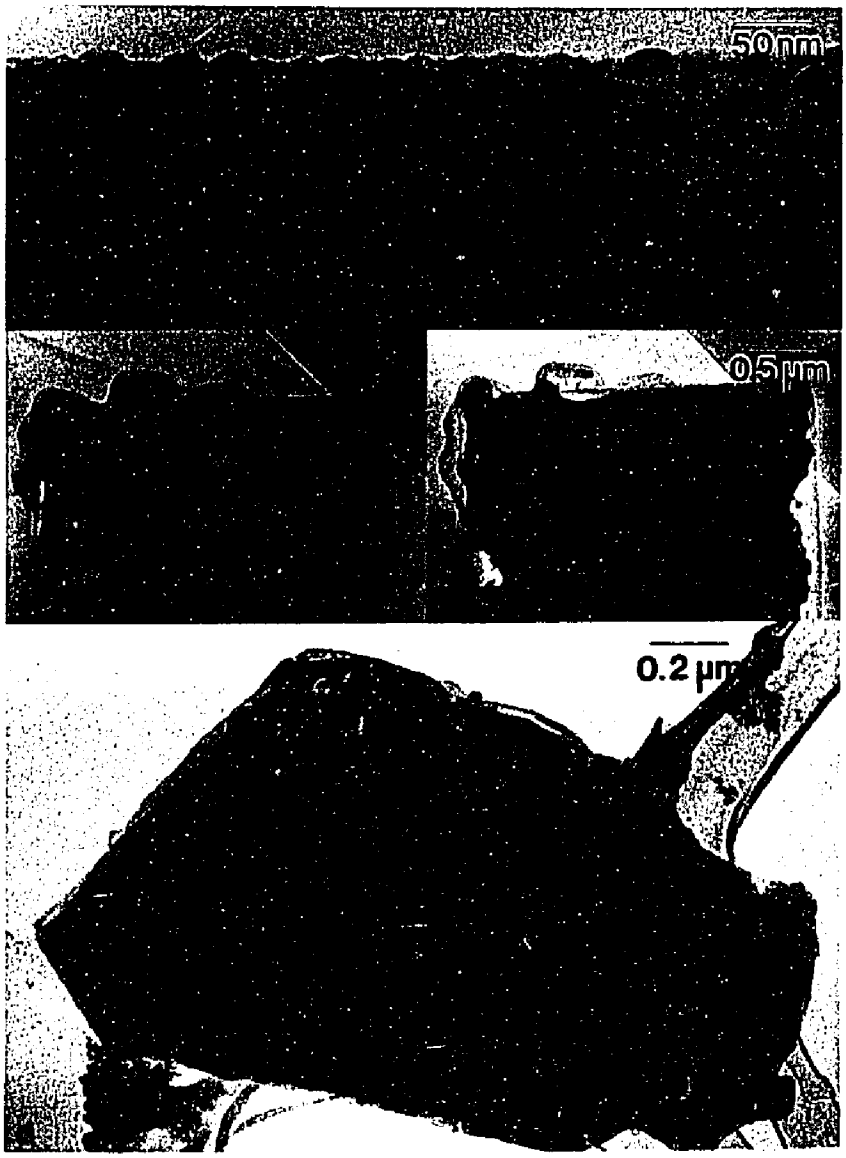

FIGURE 5.22 Varying degrees of structural damage after ESR in the presence of reactive carbon. a) Metallic nickel islands form during low flux irradiation at 300kV; b) before and c) after ESR during high flux irradiation at 300 k; d) complete disintegration after high flux irradiation at 100kV.

5.5 - GRAPHITIC CARBON ENCAPSULATION LAYERS

On occasion, a graphitic contamination layer ranging in thickness from 10 Å to 100 Å would form on the surface of a specimen. Shown in Figure 5.23, for example, are two samples which were exposed to equivalent irradiation conditions. The fully encapsulated sample in Figure 5.23(a) shows no signs of radiation damage; whereas the partially encapsulated sample in Figure 5.23(b) shows evidence of surface erosion in exposed versus encapsulated areas. Thin contamination layers (<< 10 Å) could usually be etched away with time by the electron beam without visible damage to the substrate (Marks and Smith 1984). Thicker, tenacious contamination layers were often identified as wholly or partially graphitized carbon, both very difficult to remove. Graphitic surface contamination is not uncommon in microscopy work, even though the exact conditions under which it forms is not well known (Strane et al. 1988). Nickel is also a known catalyst for the graphitization of carbon (Karu and Beer 1965; Tamai et al. 1968, Lamber, et al. 1988). Samples encapsulated under graphitic layers were exceedingly resistant to radiation damage. Even under high flux irradiation, no evidence of radiation damage at the surface or in the bulk was observed in time periods exceeding three hours for well-encapsulated layers, thus confirming that these effects are surface-controlled.

5.6 - DOSING OF THE NiO SURFACE UNDER UHV CONDITIONS

From the non-UHV observations which have been presented, one can conclude that the surface environment plays an important role in the nature and type of radiation damage processes in NiO. As the conventional electron microscope environment is for the most part uncontrolled, a series of experiments were set up to isolate specific electron-stimulated reactions. In-situ observations of the nature of CO and O_2 gas-surface

interactions were performed in the UHV side transfer chamber. Oriented [001]/(001) single crystal NiO samples were used for the investigations.

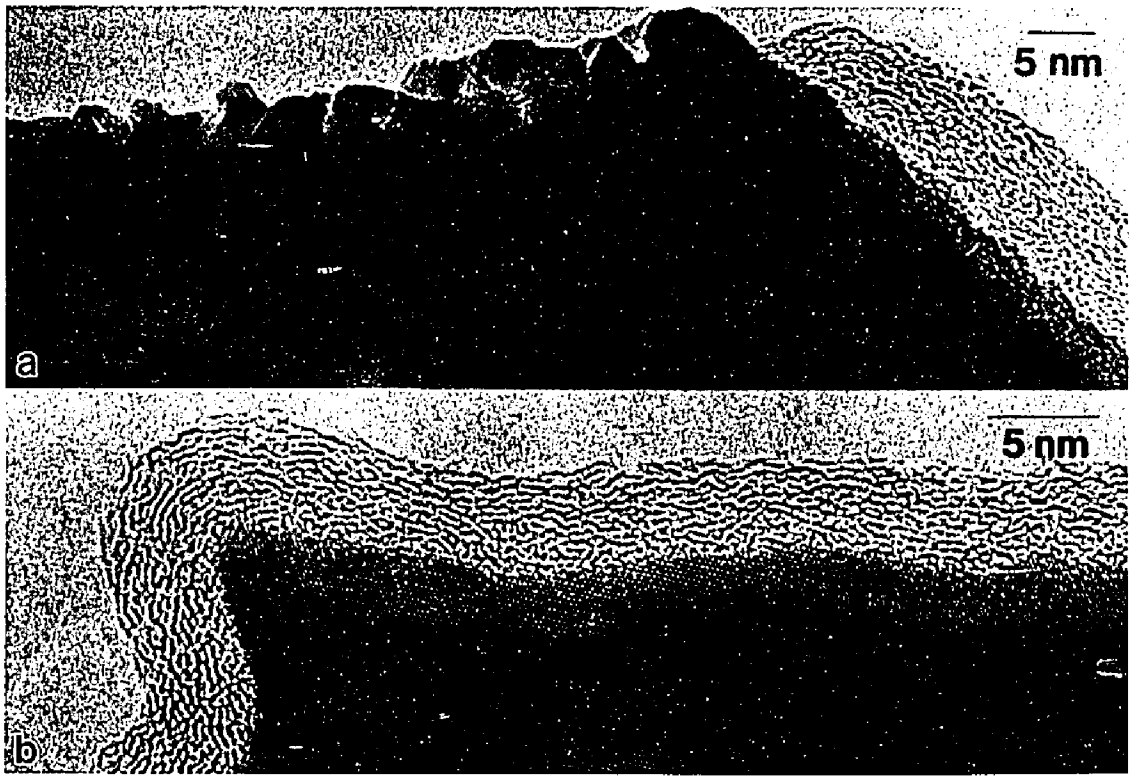

FIGURE 5.23 Encapsulation by a graphitic carbon layer provided varying degrees of protection for the surface toward prolonged exposure to both low and high flux electron irradiation.

a) Partially graphitized layer covers only part of surface. Exposed areas were seen to nucleate the spinel phase, and with time, showed extensive ballistic surface erosion.

b) Graphitized layer fully encapsulates the sample. No surface degradation was evident after 120 minutes of observation at high flux.

5.6.1 - O_2 DOSING

For the O_2 experiment, samples were inserted into the UHV chamber, sputtered with 2.1 kV, 25 mA Xe^+ ions for 15 minutes on each side at 90° incidence. The resulting surface after sputtering was a mixture of NiO and Ni, as shown in Figure 5.24(a-b). The dark field image of Figure 5.24(b), taken using the Ni(200) reflection, revealed that the Ni patches were uniformly scattered in the form of islands on the surface. The sample was then optically annealed for 35 minutes in a partial pressure of O_2 of 10^{-6} Torr. A significant portion of the resultant surface was inadvertently transformed to Ni at this stage. One drawback of this system is that it allows minimal control over the optical annealing temperature. Estimates of the annealing temperature were made by comparison to a gold thin film sample which was used to calibrate the annealing source, but apparently an underestimate of the temperature rise was made. According to the Ellingham diagram for the Ni/NiO system, the temperature achieved in the optical anneal must have been in excess of 1300°C. To maintain the NiO phase at this temperature, a pressure in the millitorr range would have been required. A subsequent optical anneal in a few millitorr of O_2 resulted in the formation of large NiO islands which had a predominantly cube-cube epitaxial relationship with the substrate Ni. The surface is shown in Figure 5.25, taken under dark field conditions using the NiO (200) reflection. White areas in the image indicate the NiO in this case. This was taken as the initial condition.

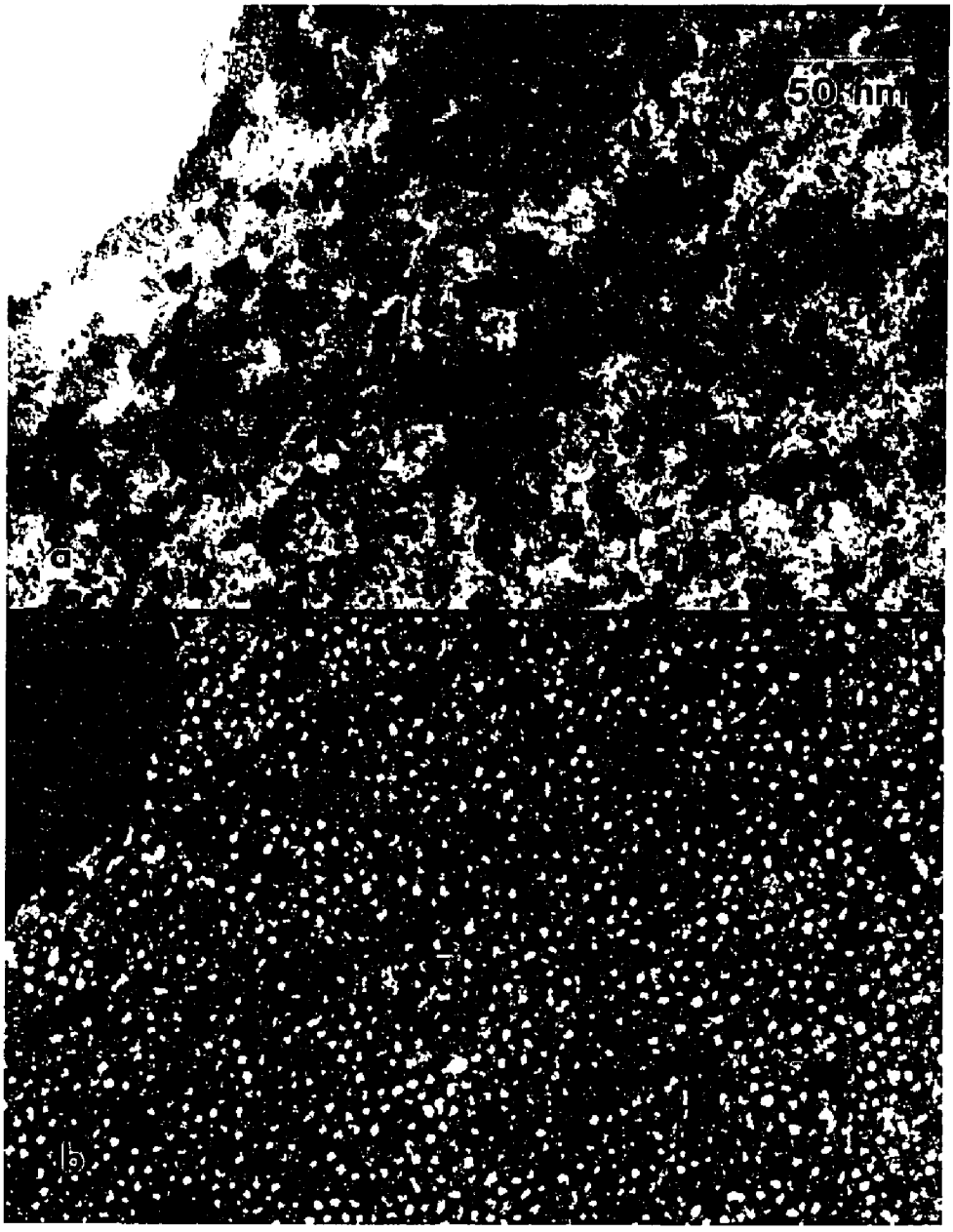

FIGURE 5.24 NiO [001]/(001) Bright field/dark field pair showing the surface in the as-sputtered condition. Dark field image was obtained using the Ni (200) reflection. Islands of Ni are evident at the somewhat disordered surface. a) Bright field image b) Dark field image.

FIGURE 5.25 Dark field image showing NiO [001]/(001) surface after optical annealing in O_2. Image was taken using the NiO (200) reflection.

Beam-stimulated oxidation of this Ni/NiO film was observed in-situ by opening the gate valve to the side transfer chamber while operating the microscope. An atmosphere of 10^{-7} Torr of O_2 was leaked into the column during observation. Shown in Figure 5.26(a-c) are dark field images (from the NiO (200) reflection) of the progressive oxidation of the surface during irradiation. The process occurred by the nucleation and growth of small fractal-like patches of NiO on the substrate Ni (Figure 5.26(a)). Both the optical anneal and the beam-stimulated oxidation showed the NiO islands often preferentially nucleating at defects such as surface steps and dislocations. The small patches of NiO were seen to coalesce and grow into larger networks with time (Figure 5.26(b-c)). Areas not within the beam did not undergo oxidation, indicating either that the beam is stimulating the oxidation process or that it is locally heating the area. No other evidence of local heating could be ascertained, while the oxidation process took place even under the minimum flux conditions for obtaining an image. These observations suggest that the oxidation process is an electron-stimulated reaction. Reoxidation of the Ni areas was solely to NiO with no evidence of the Ni_3O_4 phase, as expected from earlier surface science studies (Holloway and Hudson 1974).

Reoxidation of the areas of NiO provided inconclusive results. Evidence of a doubling of the surface cell was observed in the diffraction pattern, shown in Figure 5.27, during the initial stages of oxidation. These reflections (marked as (a) and (b)) formed within minutes of the start of irradiation, but soon disappeared - leaving only the parent NiO and Ni (marked as (c)), and inadequate time to obtain the HREM images. It is possible that in the non-UHV environment, impurities from the vacuum (in addition to oxygen) are acting to stabilize the Ni_3O_4 phase - perhaps by forming trapping sites.

FIGURE 5.26(a-c) Time evolution sequence taken during O_2 dosing of the surface. Images were taken using the NiO (200) reflection.

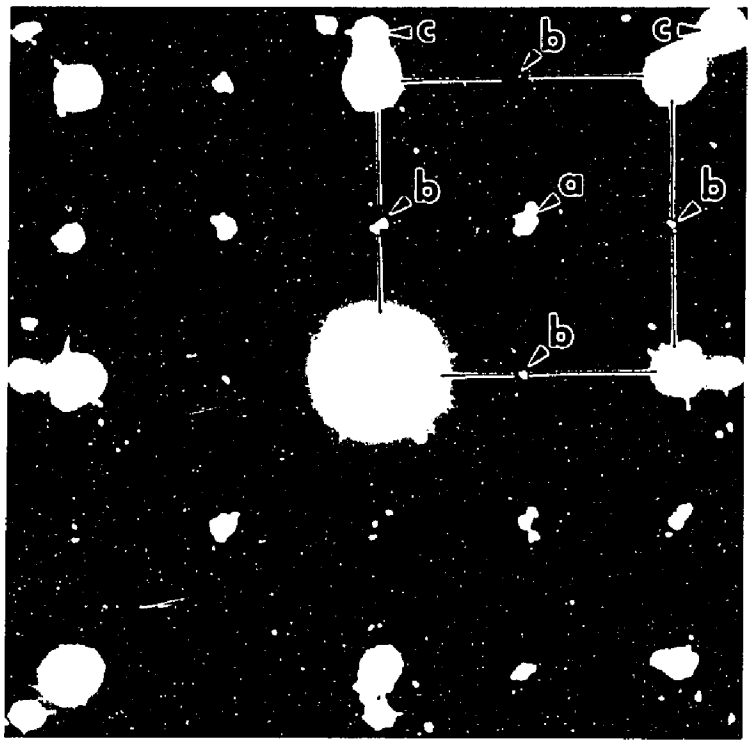

FIGURE 5.27 Diffraction pattern taken during O_2 dosing of the NiO [001]/(001) surface. Reflections marked (a) and (b) indicate a doubling of the NiO unit cell. The reflections marked by (b) are not allowed in the true spinel structure. Reflections marked (c) are due to Ni which was present from the prior annealing stage.

5.6.2 - CO DOSING

For these experiments, the annealing conditions were better optimized to retain the NiO phase during the cleaning stage. The sample was sputtered under the same conditions as described earlier, but for only 4 minutes on each side, and then optical annealed for 15 minutes in oxygen. Large, easily distinguishable islands of Ni unavoidably formed, however there was considerably more NiO surface to work with. Similar to the previous experiment, the clean NiO surface was observed in-situ in a 10^{-7} Torr atmosphere of CO. In this case, the surface exposed to the beam was rapidly reduced to tiny crystallites of Ni in the beam area only, as shown in the bright field images of Figure 5.28 (a-c). Figure 5.28(a) represents the initial surface with preexisting large islands of Ni. The images in 5.28(b-c) show the development of a speckling between the large NiO, identified as Ni crystallites, which could be observed within minutes of exposure to the beam. The crystallites did not appear to coalesce or grow together with time, which would have been expected if a substantial temperature rise were present. A dark field image of the irradiated area, using the Ni (200) reflection, is shown in Figure 5.29. Between the larger, pre-existing Ni islands, one can again see small crystallites where the beam was centered in the upper left-hand corner of this image. Note how the crystallites gradually disappear with increasing distance from the beam center. These observations are believed to correspond to a CO/CO_2 reaction being catalyzed by the NiO surface, as seen in the literature (Samsonov 1982).

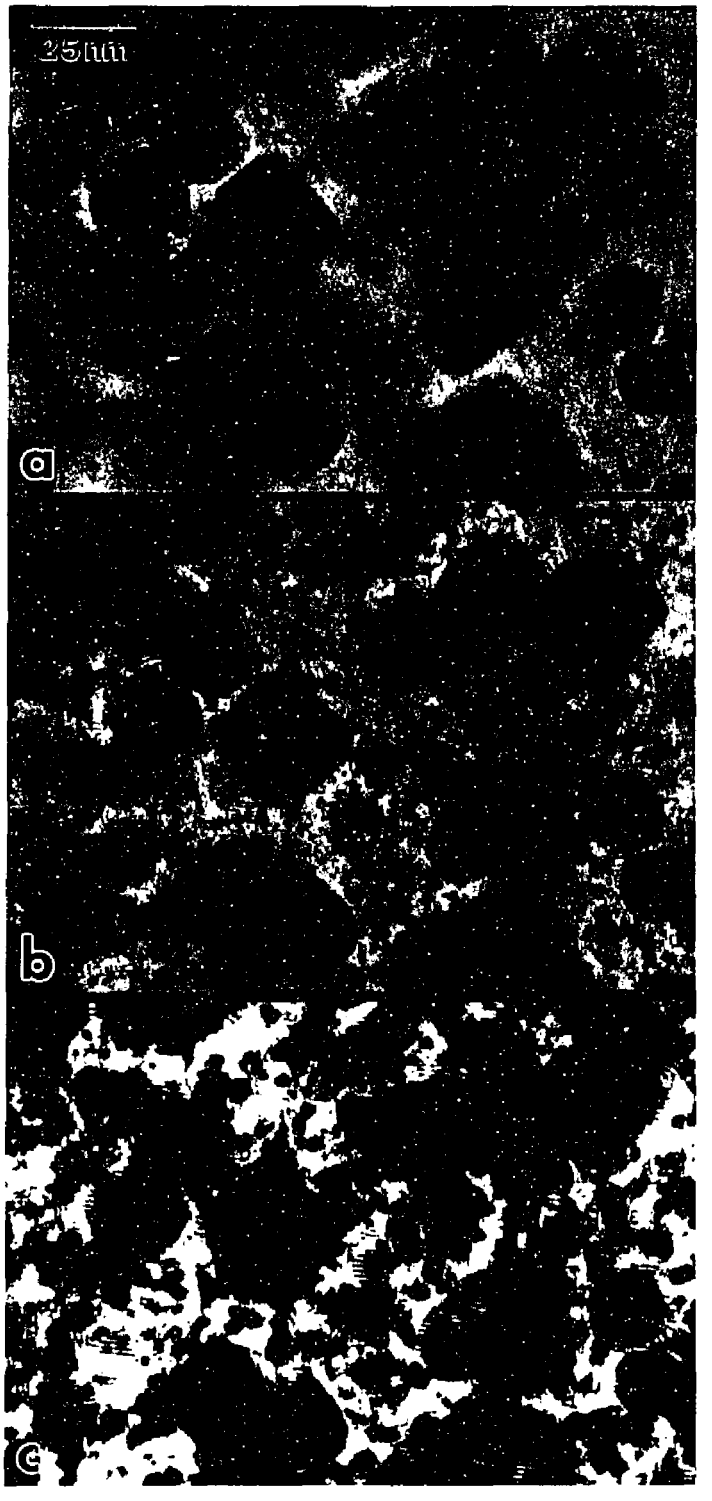

FIGURE 5.28 (a-c) Time evolution sequence taken during CO dosing of the surface. Tiny crystallites of Ni are being deposited between the larger Ni islands.

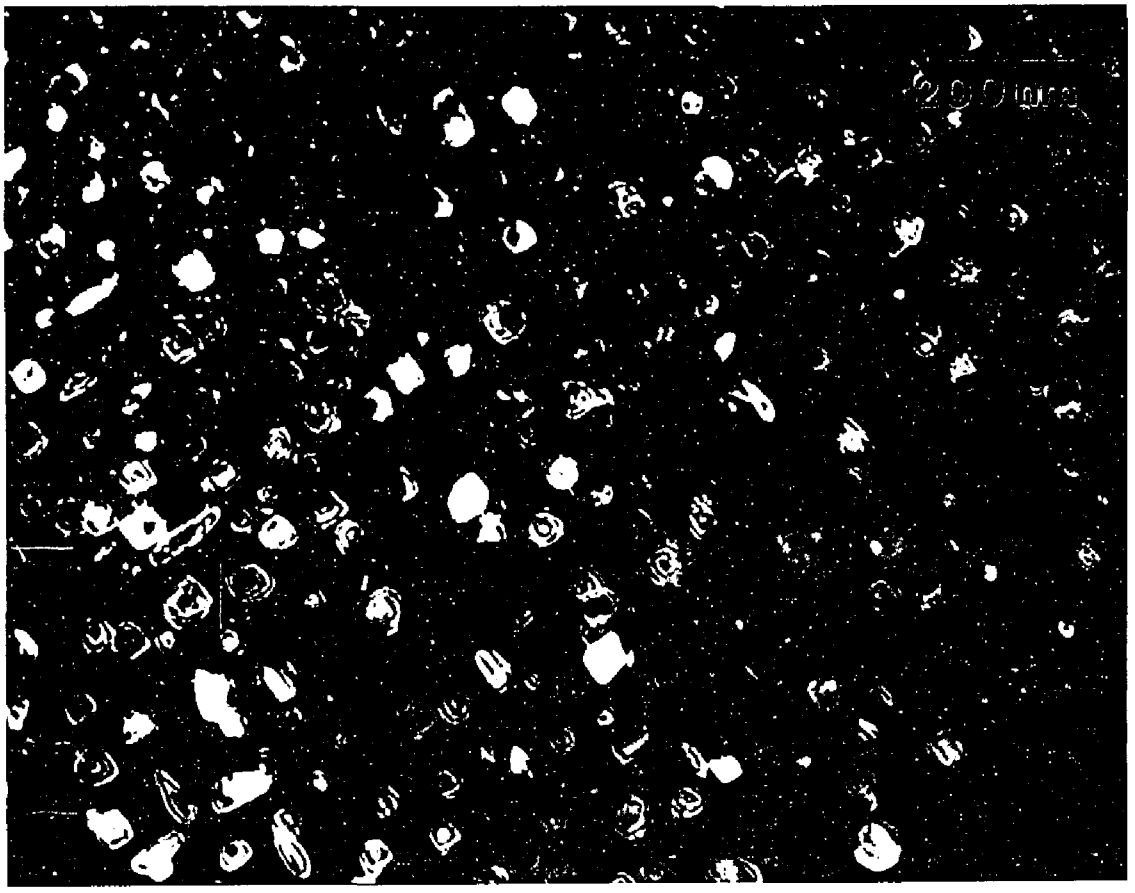

FIGURE 5.29 Dark field image showing area where Ni is being deposited during ESR in the CO atmosphere. Beam was centered in the upper left-hand corner of the image. Between the larger, pre-existing Ni islands, small crystallites of Ni can be seen.

5.7 - DISCUSSION

In summary, the primary damage process observed in NiO during electron irradiation was ballistic surface erosion, which varied directly with both electron energy and flux. In the UHV environment, ballistic surface erosion was the only form of radiation damage observed. Neither surface relaxation nor faceting were observed and surface erosion did not show a strong orientation dependence. In the non-UHV environment, surface erosion could be monitored at appreciable rates only at the higher flux irradiations at 300 kV, due to the presence of contaminants and competing surface reactions. Ballistic damage under non-UHV conditions was accelerated along certain directions in the crystal; an effect significantly more pronounced in the [110]/(110) than in the [001]/(001) orientation, which would be an expected result. The crystal planes in the [110]/(110) orientation consist of alternate (111) columns of nickel and oxygen parallel to the beam, a more favorable orientation for ballistic knock-on effects, rather than columns of mixed atoms. However, similar heavily anisotropic behavior was not observed under UHV conditions. It is concluded that the formation of the spinel phase is contributing to accelerated surface erosion along preferred orientations under non-UHV conditions.

It was further determined that the Ni_3O_4 spinel transformation was a surface-initiated reaction via interaction with the local environment, presumably oxygen, rather than a ballistic damage mechanism producing a nickel deficiency within the sample itself for the following reasons:

1). Neither the spinel phase or its precursor state formed in specimens under UHV conditions. Insertion of the same specimens into a non-UHV microscope, however, resulted in characteristic spinel formation. This also

indicates that it is not impurities within the crystal itself promoting the reaction, but the surface environment in the non-UHV microscope. Dosing a clean NiO surface with O_2 under UHV experimental conditions showed evidence of the precursor to spinel transformation.

2). No evidence of bulk-initiated damage was observed under any conditions. Upon consideration of the defect formation energies in NiO, the experimental conditions used in this study would not permit bulk defect formation by ballistic energy transfer alone.

3). Nucleation of the spinel phase occurred preferably at a high energy surface sites - a kink or step, or a NiO (111) facet as shown in Figure 5.30. The newly created Ni_3O_4 areas proceeded to grow along the surface and into the bulk such that after further irradiation time, line defects were observed from the intersections of the Ni_3O_4 grains, as shown in Figure 5.31 for the NiO [001]/(001) orientation. The spinel phase did not form when the surface was encapsulated with a graphitic carbon layer under non-UHV conditions. For example, as was shown in Figure 5.23, NiO surfaces encapsulated by graphitic layers resulted in no observable structural changes during irradiation. However, exposed surfaces showed the characteristic precursor to spinel formation within minutes of exposure to the electron beam and anisotropic ballistic damage with further time.

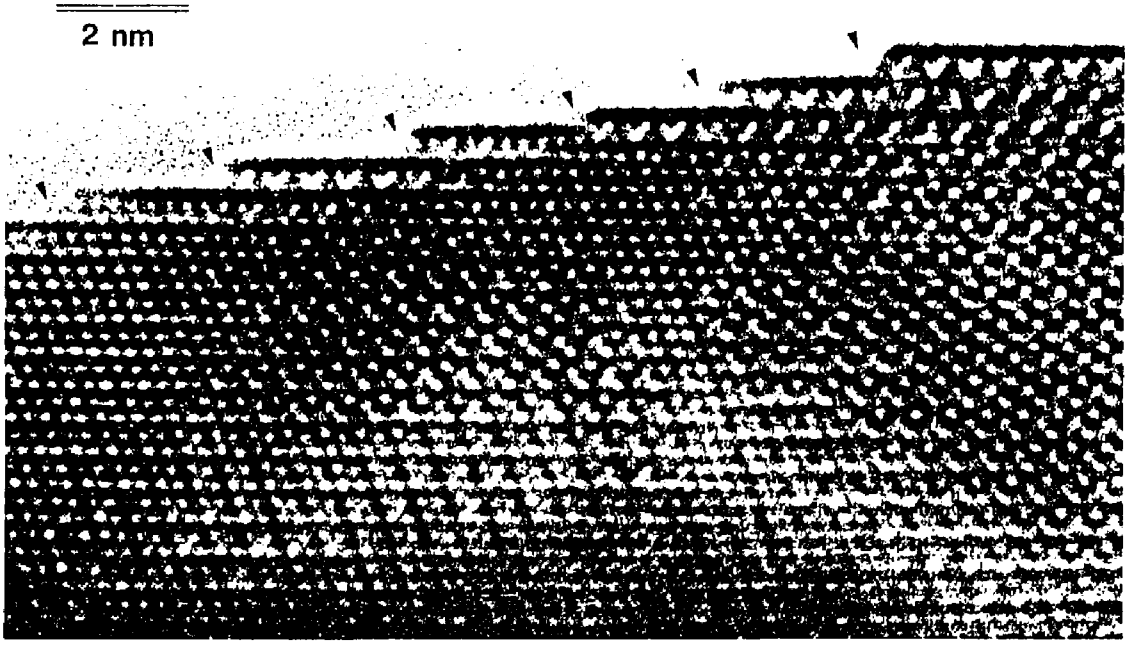

FIGURE 5.30 NiO [110]/(110) showing the Ni_3O_4 phase forming preferentially at surface ledges.

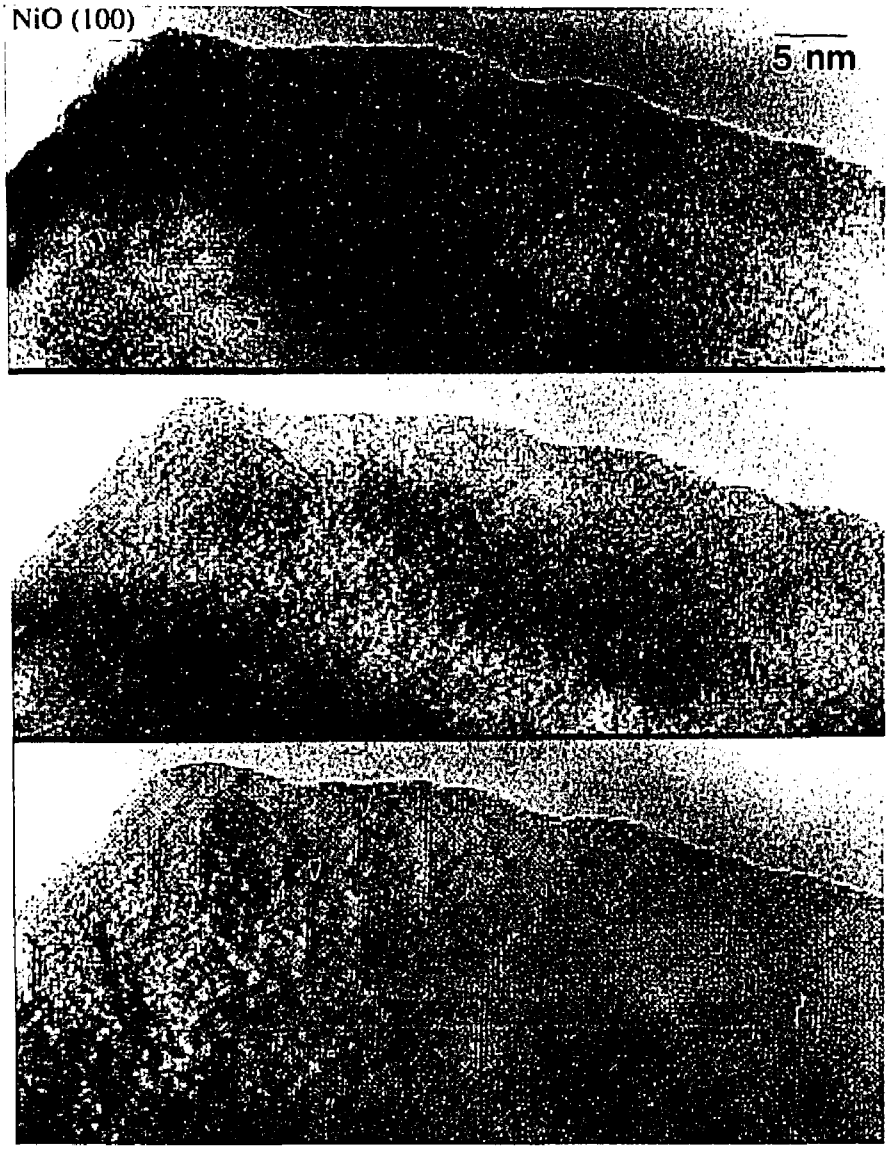

FIGURE 5.31 NiO [001]/(001) time evolution sequence showing progressive stages of Ni_3O_4 formation. Domain boundaries become apparent as the newly created grains begin to intersect .

It can only be concluded that the surface is undergoing an electron beam-stimulated interaction with some gaseous component in the microscope. The primarily components of the residual gas in the microscope are CO, CO_2, H_2O, N_2 and O_2. Reaction of these species with the NiO surface may lead to the formation of Ni_3O_4, via reactions such as the following:

(1) $NiO + 4\,CO \;\text{--->}\; V_{Ni}^{m'} + m\,h^{\circ} + O_O + Ni(CO)_4$

(2) $NiO + H_2O \;\text{--->}\; V_{Ni}^{m'} + m\,h^{\circ} + Ni(OH)_2$

(3) $1/2\,O_2 \;\text{--->}\; V_{Ni}^{m'} + m\,h^{\circ} + O_O$; m = charge on defect

(4) $4\,NiO \;\text{--->}\; Ni + Ni_3O_4$

Reaction (1) was ruled out by the CO dosing experiment. Reactions (2) and (4), a surface reaction involving H_2O vapor in the microscope and a redox reaction similar to the decomposition of wustite respectively, have not previously been observed by the described reactions (Cotton and Wilkinson 1972). Considerations of the free energies of formation show that neither are they thermodynamically favored in comparison to reaction (3) (Samsonov 1982). Values of enthalpies of oxidation and reduction, ΔH_O and ΔH_R, in NiO are shown in Table 5.7 (Mackrodt 1984). Reaction (3), the beam-stimulated addition of oxygen with corresponding creation of Ni vacancies and holes to maintain site and charge balance, is not only energetically favorable compared to other defect reactions, our experiments to date cannot provide contradictatory evidence to this conclusion that a simple beam-stimulated oxidation reaction is occurring.

TABLE 5.7

Calculated and experimental enthalpies of oxidation (ΔH_O) and reduction (ΔH_R) for various reactions in NiO.

Reaction	ΔH_O (eV)	ΔH_R (eV)	Experimental Determination
$1/2\,O_2 = V_{Ni}'' + 2\,h^\circ + NiO$	2.2		2.5 eV
$1/2\,O_2 = O_i' + h^\circ$	5.5		5.6
$1/2\,O_2 = O_i'' + 2\,h^\circ$	5.84		
$O_O = 1/2\,O_2 + V_O^{\circ\circ} + 2\,e^-$		8.3	
$Ni_{Ni} + O_O = 1/2\,O_2 + Ni_i^{\circ\circ} + 2\,e^-$		14.8	

Reaction (3), which is initiated by the chemisorption of oxygen, has been confirmed in the literature by measurements of the oxygen partial pressure dependence of conductivity in NiO (Mitoff 1961). If the temperature is low enough such that the defect migration rate is insufficient to achieve equilibrium over the entire crystal, a complicated situation arises. The chemisorption of oxygen alone causes only an electronic displacement, a transfer of electrons from the oxide to the chemisorbed oxygen. Without a simultaneous significant amount of ion diffusion, a difference in charge between the NiO oxide interior and its surface results. An enhanced concentration of defects must therefore be created in the surface boundary layer, setting up a pseudo-equilibrium at the oxide/gas interface. The result is a difference in concentrations between ionic and electronic defects in the boundary layer. Under these conditions, a flux of nickel

vacancies and holes into the bulk as well as nickel ions and electrons to the surface occur. As NiO is a p-type conductor, the oxidation rate should increase with increasing oxygen partial pressure (Hauffe 1965).

Unlike Co_3O_4, Mn_3O_4, and Fe_3O_4, the Ni_3O_4 spinel phase is not thermodynamically stable in the NiO system. All evidence points to the conclusion that it is a radiation-induced transitory product during electron bombardment. The question remains as to whether it was observed under circumstances other than high energy electron irradiation. Although few in number, there exist documented cases of observed anomalies which could be attributed to Ni_3O_4 formation. They are described below.

Doubling of the NiO lattice parameter (Palmberg et al. 1969; Suzuki et al. 1971) and precipitation of a defect spinel-type structure (Shimomura et al. 1956; Katada et al. 1970) have been previously recorded in the literature under different conditions than have been studied here. Shimomura and coworkers reported that the structure of ferromagnetic (and later corrected to ferrimagnetic) NiO crystals prepared by the flame fusion method and analyzed by x-ray diffraction was a defect tetragonal structure belonging to $I4_1/amd$ (D_{4h}^{19}). This possibility has been investigated using the ferrimagnetic structure data as a basis for image simulations. Under no conditions did the calculated images compare with the experimental images, thus ruling out antiferromagnetic NiO in our case.

The structure determined by Shimomura et al. (1956), was later modified by Katada et al. (1970), who observed precipitates with a defect structure in NiO thin films after heating to temperatures of 1400-1600°C in air. Using electron diffraction as well as the earlier x-ray data, they corrected the original structural determination to that of a deformed spinel-type based on the $Fd3m\text{-}O_h^7$ space group. They also observed the precipitates to generally have a regular octahedron shape with (111) face planes. These

data correlate well with our observations of (111) faceting. Katada and coworkers, however, were unable to account for the origin of the large nickel deficiency required for complete transformation to the Ni_3O_4 composition.

LEED studies (Palmberg et al. 1969; Suzuki et al. 1971) have reported on the appearance of half-order diffraction spots which were interpreted to result from spin ordering in antiferromagnetic NiO. These, however, were observed only below the Néel temperature (252°C) in UHV and at electron energies below 100 eV. The positions of the fractional order beams were believed to be due to a magnetic cell in antiferromagnetic NiO having double the unit cell spacing as the chemical cell and not a phase transformation.

Finally, Couput et al. (1982), reported on the anomalous enhancement of electric conductivity in NiO measured at 740°C in an oxygen pressure between 10^{-2} and 1.3 Torr. Their results can be summarized in terms of an interplay of adsorption of gas molecules on the sample surface, cation vacancies diffusing into the bulk, and Ni interstitials near the surface creating electron holes. This was interpreted to be a transitory phenomenon connected with reaching the gas-solid equilibrium. Their findings correspond remarkably well to the formation of a spinel phase.

It can be concluded that changes in the electronic structure are occurring at the surface of NiO that lead to the formation of Ni^{3+} defects on the nickel sublattice, in agreement with the surface science literature. This conclusion differs only in the determination of a resultant Ni_3O_4 spinel structure. Both the anomalous behavior of the O^+ yield during oxygen exposure of both nickel and NiO surfaces using ESD and AES techniques (Wang and Verhoeven 1986; Niehus and Losch 1981; Verhoeven et al. 1984) and the appearance of Ni^{3+} on the surface of NiO using chemical shift information (Larkins and Fensham 1970; Kim and Davis 1972/1973; Kim and Winograd 1974;

Finster et al. 1982) have been reported in the surface science literature. These combined results were interpreted as the formation of Ni_2O_3 during the early stages of the oxidation process, although no structural evidence for the formation of this phase has been reported. It has been proposed that the Ni_2O_3 phase may exist at low temperatures (Brennan et al. 1960; Wood et al. 1965), with NiO being the favorable high temperature structure. Neither NiO nor Ni_3O_4 are known stable oxide structures in the NiO system, however the spinel phase is an equilibrium low temperature structure in related systems such as CoO, MnO, and FeO.

From these observations, it is predicted that the surface oxidation of NiO seen in previous surface studies is due to the same Ni_3O_4 phase observed in this study rather than to Ni_2O_3 of undetermined structure. Direct structural observations reveal that Ni^{3+} surface species are more likely due to the presence of a Ni_3O_4 spinel structure, which is crystallographically more similar to the parent NiO phase. Electron-beam assisted oxidation of the surface appears to be the operative mechanism in these materials in the non-UHV environment. For CoO, MnO and FeO, where volume expansion is clearly observed, there is even stronger evidence to suggest that the mechanism is one of the incorporation of oxygen from the gas phase into the lattice, with the corresponding creation of a cation vacancy to maintain charge and site neutrality. Cation vacancies and holes created at the surface, diffuse into the bulk with subsequent phase transformation to the cation deficient M_3O_4 type phase. This general type of reaction is well-documented in the literature (Hauffe 1965; Kofstad 1972); however it has not been previously seen in-situ in the electron microscope. The advantage offered with HREM is that structural determination of the resultant phases may be made through direct observation.

CHAPTER 6
ELECTRON IRRADIATION DAMAGE OF MAXIMUM VALENCE TRANSITION METAL OXIDE SURFACES UNDER ULTRA-HIGH VACUUM CONDITIONS

6.1 - INTRODUCTION

It was shown that the maximum valence transition metal oxides - such as TiO_2, V_2O_5, MoO_3, and WO_3 - should be prime candidates to study because preferential electron-stimulated oxygen loss due to a Knotek-Feibelman or similar type of process is believed to occur in these materials. The initial step to this mechanism is the formation of a core hole on the metal cation by the incident radiation. The core hole is filled by a one- or two-electron interatomic Auger decay process, which becomes coupled to atomic motion, imparting 10 to 20 eV of kinetic energy to an oxygen atom - sufficient to eject it from the surface. Almost independent of whether the incident radiation is electrons, ions, or photons, the surface science reports show oxygen ions and neutrals being ejected from the surface at threshold energies at or near the 3p or 4f and 5p ionization thresholds. Clearly, if preferential electronic sputtering of oxygen is occurring, then at some stage during the irradiation the initial phase should become unstable and some sort of structural modifications should occur.

High resolution electron microscopy has recently entered the surface science arena as a complementary technique for studies of electron-stimulated damage of oxide surfaces. But despite the demonstrations that a number of transmission and reflection electron microscopy techniques can be applied to the study of surfaces (Cherns 1974; Takanayagi 1981; Marks and Smith 1984), the contribution of electron microscopy to surface science has been very limited to date. For example, shown in Table 6.1 is a

comparison of studies performed on the maximum valence transition metal oxides under non-UHV conditions.

TABLE 6.1

A comparison of HREM radiation damage studies in the non-UHV environment.

Initial Phase	Beam Energy; Flux (keV; A/cm^2)	Final Phase	Reference
$W(Nb)O_{2.93}$	400; 25-40	metallization	Smith and Bursill (1985)
WO_3	200; ----	~ W	Petford et al. (1986)
WO_3	400; 10-50	WO	Smith et al. (1987)
WO_3	300; 10	W, W_3O	Singh and Marks (1989)
CuO	100; ~ 10^4	Cu_4O_3-> Cu_2O->Cu	Long and Petford-Long (1986)
V_2O_5	400; 10	$VO_{0.9}$	McCartney and Smith (1989)
V_2O_5	100, 300; ---	VO	Fan and Marks (1989)
Al_2O_3 (Cr doped)	100; 10-30	"patchwork quilt" appearance, (0006) facets	Smith et al. (1986)
Al_2O_3	300; ---	Al	Bonevich (1991)
TiO_2	400; 20	TiO	Smith et al. (1987)
TiO_2	300, ---	TiO,Ti_2O_3	Strane 1988
TiO_2[001]	400; 10-50	TiO_2-II -> TiO	McCartney and Smith (1989)
TiO_2[110]	400; 10-50	TiO	McCartney and Smith (1989)
Nb_2O_5	400; 10-50	NbO	McCartney and Smith (1989)
$(Mo,Ta)_5O_{14}$	400, 500; ---	metallization	Smith et al.(1986)
MoO_2	400; ---	Mo (?)	Hansen and Smith (1987)
SnO_2	400; 10-50	faceting	McCartney and Smith (1990)
SnO_2	100; ~10^4	Sn	McCartney and Smith (1990)
MgO	300,400; 10-50	facets, pits	McCartney and Smith (1990)
MgO	100; 10^4	faceted pits	McCartney and Smith (1990)

Although the HREM results generally support the surface science findings of a strong tendency of these materials to undergo oxygen loss during electron irradiation, the identification of the final phases and the operative mechanisms cited in the literature show wide variation.

The reasons for the scatter in the results are basically twofold: First, conventional electron microscopes suffer from the problems of attaining sufficiently good vacuum levels and the means to adequately prepare initial surfaces. Secondly, the experimental procedures have all but neglected the relative contributions of electronic, ballistic, and thermal mechanisms in the radiation damage process. HREM contributions to surface studies of ESD or ESR can only be considered valid if performed under surface science conditions or at least in controlled environments. The problem of microscope vacuum was already illustrated in Chapter 5, where the effect of electron irradiation on NiO and CoO surfaces was shown to vary with the sample environment. It can be concluded that surface-initiated behavior where electronic damage mechanisms may be operative as well as ballistic sputtering, such as electron stimulated desorption (ESD) or electron stimulated reaction (ESR), has not been adequately studied with HREM.

In this chapter, surface-initiated radiation damage of maximum valence transition metal oxides under UHV conditions is investigated and compared to damage effects observed in conventional instruments. The focus is to evaluate the relative contributions of electronic, ballistic, thermal, and environmental effects by a comparison of observations under various experimental conditions to the theoretical predictions outlined in Chapters 2 and 3. The HREM observations which will be presented here are a result of a group effort from the surface radiation damage studies group. During the time of this study, our group at Northwestern University was the only team investigating the

maximum valence transition metal oxides under UHV conditions, it will therefore be necessary here to pool the results together to obtain an accurate picture and acknowledgements are in order. A number of oxides were investigated, including TiO_2, ZrO_2, Nb_2O_5, V_2O_5, WO_3, MoO_3, and Ta_2O_5. Dr. Tim Wagner assisted with a number of the TiO_2 experiments. He also contributed the Ta_2O_5 results. H. Fan and R. Ai contributed the V_2O_5 work, and Dr. S.R.Singh provided both the MoO_3 and WO_3 results. Typical experimental procedures used for these studies were outlined in Chapters 4 and 5. Operating pressures were 1.9 to 3.7 $\times$ 10^{-10} Torr in the UHV instrument and 3×10^{-7} to 1×10^{-6} Torr in the conventional microscope.

6.2 - A COMPARISON OF UHV VERSUS NON-UHV OBSERVATIONS

Until 1990, the only instrument equipped to do in-situ HREM under surface science conditions was at Northwestern University. Recently, Arizona State University has gone on-line with a UHV (5×10^{-9} Torr) high resolution microscope; however this facility has no means for in-situ surface preparation. A summary of the experimental observations in the UHV environment is presented in Table 6.2. In comparison to Table 6.1, the UHV results strongly indicate that although the same basic damage mechanisms are operative under both vacuum conditions, subsequent surface alteration due to reoxidation or reaction with surface contamination occurs under non-UHV conditions. Damage rates were generally enhanced under UHV conditions, owing to the cleaner initial surfaces and lesser possibility of contamination build-up in the irradiated area, which is often encountered in conventional microscopes. A pictorial summary of the Northwestern University results is given in Figures 6.1 to 6.4. It should be noted that the structural changes occurred on significantly faster time scales than that which would

be predicted by either thermal or ballistic effects.

TABLE 6.2

Electron irradiation behavior of maximum valence transition metal oxides under UHV (~ 10^{-10} Torr) conditions.

Initial Phase	Final Phase
V_2O_5 (1)	VO (*)
TiO_2	TiO
Ta_2O_5 (2)	metallic Ta
WO_3 (3)	metallic W
MoO_3 (3)	metallic Mo

* Reduction in V_2O_5 proceeds as: $V_2O_5 \rightarrow (V_6O_{13}, V_4O_9) \rightarrow VO$

(1) courtesy of H. Fan; (2) courtesy of T. Wagner; (3) courtesy of S.R. Singh.

Shown in Figure 6.1 is a WO_3 (monoclinic) crystal during low flux (10 A/cm^2) electron irradiation at 300 keV. The WO_3 [102] surface underwent reduction to a metallic tungsten overlayer under UHV conditions with a highly defective, but not necessarily amorphous, intermediate stage. Under non-UHV conditions, the resulting surface layer was still tungsten; however beam-induced surface migration and subsequent reaction lead to the formation of W_3O or a defective WO. These results can be interpreted as a reoxidation of the metallic tungsten surface in the non-UHV environment as has previously been reported in the literature (Avery 1972; Avery 1974).

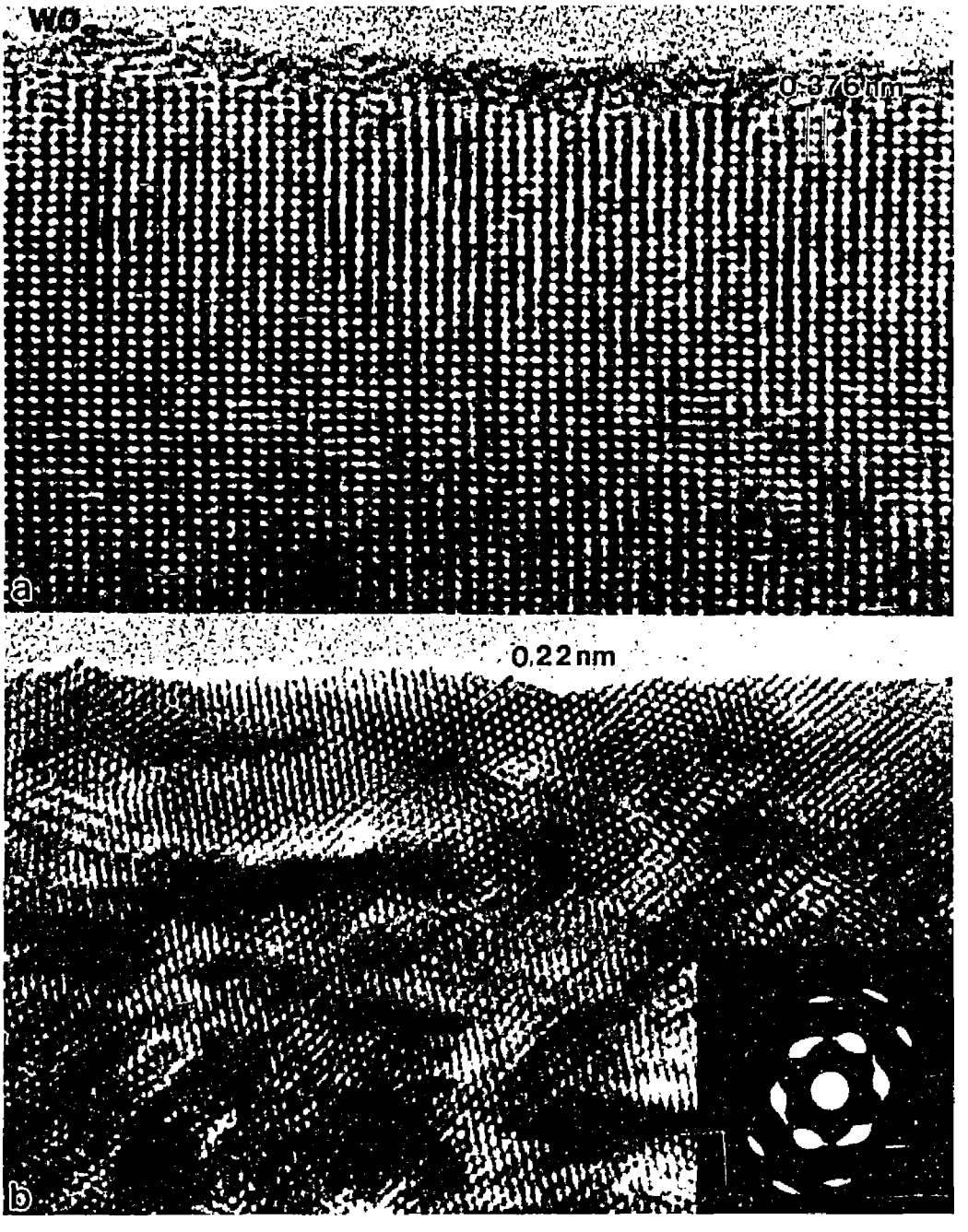

FIGURE 6.1 WO_3[102] under UHV conditions; a) initial surface; b) surface after 140 minutes of irradiation. Diffraction pattern shows W metal with a [111] texture (courtesy of S. R. Singh).

MoO_3 (orthorhombic) showed similar behavior in both the UHV and non-UHV environments (Figure 6.2). Similar to the WO_3, the MoO_3 surface underwent reduction to metallic molybdenum via a highly defective intermediate stage. None of the stable - Mo_9O_{26}, Mo_8O_{23}, Mo_4O_{11}, MoO_2 - or metastable - Mo_5O_{14}, $Mo_{17}O_{47}$, Mo_2O_3, MoO - intermediate suboxides of the Mo-O system were observed.

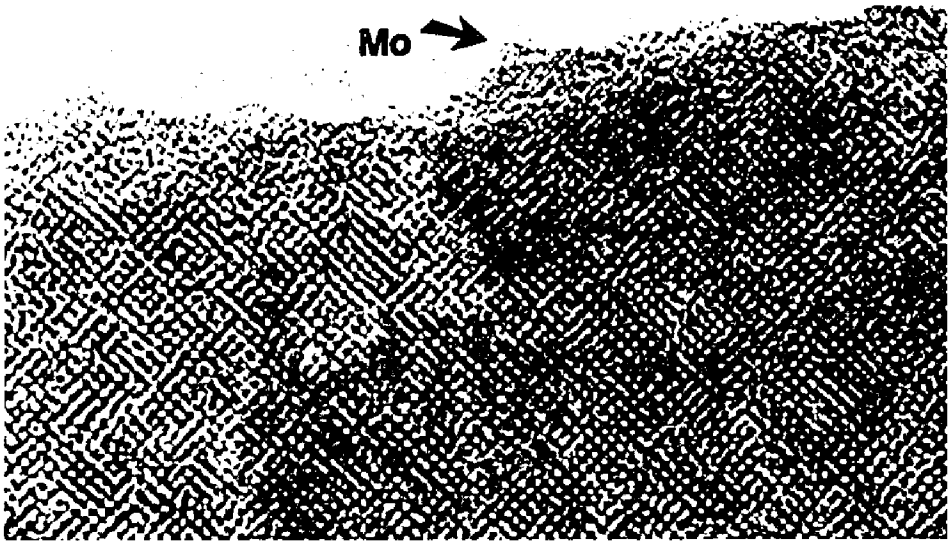

FIGURE 6.2 MoO_3 surface after extended irradiation under UHV conditions. Mo metal is evident at the profile surface (courtesy of S. R. Singh).

V_2O_5 (orthorhombic) exhibited a complex series of intermediate phase transitions to reduced oxides V_4O_9 and V_6O_{13} en route to the final phase identification of the VO (defective rocksalt) phase during 300 keV electron irradiation in both vacuum environments, as reported by Fan and Marks (1989) and shown in Figure 6.3. The phase transformation route in the non-UHV environment varied somewhat, which can be

explained by the sample environment controlling the nature and rate of defect production at the surface. As for the WO_3 case, subsequent surface reactions may be occurring in the non-UHV environment which alter the damage process.

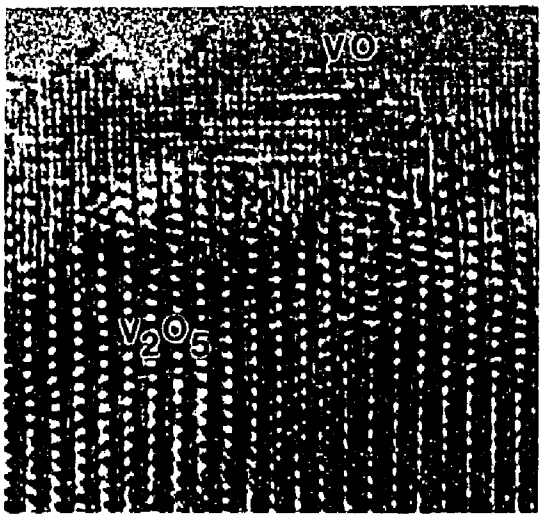

FIGURE 6.3 V_2O_5 (001) surface after extended irradiation. VO (rocksalt structure) is evident at the surface (Fan and Marks 1989).

TiO_2 (rutile) showed a direct transformation to the TiO (rocksalt) phase during high flux, 300 keV irradiation, as shown in Figure 6.4 for the TiO_2 ($\bar{1}10$) orientation. The initial surface is represented in Figure 6.4(a). During irradiation (Figure 6.4 (b-d)), the damage front progressed from the profile surface into the bulk. After long exposures, the appearance of TiO reflections and the disappearance of TiO_2 reflections were seen in the diffraction patterns, with no sign of diffuse rings characteristic of the formation of an amorphous intermediary.

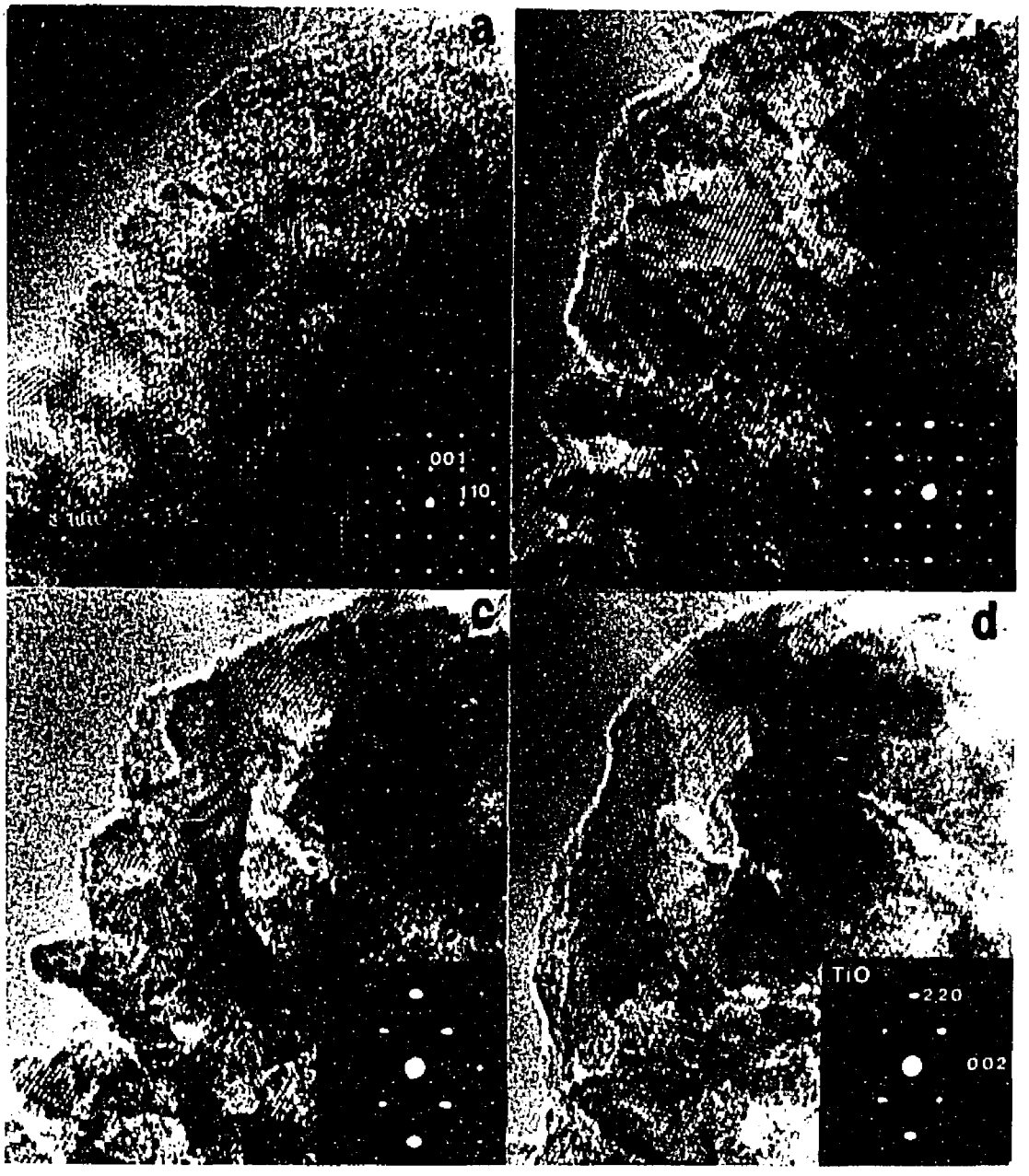

FIGURE 6.4 TiO_2 ($\bar{1}10$) during high flux irradiation under UHV conditions; a) initial surface; b) after 5 minutes; c) after 20 minutes; d) after 40 minutes, corresponding to a total dose of 1.5×10^{24} e-/cm^2 (courtesy T. Wagner).

Rather, a diffuse reciprocal lattice scattering characteristic of point defect formation, as shown in Figure 6.5 for the TiO_2 $(2\bar{1}2)$ orientation, was consistently observed. This is in contrast to ion irradiation studies of TiO_2, MoO_3, WO_3, and V_2O_5, where an amorphous intermediary is readily formed (Kelly and Lam 1973). A major change in shape of the titanium $L_{2,3}$ core edge as well as a shift in its position could also be identified in the electron energy loss spectrum by comparison to the oxygen K edge, indicating a change in the surface chemistry of the sample (Figure 6.6(a-b)) .

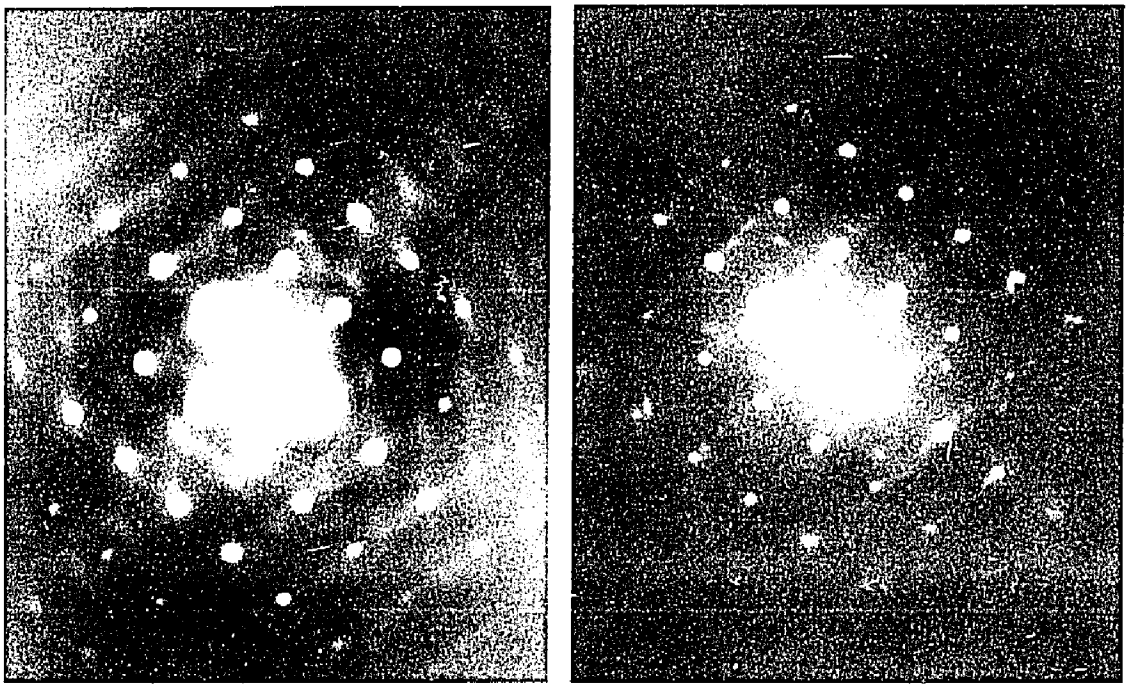

a) b)

FIGURE 6.5 TiO_2 $(2\bar{1}2)$ diffraction patterns. a) Diffuse reciprocal lattice streaking during the early stages of irradiation; b) after TiO phase formation at the surface.

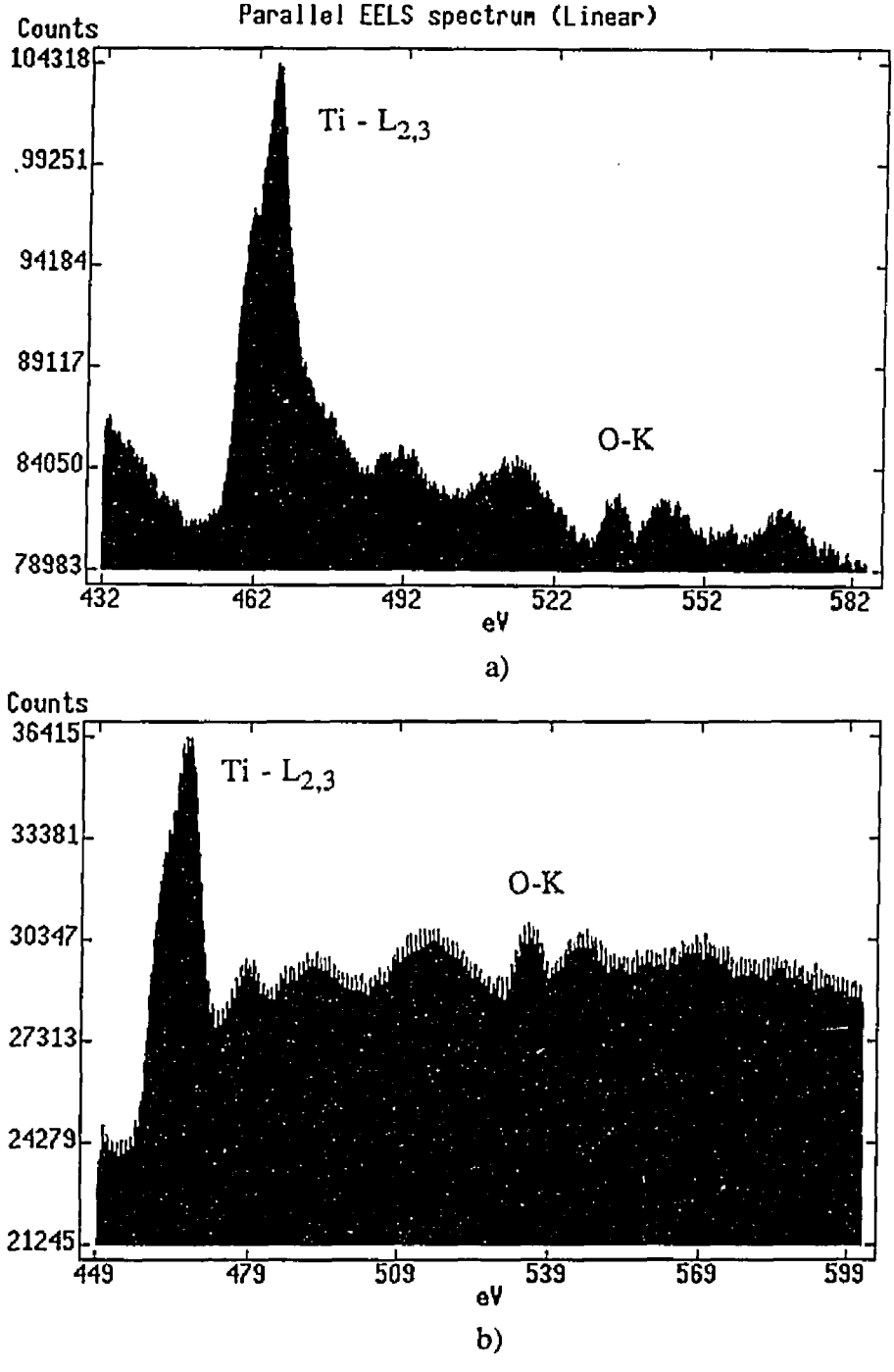

FIGURE 6.6 PEELS spectra of TiO_2 a) initial area; b) after extended irradiation.

By comparison of diffraction patterns in a number of orientations, the orientation relationship between the TiO phase and the parent TiO_2 phase was generally found to be:

TiO (100) // TiO_2 (110)

TiO (110) // TiO_2 (001)

These results can be simply explained by a coordinated loss of oxygen with a minimal shift of the remaining oxygen and titanium sublattices. Exceptions were occasionally noted, which is not surprising as there exist other variants of the orientation relation which also result in minor shifts of atomic positions, for example:

TiO (001) // TiO_2 (001)

TiO (100) // TiO_2 (110)

These observations are contrary to the orientation relationship determined by (McCartney and Smith 1989):

TiO (211) // TiO_2 (200)

TiO (220) // TiO_2 (110)

which were evaluated by optical diffraction only. In order to create a physical picture of the transformation process, McCartney and Smith invoked an intermediate TiO_2-II transition phase for which image simulation matches were reported but not shown. The TiO_2-II structure is a high pressure phase of the Ti-O system which has the orthorhombic

α-PbO_2 structure and space group symmetry of Pbcn D_{2h}^{14} (Simons and Dachelle 1967). Radiation-induced phase transitions in the electron microscope appear to follow a simple symmetry selection rule (Zhang 1989), which will be discussed further in section 6.7. The observation of the TiO_2-II phase is the only observation in the literature which is in violation of this rule.

6.3 - EFFECT OF SAMPLE ORIENTATION IN TiO_2

The effect of sample orientation was also evaluated in TiO_2. In all cases investigated, TiO was the final and only phase observed during electron irradiation at energies between 90 and 300 keV. Damage in the $(\bar{1}10)$ orientation was already presented in Figure 6.4. In comparison, shown in Figure 6.7 and 6.8 are time evolution sequences of the $TiO_2(001)$ and $TiO_2(111)$ orientations respectively. The results indicate that for all orientations except $TiO_2(001)$, propagation of the damaged layer from the profile surface inward is rapid and extensive. Resulting erosion profiles were highly anisotropic as shown in Figure 6.9(a-b) for the TiO_2 $(\bar{1}20)$ orientation, irradiated at 300 keV. The (001) orientation was alternatively more susceptible to the formation of holes, and damage was kept more localized at the profile surface in comparison.

The major structural difference between the (001) orientation and higher index orientations is that the (001) orientation offers the most open crystallographic channels between atomic columns. Regardless of the defect production mechanism, damage in TiO_2 is likely to progress along the open channels as well as along the oxygen layers because the rutile structure is not set up favorably for replacement collision sequences due to the lack of suitable focusing rows.

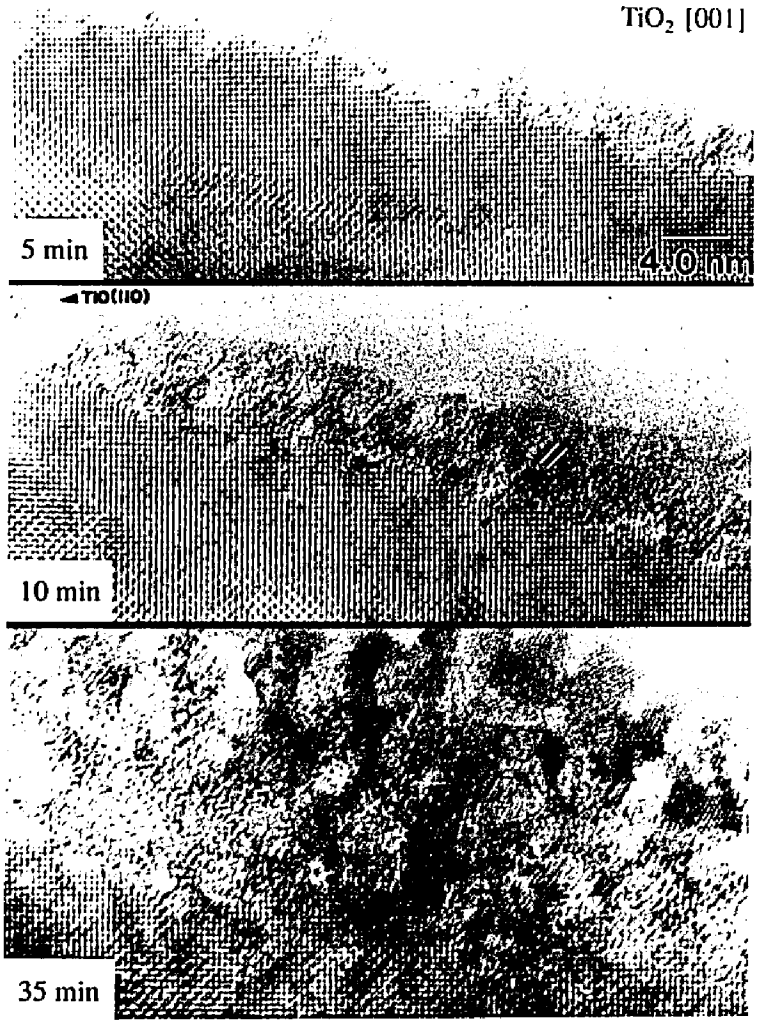

FIGURE 6.7 TiO_2 (001) under low flux irradiation at 300 keV; a) initial surface; b) after 10 minutes; c) after 35 minutes.

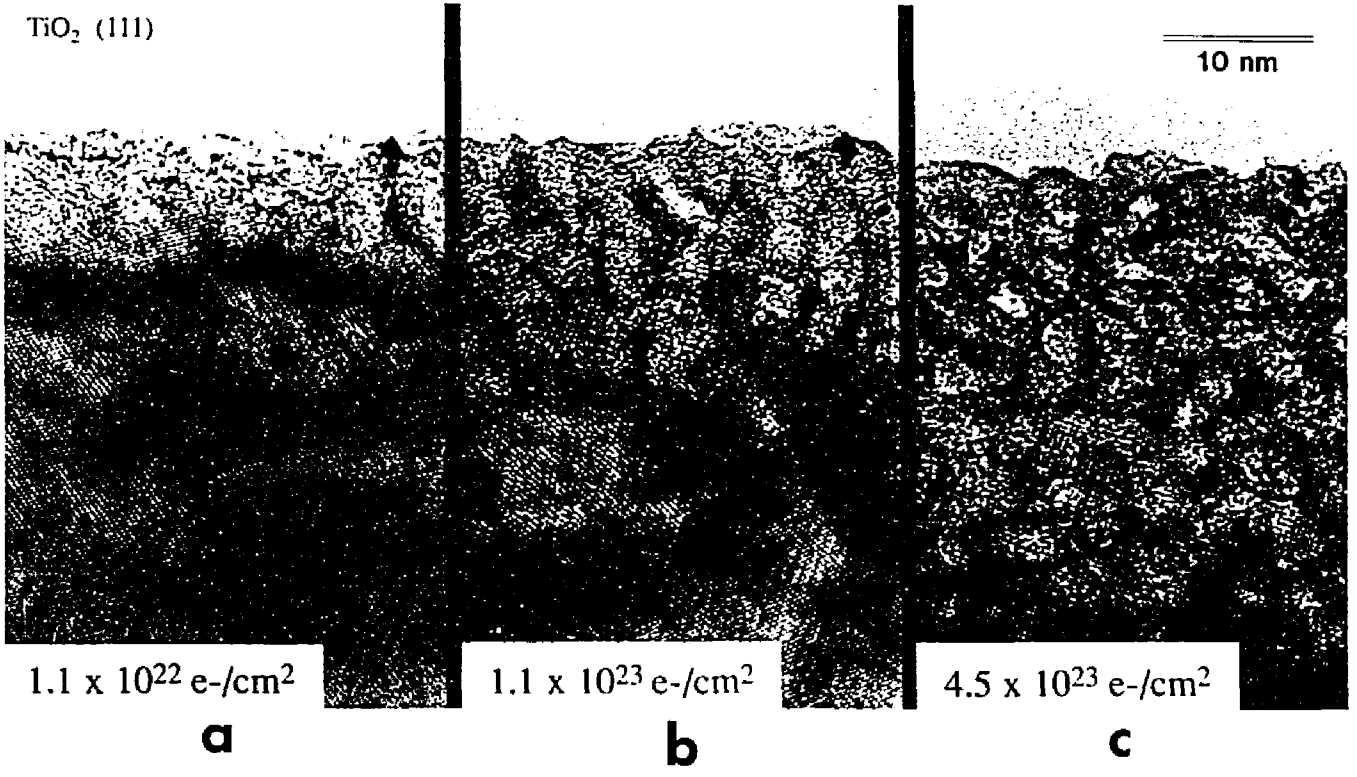

FIGURE 6.8 TiO_2 (111) under low flux irradiation at 300 keV; a) initial surface; b) after 10 minutes; c) after 35 minutes.

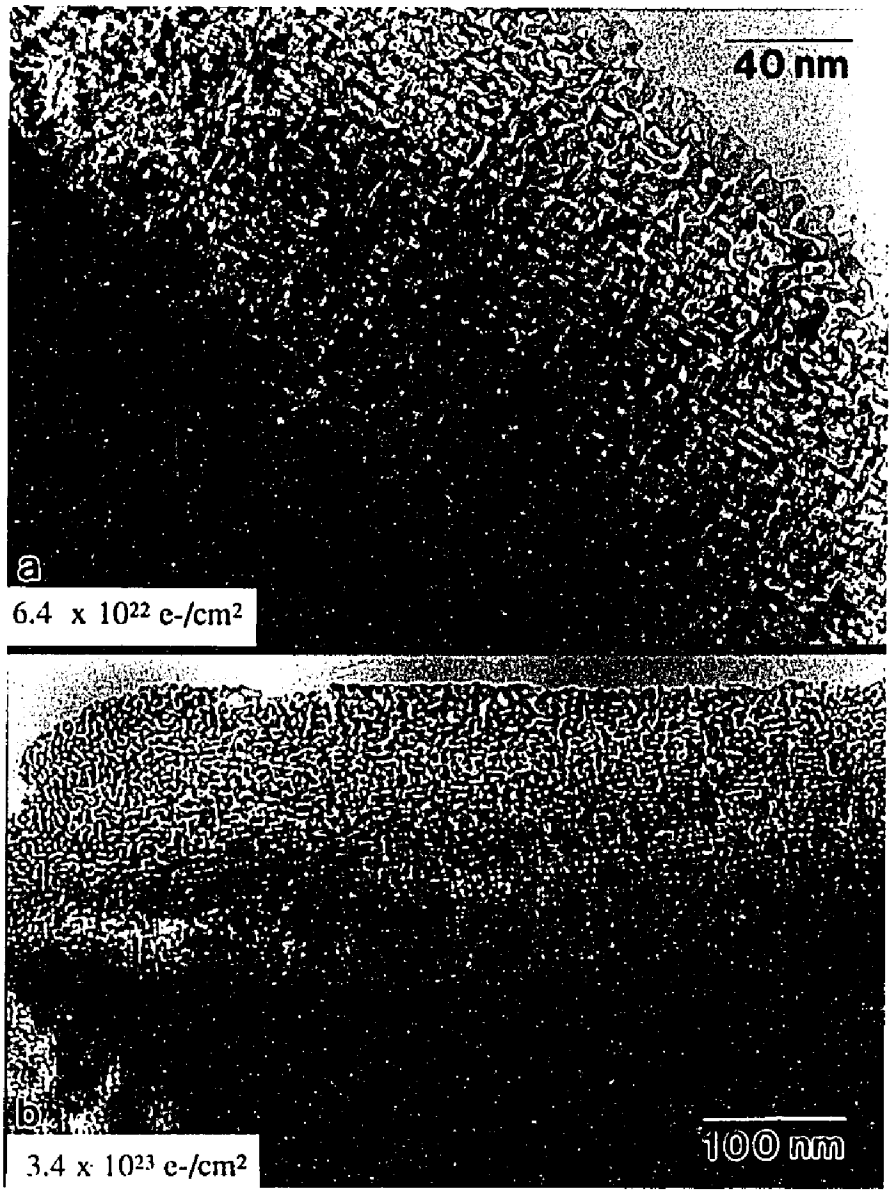

FIGURE 6.9 TiO_2 ($\bar{1}20$) after extended irradiation at 300 keV; a) high magnification; b) low magnification.

The uniqueness of damage in the (001) orientation can be therefore explained as a consequence of where the open channels are in the crystal structure relative to the beam. Shown in Figures 6.10 and 6.11 are "ball and stick" two and three dimensional comparisons of various crystal orientations. The (001) orientation can be seen to offer the most open channels and is also isotropic relative to the beam direction. Defects created by the irradiation can more effectively be routed down and out the exit surface. In contrast, the higher index orientations become increasingly anisotropic relative to the beam direction as well as being more closely-packed. If it can be assumed that damage is being propagated into the bulk by migrating defects on the oxygen sublattice with a strong influence from open migration channels, then the progression of the damaged layer will be anisotropic and the higher index orientations should show this effect more readily than the (001) orientation. From the experimental observations, it appears that this is the case. Structural damage in the (001) remains localized near the profile surface; whereas in the higher index and lower symmetry orientations, it propagates rapidly and extensively into the bulk.

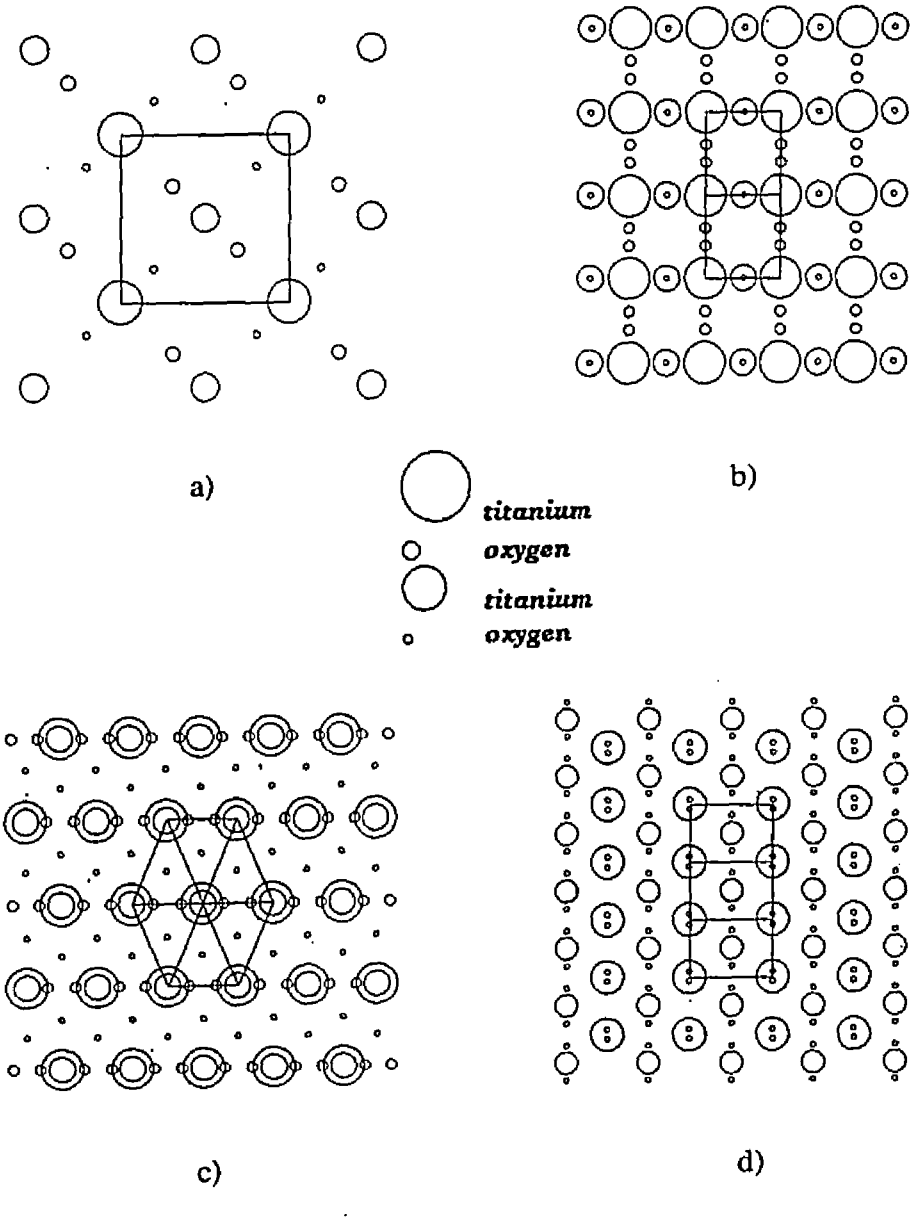

FIGURE 6.10 2-D schematic diagrams looking down various TiO_2 orientations.
a) (001) b) $(\bar{1}10)$ c) (111) d) $(\bar{1}20)$

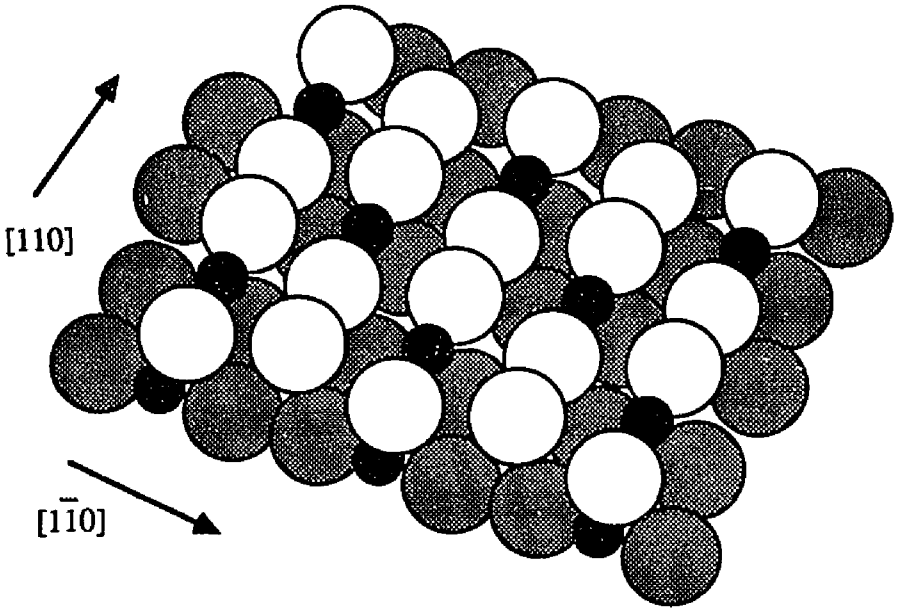

FIGURE 6.11 a) 3-D schematic diagram looking down the TiO_2 (001) orientation (after Henrich 1985). Ti atoms are black.

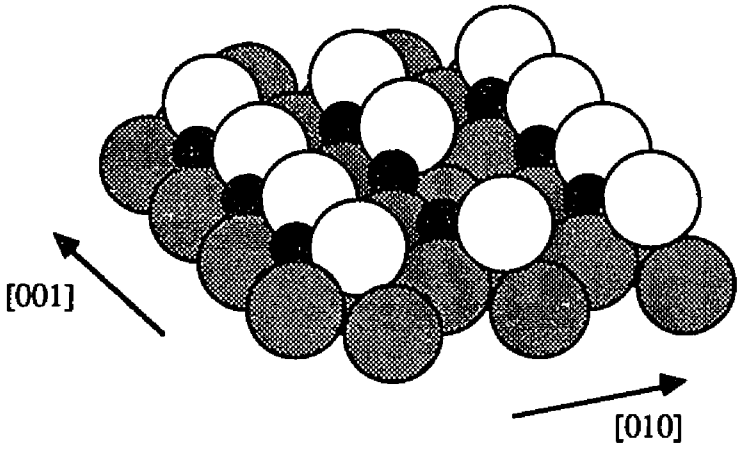

FIGURE 6.11 b) 3-D schematic diagram looking down the TiO_2 (100) orientation.

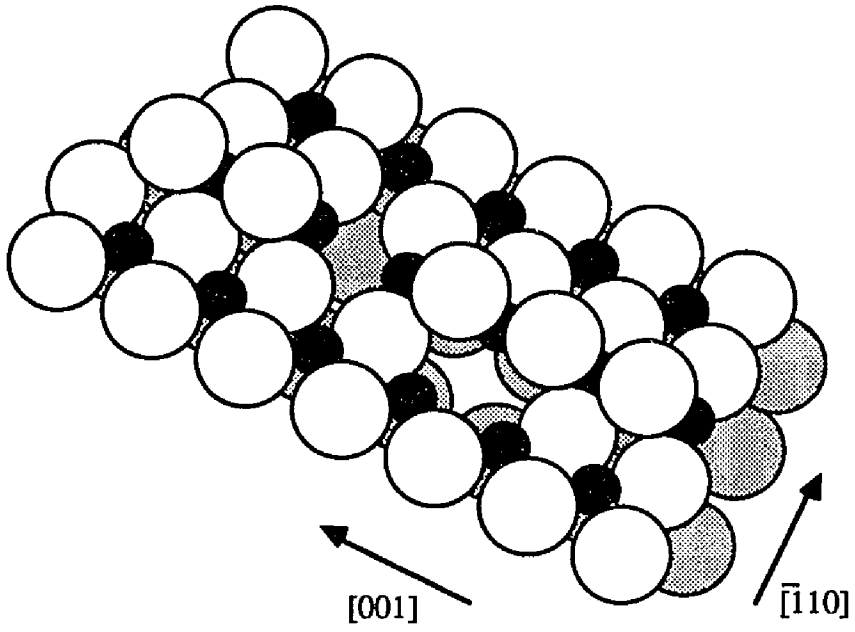

FIGURE 6.11 c) 3-D schematic diagram looking down the TiO_2 ($\bar{1}10$) orientation.

During the initial stages of irradiation, the formation of superlattices was commonly observed. As illustrated by the areas identified with arrows in the image and diffraction pattern of Figure 6.12 for the TiO_2 (111) orientation, three distinct superlattice reflections can be identified: (1) a 3 × n superlattice along the (01$\bar{1}$) type profile planes; (2) a 5 × n superlattice along the same (01$\bar{1}$) type profile planes; and (3) a 2 × n superlattice along the (1$\bar{1}$0) type profile planes. It has been previously determined that the crystallographic shear planes in TiO_2 usually lie parallel to the (111) zone axis (Bursill and Hyde 1972). By consideration of the crystal stacking in this orientation, every other (110) type profile plane is an all-oxygen layer. Selective stripping of oxygen in these layers would result in the observed 2 × n superstructure.

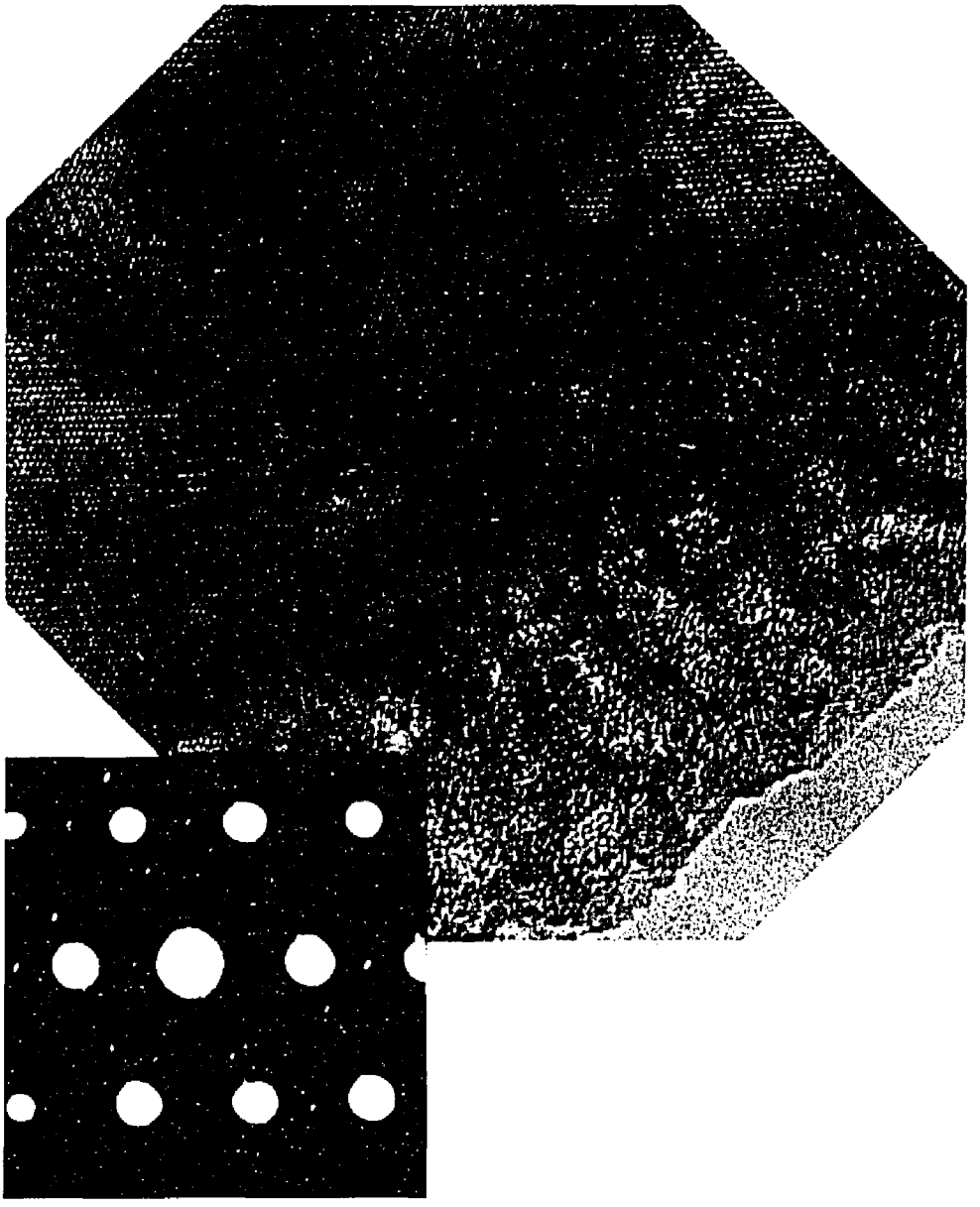

FIGURE 6.12 TiO_2 (111) image and diffraction pattern illustrating the formation of superstructures.

Stacking parallel to the (101) and (011) type layers is somewhat more difficult to visualize, however there exist two oxygen layers sandwiched between each titanium layer. Selective oxygen loss in this case may result in a number of superstructures with the general form of m × (the (101) spacing), where m is a constant. This is what is observed experimentally. In addition, the ordering of oxygen vacancies is well known to occur in TiO_2, and which leads to the formation of extended defects (Cormack et al. 1982) and gives rise to the Ti_nO_{2n-1} Magneli phases (Bursill and Hyde 1972).

6.4 - DAMAGE RATES IN TiO_2

The effect of the incident electron flux on damage rate was also evaluated in TiO_2. The extent of the damaged layer at various incident electron fluxes was measured on a cleaved, uniformly thick TiO_2 particle. Survey of the initial structure and appearance of extinction contours showed it to be fairly uniform in thickness. Sample geometry and measurement parameters were such that the beam was centered at the profile edge, and damage volume could be measured as cylinders with radius (x) parallel to the beam. Three flux conditions were evaluated: 1.2×10^{19} e-/cm^{2}s (2 A/cm^2), 2.5×10^{19} e-/cm^{2}s (4 A/cm^2), and 6.2×10^{19} e-/cm^{2}s (10 A/cm^2).

If the radiation damage kinetics are indeed due to a defect migration mechanism, what can be expected from these experiments is an insight to whether the process is diffusion-controlled or interface controlled (Christian 1965; Hayes and Stoneham 1985). Consider, for example, the case where a steady state is established at the solid/vacuum interface and that the radiation-induced defect concentration is maintained at C_o. As this value will be larger than the concentration in the bulk, C_b, a mean concentration gradient of magnitude $\Delta C/x$ is established, with $\Delta C = C_o - C_b$. According to Fick's law, the

thickness of the damaged layer should therefore increase at a rate of:

$$\frac{dx}{dt} = \frac{\Omega D \Delta C}{x} \tag{6.1}$$

where Ω is the unit transformed volume. Relation 6.1 can be thought of as a diffusion flux. Integration of this relation starting from zero thickness (r=0), yields the familiar parabolic rate law:

$$x(t) = \sqrt{2\Omega D \Delta C}\ (t)^{1/2} \tag{6.2}$$

If, however, the other extreme case of interface-control is dominant, the damage rate becomes a constant: $dx/dt = B$, and can be expressed as the linear function:

$$x(t) = Bt + (\text{constant}) \tag{6.3}$$

This type of behavior is commonly seen in thin oxide layers where diffusion can be rapid.

Results of the present study are plotted in Figure 6.13. These data indicate that the damage rates clearly start out linear and remain so for low flux irradiations - suggesting interface control, but at higher flux or longer times one observes what may be the onset of diffusion-control. The larger error bars in the 10 A/cm^2 plot could also be attributed to uncertainties in the thickness well into the bulk. The flux dependence of the damage process was also evaluated by plotting the effective damage rate constant (measured as the slope of relation 6.2) against flux as shown in Figure 6.14. It should be noted that these are initial observations and were undertaken more as a proof-of-concept experiment on whether the measurements of this type could be made and not as the final word on radiation damage rates.

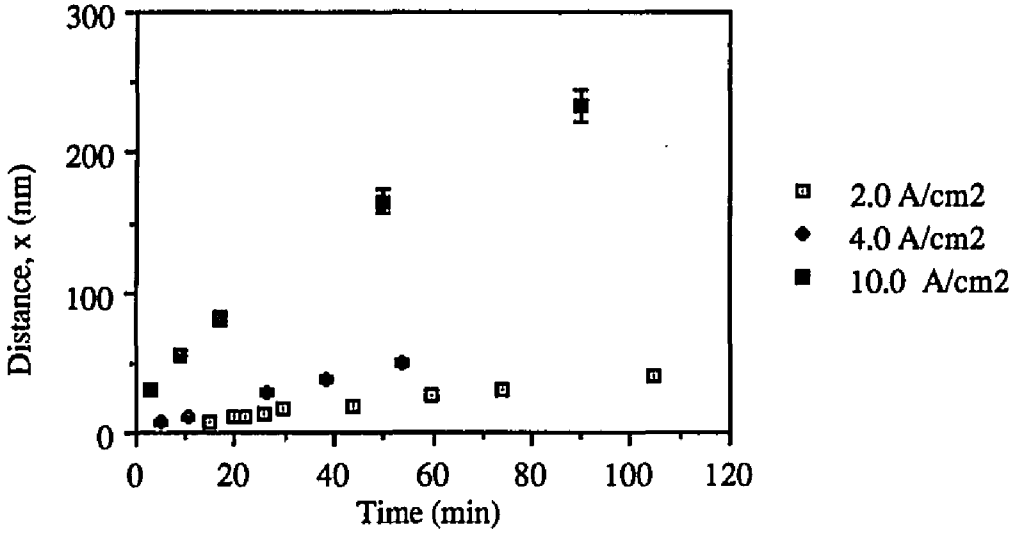

FIGURE 6.13 Plot showing the extent of the damaged layer (x) versus time (t) for varying incident flux.

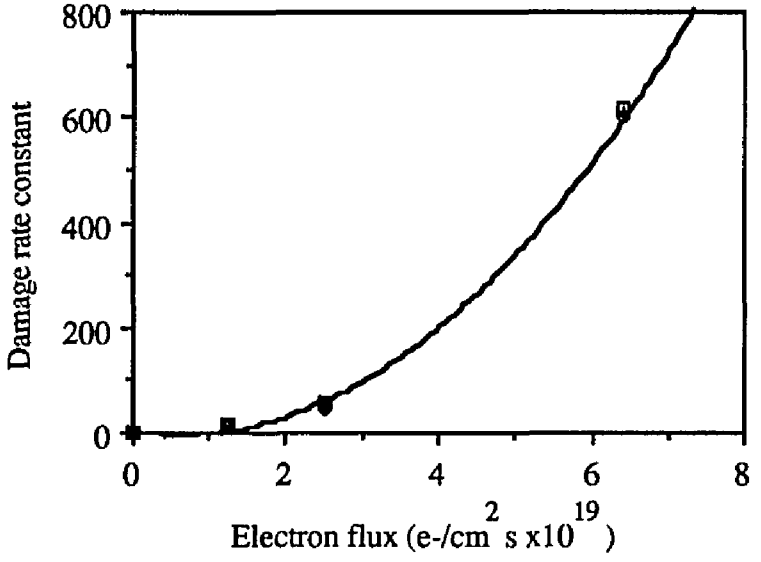

FIGURE 6.14 Graph illustrating the variation of the damage rate constant (in units of distance^2/time) with incident flux (e-/cm^{2}s). Plotted is the slope of Equation 6.2 (using the data in Figure 6.13) versus incident flux.

The rate constant was found to vary nonlinearly with flux, which illustrates that even at these "low" flux values in terms of electron microscopy, one sees a heavy dependence of the damage rate on flux. More precise measurements of this kind would be required to pin down the exact form of the dependence. However, it would be interesting to evaluate the validity of electron microscopy studies for the simulation of radiation damage of nonmetallic solids in high energy reactor environments, where usually only final dose comparisons are made. The question is raised as to whether high flux-short time irradiations are indeed equivalent to low flux-long time irradiations. For example, there exists the possibility that a given damage process could quench under high flux irradiation but not at low flux irradiation. The use of accelerated testing for accurate extrapolation of radiation damage to real systems would then certainly be under question. It would also be interesting to see how the flux dependence changes when significantly higher flux values are used, such as those obtained with field emission filaments, where the contribution of thermal effects can certainly no longer be neglected.

6.5 - LOW ENERGY IRRADIATION BEHAVIOR

In the UHV side transfer chamber, a number of low energy electron irradiation studies were performed. These results are summarized in Table 6.3. As expected, NiO was stable to low energy electron irradiation. TiO_2 was investigated to slightly below 90 keV at incident flux values less than 8 A/cm^2 to minimize thermal effects. This would correspond to a maximum ballistic energy transfer of 4.5 eV to Ti and 13.4 eV to O with a minimal temperature rise (see Chapter 2). Application of the $3\Delta H_a$ criterion predicts a displacement threshold energy of 19.2 eV, which translates to a minimum beam threshold energy of 319 keV for the sputtering of titanium and 124 keV for the sputtering of oxygen

with TiO as the final phase. Predictions of the lattice energy criterion are even higher. In contrast to the sputtering observed in NiO, surface erosion was evident within minutes of start of irradiation, which is not characteristic of ballistic sputtering. In fact, ballistic sputtering thresholds could not be evaluated due to these low energy damage processes even when the incident energy was taken below 90 keV. Similar results were seen in V_2O_5 for which the incident electron energy was taken into the eV range (Ai, et al. 1990), implying a significant contribution to the radiation damage process from electronic effects.

TABLE 6.3

Summary of low energy electron irradiation studies in the UHV-H9000.

Material	Energy	Flux (A/cm^2)	Phase Transformation
V_2O_5*	3 keV	7.0×10^{-4}	V_6O_{13}
V_2O_5*	300 keV	30 - 80	V_4O_9 -> V_6O_{13} ->VO
NiO	3 keV	7.0×10^{-4}	none
NiO	300 keV	10	sputtered NiO, Ni
TiO_2	90 keV	10	TiO
TiO_2	300 keV	10	TiO

All observations made in chamber vacuum of $\leq 2 \times 10^{-10}$ Torr.

* Results courtesy of R. Ai and H. Fan.

For comparison, shown in Tables 6.4 and 6.5 are a compilation of low energy electron and ion irradiation studies of electron irradiation damage of oxides. In both cases compositional changes are seen to occur at the surface. However, the nature of the sputtering and the final phase identification are significantly different. Ion irradiations, as pointed out in Chapter 2, give rise to primarily ballistic and thermal energy transfer through collisional cascades and thermal spikes. In these cases, predictions of the final phase by criteria such as equating the surface binding energy to the heat of sublimation, H_S, or heat of atomization, ΔH_a (as outlined in Chapter 3) have proven to be quite successful.

Low energy electron irradiations give rise to primarily electronic energy transfer with a substantial thermal component only if the flux of incident particles is high (Naguib and Kelly 1970). In materials where electronic damage mechanisms are known to occur, HREM results compare remarkably well with the low energy electron irradiation studies. The slight discrepancies, such as in the final phase identification of VO at high energies and V_6O_{13} at low energies in the V_2O_5 system can be explained by ballistic-assisted or radiation-enhanced diffusion mechanisms operating in conjunction with the creation of electronic defects. In materials where electronic mechanisms are not predicted to occur, the HREM observations for the most part fall into agreement with the ion irradiation ballistic behavior. Measurement of the ballistic sputtering threshold energy in NiO, for example, corresponded remarkably well with the ΔH_a surface binding energy criterion.

TABLE 6.4

Low energy electron bombardment of oxides.

a) Oxides which undergo reduction during low energy electron bombardment:

Initial Phase	Beam Energy	Final Phase	Method of Analysis	Reference
TiO_2	> 30 eV	$\approx Ti_2O_3$	detection of O+	Knotek and Feibelman (1979)
TiO_2	3 keV	>TiO, <TiO_2	AES	Thomas (1976)
TiO_2	160 eV	Ti_4O_7	XPS, EELS	Eriksen and Egdell (1987)
V_2O_5	10-100 eV	V_6O_{13}	AES	Colpaert, et al. (1973)
WO_3	> 30 eV	WO_{3-x}	detection of O+	Nishijima and Propst (1970)
WO_3	3 keV	$\approx$ "WO"	AES	Lin and Lichtman (1979c)
MoO_3	> 30 eV	MoO_{3-x}	detection of O+	Redhead (1964)
MoO_3	3 keV	$\approx$ "MoO_2"	AES	Lin and Lichtman (1978)
Ta_2O_5	3 keV	$\approx$ "TaO"	AES	Lin and Lichtman (1979b)
Nb_2O_5	3 keV	$\approx$ "NbO"	AES	Lin and Lichtman (1979a)
Al_2O_3	3 keV	$\approx$ Al	AES	Smith (1976)

TABLE 6.4 (continued)

b) Oxides reported to be stable to low energy electron bombardment include the final phases above and the following:

Oxide	Reference
NiO	Knotek and Feibelman (1978a)
MgO	Carriere and Lang (1977)
$W_{18}O_{49}$	Naguib and Kelly (1975)
Cr_2O_3	Knotek and Feibelman (1978)
Ti_2O_3	Parker and Kelly (1975)
V_2O_3	Kelly (1977)

TABLE 6.5

Phase changes due to ion bombardment.

Initial Phase	Ion, Energy (keV)	Final Phase	Reference
Al_2O_3	H+, 0.5	Al_2O_{3-x}	Griffiths (1960)
Al_2O_3	He+, 1.0	$Al_2O_{1.3}$	Taglauer and Heiland (1980)
Al_2O_3	Ar+, 1.0	$Al_2O_{1.54}$	Taglauer and Heiland (1980)
Al_2O_3	Ar^+, 0.5	$Al_2O_{<2.6}$	Taglauer and Heiland (1980)
NiO	Ar^+, 0.4	Ni, ~Ni_2O_3	Kim and Winograd (1974)
PbO	He^+, 0.4	Pb	Kim et al. (1976)
PbO	Ne^+, 0.4	Pb	Kim et al. (1976)
PbO	Ar^+, 0.4	Pb	Kim et al. (1976)
TiO_2	Kr^+, 30	Ti_2O_3	Murti and Kelly (1976)
TiO_2	Ar^+, 0.5	≈Ti_2O_3	Henrich et al. (1976)
TiO_2	Ar^+, 0.5	$TiO_{<1.3}$	Henrich et al. (1976)
Ta_2O_5	Kr^+, 35	δ -TaO	Murti et al. (1979)
Ta_2O_5	He^+, 1.0	$TaO_{0.5}$	Taglauer and Heiland (1978)
Ta_2O_5	Ar^+, 0.25	$TaO_{0.43}$	Oechsner et al. (1978)
Ta_2O_5	Ar^+, 0.5	$Ta_2O_{<4.1}$	Mathieu and Landolt (1977)
Ta_2O_5	He^+, 0.25	Ta_2O_{5-x}	McCune et al. (1979)
MoO_3	Kr^+, 2.5-40	MoO_2	Naguib and Kelly (1972)
MoO_3	O_2^+, 40	MoO_2	Naguib and Kelly (1972)
MoO_3	-----,-----	MoO_2	Rogers et al. (1969)
WO_3	Kr+, 35	$W_{18}O_{49}$	Lam and Kelly (1972)
WO_3	Ar+, 0.4	W	Holm and Storp (1977)
V_2O_5	Kr+, 2.5-40	V_2O_3	Naguib and Kelly (1972)
V_2O_5	Kr+, 10	V_2O_3	D.K. Murti et al. (1979)
Nb_2O_5	Kr+, 35	NbO	Murti and Kelly (1976)
CuO	Kr+, 30	Cu_2O, Cu	Parker and Kelly (1975)

6.6 - COMPARISONS OF THE EXTENT OF DAMAGED LAYERS

A qualitative comparison of the radiation damage processes in various maximum valence transition metal oxides was also performed under conventional (10^{-7} Torr) microscopy conditions. These results are presented in Table 6.6. In TiO_2 and V_2O_5, damage was observed to be extensive; whereas in oxides such as ZrO_2 and Nb_2O_5, radiation damage to the surface was either non-existent after extended periods of irradiation (ZrO_2) or the damage process quenched within a given distance (Nb_2O_5). Shown in Figure 6.15, for example, is a ZrO_2 surface which was irradiated under similar conditions to the TiO_2 sample in Figure 6.8(b). At equivalent dose levels of 1.1×10^{23} e-/cm^2, a significant amount of damage has already resulted in the TiO_2 sample while no sign of damage is yet evident in the ZrO_2. Neither the ZrO_2 nor Nb_2O_5 showed extensive damage even after prolonged irradiation. Only slightly altered surface layers were evident which never exceeded a few nanometers from the profile surface. As was mentioned previously, SnO_2 - which is isostructural with TiO_2 - also showed no such characteristic reduction except under high flux conditions using a field emission gun (FEG), where thermal effects are almost certainly affecting the outcome (McCartney and Smith 1989). In contrast, prolonged irradiation of the TiO_2 samples under equivalent experimental conditions eventually resulted in complete disintegration.

TABLE 6.6

A qualitative comparison of the extent to which damaged layers progress into the bulk.

TiO_2, V_2O_5, MoO_3, WO_3.....extensive

Nb_2O_5, ZrO_2 .....quenched

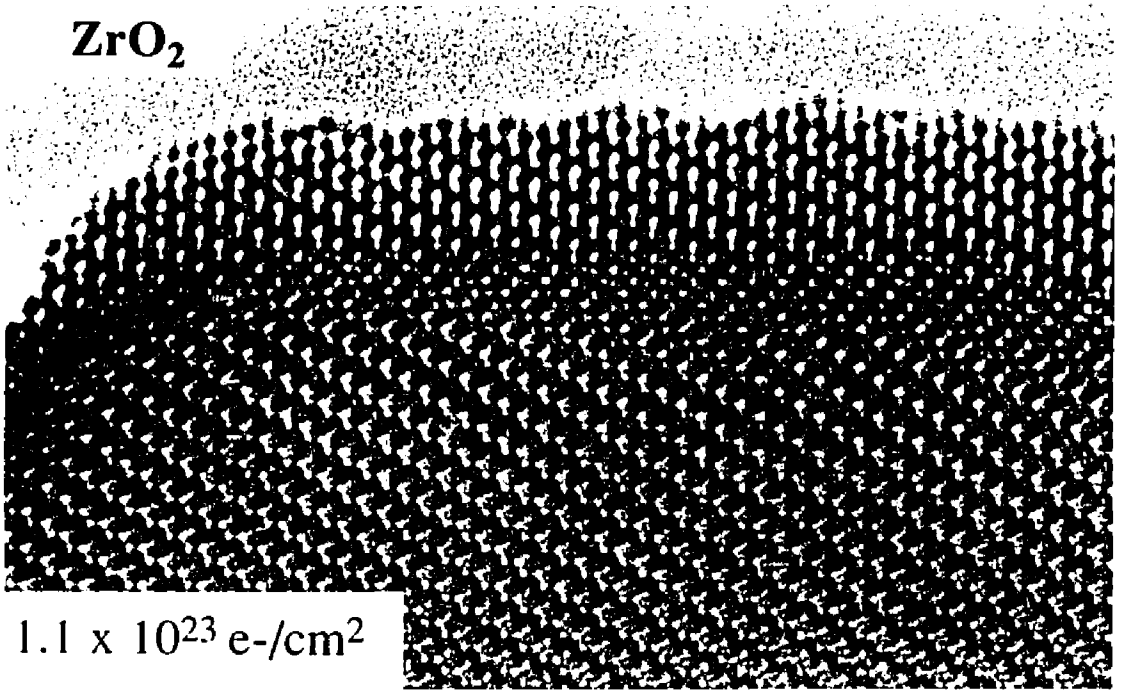

FIGURE 6.15 ZrO_2 surface irradiated at low flux for a total dose of 1.1×10^{23} e-/cm^2.

6.7 DISCUSSION

Table 6.7 shows a comparison of the HREM results to observations made by alternate techniques and predictions based on the ballistic/thermal criteria outlined in Chapter 3. With one exception (SnO_2), each of the maximum valence transition metal oxides investigated under varying incident energy and flux conditions show preferential oxygen loss to either the fully reduced metal oxide phase or the corresponding metal via a preferential loss of oxygen. Anomalous observations under non-UHV conditions could be explained by the effect of the surface environment or by thermal effects if the incident flux was high. Oxides which were predicted to be stable to electronic damage mechanisms behaved exactly as expected. The variations which occurred were slight

deviations in the reduction path, variations in the damage rates depending on orientation, and significant variations in the extent of the damaged layer in the maximum valence transition metal oxides.

TABLE 6.7

A comparison of final phase observations under various irradiation conditions.

Initial Phase	HREM (300 keV)		Low Energy e- (< 3 keV)	Ions (10-40 keV ions)	Sputtering Model Predictions
	10^{-10} Torr	10^{-7} Torr			
WO_3	W	WO	~WO	$W_{18}O_{49}$, W	$W_{18}O_{49}$
MoO_3	Mo	Mo	reduction	MoO_2	MoO_2
Ta_2O_5	Ta	ß -Ta	~"TaO"	∂ -TaO	∂ - TaO
TiO_2	TiO	TiO	reduction, Ti_4O_7	Ti_2O_3	Ti_2O_3
V_2O_5	VO V_6O_{13}	VO	V_6O_{13}	V_2O_3	V_2O_3
Nb_2O_5	---	NbO	reduction, ~NbO	NbO	NbO
NiO	NiO Ni	NiO Ni_3O_4 Ni (carbon)	NiO	NiO (a) ~Ni_2O_3 (b) Ni (c)	NiO, Ni
CoO	CoO	CoO Co_3O_4	CoO	CoO	CoO

(a) 0.4 keV O_2^+, 200 °C; (b) 0.4 keV O_2^+, - 80 °C; (c) 0.4 keV Ar^+

As each of the radiation sensitive samples are maximum valence transition metal oxides, one is inclined to attribute the observations to electronic sputtering due electron-stimulated desorption via the Knotek-Feibelman mechanism. This, however, is only the beginning of the problem. The variation in extent of the damaged layer into the bulk strongly suggests that other processes are making significant contributions to the overall damage process.

These HREM observations can best be explained as a result of a synergistic operation of mechanisms. As was discussed in Chapter 3, ballistic sputtering alone cannot account for the experimental observations as there is a poor correlation with mass of the target particles. In materials where electronic mechanisms are not operative, the observed threshold energies and final phase identification correspond well to estimates of the surface binding energy based on an enthalpy of atomization criterion. In the maximum valence transition metal oxides, the energy dependence of the damage process as well as the final phase identification suggests that defects are created by electronic mechanisms rather than ballistic mechanisms. However, the orientation dependence and the variation in the extent of the damaged layer in samples subject to 100 – 300 keV irradiations suggests that beam-enhanced diffusional mechanisms are assisting in the migration of the defects. The lack of observation of an amorphous intermediary and the final phase identification suggest that the phase transformations to lower oxides occurs by a diffusing defect mechanism, constrained in this case to the oxygen sublattice, without the aid of a significant temperature excursion. TiO_2 diffraction patterns in the various orientations confirm that the phase transformations take place with a minimal distortion to the parent lattice. This type of behavior has also been observed in V_2O_5 (Fan and Marks 1989).

Furthermore, there appears to be a simple symmetry selection rule which can be used to predict the phase transition route, as was determined by Zhang and Marks (1989), and illustrated for representative materials in Table 6.8. In all cases, only those phases with equal or higher space and point group symmetries occurred. If no stable intermediate was allowed under this criteria, then transformation was either direct or via an amorphous intermediate. For example, TiO_2 went directly to the higher symmetry TiO phase and not to Ti_2O_3 as would be predicted by a ballistic or thermal sputtering model described in Chapter 3.

The experimental data and symmetry considerations also rule out the idea which has been circulating the microscopy community (e.g., McCartney and Smith 1989) that quenching of this preferential oxygen loss mechanism should occur when the concentration of defects is such that "metallization" of the outer layer occurs. Shown in Table 6.9 are representative resistivities for a number of oxides. If this were the case, then the process in MoO_3 should have quenched at the MoO_2 composition, WO_3 to WO_2, and so on.

The experimental results on both NiO and TiO_2 support the earlier conclusions that radiation-enhanced diffusion in either the cation or anion sublattice are playing a significant role in the propagation of defects into the bulk. There exists a situation where a large number of point defects are being created at the surface. If there are easy diffusion paths or open crystallographic channels for damage propagation, then damage occurs as rapidly as the defect creation and migration processes allow. The rate limiting step will determine whether the process is interface or diffusion controlled. Crystals with open channels to the beam or efficient RCS focusing rows should damage more readily. This is seen in the non-cubic materials TiO_2, MoO_3, WO_3, and to a lesser extent, Nb_2O_5, as

opposed to cubic structures such as NiO (NaCl structure) and ZrO_2 (CaF_2 structure).

TABLE 6.8

Predictions of the observed final phase based on a symmetry criterion. (Point group symmetries are given in parentheses)

Initial Phase	Secondary Phases Possible	Impossible Phases	
CoO	Co_3O_4		
($Fm3m$, O_h)	($Fd3m$, O_h)		
CuO	Cu_2O		
($C2/c$, C_{2h})	($Pn3m$, O_h)		
NiO	Ni_3O_4 [(a)]	$Ni_{15}O_{16}$	($I4_1/amd$, D_{4h})
($Fm3m$, O_h)	($Fd3m$, O_h)		
MoO_3		MoO_2	($P2_1/c$, C_{2h})
$Pbnm$, D_{2h}		$MoO_{2.8}$	($P2_12_12$, D_2)
		Mo_4O_{11}	($P2_1/a$, C_{2h})
		Mo_9O_{26}	($P1$, C_i)
		Mo_8O_{23}	($P2/a$, C_{2h})
TiO_2	TiO	Ti_2O_3	($R3c$, D_{3d})
(P_{42}/mnm, D_{4h})	($Fm3m$, O_h)	Ti_3O_5	($C2/m$, C_{2h})
		Ti_5O_9	($P1$, C_1)
		Ti_2O	($P3m1$, D_{3d})
		Ti_3O	($P31c$, D_{3d})
		Ti_6O	($P31c$, C_{3v})
V_2O_5	VO	VO_2	($P2_1/a$, C_{2h})
($Pmmn$, D_{2h})	($Fm3m$,O_h)	V_2O_3	($R3c$, D_{3d})
	$V_2O_{0.532}$	$V_{12}O_{26}$	($C2/m$, C_{2h})
WO_3		WO_2	($P2_1/c$, C_{2h})
($P2_1/a$, C_{2h})		$W_{18}O_{49}$	($P2/m$, C_{2h})
		$W_{20}O_{58}$	($P2/m$, C_{2h})
		$WO_{2.96}$	($P2/c$, C_{2h})
		$WO_{2.98}$	($P2_1/c$, C_{2h})

(a) The spinal structure reported earlier as γ-$Ni_{28}O_{32}$ by electron diffraction is believed to be Ni_3O_4 as identified by HREM.

TABLE 6.9

A categorization of oxides based on room temperature resistivities (in Ωcm).

Insulators		Intermediate		Metallic	
MnO	~10^{15}	Mn_3O_4	~10^{7}	MnO_2	~1.1×10^{-1}
NiO	10^{13}	Nb_2O_5	10^{-4} (at 1000 K)	NbO	10^{-5}
CoO	10^{7}-10^{11}	Co_3O_4	10^{3}-10^{4}	VO	10^{-3}-10^{-4}
MoO_3	~10^{10} (at 450 K)			MoO_2	~8.8×10^{-5}
		WO_3	10^{3} (at 200 K)	WO_2	2.9×10^{-3}
			5 (at 400 K)	ReO_3	~10^{-5}
		Ta_2O_5	~10^{5} (at 1000 K)		

A correlation was also noted between the extent of the damaged layer and ionic size, which again illustrates the requirement of open channels for defect migration. Radiation damage was more extensive in oxides of non-cubic structure with cation/anion ratios less than 0.5. Coordination numbers, however, appeared to have no significant effect on an oxides stability toward radiation damage. This data is shown in Table 6.10.

With thin samples such as those used in TEM, the added consideration of possible channels along open directions and ballistic momentum transfer in the forward directions, such as TiO_2 (001) will aid the defect migration process. The rapid formation of holes in the TiO_2 (001) sample is evidence of this type of scenario. If no such optimally oriented channels exist, the defects accumulate in the near surface region until the parent structure can hold them no longer and phase transformation occurs. RCS focusing rows are increasingly more unlikely with lowering crystal symmetry due to the lack of suitable close-packed focusing rows. It should also be noted that a strong correlation is evident in the stability toward electron irradiation and degree of nonstoichiometry a crystal can accommodate (see Table 3.1).

TABLE 6.10

Ionic ratios for a number of oxides.

Material	Structure	r+/r- (Pauling, Goldschmidt)
MnO_2	Rutile	0.39
TiO_2	Rutile	0.48
MoO_2	Rutile	0.52
PbO_2	Rutile	0.64
TeO_2	Rutile	0.67
HfO_2	Fluorite	0.62
ZrO_2	Fluorite	0.66
UO_2	Fluorite	0.80
ThO_2	Fluorite	0.84
NiO	Rocksalt	0.49, 0.52
CoO	Rocksalt	0.53, 0.545
MnO	Rocksalt	0.48, 0.61
FeO	Rocksalt	0.55, 0.56
NbO	Rocksalt	0.5
VO	Rocksalt	0.56, 0.67
MgO	Rocksalt	0.51, 0.5
CaO	Rocksalt	0.71, 0.75
V_2O_5	Orthorhombic	0.45
Nb_2O_5	Monoclinic	0.52
Ta_2O_5	Tetragonal	0.52
WO_3	Monoclinic	0.47
MoO_3	Orthorhombic	0.47
Al_2O_3	Corundum	0.36

References: Burns (1985), Shannon (1976), Samsonov (1982)

In summary, the key to the radiation damage processes in oxides has been determined to be electron-stimulated defect creation at the surface. If this does not occur,

oxide crystals appear to be stable to electron irradiation, except for the slow ballistic sputtering which occurs at energies above the displacement threshold energy. If it does occur, then consideration of the open channels and available mechanisms for migration is required. It should be noted that the energy needed for migration is significantly smaller than that required for defect formation so that even energy transfer mechanisms not sufficiently energetic or localized to form defects may aid in their mobility. In the electron microscope operating at 300 keV, ballistic damage mechanisms are inefficient due to energy transfer considerations, and consequently are generally confined to the extreme outer surface. Only after prolonged periods of irradiation and doses exceeding 10^{24} e–/cm^2 (as was shown for NiO) do they become evident.

Once a defect is created, however, a number of radiation-enhanced migration mechanisms exist to accelerate the damage rate. Unlike metals, there is no regularity of migration processes for nonmetals in terms of activation energies and migration temperature. In fact, it is known that in some systems there exist strong charge state effects for vacancy migration as well as athermal migration mechanisms for certain defects as is outlined by Bourgoin and Corbett (1975).

Migration energies are sufficiently low that any number of mechanisms may contribute to the damage process once a defect is created. These radiation-enhanced diffusion mechanisms fall into categories ranging from ballistic-enhanced, field-enhanced, ionization-enhanced, and energy-release enhanced (where release of the stored energy in an electronic defect is released in the form of phonons to enhance diffusion) processes (Corbett and Bourgoin 1972; Corbett 1979). Thermal migration processes may also contribute to the damage process at sufficiently high flux irradiations.

CHAPTER 7
CONCLUSIONS AND SUGGESTIONS FOR FUTURE WORK

The theory of radiation damage in oxides, the mechanisms by which defects are formed, and experimental results illustrating electron beam-induced structural changes in a number of transition metal oxides have been presented. It has been shown that in-situ HREM observations can give an insight to what happens as a consequence to the initial events occurring the surface - the identification of structure, composition, atomic registry, and the extent and rate at which the radiation damage effects extend into the bulk.

Bombardment of a number of transition metal oxides with electrons at sub-threshold energies under UHV conditions resulted in the preferential loss of oxygen at the surface and subsequent reduction of the near-surface region to either the fully reduced metal oxide phase or corresponding metal. This did not occur in all transition metal oxides, only those with with the cation in its maximum valence state - TiO_2, V_2O_5, MoO_3, Nb_2O_5, and WO_3 - strongly suggesting an electron-stimulated defect production mechanism is operative in these systems. Propagation of surface-initiated defects into the bulk required a diffusional process as evidenced by the orientation and crystal structure dependences of the defect rates and observations of the extent to which the damage layers propagated into the bulk.

For the case of oxides, it was found that the conventional ideas for considering radiation damage as outlined in the literature (Hobbs 1979) - such as equating the available energy for ionization damage to the band gap energy - do not hold. Materials exhibiting semiconducting behavior (such as V_2O_5) proved to be quite sensitive toward electron irradiation, while some materials with wide band gaps (such as MgO) appear to be stable toward high energy electron irradiation. The observance of a reduced surface

phase in the maximum valence transition metal oxides did not follow an ionicity criterion or an enthalpy of atomization criterion as presented in Chapter 3. Nor did the observations of radiation damage follow a thermodynamic criterion where the reactivity of an oxide is related to its room temperature standard free energy of formation. A number of previous studies have attempted to categorize oxide stability under one or more of these criteria. It has been suggested, for example, that oxides with $-\Delta G_F^o$ below 60 kcal/mole were generally reduced by particle bombardment while oxides with $-\Delta G_F^o$ above 118 kcal/mole were generally stable (Kim et al. 1974). Free energy data for the oxides used in this and other radiation damage studies are presented in Table 7.1, illustrating the point that direct comparisons between ion irradiation studies and high energy electron irradiation studies are not always valid. These results also show that radiation damage in the electron microscope is limited by kinetics rather than equilibrium thermodynamics.

Damage processes in oxides under electron irradiation did, however, follow a simple symmetry selection rule, exhibited characteristics of radiation-enhanced diffusional processes, and were sensitive to the surface environment. Predictions on the extent to which radiation damage propagated into the bulk could be made based on ionic size and crystal structure arguments of RCS focusing and open crystallographic channels.

It is concluded that the contribution of electronic damage mechanisms are significant at the energies used for electron microscopy. The consequential, synergistic operation of defect migration processes - ballistic or otherwise - contributes to an accelerated damage rate over and above that which would be predicted by any singular mechanism.

TABLE 7.1

A comparison of the room temperature standard free energy of formation to the observation of reduction in oxides during particle bombardment.

a) Materials for which the criterion holds: (according to Kim et al. 1974)

Oxide	$-\Delta G_F^o$ (kcal/mole)	Reduction Observed?
CuO	30.88	yes
PbO	45.0	yes
NiO	52.0	yes
PbO_2	52.3	yes
FeO	58.0	yes
ZnO	76.0	no
MoO_2	120.1	no
SnO_2	124.0	no
Ti_2O_3	346.0	no
Al_2O_3	377.0	no
Ta_2O_5	471.0	no

b) Materials studied by electron microscopy for which the criterion fails:

Oxide	$-\Delta G_F^o$ (kcal/mole)	Reduction Observed?
ReO_3	128.1	yes
WO_3	182.6	yes
TiO_2	212.6	yes
Al_2O_3	377.0	yes
V_2O_5	341.5	yes
Nb_2O_5	423.3	yes
Ta_2O_5	456.7	yes

a) Materials for which the criterion fails: (according to Kim et al. 1974)

Oxide	$-\Delta G_F^o$ (kcal/mole)	Reduction Observed?
MoO_3	162.0	yes
WO_3	182	yes

b) Materials studied by electron microscopy for which the criterion holds:

Oxide	$-\Delta G_F^o$ (kcal/mole)	Reduction Observed?
NiO	52.0	yes
MgO	136.21	no
CeO_2	246.18	no
ZrO_2	247.85	(?)

It is also concluded that the surface environment plays a significant role in the interpretation of surface radiation damage processes. Consideration of the reactive species present on the surface is essential in determining the nature of the operative damage mechanisms. This may be a critical consideration for understanding the survivability of materials in space, where approximately 80% of the atmosphere is comprised of atomic oxygen. To study processes inherent of the surface itself, UHV is a necessity. On the other hand, for such research topics as catalysis, thin films, and microelectronics, as well as certain radiation damage processes, certain controlled surface environments in the electron microscope will provide interesting research.

And finally, high resolution electron microscopy and surface science studies can be used as complementary techniques. What the in-situ HREM observations provide is an insight to what happens as a consequence to the initial events occurring at the surface.

The results presented in this study are only the initial observations of the UHV-H9000 surface analytical microscope. Our group is continually in the process of developing methods to better quantify the HREM results and bring the in-situ surface analytical instrumentation on-line. Further studies on oxides of the effect of incident flux are needed not only to sort out the radiation damage question but for further insight to processes such as hole drilling in titanium oxides and alumina (Berger et al. 1987), which may be significant for the application of electron beam lithography. Further studies on the technologically important M_2O_3 structures are also needed. Preliminary studies on the Al_2O_3 system (Bonevich 1991) showing reduction to metallic Al have already proven interesting. In addition, initial observations of multiple component oxides (the high T_c superconductors and optical materials such as $LiNbO_3$) show that these materials may be well-suited for the investigation of processes such as surface segregation. Preliminary

results also indicate that the UHV side transfer chamber may be well-suited for the production of metal-metal oxide interfaces by a combination of sputtering and annealing under controlled atmospheric conditions to minimize impurity levels.

The role of impurities is also a crucial consideration which has not been investigated in depth by this study. It may be argued that electron-stimulated defect processes may well be impurity-controlled. An interesting test would be to investigate artificially doped materials to evaluate the effect of impurities or to control the dominant type of point defect being created.

As always for the electron microscopist, sample preparation techniques need to be continually improved for these materials. Further development and testing is needed for the Multislice algorithm to reliably simulate complex noncubic crystal systems. And finally, as HREM imaging is becoming used more frequently for the study of dynamic localized phenomena at surfaces and internal interfaces, the continuing development of techniques to recover information from a real image should be pursued.

REFERENCES

Ai, R., H.J. Fan, P.C. Stair, and L. D. Marks, "In-Situ Study of Radiation Damage in V_2O_5 Induced by Low Energy electrons." *Materials Research Society Symposium Proceedings - Fall 1989* 157 (1990): 599-604.

Anderson, A. B., R.W. Grimes, and A. H. Heuer, "A Predictive Molecular Orbital Theory Applied to Defects and Structures of Transition Metal Oxides." *Transport in Nonstoichiometric Compounds* NATO-ASI Series B 129 (1985): 527-537.

Anderson, P. W., "Models for Electronic Structure of Amorphous Semiconductors" *Phys. Rev. Lett.* 34 (1975): 953-954.

Antoniewicz, P. R., "Model for Electron- and Photon-Stimulated Desorption." *Phys. Rev. B* 21.9 (1980): 3811-3815.

Avery, N.R., "LEED Auger Study of Oxide Formation at 650-1100 K." *Surface Science* 41 (1974): 533.

Avery, N.R., "LEED Study of Oxide Formation at 1000 K." *Surface Science* 33 (1972): 107.

Avouris, P., and R. E. Walkup, "Fundamental Mechanisms of Desorption and Fragmentation Induced by Electronic Transitions at Surfaces." *Annu. Rev. Phys. Chem.* 40 (1989): 173-206.

Banks, B., M.J. Mirtich, S. K. Rutledge, D. M. Swec, and H. K. Nahra, "Ion Beam Sputter-Deposited Thin Film Coating for Protection of Spacecraft Polymers in Low Earth Orbit." *NASA TM 87051*. AIAA 23rd Aerospace Sciences Meeting at Reno, Nevada. January 14-17, 1985.

Bauer, W., and A. Sosin, "Evaluation and Interpretation of Threshold Displacement Energy Measurements." *J. Appl. Phys.* 37 (1966): 1780.

Berger, S. D., I. G., Salisbury, R. H. Milne, D. Imeson, J. C. Humphreys, "Electron Energy-Loss Spectroscopy Studies of Nanometer Structures in Alumina Produced by Intense Electron Irradiation" *Phil. Mag. B* 55.3 (1987a): 341-358.

Berger, S. D., Macaulay, M. and L. M. Brown, "Radiation damage in TiO_x at high current density." *Phil. Mag. Letters* 56.5 (1987b): 179-185.

Bethe, H.A., *Handbuch der Physik* 24 ed: H. Geiger and K. Scheel. Berlin: Springer Verlag (1933): 273.

Bloch, F., "Bremsvermogen von Atomen mit Mehreren Elektronen."*Z. Phys.* 81 (1933): 363.

Bonevich, J., and L. D. Marks, "The development of ultra-high vacuum high resolution electron microscopy". *Hitachi Instrument News* 17 (1989):4-17.

Bonevich, J., *unpublished research* (1991).

Bourgoin, J. C., and J. W. Corbett, "A New Mechanism for Interstitial Migration." *Phys. Letters A* 38 (1972): 135-137.

Bourgoin, J. C., and J. W. Corbett, "Enhanced Diffusion Mechanisms." *Radiation Effects* 36 (1978): 157-188.

Bourret, A., "Irradiation Damage in Nickel and Iron in a High-Voltage Electron Microscope and Threshold Energy Determination."*Phys. Stat. Sol.* 4 (1971): 813-825.

Bradley, C. R., "Calculations of Atomic Sputtering and Displacement Cross-Sections in Solid Elements by Electrons with Energies From Threshold to 1.5 MV." *Argonne National Laboratory ANL 88-48* December 1988.

Brennan, D., D. O. Hayward and B.M.W. Trapnell, "The Calorimetric Determination of the Heats of Adsorption of Oxygen on Evaporated Metal Films." *Proc. Roy. Soc. (London)* A256 (1960): 81.

Breunig, W., "The Role of the Excited State in DIET Electronic Structure and Evolution in Time." *DIET I Desorption Induced by Electron Transitions.* ed: N.H. Tolk, M. M. Traum, J. C. Tully, T. E. Madey. Berlin: Springer Verlag (1983): 90-101.

Buckett, M. I., L. D. Marks and D. E. Luzzi, "Correlation Analysis of Structure Images." *Proceedings of the 45th Annual Meeting of the Electron Microscopy of America* (1987): 752-753.

Buckett, M. I., J.W. Strane, D.E. Luzzi, J.P. Zhang, B.W. Wessels and L. D. Marks, "Electron Irradiation Damage in Oxides." *Ultramicroscopy* 29 (1989): 217-227.

Buckett, M. I. and L. D. Marks, "Formation of a Ni_3O_4 Spinel Phase on the Surface of NiO During Electron Irradiation." *Materials Research Society Symposium Proceedings - Fall 1988* 129 (1989): 521-526.

Buckett, M. I., S. R. Singh, H. Fan, T. Wagner and L. D. Marks, "Electron-Stimulated Damage Processes in Oxides Under Ultra-High Vacuum Conditions." *Proceedings of the 47th Annual Meeting of the Electron Microscopy of America* (1989): 636-637.

Buckett, M. I., and L. D. Marks, "Electron Radiation Damage in NiO." *Surface Science* 232 (1990): 353-366.

Burns, G., *Solid State Physics*. Orlando, FL: Academic Press (1985).

Bursill, L.A., and B.G. Hyde, "Crystallographic Shear in the Higher Titanium Oxides: Structure, Texture, Mechanisms and Thermodynamics." *Prog. Solid State Chem.* 7 (1972): 177.

Bursill, L. A., M. G. Blanchin, A. Mebarek, and D. J. Smith "Point, Linear and Extended Defect Structures in Nonstoichiometric Rutile."*Radiation Effects* 74 (1983): 253-265.

Catlow, C.R.A. and A.M. Stoneham, "Defect Equilibria in Transition Metal Oxides." *J. Am Ceram.Soc.* 64.4 (1981): 234-236.

Carriere, B. and B. Lang, "A Study of the Charging and Dissociation of SiO_2 Surfaces by Auger Electron Spectroscopy." *Surface Science* 64 (1977): 209-223.

Chen, Y., and W. A. Sibley, "Study of Ionization -Induced Radiation Damage in MgO." *Phys. Rev.* 154 (1967): 842.

Cherns, D., "Direct Resolution of Surface Atomic Steps by Transmission Electron Microscopy." *Phil. Mag.* 30 (1974): 549-556.

Cherns, D., "High-Resolution Transmission Electron Microscopy of Surface and Interfaces." *Treatise on Materials Science and Technology* 27 (1988): 297-335.

Christian, J. W., *The Theory of Transformation in Metals and Alloys* Oxford: Pergamon Press (1965).

Chuang, T. J., C. R. Brundle and D. W. Rice, "Interpretation of the X-Ray Photoemission Spectra of Cobalt Oxides and Cobalt Oxide Surfaces." *Surface Science* 59 (1976): 413-429.

Chuang, T. J., C.R. Brundle and K. Wandelt, "An X-Ray Photoelectron Spectroscopy Study of the Chemical Changes in Oxide and Hydroxide Surfaces Induced by Ar+ Ion Bombardment." *Thin Solid Films* 53 (1978): 19.

Chung, Y. W., W. J. Lo and G. A. Somarjai, "Low Energy Electron Diffraction and electron Spectroscopy Studies on the clean (110) and (100) Titanium Dioxide (Rutile) Crystal Surfaces." *Surface Science* 64 (1977): 588-602.

Clinard, F. W., and L. W. Hobbs, "Radiation Effects in Non-Metals." *Physics of Radiation Effects in Crystals* ed: R. A.Johnson and A. N.Orlov. Amsterdam: Elsevier Science Publishers B.V. (1986): 387-470.

Colpaert, M. N., P. Clauws, L. Fiermann and J. Vennik, "Thermal and Low energy Electron Bombardment Induced Oxygen Loss of V_2O_5 Single Crystals: Transition into V_6O_{13}." *Surface Science* 36 (1973): 513-525.

Corbett, James W., "Electron Radiation Damage in Semiconductors and Metals" *Solid State Physics 7.* ed: F. Seitz and D. Turnbull. New York: Acad. Press (1966) 10-37.

Corbett, J., "Radiation Damage, Defects and Surfaces."*Surface Science* 90 (1979): 205-239.

Corbett, J. and J. C. Bourgoin, "Defect Creation in Semiconductors." *Point Defects in Solids 2.* ed: J. H. Crawford, Jr. and L. M. Slifkin. New York: Plenum Press (1975): 1-161.

Cormack, A. N., C. R. A. Catlow, and P. W. Tasker, "Long-Range Ordering of Extended Defects in Non-Stoichiometric Oxides." *Radiation Effects* 74 (1983): 237-245.

Cormack, A.N., R.M. Jones, P.W. Tasker and C.R.A. Catlow, "Extended Defect Formation in Oxides with the ReO_3 Structure, I." *J. Sol. State Chem.* 44 (1982): 174-185.

Cormack, A.N., G. V. Lewis, S. C. Parker, and C. R. A. Catlow, "On the Cation Distribution of Spinels." *J. Phys. Chem. Solids* 49.1 (1988): 53-57.

Cotton, F. A., and G.Wilkinson, *Advanced Inorganic Chemistry* New York: Interscience Publishers (1972).

Couput, J. P., R. L. Lalauze and J. H. Meunier, "Study on O_2-NiO Interaction by Electric Conductivity and Thermal Flux." *Transport in Non-Stoichiometric Compounds - Materials Science Monographs 15.* New York: Elsevier Scientific Publishing Co., Inc. (1982): 38-50.

Cowley, J. M. and A. F. Moody, "The Scattering of Electrons by Atoms and Crystals. I. A New Theoretical Approach." *Acta. Cryst.*10 (1957): 609-619.

Crawford Jr., J. H. and L. M. Slifkin, *Point Defects in Solids 1* New York: Plenum Press (1972).

Darwin, C.G., "On some orbits of an electron." *Phil. Mag.* 25 (1913): 201.

Davis, R. F., "Point (Atomic) Defects in Stoichiometric Ceramic Materials Part Two: Schottky and Frenkel Defects" *Journal of Educational Modules for Materials Science and Engineering* 3.1 (1981): 843-859.

Dexter, D. L., "Varley Mechanism for Defect Formation in Alkali Halides."*Phys. Rev.* 118 (1960): 934-935.

Dieckmann, R., "Cobaltous Oxide Point Defect Structure and Non-Stoichiometry, Electrical Conductivity, and Cobalt Tracer Diffusion." *Zeit. fur Physik. Chemie Neue Folge* 107 (1977): 189-210.

Dienes, G. J.,*Studies in Radiation Effects in Solids 3.* New York: Gordon and Breach Science Publishers (1969).

Dienes, G.J., D. O. Welch, C.R. Fischer, R. D. Hatcher, O. Lazareth and M. Samberg, "Shell-Model Calculations of Some Point Defect Properties in α-Al_2O_3." *Phys. Rev. B* 11 (1975): 3060.

Dienes, G. J. and R. Smoluchowski, "Dynamics of Replacement Sequences and Crowdions."*J. Phys. Chem. Solids 37* (1976): 95-98.

DIET II "Desorption Induced by Electronic Transitions" *Proceedings of the Second International Workshop* ed: W. Brenig, D. Menzel. Berlin: Springer-Verlag (1984).

Drinkwine, M.J. and D. Lichtman, "Electron Stimulated Desorption: A Critical Review". *Progress in Surface Science* 8 (1977): 123-142.

Egerton, R. F., *Electron energy-loss spectroscopy in electron microscopy.* New York: Plenum Press (1986).

Elliott, D.J., and P. D. Townsend, "Defect Formation and Sputtering of Alkali Halides with Low Energy Irradiation" *Phil. Mag.* 23 (1971): 249-257.

Eriksen, S., and R. G. Egdell, "Electronic excitations at oxygen deficient TiO_2 (110) surfaces: A study by EELS" *Surface Science* 180 (1987): 263-278.

Fan, H., and L. D. Marks, "Phase Transitions in V_2O_5 in a High Resolution Electron Microscope."*Ultramicroscopy* 31 (1989): 357-364.

Fano, U., *Ann. Rev Nucl. Sci.* 13 (1963): 1.

Faust, W.E., T. N. O'Neal and R. L. Chaplin "Measurements of Electron Irradiation Damage Rates in Magnesium." *Phys. Rev.* 183 (1969): 609-610.

Feibelman, P. and M. Knotek, "Reinterpretation of electron stimulated desorption data from chemisorption systems" *Phys. Rev. B* 18.12 (1978): 6531-6539.

Feldman, Leonard C., and James W. Mayer, *Fundamentals of Surface and Thin Film Analysis* New York: Elsevier Science Publishing Co. (1986).

Fellas, C. N., and S. Richardson, "Internal Charging of Indium Oxide Coated Mirrors." *IEEE Trans. on Nuclear Science* NS-28.6 (1981): 4523-4528.

Felton, R. C., M. Prutton, S. P. Tear and M. R. Welton-Cook, "A LEED Analysis of the CoO(100) Surface" *Surface Science* 88 (1979): 474-483.

Finster, J., P. Lorenz, F. Fievet and M. Figlarz, "Surface Analysis of Nickel Oxides by X-Ray Photoelectron Spectroscopy." *Matl. Sci. Monographs 10* ed: Krystyna Dyrek, J. Haber, and J. Nowotny. Amsterdam: Elsevier Scientific Publishing Company (1982): 391-396.

Firsov, O.B., *J. Exp. Theor. Phys.32 (USSR)* (1957): 1364 (English translation: *Sov. Phys. JETP* 5 (1957): 1192.

Firsov, O.B., *J. Exp. Theor. Phys. (USSR) 33* (1958a): 696 (English translation: *Sov. Phys. JETP* 6 (1958a): 534.

Firsov, O.B. *J. Exp. Theor. Phys. (USSR)* 34 (1958b): 447 (English translation: *Sov. Phys. JETP* 7 (1958b): 308.

Fisher, S.B., "On the Temperature Rise in Electron Irradiated Foils." *Radiation Effects* 5 (1970): 239-243.

Franchy, R. and D. Menzel, "Adsorbate Core Ionization as Primary Process in Electron- and Photon-Stimulated Desorption from Metal Surface." *Phys. Rev. Lett.* 43.12 (17 Sept. 1979): 865-867.

Frank, J., "The Role of Correlation Techniques in Computer Image Processing". *Computer Processing of Electron Microscope Images.* ed: P.W. Hawkes. 187-201. New York: Springer-Verlag, 1980.

Gaines, E. E., R. W. Nightingale, W. L. Imhof and J. B. Reagan, "Enhanced Radiation Doses to High-Altitude." *IEEE Transactions on Nuclear Science* NS-28.6 (December 1981): 4502-4504.

Gale, B.and K. F. Hale, "Heating of Metallic Foils in an Electron Microscope." *British Journal of Applied Physics* 12 (March 1961): 115-117.

Gehlen, P. C., J. R. Beeler, Jr. and R. I. Jaffee, *Interatomic Potentials and Simulation of Lattice Defects* New York: Plenum (1972).

Gerritson, H. C., M. P. Bruijn, J. Verhoeven and M. J. van der Wiel, "Electron Stimulated Desorption of Oxygen from Nickel" *Surface Science* 139 (1984): 16.

Gittus, J., *Irradiation Effects in Crystalline Solids.* London: Applied Science Publishers, Ltd. (1978).

Goland, Allen N., "Radiation Damage of Nonmetallic Solids" *Radiation Damage in Metals* ed: N.L. Peterson. Metals Park, OH: American Society of Metals (1976).

Good-Zamin, C. J., M. T. Shehata, D. B. Squires and R. Kelly, "On the Problem of Whether Excited States Amongst Sputtered Particles are of Thermal Origin." *Radiation Effects* 35 (1978): 139-149.

Gravelles, P. C. , and S. J. Teichner, *Advan. Catal.* 20 (1969): 168.

Green, B. D., and E. Murad, "The Shuttle Glow as an Indicator of Material Changes in Space." *Planet. Space Sci.* 34.2 (1986): 219-224.

Griffiths, L. B., "Effect of Hydrogen-Ion Bombardment on the Oxides of Aluminum and Magnesium" *Nature* 188 (1960): 43.

Haffner, J. W., R. J. Dempsey, D. E. Anderson and J. G. Kelley, "Environmental Effects on Spacecraft Material" *AFGL-TR-88-0128* Air Force Geophysics Laboratory, Air Force Systems Command, USAF, Hanscom Air Force Base, MA (May 1988).

Hansen, S., and D. J. Smith, "Electron-Beam-Induced Chemical Reactions in $CrVO_4$ and MoO_2 Studied by Surface Profile Imaging." Inst. Phys. Conf. Ser. 90 (1987): 151-154.

Hauffe, K., *Oxidation of Metals*. New York: Plenum Press (1965).

Hayes, W. and A.M. Stoneham, *Defects and Defect Processes in Nonmetallic Solids* New York: John Wiley & Sons (1985).

Heitler, W., *The Quantum Theory of Radiation* Oxford: Clarendon Press (1954): 367-371.

Henrich, V. E., "The Nature of Transition-Metal-Oxide Surfaces." *Progress in Surface Science* 14 (1983): 175-200.

Henrich, V. E., G. Dresselhaus, and H. J. Zeiger, "Observation of Two-Dimensional Phases Associated with Defect States on the Surface of TiO_2." *Phys. Rev. Letters* 36 (1976): 1335-1338.

Hersh, Herbert N., "Proposed Excitonic Mechanism of Color-Center Formation in Alkali Halides" *Phys. Rev.* 148.2 (1966): 928-932.

Hirsh, P. A. Howie, R. B. Nicholson, D.W. Pashley, and M. J. Whelan, *Electron Microscopy of Thin Crystals*. Malabar, FL: Robert E. Krieger Publishing Co. (1977).

Hobbs, L., "Radiation effects in analysis of inorganic specimens by TEM." *Introduction to Analytical Electron Microscopy*. ed: J. J. Hren, J. I. Goldstein and D. C. Joy. New York: Plenum Press (1979): 437-480.

Hobbs, L. W., "Radiation Effects in Analysis by TEM" *Quantitative Electron Microscopy* ed: J. N. Chapman and A. J. Craven. Proceedings of the Twenty-Fifth Scottish Universities Summer School in Physics (1983).

Hobbs, L. W., "Electron-Beam Sensitivity in Inorganic Specimens."*Ultramicroscopy* 23 (1987): 339-344.

Holloway, P. H., and J. B. Hudson, "Kinetics of the Reaction of Oxygen with Clean Nickel Single Crystal Surfaces 1. Ni (100) surface." *Surface Science* 43 (1974): 123-140.

Holm, R. and S. Storp, "ESCA Studies on Changes in Surface Composition Under Ion Bombardment." *Appl. Phys.* 12 (1977): 101.

Hotop, H. and W. C. Lineberger, *J. Phys.Chem. Ref. Data* 4 (1975): 539.

Howitt, D. G., "Radiation Effects Encountered by Inorganic Materials in Analytical Electron Microscopy" *Introduction to Analytical Electron Microscopy.* ed: D. C. Joy, A. D. Romig, Jr., and J. I. Goldstein. New York: Plenum Press (1986).

Huang, Jin and D. N. Seidman, "Molecular Dynamics Study of the Primary State of Radiation Damage in Metal Oxide Crystals." *Proceedings of the AFOSR Workshop*, September 1990, in press.

Inokuti, M., Y. Itikawa and J. E. Turner, "Addenda: Inelastic Collisions of Fast Charged Particles with Atoms and Molecules - the Bethe Theory Revisited." *Rev. Mod. Phys.* 50 (1978): 23.

Iseler, G. W., H.I. Dawson, A. S. Mehner and J. W. Kauffman, "Production Rates of Electron Resistivity in Copper and Aluminum Induced by Electron Irradiation." *Phys. Rev.* 146 (1966): 468.

Ishizuka, K., "Contrast transfer of crystal images in TEM." *Ultramicroscopy* 5 (1980): 55-65.

Itoh, N., *Crystal Lattice Defects and Amorphous Materials* 3 (1972): 115.

Itoh, N., "Sputtering and Dynamic Interstitial Motion in Alkali Halides." *Nuclear Instr. and Methods* 132 (1976): 201-211.

Itoh, N., "Mechanism of Electron-Excitation-Induced Defect Creation in Alkali Halides." *Radiation Effects* 64 (1982): 1661-169.

Itoh, N. "Defect Processes Induced by Electronic Excitation in Insulators and Compound Semiconductors." *Crystal Lattice Defects and Amorphous Materials* 12 (1985): 1103-126.

Itoh, N. and T. Nakayama, "Mechanism of Neutral Particle Emission from Electron-Hole Plasma Near Solid Surface."*Physics Letters A* 92.9 (13 December 1982): 471-475.

Jennison, D.R., "An Analysis of Electronic Desorption" *Desorption Induced by Electronic Transitions DIET I* ed: N. H. Tolk, M. M. Traum, J. C. Tully, and T. E. Madey. Berlin: Springer-Verlag (1983) 26-30.

Jung, P., and G. Lucki, "Damage Production by Fast Electrons in Dilute Alloys of Vanadium, Niobium, and Molybdenum." *Radiation Effects* 26 (1975): 99.

Jung, P., and W. Schilling, "Anisotropy of the Threshold Energy for the Production of Frenkel Pairs in Tantalum." *Phys. Rev. B* 5 (1972): 2046.

Kabler, M. N., and R. T. Williams, "Vacancy-Interstitial Pair Production via Electron-Hole Recombination in Halide Crystals." *Phys. Rev. B* 18.4 (1978): 1948-1960.

Kang, Z. C., Eyring, L. and D. J. Smith, "Dynamic Edge and Surface Processes in Terbium Oxide." Ultramicroscopy 22 (1987): 71-80.

Karu, A. E., and M. Beer, "Pyrolytic Formation of Highly Crystalline Graphite Films." *J. Appl. Phys.* 37 (1966): 2179.

Katada, K. Nakahigashi and Y. Shimomura, "Precipitates with a Defect Structure in Thin Film of NiO."*Japanese Journal of Applied Physics* 9.9 (1970): 1019-1028.

Kelly, R., "Theory of Thermal Sputtering." *Radiation Effects* 32 (1977): 91-100.

Kelly, R. "Thermal Effects in Sputtering." *Surface Science* 90 (1979): 280-318.

Kelly, R., "On the Problem of Whether Mass or Chemical Bonding is More Important to Bombardment Induced Compositional Changes in Alloys and Oxides." *Surface Science* 100 (1980): 85-107.

Kelly, R. "Phase Changes in Insulators Produced by Particle Bombardment" *Nucl. Inst. Meth.* 182/3 (1981): 371-378.

Kelly, R. and N.Q. Lam, "The Sputtering of Oxides Part I: A Survey of the Experimental Results."*Radiation Effects* 19 (1973): 39-47.

Kim, K. S., W. E. Baitinger, J. W. Amy, and N. Winograd, "ESCA Studies of Metal-Oxygen Surfaces Using Argon and Oxygen Ion-Bombardment." *J. Electron Spectroscopy and Related Phenomena* 5 (1974): 351-367.

K.S. Kim, W.E. Baitinger, and N. Winograd, "X-Ray Photoelectron Spectroscopy Studies of PbO Surfaces Bombarded with He^+, Ne^+, Ar^+, Xe^+, and Kr^+" *Surface Science* 55 (1976): 285-290.

Kim, K. S., and R. E. Davis, "Electron Spectroscopy of the Nickel-Oxygen System." *J. Electron Spectrosc. and Rel. Phenom.* 1 (1972/73): 251-257.

Kim, K. S., and N. Winograd, "X-Ray Photoelectron Spectroscopic Studies of NiO Surfaces Using Oxygen and Argon Ion Bombardment." *Surface Science* 43 (1974): 625-643.

Kinchin, G.H., and R.S. Pease, "The Displacement of Atoms in Solids by Radiation." *Rept. Prog. Phys.* 18 (1955): 1-53.

Kingery, W. D., H. K. Bowen, and D. R. Uhlmann, *Introduction to Ceramics.* New York: John Wiley & Sons (1975) .

Kinniburgh, C. G., and J. A. Walker, "LEED Calculations for the NiO (100) Surface."*Surface Science* 63 (1977): 274-282.

Klick, Clifford C., "A Mechanism for Coloration of Alkali Halides at Low Temperatures." *Phys. Rev.* 120.3 (1960): 760-762.

Knotek, M. L., "Surface Chemical Information from Electron- and Photon-Stimulated Desorption." *Physica Scripta* T6 (1983): 94-103.

Knotek, M. L., "Stimulated Desorption from Surfaces." *Physics Today* (Sept. 1984): 24-32.

Knotek, M. L., and P. J. Feibelman, "Ion Desorption by Core-Hole Auger Decay."*Phys. Rev. Letters* 40.14 (1978a): 964-967.

Knotek, M. L., and Peter J. Feibelman, "Reinterpretation of Electron-Stimulated Desorption Data from Chemisorption Systems." *Phys. Rev. B* 18.12 (1978b): 6531-6539.

Knotek, M. L. and P. Feibelman , "Stability of Ionically Bonded Surfaces in Ionizing Environments." *Surface Science* 90 (1979): 78-90.

Kofstad, Per, *Nonstoichiometry, Diffusion, and Electrical Conductivity in Binary Metal Oxides*. New York:Wiley-Interscience (1972).

Lam, N. Q. and R. Kelly, "Bombardment-Induced Amorphization in WO_3 and its Use in Deducing Mean Damage Ranges." *Canadian J. Phys.* 50 (1972): 1887.

Lamber, R., N. Jaaeger, and G. Schulz-Ekloff, "Electron Microscopy Study of the Interaction of Ni, Pd and Pt with Carbon I: Nickel catalyzed graphitization of amorphous carbon." *Surface Science* 197 (1988): 402-414.

Larkins, F. P., and P. J. Fensham, *Trans. Faraday Soc.* 66 (1970): 1755.

Lehman, C., *Interaction of Radiation With Solids and Elementary Defect Production.* Amsterdam: North Holland Publishing Co. (1977).

Lin, T. T, and D. Lichtman, "AES Studies of Chemical Shift and Beam Effects on Molybdenum Oxides." *J. Vac. Sci. Technol.* 15 (1978): 1689.

Lin, T. T, and D. Lichtman, "Electron Irradiation Effects on Oxidized Nb Foil and NbO." *J. Materials Science* 14 (1979a): 455.

Lin, T. T, and D. Lichtman, "The effects of electron bombardment on the surface composition of WO_3, oxidized W and Ta foils." *J. Appl Phys.* 50 (1979b): 1298.

Lindhard, J., V. Nielse, and M. Scharff, *Mat. Fys. Medd. Dan.Vidensk. Selsk.* 36.10 (1968).

Lindhard, J. M. Scharff, and H. E.Schiott, *Mat. Fys. Medd. Dan. Vid. Selsk.* 33.14 (1963).

Liu, P. L., R. Yen, N. Bloemberger, P. T. Hodgson, "Picosecond Laser-Induced Melting and Resolidification Morphology on Si." *Appl. Phys. Lett.* 34 (1979): 864.

Liu, J., and J. M. Cowley, "Electron Beam Radiation Effects on NiO Crystals." *Proceedings of the 45th Annual Meeting of the Electron Microscopy Society of America* ed: G. W. Bailey. San Francisco: San Francisco Press (1987): 176-177.

Long, N., and A. K. Petford-Long, "In-Situ Electron-Beam-Induced Reduction of CuO: A Study of Phase Transformation in Cupric Oxide." *Ultramicroscopy* 20 (1986): 151-160.

Lucasson, P. G., and R. M. Walker, "Production and Recovery of Electron-Induced Radiation in a Number of Metals." *Phys. Rev.* 127 (1962): 485.

Luzzi, D. E., L. D. Marks, M. I. Buckett, J. W. Strane, B. W. Wessels and P. C. Stair, "HREM In-Situ Studies of Electron Irradiation Effects in Oxides." *Materials Research Society Symposium Proceedings - Fall 1987.* 100 (1988): 635-640.

Luzzi, David., "The Electron Irradiation Induced Crystal to Amorphous Transition in Cu-Ti Intermetallic Compounds." *Ph.D. thesis.* Northwestern University (1986): 266-272.

Mackrodt, W.C., "Defect Energetics and Their Relation to Nonstoichiometry in Oxides." *Solid State Ionics* 12 (1984): 175-188.

Mandelcorn, L., *Non-Stoichiometric Compounds.* New York: Academic Press (1964).

Marks, L. D., "Direct Imaging of Carbon-Covered and Clean gold (110) Surfaces." *Phys. Rev. Letters* 51 (1983): 1000-1002.

Marks, L.D., "Direct Atomic Imaging of Solid Surfaces, I. Image simulation and interpretation." *Surface Science* 139 (1984): 281-298.

Marks, L. D, "Image Localization." *Ultramicroscopy* 18 (1985): 33-38.

Marks, L.D., A. K. Petford and M. O'Keefe, "Atomic Imaging of Oxygen Desorption from Tungsten Trioxide." *Surface Science* 172 (1986): 496.

Marks, L. D., and D. J. Smith, "Direct surface imaging in small metal particles." *Nature* 303 (26 May 1883): 316-317.

Marks, L. D., and D. J. Smith, "Direct Atomic Imaging of Solid Surfaces II: Gold (111) Surfaces during and After In-situ Carbon Etching."*Surface Science* 143 (1984): 495.

Mathieu, H. J., and D. Landolt, *Proc. 7th Int. Vacuum Congress.* Vienna (1977): 2023.

Matzke, Hj., "Inert Gas Diffusion and Radiation Damage in Ionic Crystals and Sinters Following Ion Bombardment."*Canadian J. Phys.* 46 (1968): 621.

Matzke, Hj,. "Diffusion in Nonstoichiometric Oxides." *Materials Science and Technology Series - Nonstoichiometric Oxides.* New York: Academic Press (1981).

Maury, F., P. Vajda, A. Lucasson and P. Lucasson, "Atomic Displacements in Low-Temperature Electron Irradiated Cobalt." *Radiation Effects* 21 (1974): 65.

Mayer, J. W., and S. S. Lau *Electronic Materials Science: For Integrated Circuits in Si and GaAs* New York: Macmillan Publishing Co. (1990): 232-239.

McCartney, M. R., and D. J. Smith, "Epitaxial Relationships in Electron-Stimulated Desorption Processes at Transition Metal Oxide Surfaces." *Surface Science* 221 (1989): 214-232.

McCartney, M. R., and D. J. Smith, "Surface Structures and Rearrangements in Oxides." *Materials Research Society Symposium Proceedings* 183 (1990): 311-316.

McCune, J., E. Chelgren and M. Wheeler, "^{4}He+ Ion Scattering Spectroscopy of Tantalum Oxide Below 1.0 keV." *Surface Science* 84 (1979) L515-L520.

McGuire, E., "Electron ionization cross section in the Born approximation." *Phys. Rev A* 16.1 (1977): 62-79.

McKinley, W.A., and H. Feshbach, "The Coulomb Scattering of Relativistic Electrons by Nuclei." *Phys. Rev.* 74 (1948): 1759-63.

Menzel, D., "Electron Stimulated Desorption: Principles and Recent Developments." Surface Science 47 (1975): 370-383.

Menzel, D., "Desorption Induced by Electronic Transitions." *Nucl. Instr. and Methods in Phys Res.* B13 (1986): 507-517.

Menzel, D. and R. Gomer, "Desorption from Metal Surfaces by Low Energy Electrons." *J. Chem. Phys.* 41[11] (1964): 3311-3328.

Merkle, K., "Heavy Ion Damage in Metals." *Proc. Physics of Ionized Gases 1974* ed: V. Vujnovic, V. Rovinj. Yugoslavia, September 16-21, 1974.

Mitoff, S. P., "Electrical Conductivity and Thermodynamic Equilibrium in Nickel Oxide." *J. Chem. Phys.* 35 (1961): 882-889.

Monty, C., "Diffusion in Stoichiometric and Non-Stoichiometric Cubic Oxides." *Radiation Effects* 74 (1983): 29-55.

Mott, N. F., "The Scattering of Fast Electrons by Atomic Nuclei." *Proc. Roy. Soc. (London)* A124 (1929): 425-442; "The Polarisation of Electrons by Double Scattering." A135 (1932): 429.

Mott, N. F. and H. S. W. Massey, *The Theory of Atomic Collisions* Oxford: Clarendon Press (1965).

Mott, N. F., "Metal-Insulator Transition." *Reviews of Modern Physics* 40 (1968): 677-683.

Murti, D. K., and R. Kelly, "Preferential Oxygen Sputtering from Nb_2O_5." *Thin Sol. Films* 33 (1976): 149-163.

Murti, D. K., R. Kelly, Z. L. Liau and J. M. Poate, "Structural and Compositional Changes in Ion-Bombarded Ta_2O_5" *Surface Science* 81 (1979): 571.

Naguib, H. M., and R. Kelly, "The crystallization of amorphous ZrO_2 by Thermal Heating and by Ion Bombardment." J. Nuc. Materials 35 (1970): 293-305.

Naguib, H. M. and R. Kelly, "On the Increase in the Electrical Conductivity of MoO_3 and V_2O_5 Following Ion Bombardment." *J. Phys. Chem.Solids* 33 (1972): 1751-1759.

Naguib, H. M. and R. Kelly, "Criteria For Bombardment-Induced Structural Changes in Non-metallic Solids." *Radiation Effects* 25 (1975): 1-12; "The Effect of Ion Bombardment on the Structure of Bi_2O_3, MoO_3, TeO_2, and V_2O_5." *Radiation Effects* 25 (1975): 79-89.

Netzer, F. P., and M. Prutton, "LEED and Electron Spectroscopic Observations on NiO (100)." *J. Phys. C* 8 (1975): 2401.

Niehus, H., and W. Losch, "ESD on Metal Oxides and Oxygen Adsorption Layers: Evidence for Different Mechanisms in Electron Stimulated Desorption." *Surface Science* 111 (1981): 344-350.

Nishijima, M., and F. M. Propst, "Electron Impact Desorption of Ions from Polycrystalline Tungsten." *Phys. Rev B* 2 (1970): 2368.

Oechsner, H. , H. Schoof and E. Stumpe, "Sputtering of Ta_2O_5 by Ar+ Ions at Energies Below 1 keV."*Surface Science* 76 (1978): 343.

Olander, Donald R. *Fundamental Aspects of Nuclear Reactor Fuel Elements* Technical Information Center Energy Research and Development Administration (1976): 373-417.

O'Neill, H., and A. Navrotsky, "Simple spinels: crystallographic parameters, cation radii, lattice energies, and cation distribution." *American Mineralogist* 68 (1983): 181-194.

Ostyn, K. M. , and C. B. Carter, "Effects of Ion-Beam Thinning on the Structure of NiO." *Electron Microscopy* 2 (1982): 191.

Overeijnder, H., A. Haring and A. E. de Vries, "The Sputtering Processes of Alkali Halides During 6 keV Xe^+ Bombardment." *Radiation Effects* 37 (1978a): 205-210.

Overeijnder, H., M.Szymonski, A. Haring and A. E. de Vries "Energy Distribution of Atoms Sputtered from Alkali Halides by 540 eV Electrons" *Radiation Effects* 36 (1978b): 63-71.

Palmberg, P. W., R.E. De Wames, L.A. Vredevoe and T. Wolfram, "Coherent Exchange Scattering of Low-Energy Electrons by Antiferromagnetic Crystals." *J. Appl. Phys.* 40.3 (1969): 1158-1163.

Parker, T. E., and Roger Kelly, "Ion-Impact Chemistry in the System Titanium-Oxygen (Studies on Bombardment-Enhanced Conductivity-III)." *J. Phys. Chem. Solids* 36 (1975): 377-385.

Pauling, L., *The Nature of the Chemical Bond* Ithaca, N.Y.: Cornell University Press (1939).

Pells, G.P. and D. C. Phillips, "Radiation Damage of α-Al_2O_3 in the HVEM" *J. Nuc. Matl.* 80 (1979): 207-214.

Peterson, N. L., "Impurity Diffusion in Transition-Metal Oxides."*Solid State Ionics* 12 (1984): 201-215.

Peterson, N. L., and C. L Wiley, "Point Defects and Diffusion in NiO." *J. Phys. Chem. Solids* 46.1 (1985): 43-52.

Petford, A. K., L. D. Marks, and M O'Keefe, "Atomic Imaging of Oxygen Desorption form Tungsten Trioxide." *Surface Science* 172 (1986): 496-508.

Phillips, J. C., "Ionicity of the Chemical Bond in Crystals." *Rev. Modern Phys.* 42 (1970): 317.

Pines, D., "Electron Interaction in Metals" *Solid State Physics* 1. ed: F. Seitz and D.Turnbull. New York: Academic Press (1955): 367-449.

Pooley, D., "F-Center Production in Alkali Halides by Radiationless Electron Hole Recombination."*Solid State Communications* 3 (1965): 241-243.

Prutton, M., J. A. Walker, M. R.Welton-Cook and R.C. Felton, "LEED Studies of the Structures of the (100) Surfaces of Divalent Metal Oxides." *Surface Science* 89 (1979): 95-101.

Redhead, P. A., "Interaction of Slow Electrons with Chemisorbed Oxygen." *Canadian J. Phys.* 42 (1964): 886-905.

Rogers, D.B., R. D. Shannon, A. W. Sleight and J. L. Gillson, *Inorganic Chemistry* 8 (1969): 841.

Roth, W. L, "Magnetic Structures of MnO, FeO, CoO, and NiO." *Physical Review* 110.6 (1958): 1333-1341.

Sangster, M. J. L., and D. K. Rowell, "Calculation of Defect Energies and Volumes in Some Oxides." *Phil. Mag. A* 44.3 (1981): 613 - 624.

Saxton, W. O., *Computer Techniques for Image Processing in Electron Microscopy.* New York: Academic Press (1978).

Seitz, F., and J.S. Koehler, "Displacement of Atoms during Irradiation." *Solid State Physics* 7 ed: F. Seitz and D. Turnbull. New York: Academic Press, Inc. (1958): 305-448.

Seitz, F., *Discussions of the Faraday Soc.* 5 (1949): 571.

Shannon, R. D., "Revised Effective Ionic Radii and Systematic Studies of Interatomic Distances in Halides and Chalogenides." *Acta Cryst. A* 32 (1976): 751.

Sharp, J. V., and D. Rumsby, "Electron Irradiation Damage in Magnesium Oxide." *Radiation Effects* 17 (1973): 65-68.

Shimomura, Y., M. Kojima and S. Saito, "Crystal Structure of Ferromagnetic Nickel Oxide." *J. Phys. Soc. (Japan)* 11.11 (1956): 1136-1146.

Shvarts, K. K., "Radiation Damage in Crystalline and Amorphous Dielectrics" *Radiation Effects* 74 (1983): 77-85.

Sigmund, P., "Sputtering by Ion Bombardment: Theoretical Concepts." *Sputtering by Particle Bombardment I* ed: R. Behrisch. Berlin: Springer-Verlag (1981): 9-71.

Sigmund, P., "Theory of Sputtering. I. Sputtering Yield of Amorphous and Polycrystalline Targets." *Phys. Rev. B* 184.9 (1969): 383-395; "Errata" 187.2 (1969): 768.

Sigmund, P., "Selected Aspects of Ion Scattering, Energy Deposition and Sputtering." *Physics of Ionized Gases* ed: M.V. Kurepa. Beograd: Institute of Physics (1972).

Simons, P.Y. and F. Dachelle, "The Structure of TiO_2-II, a High Pressure Phase of TiO_2." *Acta Cryst.* 23 (1967): 334.

Singh, S. R. , and L. D. Marks, "Diffusion during electron-beam-induced reduction of tungsten trioxide." *Phil. Mag. Letters* 60.1 (1989): 31-36.

Smeltzer, W. W., and K. J. Young, "Oxidation Properties of Transition Metals." *Progress in Solid-State Chemistry* 10.1 (1975): 17-54.

Smith, D. J., and L. A. Bursill, "Metallization of Oxide Surfaces Observed by In Situ High Resolution Electron Microscopy." *Ultramicroscopy* 17 (1985): 387.

Smith, D. J., L. A. Bursill, and D. A. Jefferson, "Atomic Imaging of Oxide Surfaces I: General Features and Surface Rearrangements."*Surface Science* 175 (1986): 673-683.

Smith, D. J., and L. D. Marks, "Direct Atomic Imaging of Solid Surfaces III: Small Particles and Extended Au Surfaces." *Ultramicroscopy* 16 (1985): 101-114.

Smith, D. J. , M. R. McCartney and L.A. Bursill, "The Electron-Beam-Induced Reduction of Transition Metal Oxide Surfaces to Metallic Lower Oxides."*Ultramicroscopy* 23 (1987): 299-304.

Smith, T., "Auger Electron Spectroscopy and Ion Sputter Profiles of Oxides on Aluminum." *Surface Science* 55 (1976): 601-604.

Sommerfeld, A., "Asymptotische Integration der Differentialgleichung des Thomas-Fermischen Atoms." *Z. Phys.* 78 (1932): 283.

Sonder, E., and W. A. Sibley, "Defect Creation by Radiation in Polar Crystals." *Point Defects in Solids 1* ed: J. H. Crawford, Jr. and L. M. Slifkin. New York: Plenum Press (1972): 201-283.

Sosin, A., and W. Bauer, "Atomic Displacement Mechanism in Metals and Semiconductors." *Studies in Radiation Effects in Solids* 3 ed: G.J. Dienes. New York: Gordon and Breach Science Publishers (1969).

Spence, J. C. H., *Experimental High Resolution Electron Microscopy* New York: Oxford Press (1980).

Strane, J., "Irradiation Damage on Rutile Surfaces Observed in a High Resolution Electron Microscope" *M.S. Thesis*, Northwestern University (1988).

Strane, J., L. D. Marks, D. E. Luzzi, M. I. Buckett, J. P. Zhang and B. W. Wessels, "Encapsulation, Diffusion and DIET in the Electron Microscope."*Ultramicroscopy* 25 (1988): 253-258.

Suzuki, T., N. Hirota, H.Tanaka and H. Watanabe, "Exchange Scattering of Low-Energy Electrons from Antiferromagnetic NiO." *J. Phys. Soc. (Japan)* 30 (1971): 888.

Taglauer, E. and W. Heiland, "Mass and energy dependence of the equilibrium surface composition of sputtered tantalum oxide." *Applied Phys. Letters* 33 (1978): 950-952.

Takanayagi, K., "Ultra High Vacuum Transmission Electron Microscopy on the Monolayer Condensation Process of Lead on Silver (111) Surface." *Surface Science* 104 (1981): 527-548.

Tamai, Y., Y. Nishiyama and M. Takahashi, "Carbon Deposition on Iron and Nickel Sheets from Light Hydrocarbons."*Carbon* 6 (1968): 593-602.

Tasker, P. W., and D. M. Duffy, "The Structure and Properties of the Stepped Surfaces of MgO and NiO."*Surface Science* 137 (1984): 91.

Townsend, P. D., "A New Interpretation of the Rabin and Klick Diagram." *Journ. Phys. C* 6 (1973): 961-966.

Townsend, P. D., R. Browning, D. J. Garlant, J. C. Kelly, A. Mahjoobi, A. J. Michael, and M. Saidoh, "Sputtering Patterns and Defect Formation in Alkali Halides." *Radiation Effects* 30 (1976a): 55-60.

Townsend, P. D., Kelly, J. C., and N. Hartley, *Ion Implantation, Sputtering, and Their Applications* London: Academic Press (1976b): 11-27.

Toyozawa, Y., *Vacuum Ultraviolet Radiation Physics* Braunschweig: Pergamon Vieweg (1973).

Tully, J. C., "Direct and Indirect Mechanisms of Stimulated Desorption." *DIET I Desorption Induced by Electronic Transitions* ed: N. H. Tolk, M. M. Traum, J. C. Tully, Madey, T. E. Berlin: Springer Verlag (1983): 31-38.

Urban, K., "Studies on Radiation-Induced Point Defects in Metals by Means of High-Voltage Electron Microscopy." *Fundamental Aspects of Radiation Damage in Metals* 11 ed: M. T. Robinson and F. W. Young, Jr. (1975): 675-691.

U.S. Standard Atmosphere 1976. Washington, D. C.: U.S. Government Printing Office (1976): 30.

Vajda, Peter, "Anisotropy of electron radiation damage in metal crystals." *Reviews of Modern Physics* 49.3 (1977): 481-520.

Van Vechten, J. A., R. Tsu and F. Saris, "Nonthermal Pulsed Laser Annealing." *Physics Letters* 74A.6 (10 December 1979): 422-426.

Varley, J. H. O., "A Mechanism for Displacement of Ions in an Ionic Lattice." *Nature* 174.4436 (6 November 1954): 886-887.

Verhoeven, J., Wang Wen-hao and J. J. Czyzewski, "The Role of Inner Shell Excitations in ESD of Oxygen Ions From a Nickel Oxide Surface." *Surface Science* 143 (1984): 31-36.

Wang, Wen-hao, and J. Verhoeven, "The Anomalous Behavior of the ESID O+ Yield From a Ni(110) Surface During Oxygen Adsorption." *Surface Science* 175 (1986): 325-335.

Wedepohl, P. T., "A Simple Analytical Form of the Thomas-Fermi Screening Function and of Firsov's Atomic Interaction Potential." *J. Phys. B (Proc. Phys. Soc.)* 2.1 (1968): 307.

Wedepohl, P.T., "The Atomic Interaction Potential." *Radiation Effects* 1 (1969): 77.

Welton-Cook, M. R., and M. Prutton, "LEED calculations for the NiO (100) surface: extension to lower energies." *J. Phys. C* 13 (1980): 3993-4000.

Williams, Fred E., "Theory of Defect Formation in Alkali Halides by Ionizing Radiation." *Phys. Rev. 126.1* (1961): 70-72.

Williams, R. T., C. L. Marquardy, J. W. Williams and M. N. Kabler, "Transient Absorption and Luminescence in MgF_2 Following Electron Pulse Excitation." *Phys. Rev. B* 15 (1977): 5003-5011.

Wood, G. C., I. G.Wright and J. M. Ferguson, "The Oxidation of Ni and Co and of Ni/Co Alloys at High Temperatures." *Corrosion Science* 5 (1965): 645.

Zhang, J. P., and L. D. Marks, "Symmetry in Diet Phase Transitions." *Surface Science* 222 (1989): 13-20.

JCPDS Crystal Data, Determinative Tables Vol II ed: J. D. H. Donnay and H. M. Ondik. U.S. Department of Commerce, National Bureau of Standards, and the Joint Committee on Powder Diffraction standards (1973).